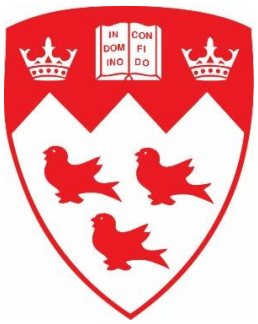

Advanced quality assurance methodologies in image-guided high-dose-rate brachytherapy

Saad Aldelaijan

Department of Biomedical Engineering

McGill University

Montréal, Québec

December, 2020

A thesis submitted to McGill University in partial fulfillment of the requirements of the degree of Doctor of Philosophy

إهداء إلى تاج راسي: أمي و أبوي.

(To "Taj Rasi"; Ommi o Oboi.)

To my big brother; Mohammed.

To the love of my life; my girls.

For all your sacrifices and patience.

ABSTRACT

Brachytherapy (BT) was the first form of radiotherapy and it is still effectively used because of its unique physical and biological advantages. Although the principles of BT operation are considered to be relatively simple (since it is based on the correct timing and positioning of radioactive sources), BT has also benefitted from technological advances. The rate of technical inventions and their incorporation into BT treatments has necessitated development of more precise quality assurance (QA) tools. The purpose of this thesis is to introduce a robust QA framework based on radiochromic film (RCF) dosimetry for image-guided high-dose-rate (HDR) BT. These films can be digitized allowing for high spatial resolution visualization of the source dosimetric trace, which can be used to reconstruct the source positions and evaluate the dose distribution simultaneously.

To increase the HDR source-tracking reliability, a film-digitization protocol was developed. This protocol evaluates issues related to film scanning and handling, and specifies parameters of film response and mathematical models that relate this response to absorbed dose. The protocol is based on a new linear response function, 'normalized pixel value' (*nPV*), and it was designed to achieve high accuracy while maintaining practicality. It was further improved by using all RGB (Red, Green, Blue) color information available in RCF scanned images, to correct for scanning-related issues. This protocol was tested and validated for six independent RCF dosimetry systems in three different clinics, demonstrating robustness of the method and its ability to mitigate systematic response shifts.

The first application of this dosimetry protocol was in the QA of Freiburg Flap (FF) based treatments in HDR surface BT. The current standard of care in treatment planning of surface BT does not take into account the lack of backscatter above the FF and patient skin, since it assumes the HDR source is always surrounded by water. Before comparing planned and

delivered doses, the film response was calibrated and a detailed uncertainty budget was discussed. The RCF dosimetry system was able to report the difference between the calculated and delivered doses for different setups and to evaluate the use of bolus to reduce these differences.

Subsequently, the source-tracking algorithm was developed to precisely localize the HDR source within catheters based on the acquired 2D distribution from the RCF. The algorithm relies on measured-features of the relative isodose lines (blob analysis) such as area, perimeter, weighted-centroid, elliptic orientation, and circularity. A reference library of features was prepared based on the AAPM TG-43 datasets and correlations were derived between these features and the source coordinates (x, y, z, θ_y, θ_z). The measured features are then compared to the reference ones and the most probable source coordinates are reported. The source-tracking algorithm was verified experimentally with an accuracy of 0.1 mm by having two film sets on opposing ends of the source. This technique offers a novel method having the potential to be used for source QA of commercial and customized applicators.

This thesis addressed the acquisition of accurate 2D dose maps with RCF which is essential for the detection of the HDR source dosimetric trace when using the source-tracking algorithm. This included the calibration of RCF for HDR BT dosimetry and their use in dose verification. The thesis also demonstrated the potential incorporation of these findings into a comprehensive image-guided HDR BT QA framework. In the future, the framework is intended to encompass all the software and strategies developed thus far and adapt new algorithms taking advantage of simple irradiation patterns yet revealing many QA metrics accurately.

RÉSUMÉ

La curiethérapie (CRT) a été la première forme de radiothérapie et elle est toujours utilisée de manière efficace en raison de ses avantages physiques et biologiques uniques. Bien que les principes de fonctionnement de la CRT soient considérés comme relativement simples (car ils sont basés sur la synchronisation et le positionnement adéquats des sources radioactives), la CRT a aussi bénéficié d'avancées technologiques. Le taux d'inventions techniques et leur incorporation dans les traitements de CRT ont nécessité le développement d'outils d'assurance de la qualité (AQ) plus précis. Le but de cette thèse est d'introduire un cadre d'AQ haute résolution basé sur la dosimétrie à film radiochromique (FRC) pour la CRT à débit de dose élevé (HDR) assistée par imagerie médicale. Ces films peuvent être numérisés et permettre une visualisation haute résolution de la trace dosimétrique source, qui peut être utilisée pour retracer les positions de la source et évaluer sa répartition de dose de façon simultanée.

Pour augmenter la fiabilité du suivi des sources à HDR, un protocole de numérisation des films a été développé. Ce protocole évalue et détaille tous les problèmes liés à la numérisation, à la manipulation, à la définition de la réponse du film et aux modèles mathématiques qui associent cette réponse à la dose absorbée. Le protocole est basé sur une nouvelle fonction de réponse linéaire, la valeur des pixels normalisée (*nPV*), et il a été conçu pour obtenir une grande précision tout en restant pratique. Il a été encore plus amélioré en utilisant toutes les informations disponibles sur les couleurs RVB dans les images numérisées et les caractéristiques spécifiques d'image pour corriger les problèmes liés à la numérisation. Ce protocole a été testé et validé pour six systèmes de dosimétrie à FRC indépendants dans trois cliniques différentes, démontrant la durabilité de la méthode et sa capacité à diminuer les changements de réponse systémiques.

La première application de ce protocole de dosimétrie a été dans l'AQ des traitements à base de Freiburg Flap (FF) en CRT de surface à HDR. La norme des soins actuelle dans la planification du traitement de CRT de surface ne prend pas en compte le manque de rétrodiffusion

au-dessus du FF et de la peau du patient, car elle suppose que la source à HDR est toujours entourée d'eau. Avant de comparer les doses prévues et administrées, la réponse du film a été calibrée et un bilan d'incertitude détaillé a été discuté. Le système de dosimétrie à FRC a pu rapporter la différence entre les doses calculées et administrées pour différentes configurations et suggérer des façons de réduire ces différences.

Par la suite, l'algorithme de suivi des sources a été développé pour localiser précisément la source à HDR dans les cathéters en fonction de la distribution 2D acquise à partir du FCR. L'algorithme repose sur des éléments mesurés des lignes isodose relatives (analyse de taches) telles que l'aire, le périmètre, le centroïde pondéré, l'orientation elliptique et la circularité. Une bibliothèque de référence d'éléments a été préparée sur la base des ensembles de données AAPM TG-43 et des corrélations ont été déterminées entre ces éléments et les coordonnées sources (x, y, z, θ_y, θ_z). Les éléments mesurés sont ensuite comparés à ceux de référence et les coordonnées sources les plus probables sont rapportées. L'algorithme de suivi des sources a été vérifié à titre expérimental avec une précision de 0,1 mm en plaçant deux films sur les extrémités opposées de la source. Cette technique offre une nouvelle méthode pouvant être utilisée pour l'AQ source des applicateurs commerciaux et sur mesure.

Cette thèse portait sur l'acquisition de cartes de dose 2D précises avec FRC, ce qui est essentiel pour la détection de la trace dosimétrique source à HDR lors de l'utilisation de l'algorithme de suivi des sources. Cela comprenait le calibrage du FRC pour la dosimétrie de CRT à HDR et son utilisation dans la vérification de la dose. La thèse a également démontré l'intégration potentielle de ces résultats dans un cadre détaillé d'AQ de CRT à HDR assistée par imagerie médicale. À l'avenir, le cadre vise à englober tous les logiciels et les stratégies développés jusqu'à présent et à adapter de nouveaux algorithmes en tirant parti de modèles d'irradiation simples, mais qui révèlent avec précision de nombreuses mesures d'AQ.

ACKNOWLEDGMENTS

In the beginning I would like to thank Almighty Allah for his blessings, guidance, mercy and support through all hardships. I was very lucky during my PhD to get the opportunity to work and learn from three different academic departments (Biomedical Engineering Department of McGill University, Medical Physics Unit (MPU) of McGill University, and Medical Physics & Biophysics Division of Brigham & Women's Hospital/Harvard Medical School).

I would like to thank King Faisal Specialist Hospital & Research Center for supporting me through my studies, and specifically Dr Belal Moftah, Mr Abdulaziz AlBahkaly, all the academic and training administration and the research center administration for their continuous support through my scholarship, especially in unforeseen situations. I would like to thank the Saudi Arabian Cultural Bureau in Canada, especially Dr Fawzy Bukhary, Ms Amira Atris, Dr Ali Elghirani for their care and support throughout my PhD. Without their diligence I would not have accomplished the goals of my PhD.

I would like to extend my sincere thanks to my supervisor Dr. Slobodan Devic for his continuous support, guidance and encouragement during my PhD. I have known Dr Devic since I started my M.Sc. at McGill, that is 12 years ago, and we have been doing research together since then. I always have felt that our research brought us closer and we indeed feel more like a family; as you would expect in any student-supervisor relationship. That is not the same in our case because it is my sheer belief that there is more to it. Dr Devic is a friend, a family, a mentor, a coach, and a big brother. I cannot recall how many times he and his beautiful family (Nada, Milosh, Ana, parents in law) welcomed me to their own home and helped me adapt. Indeed, they are my family in North America. Dr Devic convinced me to seek my PhD and helped me countless times in unforeseen situations. He literally paved the way for my success and facilitated my admission to McGill and transfer to Boston. He always spoke up for me, supported me, listened to all my ideas (!), guided me and helped me see what is important no matter where I was. I owe everything to him and will never be able to return the countless favors and hours he spent with me during all these years.

I would like to thank my committee members: Prof Louis Collins, Prof Jan Seuntjens, Prof Robert Funnell, Dr Ivan Buzurovic, Dr Slobodan Devic; for their guidance, support, enthusiasm and inspiration. I am very thankful to Prof Louis Collins for accepting me as his PhD student, warmly welcoming me at the Biomedical Engineering Department and providing very helpful guidance during my PhD meetings and progress reports. I am also very thankful to Prof Jan Seuntjens for always believing in me and providing much-needed support at moments of need. He transformed the MPU into something we are all proud of and inspired us in the process. I would like to thank Prof Funnell for chairing my committee and professionally guiding me during the comprehensive examination process and afterwards. I cannot thank enough Ms Pina Sorini for all the guidance she provided and timely support during regular and unforeseen times. She always went up and beyond in the organization of my PhD while always keeping a smile! I am also thankful to Mr Daniel Caron and Ms Sabrina Teoli for their professional and kind support during my admission and PhD meetings. I cannot thank enough Ms Margery Knewstubb and Ms Tatjana Nisic of the Medical Physics Unit whom I have known since 2008. They have always supported me personally and shared smiles whenever I passed by. I would like to thank Dr Pavlos Papaconstadopoulos, Dr Hamed Bekerat, James Schneider for all the enlightening discussions (and fun) we had together and ideas that technically improved me a lot. I would like to also thank all my Montreal friends and colleagues who really helped me in different ways: Mosaab and Maryam, Nada, Liang, Krum, Phil, Francois, Alban, Nicole, Vincent, Stella, Jessica, Yana, Logan, Joel, Marc, Georges, Andre, Gabriel, Haley, Ali, Judy, Veronique, Peter T.

I would like to thank Dr Ivan Buzurovic for welcoming me at the Brigham and Women's Hospital (BWH) in Boston and supporting me professionally and personally through very fruitful two years. His help, inspiration and guidance was essential for me. Together, we established the radiochromic film dosimetry lab at BWH and we also started an *in-vivo* dosimetry program for HDR brachytherapy and applicator quality assurance procedure. Dr Buzurovic understood my personality and pushed me to achieve more at so many levels. I am so thankful and indebted to him for the many hours he spent discussing ideas and improving my academic skills. Without his help and guidance, I would not be where I am today. I would like to thank Prof Mike Makrigiorgos for welcoming me at the Medical Physics & Biophysics Division of BWH and for providing continuous support and enthusiasm about my research. I would like to thank Dr Phillip M. Devlin for supporting my research on *in-vivo* dosimetry in surface brachytherapy. He is a true inspiration in leadership and I learned many things by watching him and his approach. I would like to thank other members of the brachytherapy group: Desmond, Tom, Scott, Robert, Emily, Mandar, Yasser, Marjan, Marianne, Kristin,

Tania, Kep, Alicia, Jennifer, Peter, Kyle. These people have truly showed me how brachytherapy can be run at the highest levels while always keeping a smile. I learned a lot from all of them and I will always cherish their friendships. I would like to thank Dr Matt Jacobson for all the gardening and programing experience he shared with me. I would like to thank Carolyn Dahlberg (best smile!) and Bonnie Baines for all the administrative help they provided me at Boston and the positive vibes they always emit! I would like to especially thank Yasser Khouj for making my Boston experience feels like home. I cannot express the countless laughs we shared and the fun times we spent together. I learned a lot from him and can never repay his kindness. I would like to also thank all my Boston friends and colleagues who taught me a lot and helped me in different ways: Jihun, Ingrid, Davide, Christian, Romy, Dianne, Needa, Michelle, Mengying, Yiwen, Steffen, Tim, Lubna, Salameh, Sarah, Mohsin, Johann, Nick, Caitlyn, Cindy, Yaguan, Tony, Anand, Rebecca, Noelle, Iquan, Eddie, Will, Ross, Yulia, Elizabeth, Hyrei, Chris, Jeremy, Zhaohui, Maria, David, Piotr, Jackie, Amber, Kellie, Marissa, Alex, Lina.

My journey included a lot of travel and no one has sacrificed more than my family during those times. I am indebted to my wife (Laila) for all the sacrifices she's gone through so that I get my PhD (and still!). I am so proud of her and I sincerely believe she's the smartest person I know. She's the perfect role model for our beautiful daughters. To Leen and Reema: I have not been there for you for most of the time but your love is what made everything possible and will bring us together soon. I hope this thesis inspire you when it is time for you to set sail on your own journeys. To my mother (Rajaa) and father (Ibrahim): I am where I am today because of your love, tireless prayers and inspiration. Growing up watching you sculpted my character and deeply paved my way with the world. I see you in every decision I make and I cannot thank you enough. To Raneem and Emad: your love and support kept me moving, more than you imagine.

I hope that those, whom I forgot to mention, forgive my ignorance and accept my gratitude and apologies.

TABLE OF CONTNETS

ABSTRACT **4**

RÉSUMÉ **6**

ACKNOWLEDGMENTS **8**

TABLE OF CONTNETS **11**

LIST OF FIGURES **16**

LIST OF TABLES **25**

CHAPTER 1: Introduction **26**

1.1 Motivation 26

1.2 Overview of thesis 27

1.3 Author contributions 27

1.4 Scientific contributions 29

CHAPTER 2: Background and literature review **31**

2.1 Introduction to brachytherapy 31

2.1.1 Types of brachytherapy 31

2.1.2 Advantages of brachytherapy 32

2.1.3 Clinical outcomes of brachytherapy 35

2.2 Image-guided brachytherapy 37

2.2.1 Transition from 2D to 3D image-guidance 37

2.2.2 Process of image-guided brachytherapy 41

2.3 Quality assurance in brachytherapy 43

2.3.1 Importance of quality assurance 43

2.3.2 Current practice in HDR brachytherapy quality assurance 44
2.3.3 Temporal and positional accuracy 45
2.3.4 HDR source description and absolute dose determination 46
2.3.5 Dose distribution of HDR brachytherapy sources 47
2.4 Technological advancement in HDR brachytherapy QA 49
2.4.1 Dosimetric tools 49
2.4.2 Dose calculation and optimization 50
2.4.3 Applicator fabrication and customization 52
2.4.4 Intensity modulation 52
2.5 Background on radiochromic film dosimetry 54
2.5.1 General characteristics 54
2.5.2 Definition of radiochromic film dosimetry system 54
2.5.3 Use of radiochromic film for dosimetry 56
2.6 Use of radiochromic film dosimetry for HDR brachytherapy QA 57
CHAPTER 3: Comparison of dose response functions for EBT3 model GafChromic™ film dosimetry system 58
Preface 58
Abstract 59
3.1 Introduction 60
3.2 Materials and Methods 62
3.3 Results and Discussion 68
3.4 Conclusions 72
3.5 Acknowledgement 73
3.6 References 73
CHAPTER 4: Dose response linearization in radiochromic film dosimetry based on multichannel normalized pixel value with an integrated spectral correction for scanner response variations 76
Preface 76
Abstract 77
4.1 Introduction 79

4.2 Materials and Methods 80
4.2.A Radiochromic film dosimetry system 80
4.2.B Film calibration and irradiation setups 80
4.2.C Film scanning and image analysis 81
4.2.D Multichannel normalized pixel value 82
4.3 Results 88
4.3.A Multichannel normalized pixel value 88
4.3.B Testing the multichannel normalized pixel value and correction protocol 90
4.4 Discussion 96
4.4.A Advantages and limitations of linearization 96
4.4.B The fingerprint correction protocol 98
4.4.C Short term scanner response variability 99
4.4.D Scanner bed inhomogeneity and recommended film positioning 100
4.4.E Long term verification and stability 100
4.5 Conclusion 101
4.6 Acknowledgment 102
4.7 References 102
CHAPTER 5: Dose comparison between TG-43 based calculations and radiochromic film measurements of the Freiburg flap applicator used for high-dose-rate brachytherapy treatments of skin lesions 106
Preface 106
Abstract 107
5.1 Introduction 108
5.2 Methods and materials 109
5.2.1 Radiochromic film dosimetry system 109
5.2.2 Experimental setup 111
5.2.3 Image processing 112
5.3 Results 113
5.4 Discussion 116
5.5 Conclusions 119
5.6 Acknowledgement 119

5.7 References 119
CHAPTER 6: Positional and angular tracking of HDR ^{192}Ir source for brachytherapy quality assurance using radiochromic film dosimetry 124
Preface 124
Abstract 125
6.1 Introduction 126
6.2 Materials and methods 128
6.2.A HDR source positional uncertainty 128
6.2.B Source tracking model 133
6.2.C Source distribution digitization uncertainties 135
6.2.D Source tracking with radiochromic film dosimetry 136
6.3 Results 136
6.3.A HDR source positional uncertainty 136
6.3.B Source tracking model 140
6.3.C Source dose distribution digitization uncertainties 144
6.3.D Source tracking with radiochromic film dosimetry 148
6.4 Discussion 149
6.4.A Impact of source positional uncertainty 149
6.4.B Performance of the source tracking models 151
6.4.C Source dose distribution digitization uncertainties 152
6.4.D Source tracking with radiochromic film dosimetry versus other systems 153
6.4.E Practical aspects, limitations and summary of the tracking algorithm 154
6.5 Conclusion 155
6.6 Acknowledgment 156
6.7 References 156
CHAPTER 7: Conclusion and future work 162
7.1 Discussion 162
7.2 Future work 166
7.2.1 Film dosimetry protocol development, validation and optimization: 166
7.2.2 Equipment QA 167

7.2.3 Source QA 170
7.2.4 Treatment planning system QA 170
7.2.5 Treatment QA 170
7.2.6 Software development and design improvement 172
7.3 Conclusion 173
OTHER PUBLICATIONS 174
REFERENCES 177

LIST OF FIGURES

Figure 2.1: Classification of brachytherapy in accordance to source placement methodology. For each methodology, the main treatment sites and examples of applicators are provided. 32

Figure 2.2: Brachytherapy treatment options. Some cancer/treatment sites area provided as common examples. 33

Figure 2.3: The physical difference between external beam radiotherapy and brachytherapy. The thick dashed lines across the dose distributions are indicative of the dose profiles shown at the bottom. 34

Figure 2.4: Left: the overall survival in cervical cancer with and without brachytherapy. Right: brachytherapy utilization rate between 1988 and 2009. Figures (with permission) are from Han *et al*. 2013. 36

Figure 2.5: The overall survival in cervical cancer with either brachytherapy or SBRT/IMRT boost. SBRT: stereotactic Body Radiation Therapy, IMRT: intensity modulated radiation therapy. Figure (with permission) from Gill *et al.* 2014. 36

Figure 2.6: Transition from 2D to 3D image-guided brachytherapy. All figures show the superior tissue contrast offered by MRI. Figures A, B show the dose distribution if standard "point A" planning was performed following 2D approach. Figures C, D show that for this specific patient it was necessary to sculpt the dose distribution by taking extra measures i.e. use of interstitial needles. Figures (with permission) are taken from Damato and Viswanathan 2015. 38

Figure 2.7: Images of the prostate at different locations using different imaging modalities. The figure highlights the advantage of MRI in providing superior soft tissue contrast over ultrasound and CT. Figure (with permission) is taken from Tanderup *et al.* 2014b. 39

Figure 2.8: Adoption of image guidance modalities in HDR brachytherapy in the United States (left) and Canada (right). Figures (with permission) were taken from Grover *et al.* 2016 and Taggar *et al.* 2017. N: number of plans. 40
Figure 2.9: Ultrasound-based target delineation in HDR planning for GYN cases correlates well with MRI-based delineation while CT tends to overestimate the target size. Figure (with permission) was taken from Schmid *et al.* 2016. 40
Figure 2.10: A typical treatment process in a contemporary HDR brachytherapy procedure. Steps involving imaging procedures are highlighted in grey and solid lines. Steps involving the use of 3D image datasets are highlighted in grey and dashed lines. *EBRT: External Beam Radiotherapy; HDR: High Dose Rate; BT: Brachytherapy; *: BT given after surgery/EBRT as a boost; **: BT given as preoperative treatment. .....* 41
Figure 2.11: Visual illustration of the main steps involved in brachytherapy planning process. . 42
Figure 2.12: Visual illustration of the main steps involved in brachytherapy planning and treatment verification process. Three doses are to be reported as per the ICRU 89: planning aim during planning, prescribed dose as approved by the physician after planning and the actual delivered dose during treatment (requiring in-vivo dosimetry). 43
Figure 2.13: Average passing points of 15 endorectal brachytherapy plans based on different passing-rate criteria. Figure (with permission) was taken from Asgharizadeh *et al.* 2015. 46
Figure 2.14: Left: the Nucletron microSelectron afterloader unit (Elekta, Sweden). Right: microSelectron b2 source specification (Elekta, Sweden). Source specification is adapted from ref Perez-Calatayud J 2012. 47
Figure 2.15: Left: well-type ionization chamber used for calibration of BT sources. Right: summary of calibration traceability from source manufacturer to the end user at the clinic. Typical uncertainty in dose determination is provided as well. This figure (with permission) is taken from ref DeWerd *et al.* 2011. 47
Figure 2.16: Geometry assumptions in the AAPM TG-43 dose calculation formalism. Angle β is that subtended by the active length L at point P. The reference point is represented by $P(r_0, \theta_0)$. Figure (permission not required) is taken from Rivard *et al.* 2004. 48

Figure 2.17: Dosimetric tools used for quality assurance at different HDR brachytherapy process. This figure is taken from Palmer *et al.* 2012. 49
Figure 2.18: Mass energy absorption coefficients for the indicated materials relative to those for water for different energies, calculated with the EGSnrc Monte Carlo simulation code. Figure (with permission) is taken from Beaulieu *et al.* 2012. 50
Figure 2.19: Typical 3D printing workflow for HDR brachytherapy. Figure (with permission) is taken from Cunha *et al.* 2020. 51
Figure 2.20: Summary of technological advancements in Intensity Modulated Brachytherapy (IMBT) delivery. DirMBT: direction-modulated brachytherapy; DMBT: dynamic modulated brachytherapy; RSBT: rotating-shield brachytherapy; D-RSBT: dynamic RSBT; H-RSBT: multihelix RSBT; P-RSBT: paddle-based RSBT; eBT: electronic brachytherapy; ICMA: intracavitary mold applicator; LDR: low-dose-rate; SAVI: Strut-Adjusted Volume Implant. Figure (with permission) and abbreviations are taken from Callaghan *et al.* 2019. 53
Figure 2.21: Various radiochromic film dosimetry applications. Figure (with permission) was taken from Devic 2011. 55
Figure 2.22: Structure and dimensions of different radiochromic film dosimetry models. Figure (with permission) is taken from Devic *et al.* 2016a. 56
Figure 2.23: Summary of radiochromic film dosimetry protocol showing the calibration and measurement phases. Δt refers to the post exposure waiting time. 57
Figure 3.1: Sampling response of irradiated and un-irradiated film piece using both transmission and reflection mode scanned TIFF images from a flat-bed document scanner. (ROI sizes are for illustrative purposes and are not to scale) 63
Figure 3.2: Measured “raw” data using flat-bed document scanners in transmission (left) and reflection (right) scanning mode. 65
Figure 3.3: Dose response curves for various response functions obtained from transmission (top-left) and reflection (top-right) images; sensitivity curves for various dose response functions from transmission (bottom-left) and reflection (bottom-right) images. 68
Figure 3.4: Uncertainty vs error analysis for various dose response functions from transmission images in a dose range up to 11 Gy; left column corresponds to double scan

functions that for their definition require scan of the film pieces prior to exposure. Right column corresponds to single scan functions. 71
Figure 3.5: Uncertainty vs error analysis for various dose response functions from reflection images in a dose range up to 5 Gy; left column corresponds to double scan functions that for their definition require scan of the film pieces prior to exposure. Right column corresponds to single scan functions. 72
Figure 4.1: Introducing the concept of "fingerprint" correction. At the time of calibration, nPV_{RGB} and the calibration "fingerprint" ($c^{cal}_{X=R,G,B}$) are acquired. At the time of measurement, nPV_{RGB} and $c^{meas}_{X=R,G,B}$ are acquired for each pixel in the image, compared to $c^{cal}_{X=R,G,B}$ (as described in the text), and a correction ($c_{X=R,G,B}$) is generated and re-applied to nPV_{RGB}. 86
Figure 4.2: Concept of dose-response linearization based on multichannel normalized pixel value response (nPV_{RGB}). (a) nPV_{RGB} response and its constituent terms $r \cdot nPV_R$, $g \cdot nPV_G$ and $b \cdot nPV_B$ representing individual responses in red, green and blue color channels. (b) sensitivity curves of nPV_{RGB} and its constituents. 88
Figure 4.3: The impact of dose range on dose uncertainty and error analysis of one of the EBT3 GAFCHROMIC™ film dosimetry systems used in this work (lot#1, 10000 XL). (a) Uncertainty/error analysis for the dose range 0 – 40 Gy, (b) 0 – 10 Gy focused view of the same figure in (a), (c) Uncertainty/error analysis for the dose range 0 – 10 Gy when the system was re-fit to maximum dose of 10 Gy (instead of 40 Gy), and (d) the impact of dose range (maximum calibration dose, indicated by the arrows) on linearity of the dose-response. 89
Figure 4.4: Applying the concept of nPV_{RGB} to six different EBT3 GAFCHROMIC™ film dosimetry systems used in this work. (a) Linearization of the dose-response and comparison to the unity curve, and (b) Achievable accuracy represented as the percentage relative dose error at different dose levels. 90
Figure 4.5: Visualization of the "fingerprint" at the time of calibration ($c^{cal}_{X=R,G,B}$) for the six EBT3 GAFCHROMIC™ film dosimetry systems used in this work. 91
Figure 4.6: EPSON 12000XL scanner response variability in terms of pixel values relative to the 1st scan. (a) for neutral density filters, and (b) for EBT3 GAFCHROMIC™ film. .. 92

Figure 4.7: EPSON 12000XL scanner response variability in terms of dose relative to the 1st scan. (a) using nPV_{RGB} with and without correction, and (b) using $netOD_{X=R,G,B}$. Global control refer to the use of control film from scan#1 image in all subsequent measurement film images while specific control means using the control film from the same scanned image as the measurement film. (s.ctrl: specific control, g.ctrl: global control). 93

Figure 4.8: EPSON 12000XL scanner bed inhomogeneity with respect to the scanner center. First and second rows show the RGB relative responses in pixel values (PV) for a control and an exposed film piece (8 Gy). Third and fourth rows show the RGB dose conversion based on $netOD_{X=R,G,B}$, when using a global or specific controls. Fifth row shows the use of nPV_{RGB} with global control, specific control (no correction) and specific control (with correction). 94

Figure 4.9: Box plot demonstration of the accuracy and precision of RCF dosimetry at different time points and using different response signals. (a) at the time of calibration, using 0 – 10 Gy fit, (b) at the time of calibration, using 0 – 40 Gy fit, (c) three months after calibration, using 0 – 40 Gy fit, and (d) six months after calibration, using 0 – 40 Gy fit. 95

Figure 4.10: Changes in the values of *r*, *g*, *b* fitting parameters (equation 4) among the six GAFCHROMIC™ film dosimetry systems used in this work. The figure shows that each system has its own unique pattern of these parameters and that the values of parameters depend on the maximum calibration dose. 97

Figure 5.1: Experimental setup (with 3 cm bolus on top of the Freiburg Flap). Solid Water™ slabs are 30 cm × 30 cm in size. Dimensions are not to scale..... 112

Figure 5.2: Reference radiochromic film dosimetry system used: calibration curve (5.2A); two-component (experimental and fit) relative uncertainty (5.2B); and error vs. uncertainty assessment (5.2C). 115

Figure 5.3: The impact of bolus thickness on absolute dose ratio between measurements (using radiochromic film based reference dosimetry system) and treatment planning system (Oncentra - MasterPlan™) at the downward vertical plane to the central sphere of the Freiburg flap for two experimental setups: dose distributions for 5 cm × 5 cm loading (5.3A), and 11 cm × 11 cm loading (5.3B); dose ratio histograms with

numbers above representing dose values calculated by TPS at corresponding depths for 5 cm × 5 cm loading (5.3C), and 11 cm × 11 cm loading (5.3D). Error bars include the uncertainty in dose calculation and measurement per dose level. 116
Figure 6.1: Geometric coordinate systems and setups. Dimensions are not to scale. a) coordinate systems used for this work: source coordinate system is used mainly for TG-43 calculations, and phantom coordinate system is used to describe the location of the film and the tracked source position for experimental setups. The default orientation is when the origins of both systems are aligned (source at nominal first dwell position) , b) sectional dimensions of different HDR brachytherapy catheters that are typically used in the clinic seen at the default orientation. Different Solid Water® (SW) slabs were grooved for 6F and 4F catheters in order to mitigate catheter movement, c) the SW phantom (30 × 50 × 30 cm^3) designed to satisfy TG-43 full scattering conditions for all dosimetry points of the EBT3 GAFCHROMIC™ film. 130
Figure 6.2: The AAPM TG-43 protocol implementation in MATLAB. Left panels show the distance to source ($r_{i,j}$), middle panels show the angular distribution ($\theta_{i,j}$), and right panels show the relative dose rate distributions ($D_{i,j}$). Four different geometries are shown to highlight the impact on the individual 2D maps. Pixel size for all maps is 1 by 1 mm^2. The unit of the abscissas and ordinates of all images are “mm” and the units of the pixels are “mm”, “deg”, or “%” for the left, middle or right panels, respectively. 138
Figure 6.3: The HDR Ir^{192} source positional uncertainty of a single dwell position. (a) limits of the dosimetric error based on the AAPM TG-43 protocol calculations for different catheter geometries, (b) experimental confirmation of source positional uncertainty of a single dwell position repeated nine times, (c) demonstration of the surface dose gradient difference between the 4F and 6F catheters. 139
Figure 6.4: Impact of HDR ^{192}Ir source positional uncertainty on a clinical surface brachytherapy case. At two different distances to source (5 mm and 8 mm, exposed simultaneously): the left panel shows the average dose map of five repeated EBT3-film based dose measurements, middle panel shows the per-pixel standard deviation of these repeats normalized to the maximum dose within the image, left panel shows

the 80% isodose lines of a selected dwell position (red squares, right panel) from the five film images. 140
Figure 6.5: Relative dose profiles at different distances away from the HDR source based on the AAPM TG-43 protocol data of the mHDR-V2 source: (a), (b) and (c) show data fitting with different models: *Gauss*, *Lorentz* and *Pearson VII*, respectively. (d) Linear fit of the distance to source as a function of the full width at half maximum (FWHM). 141
Figure 6.6: Dimensions and shapes of the HDR source isodose lines at different distances away from the HDR source based on the AAPM TG-43 protocol data for the mHDR-V2 source. 142
Figure 6.7: Variation of 2D features of the HDR source isodose lines: area, perimeter and circularity, with respect to the distance to the source for θ_y= 0 deg (left panel) and θ_y= 15 deg (right panel). 143
Figure 6.8: Finding the HDR source center (*x*, *y*) at different distances to source based on different dose distribution features: weighted centroids (H for high isodose lines, L for low isodose lines), mean dose, median dose, and max dose. 144
Figure 6.9: Effect of noise on the accuracy of the source center determination at three different noise levels: 2% (left panel), 3% (middle panel), and 5% (right panel). Top figures are dose maps at z=10 mm and they are provided to visualize the noise only. 145
Figure 6.10: Model performance in finding the source orientation θ_z from different isodose line levels, at different distances to the source. Beyond 5 mm, it is not possible to determine the orientation of the source irrespective of the IDL level. 146
Figure 6.11:Effect of choosing different size regions of interest (ROI) on the standard deviation of dose within the ROI. Data are shown for different distances to the HDR source and digitizing resolutions. The data are generated from the AAPM TG-43 protocol based MATLAB model. 146
Figure 6.12: Effect of Wiener filter size on the dose reading in noise-free data (left panel), and on noise reduction in data with added noise (right panel). Data are shown for different distances to source and digitizing resolutions. The noise-free data are generated from the AAPM TG-43 protocol based MATLAB code. 147

Figure 6.13: Noise reduction performance of a 5 by 5 pixel^2 Wiener filter applied to noisy dose rate profiles (red lines). Symbols show the noise added to the noise-free profiles (black lines). Data are shown for different distances to source. The digitizing resolution is 0.1 mm/pixel. 148
Figure 6.14: Using the source tracking model with a dose map measured by the EBT3 GAFCHROMIC™ film model. The measured dose map (a) is converted to a curve (b) and compared to the AAPM TG-43 protocol reference library of the isodose lines area in this example. 149

Figure 7.1: The future framework for HDR brachytherapy QA with radiochromic film dosimetry. The framework consists of six specific areas to be optimized (sub-circles). HDR: high-dose-rate, QA: quality assurance. 167
Figure 7.2: Phantom design for afterloader quality assurance made of Solid Water™ (SW): (a) choice of 4F or 6F catheters, (b) illustration of phantom design with EBT3 radiochromic film location. The dashed slab above the film is also made of SW but was made transparent for visibility. (c) Photograph of the assembled phantom. The large clamps are used to minimize the effect of air gaps. (d) Photograph of the full setup with the phantom connected to the afterloader through five transfer tubes... 168
Figure 7.3: Decomposition of dose profile fit across five dwell positions using a Pearson VII model: (a) film images at 11 mm and at the surface. (b) decomposition analysis of a 1D profile across the film at 11 mm with fixed dwell times (30 sec each). (c) decomposition analysis of a 1D profile across TG43 data at 11 mm with fixed dwell times. (d) decomposition analysis of a 1D profile across the film at 11 mm with fixed dwell times. This test can reveal dwell positions, dwell times and timer linearity. 168
Figure 7.4: Demonstration of applicator QA with radiochromic film dosimetry and source tracking. (A) applicators attached to the film with inkdots/BBs on the corners, (B) post exposure image highlighting inkdots, (C) *x*-ray image highlighting registration BBs, (D) image overlay and application of source/marker auto tracking, (D) visual QA examples of different applicator sets, and (F) histogram of all displacements (total of 64 applicators, 0.10 ± 0.39 mm) 169

Figure 7.5: HDR surface brachytherapy *in-vivo* dosimetry with EBT3 model RCF. (a) photographs of different film pieces placed on different cases. (b) highlighting inter-fractional variability and ability to improve the applicator positioning. (c) comparison between heterogeneity-corrected dose calculation, the current standard in dose calculation and film measurements. (d) how in-vivo measurements can help in adapting radiation treatments.. 171
Figure 7.6: Histogram of dose measurements in the *in-vivo* study of HDR surface brachytherapy. The figure shows that a more accurate dose calculation engine might help in improving the dose delivery accuracy (*i.e.* tighten the peak and push it to the right while limiting the maximum dose to the skin). 171
Figure 7.7: The types of tests that can be achieved with a single irradiation session in HDR brachytherapy QA: (1) First dwell position: a line connecting the physical points on the phantom that represents where the FDP should be will be compared to the measured position per catheter. (2) Dwell positions, (3) Dwell times, (4) Timer linearity (5) Source strength (S_k) verification: via source tracking and dosimetry, (6) Step size, (7) This can be done for multiple channels: five shown here. 172
Figure 7.8: Comprehensive QA: incorporating treatment planning system quality assurance with afterloader quality assurance. This involves scanning the phantom, creating a plan and transferring it from planning unit to the treatment unit. Currently (top), a TG43 phantom is used. In the future (bottom), a simpler phantom will be created whereby dose will be calculated using a Model-Based Dose Calculation Algorithms (MBDCAs). 173

LIST OF TABLES

Table 5.1: Uncertainty budget example of overall dose calculation and measurement at depth of 1 cm from the phantom surface for an 11 cm × 11 cm loading area. 114

Table 6.1: Dimensions of the 80% isodose line (IDL) of each blob in right panel of Figure 6.4. 137

CHAPTER 1: Introduction

1.1 Motivation

Brachytherapy (BT) became an essential component of radiotherapy for many cancer treatments such as in gynecologic, prostate and skin cancers. It refers to the placement of radioactive sources temporarily or permanently into or near target volumes giving a high dose of radiation to the target while sparing surrounding healthy tissues and organs-at-risk. The clinical outcome in terms of overall survival when using BT has been shown to be superior to other boosting techniques. This advantage is attributed to the increased therapeutic ratio achievable with BT because of the high dose gradient near the source and also special time-dose patterns (dose rate, fractionation, total treatment time) depending on the type of the source used. The majority of contemporary brachytherapy treatments are delivered under image-guidance using a small high-dose-rate (HDR) ^{192}Ir source. This source resides in an afterloader unit where it is welded to a cable attached to a stepping motor that drives the source to the required set position(s) for the pre-set amount of time. However, the high dose gradient and dose rate impose more strict restrictions on the quality assurance (QA) requirements of source(s) positioning and exposure time(s). These restrictions are justified given the severity of harm in misadministration and there is in fact a global consensus about the importance of proper QA to ensure safety and high quality BT treatments. Although BT is in general a safe treatment modality, severe accidents had happened in the past according to reports from the World Health Organization (WHO) and the American Brachytherapy Society (ABS). Analysis of these reports and more recent surveys revealed that there is a need for new approaches in QA that can accommodate the increased work pressures and rapid technological advancements in BT such as treatment delivery modulation, use of different sources and customization of in-house applicators.

The main purpose of this thesis is to propose a comprehensive QA system for contemporary image-guided HDR brachytherapy. This is achieved by tracking the source based on its dosimetric trace using a high resolution radiochromic film (RCF). Firstly, an RCF dosimetry protocol was developed and validated to correctly acquire dose images. Furthermore, a 3D source-

tracking algorithm was developed to localize the HDR source within catheters and consequently used to provide a holistic QA solution at different stages of the BT treatment process.

1.2 Overview of thesis

This thesis consists of seven chapters. Chapter 2 provides a background and literature review on brachytherapy, quality assurance in brachytherapy, radiochromic film dosimetry and its application in brachytherapy QA.

Chapters 3-6 are individual manuscripts that are aimed to fulfill the purpose of this thesis. Chapter 3 presents our investigation into RCF response functions, scanning modes, need for pre-scanning, and overall achievable dosimetric uncertainty. Chapter 4 builds on results of Chapter 3 and introduces an RCF dosimetry protocol with an integrated spectral correction for scanner response variations and inhomogeneities. The chapter also discusses validation of the protocol and how it solved key scanning problems that were considered downfalls of the existing RCF protocols. Chapter 5 presents our first paper on using the RCF dosimetry system for brachytherapy QA. It specifically addresses the problem of assuming full-scattering conditions in all HDR brachytherapy planning, which is not true for surface brachytherapy. In Chapter 6, a 3D source-tracking algorithm was developed to precisely localize the HDR source within catheters based on a 2D dose map that can be acquired with RCF. The paper discusses advantages and challenges using RCF and its potential use for commercial and customized applicators QA.

Finally, Chapter 7 summarizes the results presented in this thesis and discusses how the combination of RCF dosimetry and source tracking can provide an end-to-end QA solution to the challenges associated with rapid technological advancements in HDR brachytherapy.

1.3 Author contributions

I am the first author of all four manuscripts included in this thesis and I have performed all of the experiments, methodological developments, and the analysis. The contributions of all co-authors included research supervision, technical discussions, data acquisition, and the review of manuscripts. The following summarizes the contributions of each author by manuscript:

Chapter 3: Comparison of dose response functions for EBT3 model GafChromic™ film dosimetry system

- *Authors:* Saad Aldelaijan, and Slobodan Devic
- *Contributions:* Study concepts and design: S. A., S. D.; Experimental work and data collection: S. A.; Method analysis and implementations: S. A., S. D., Guidance and supervision: S. D.; Manuscript preparation: S. A.; Manuscript revision: S. A., S. D.; Editing and final version approval: S. A., S. D.

Chapter 4: Dose response linearization in radiochromic film dosimetry based on multi-channel normalized pixel value with an integrated spectral correction for scanner response variations

- *Authors:* Saad Aldelaijan, Slobodan Devic, Pavlos Papaconstadopoulos, Hamed Bekerat, Robert A. Cormack, Jan Seuntjens, Ivan M. Buzurovic
- *Contributions:* Study concepts and design: S. A., S. D..; Experimental work and data collection: S. A., P. P., H. B., R. A. C.; Method analysis and implementations: S. A., S. D., P. P., J. S., I. M. B.; Guidance and supervision: S. D., I. M. B.; Manuscript preparation: S. A.; Manuscript revision: all authors.; Editing and final version approval: S. A., S. D., I. M. B.

Chapter 5: Dose comparison between TG-43 based calculations and radiochromic film measurements of the Freiburg flap applicator used for high-dose-rate brachytherapy treatments of skin lesions

- *Authors:* Saad Aldelaijan, Hamed Bekerat, Ivan Buzurovic, Phillip Devlin, Francois DeBlois, Jan Seuntjens, Slobodan Devic
- *Contributions:* Study concepts and design: S. A., I. B., P. D., S. D.; Experimental work and data collection: S. A., H. B., F. D.; Method analysis and implementations: S. A., J. S., S. D., Guidance and supervision: S. D., J. S.; Manuscript preparation: S. A.; Manuscript revision: all authors; Editing and final version approval: S. A., S. D.

Chapter 6: Positional and angular tracking of HDR sources for brachytherapy quality assurance using radiochromic film dosimetry

- *Authors:* Saad Aldelaijan, Slobodan Devic, Hamed Bekerat, Pavlos Papaconstadopoulos, James Schneider, Jan P. Seuntjens, Robert A. Cormack, Ivan M. Buzurovic
- *Contributions:* Study concepts and design: all authors; Model development: S. A.; Experimental work and data collection: S. A., H. B., P. P., J. S., R. A. C.; Method analysis and implementations: S. A., Guidance and supervision: S. D., J. P. S., I. M. B.; Manuscript preparation: S. A.; Manuscript revision: all authors; Editing and final version approval: S. A., S. D., I. M. B.

1.4 Scientific contributions

The original scientific contributions in this work are mainly in the areas of RCF dosimetry and HDR brachytherapy QA. These contributions are listed below per area in chronological order:

1) Radiochromic film dosimetry:
    a. Introduction of a green-channel based normalized pixel value as a linear response function for the EBT3 GAFCHROMIC™ film model to doses up to 11 Gy.
    b. Development of a novel linearized RCF dosimetry protocol with extended dose range up to 40 Gy taking advantage of all available RGB channels.
    c. Development of the "fingerprint" correction; an integrated spectral correction, generated from the same scanned images, which corrects for scanner temporal and spatial response variation between times of calibration and measurement.
2) HDR brachytherapy quality assurance:
    a. Design and implementation of RCF dosimetry in phantom studies to experimentally measure the deviation between delivered and calculated doses based on current surface brachytherapy planning approaches that do not account for tissue heterogeneities.
    b. Development and validation of a novel HDR source tracking algorithm for 3D source positional and angular information detection based on a 2D isodose map away from the source, obtainable from RCF.
    c. Design and implementation of an automatic applicator and source marker QA procedure using the source tracking algorithm and image registration.

d. Design of a phantom and software for end-to-end HDR brachytherapy QA based on dose decomposition analysis of unique irradiation patterns acquired by RCF dosimetry. The novel method decomposes source dwell positions and times for multiple channels simultaneously and it also compares the measured pattern to the calculated one from the treatment planning system (TPS) integrating source, afterloader and TPS QA.
e. Design and implementation of a clinical protocol to perform 2D *in-vivo* dose measurements of surface brachytherapy based on RCF dosimetry and clinically evaluate the need to include tissue heterogeneity corrections into the planning process.

CHAPTER 2: Background and literature review

2.1 Introduction to brachytherapy

Brachytherapy (BT) is a method of cancer treatment whereby radioactive sources are placed temporarily or permanently into or near target volumes giving a high dose of radiation to them while sparing surrounding healthy tissues and organs-at-risk (OARs). BT has existed for more than 100 years commencing shortly after the discovery of radioactivity in 1896 by Henry Becquerel (Becquerel 1896). The term "radioactivity" was coined by Marie Skłodowska Curie and she received the Nobel Prize in 1903 jointly with Pierre Curie and Henry Becquerel for their work on radioactivity. The first BT case was reported in 1901 when Pierre Curie (a French physicist) suggested the use of radioactivity to Henri-Alexandre Danlos (a French physician) and Danlos successfully used a Radium source to treat tuberculous skin lesions (MacKee 1921). Thereafter, BT has been used for different types of cancer including cervical (1903, Aronowitz *et al*. 2007), prostate (1909, Aronowitz 2008) and breast (1932, Keynes 1932). However, the use of BT has declined afterwards in favor of surgery because the sources were manually placed, which raised safety concerns about staff exposure to hazardous radiation (Williamson 2006, Aronowitz 2015). It was not until the 1960s and 1970s that BT regained global interest due to the introduction of artificial radioactive sources and remote afterloading systems, respectively (Williamson 2006, Aronowitz 2015). It is of note that Irene Joliot-Curie and Frédéric Joliot-Curie were jointly awarded the Nobel Prize in Chemistry in 1935 for their discovery of artificial radioactivity. The introduction of the single-stepping source has revolutionized the use of high-dose-rate (HDR) BT as we know it today (Williamson 2006, Aronowitz 2015).

2.1.1 Types of brachytherapy

Depending on the source placement methodology and treatment site, BT can be categorized into intracavitary, interstitial, intraluminal, surface, intraoperative or intravascular (Podgorsak 2005). Most of the BT cases are intracavitary (source placement into a body cavity using specialized applicators), interstitial (surgical catheter or source placement into or near targets) and/or surface treatments (catheter or applicator placement on top or over the tissue). Figure 2.1 shows the main

treatment sites per placement methodology and some examples of the applicators or catheters used.

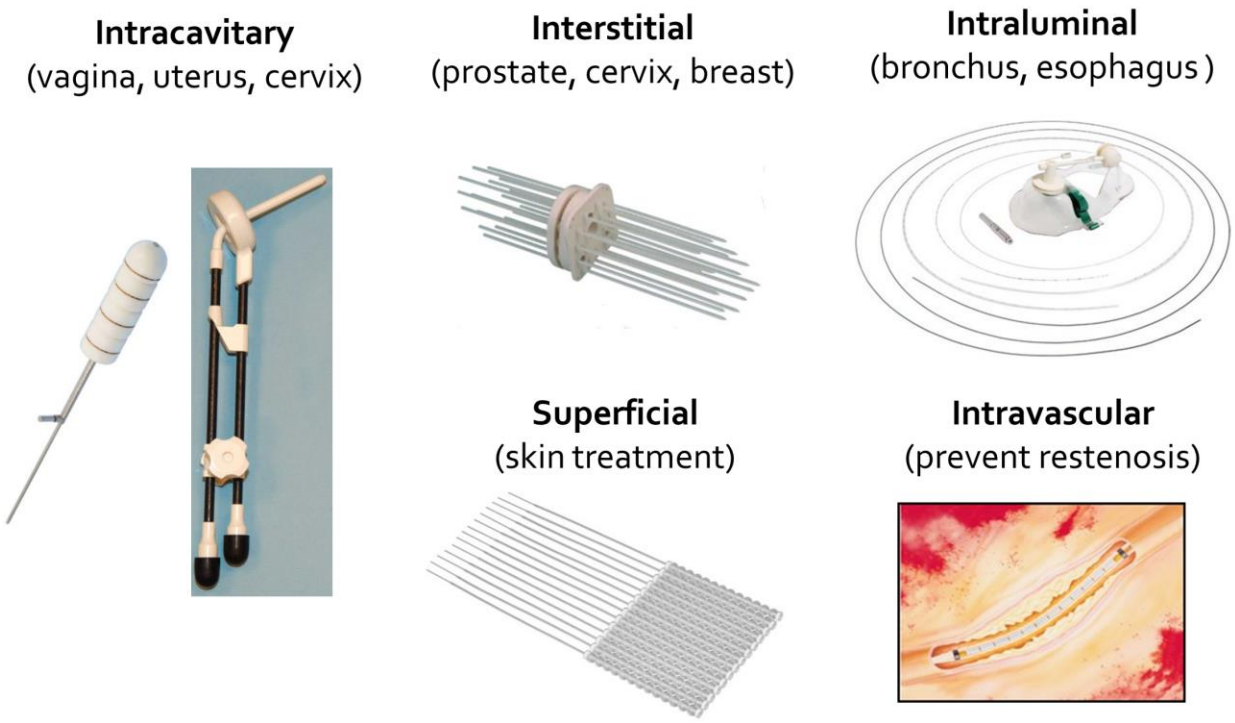

Figure 2.1: Classification of brachytherapy in accordance to source placement methodology. For each methodology, the main treatment sites and examples of applicators are provided.

2.1.2 Advantages of brachytherapy

Brachytherapy differs from megavoltage external beam radiotherapy (EBRT) in its physical and biological characteristics (ICRU Report 89 2016). Although EBRT has gone through several technological advancements that lead to increasingly conformal dose distributions (Bortfeld 2006, Teoh *et al*. 2011), BT still retains its physical and biological uniqueness because of its high dose gradient and time-dose patterns (dose rate, fractionation, total treatment time, ICRU Report 89 2016). This is not to suggest BT as an alternative to EBRT, but rather to highlight its successful implementation based on clinical outcomes. Generally, BT can be used alone preoperatively in early disease, or mostly combined as a boost with EBRT and chemotherapy in advanced disease (See Figure 2.2).

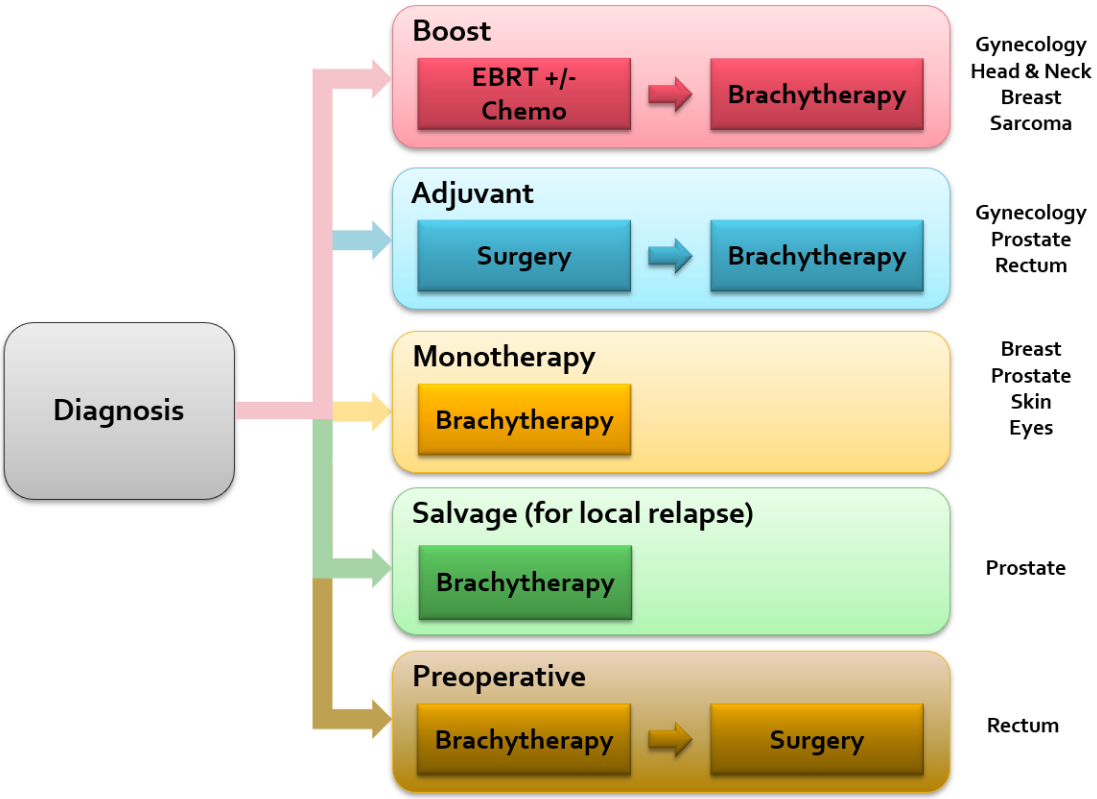

Figure 2.2: Brachytherapy treatment options. Some cancer/treatment sites area provided as common examples.

Physical advantages of brachytherapy

Figure 2.3 shows the physical difference between EBRT and BT in terms of application and dose distribution inside the tumor. It demonstrates the high dose gradient within the target in BT, which also results in the better sparing of nearby OARs when compared to EBRT. Quantitatively, according to the International Commission on Radiation Units and Measurements (ICRU) report no. 89 (ICRU Report 89 2016, Tanderup *et al*. 2017), the median target dose in cervical BT, for example is typically higher than 150 to 200% of the prescribed dose at the periphery of the target. On the other hand, in conventional EBRT, the variation of dose across the target is maintained between 95 to 107% of the prescribed dose (ICRU Report 50 1993). Another physical advantage of BT is the fact that it provides more geometrical assurance since the source(s) are implanted near or into the treatment site directly. Consequently, there is no planning target volume (PTV) in BT, making the total irradiated volume during BT more conformal.

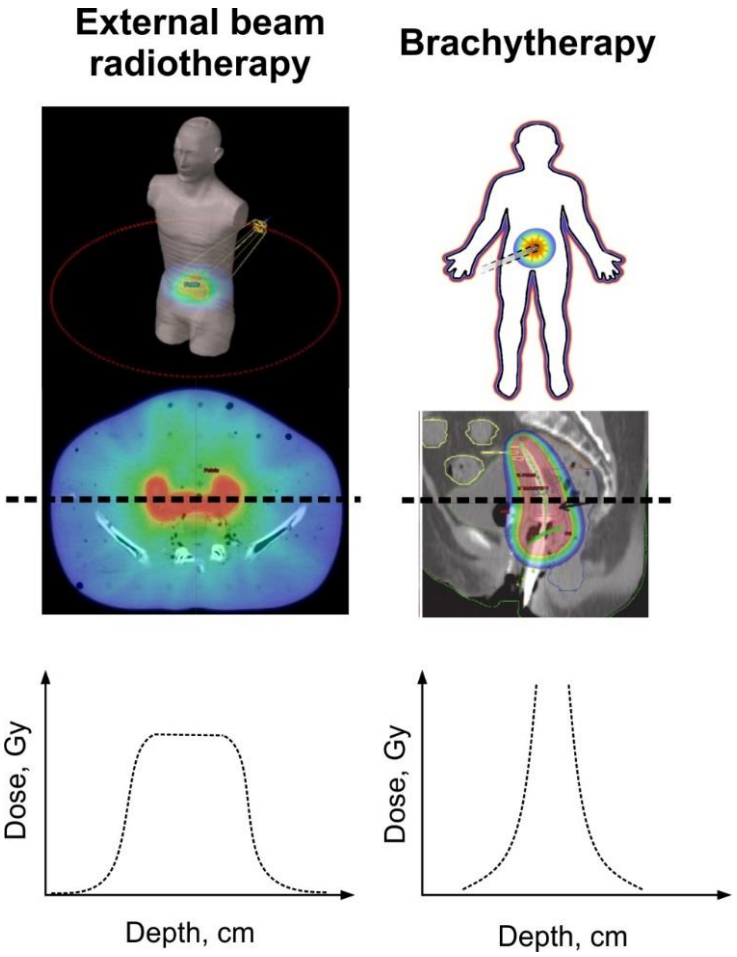

Figure 2.3: The physical difference between external beam radiotherapy and brachytherapy. The thick dashed lines across the dose distributions are indicative of the dose profiles shown at the bottom.

Biological advantages of brachytherapy

Biological efficacy of BT can be emphasized by its dose-volume-time patterns (ICRU Report 89 2016). The higher dose gradient (dose-volume) is acceptable for OARs because of the volume-effect relationship: high dose to a small volume (2 cc for example) of an OAR is acceptable but not for a larger volume (Mazeron *et al*. 2003). The answer to the question whether heterogeneous or homogenous dose distribution pattern is more effective on target volumes is site-specific. For example, dose heterogeneity is important in cervical cancer, while for interstitial breast implants, dose homogeneity is preferred (Devlin 2016). Regarding time-dose patterns, according to ICRU 89 (ICRU Report 89 2016), they are determined by dose rate, dose per fraction and total treatment time. BT can be classified according to dose rate as: low dose rate (LDR, <0.5 Gy/hr), medium dose rate (MDR, 0.5 – 12 Gy/hr), high dose rate (HDR, >12 Gy/hr), and pulsed dose rate

(PDR, 40 – 80 pulses at 0.5 – 1 Gy/hr/pulse). Radiobiology in BT can be emphasized by the move from LDR to fractionated HDR and PDR (Stewart and Bentzen 2011). Viani *et al*. 2009 showed that there are no differences between HDR and LDR cervical BT in terms of overall survival, local recurrence and late complications. Nowadays, most of the intracavitary and interstitial BT procedures are HDR based, except for permanent seeds (Williamson 2006).

2.1.3 Clinical outcomes of brachytherapy

To highlight the outcomes of BT, it is more convenient to concentrate on specific types of cancer whereby BT was shown to be effective.

Gynecologic cancer

Figure 2.4 (left, from Han *et al*. 2013) shows the improvement of overall survival when using BT based on 7359 patients with stages IB2-IVA cervical cancer treated with EBRT (63% of them received BT) between 1988 and 2009. This figure shows that there is almost 10% improvement when using BT ($p<0.001$). In the same study, the authors show (Figure 2.4, right) that irrespective of this improvement, the utilization rate of BT has dropped significantly in 2003. They postulated that this decline was the result of increased implementation of highly conformal radiation therapy techniques including intensity modulated RT (IMRT) and stereotactic body radiation therapy (SBRT). Shortly thereafter, an editorial statement was issued in the red journal by Tanderup *et al*. 2014a stressing on the fact that the use of BT is not optional. Additionally, Sturdza *et al*. 2016 showed that there is another 10% gain in target local control when using image-guided adaptive BT. Irrespective of the efficacy of BT, the current technological advancement in EBRT showed that it is possible to get high dose gradients with EBRT suggesting that SBRT/IMRT may replace BT (Ishmael Parsai *et al*. 2017). However, the validity of this conclusion is questionable given the results of another large study by Gill *et al*. 2014. This study consisted of 7654 patients treated with BT or SBRT/IMRT between 2004 and 2011 and showed that BT has almost more than 20% improved overall survival (Figure 2.5, from Gill *et al*. 2014).

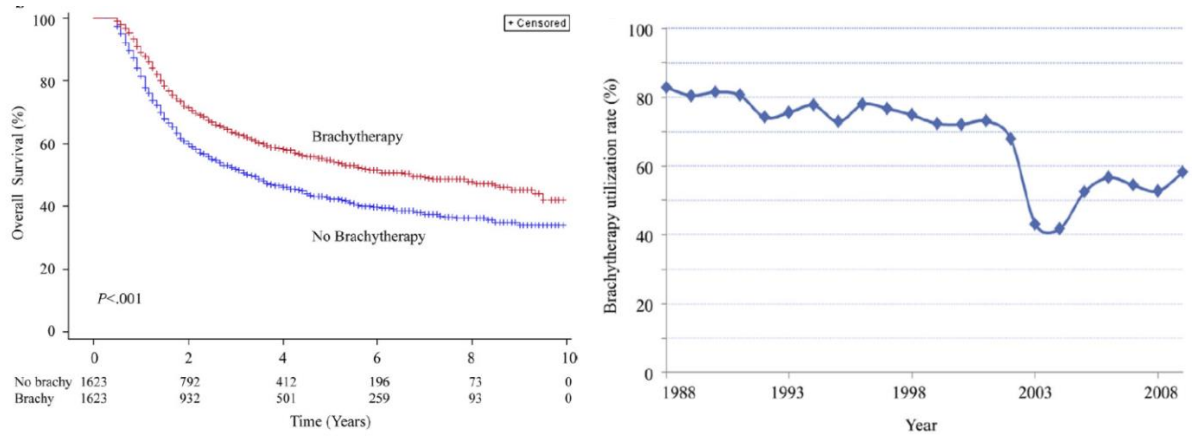

Figure 2.4: Left: the overall survival in cervical cancer with and without brachytherapy. Right: brachytherapy utilization rate between 1988 and 2009. Figures (with permission) are from Han *et al*. 2013.

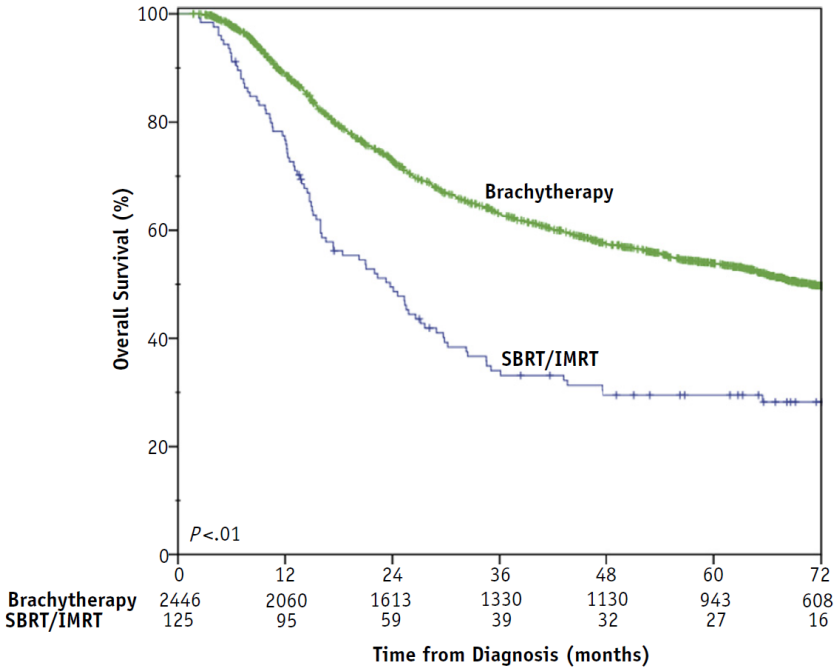

Figure 2.5: The overall survival in cervical cancer with either brachytherapy or SBRT/IMRT boost. SBRT: stereotactic Body Radiation Therapy, IMRT: intensity modulated radiation therapy. Figure (with permission) from Gill *et al*. 2014.

Prostate Cancer

Treatment of prostate cancer depends on the cancer risk level. Depending on the level of prostate-specific antigen (PSA), there are three main risk levels: low-, intermediate- and high-risk. Low-

and intermediate-risk prostate cancer are treated with prostatectomy, EBRT, or BT (D'Amico *et al*. 1998). To evaluate the treatment effectiveness, clinical studies report the long-term freedom of biochemical failure rate. Recently, Goy *et al*. 2020 reported the adjusted 10-year freedom from biochemical failure was 80.2% for BT, 57.1% for prostatectomy, and 57.0% for EBRT. Zaorsky *et al*. 2017 reported the 5-year biochemical failure-free rates of low-, intermediate- and high-risk diseases to be >85%, 69–97%, and 63–80%, respectively, when using BT. Similarly, Sylvester *et al*. 2011 reported the 15-year rates of 86%, 80%, and 62% when using BT. Zaorsky *et al*. 2017 also reported the LDR BT and HDR BT overall survival rates of more than 85% and 95% over 10-years and 5-years, respectively. Additionally, BT was shown to be a better mono-therapy treatment than prostatectomy and EBRT, especially in terms of functional outcome (Spratt *et al*. 2014, Crook 2015). As a boost, Morris *et al*. 2017 showed that combining BT with EBRT was better than an additional EBRT boost in terms of disease-free survival.

Irrespective of the promising BT statistics in treating prostate cancer, Mahmood *et al*. 2014 showed that its use has actually declined in favor of prostatectomy and EBRT. Petereit *et al*. 2015 and Zaorsky *et al*. 2017 showed that this is mainly caused by the introduction of robotic surgery and IMRT for prostatectomy and EBRT, respectively. Other reasons for the decline in using BT is that it has less financial incentive compared to EBRT, it has higher operating cost, and it requires a more skillful team (Han *et al*. 2017).

2.2 Image-guided brachytherapy

2.2.1 Transition from 2D to 3D image-guidance

One of the important steps in BT is the reconstruction of source positions for dose calculation. This was historically achieved by acquiring two dimensional (2D) radiographs of the treatment site including applicators, needles or seeds. Initially, doses were calculated at reference points according to the ICRU 38 recommendations for intracavitary BT (ICRU Report 38 1985). This 2D BT approach provided a robust method for an interactive applicator positioning and source position reconstruction but lacked the anatomical visualization of tumors and OAR.

The introduction of three dimensional (3D) imaging into BT facilitated the transition from 2D BT to 3D image-guided BT (IGBT, ICRU Report 58 1997, Nag *et al*. 2004, Haie-Meder *et al*. 2005, Pötter *et al*. 2006, Devic *et al*. 2007, Hellebust *et al*. 2010, Dimopoulos *et al*. 2012, Damato

and Viswanathan 2015, Schmid *et al*. 2020). Namely, computed tomography (CT), magnetic resonance imaging (MRI) and ultrasonography (US) provided 3D anatomical image datasets, enabling more accurate patient-specific delineation of target volumes and OARs, and dosimetric evaluation based on dose-volume relationships instead of point doses (Georg *et al*. 2011). Figure 2.6 shows the IGBT advantage in two ways: 1) better visualization of the tumor when using an imaging modality such as MRI, and 2) ability to sculpt the dose distribution because of the improved tumor visualization. This in turn allowed dose escalation to tumor volumes resulting in better clinical outcomes (Pötter *et al*. 2011, Tanderup *et al*. 2010, Rijkmans *et al*. 2014, Simpson *et al*. 2015, Sturdza *et al*. 2016). Figure 2.7 shows prostate images from different imaging modalities highlighting their advantages and limitations. The two previous figures showed that MRI has an advantage over US and CT in target delineation. For cervical cancer, this was recognized in one of the main conclusions from the five GYN GEC-ESTRO reports cited above that the MRI is the golden standard for accurate definition of the tumor.

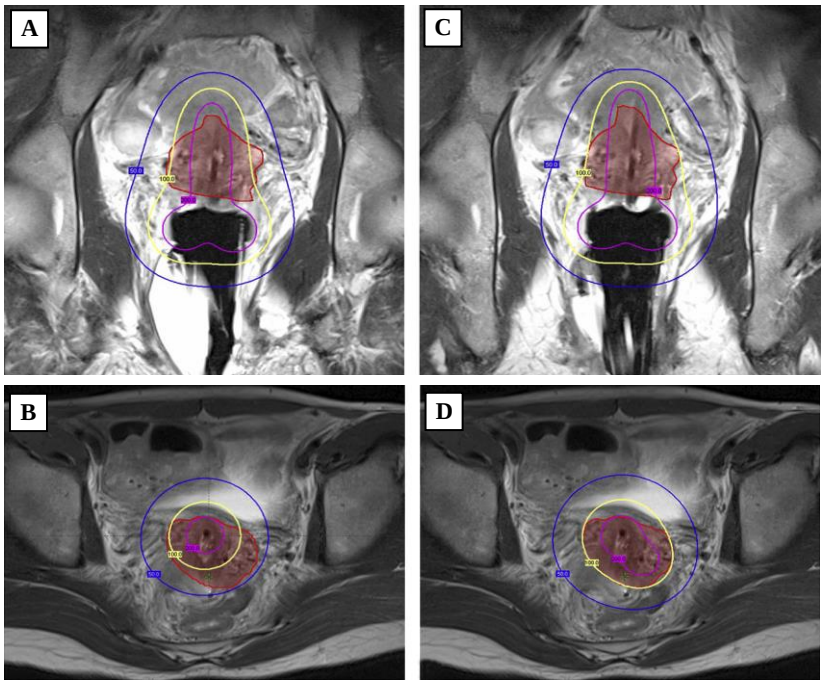

Figure 2.6: Transition from 2D to 3D image-guided brachytherapy. All figures show the superior tissue contrast offered by MRI. Figures A, B show the dose distribution if standard "point A" planning was performed following 2D approach. Figures C, D show that for this specific patient it was necessary to sculpt the dose distribution by taking extra measures i.e. use of interstitial needles. Figures (with permission) are taken from (Damato and Viswanathan 2015).

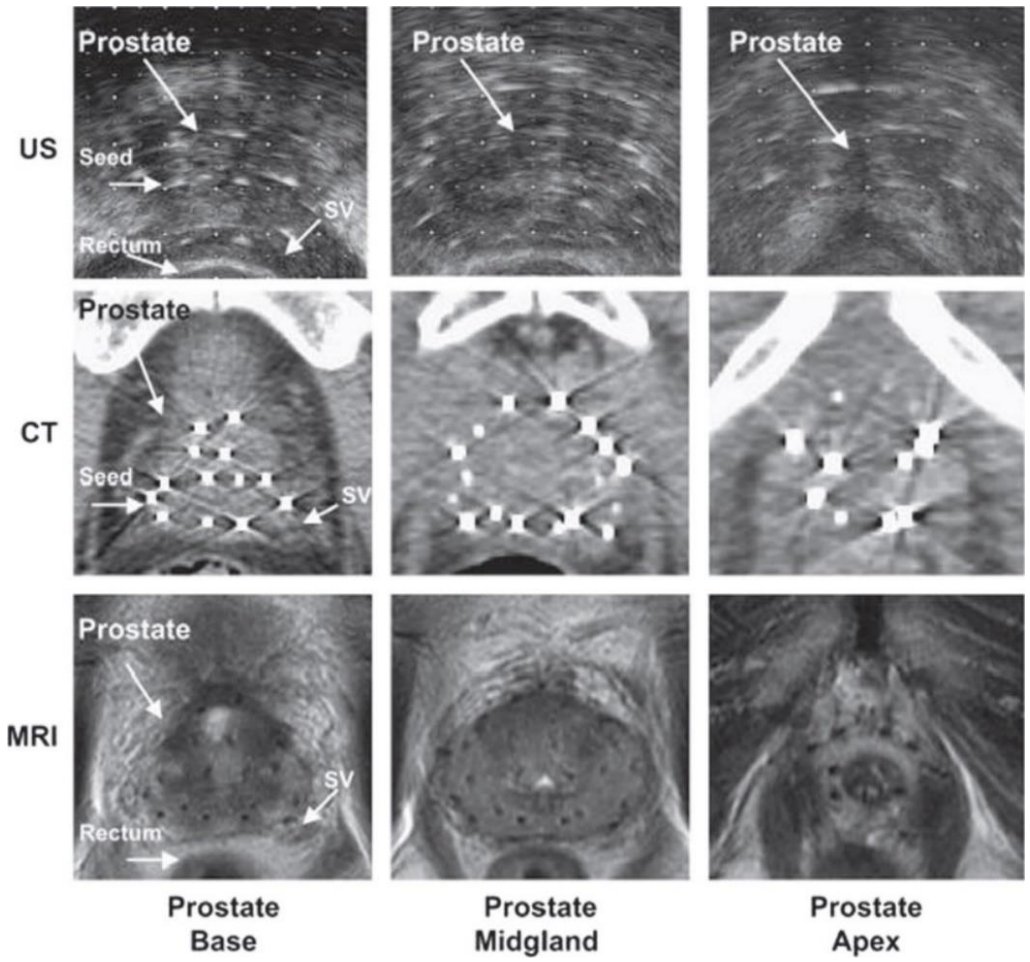

Figure 2.7: Images of the prostate at different locations using different imaging modalities. The figure highlights the advantage of MRI in providing superior soft tissue contrast over ultrasound and CT. Figure (with permission) is taken from Tanderup *et al*. 2014b.

Currently, CT is the mostly-utilized modality in IGBT owing to its availability in radiation oncology clinics. Figure 2.8 displays IGBT surveys from the United States (Grover *et al*. 2016) and Canada (Taggar *et al*. 2017) from two independent studies. The numbers show three key points: 1) CT is the most used modality in IGBT, 2) there is an increased use of 3D-based planning, and 3) interest in MRI is increasing. However, it should not be concluded that US-based IGBT is less important than MRI and CT. On the contrary, target volumes delineated with US were shown to correlate well with MRI-based volumes, which is very advantageous given the vast cost difference between the two modalities (Schmid *et al*. 2016, See Figure 2.9).

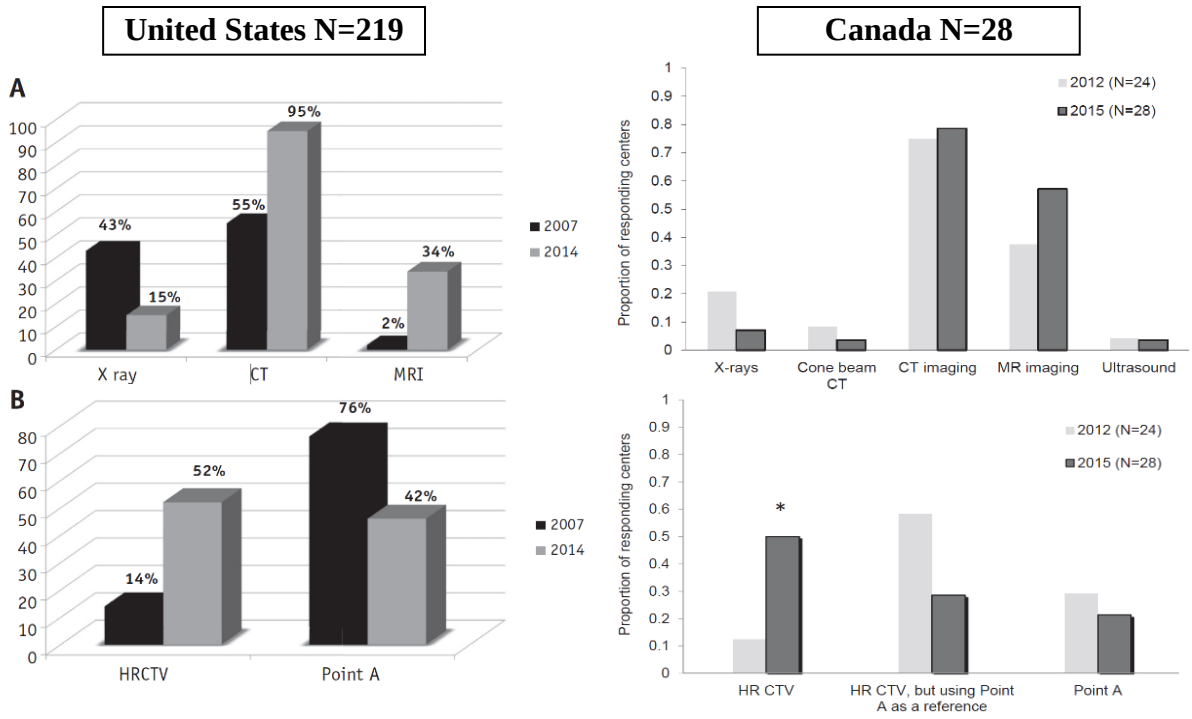

Figure 2.8: Adoption of image guidance modalities in HDR brachytherapy in the United States (left) and Canada (right). Figures (with permission) were taken from Grover *et al*. 2016 and Taggar *et al*. 2017. N: number of plans.

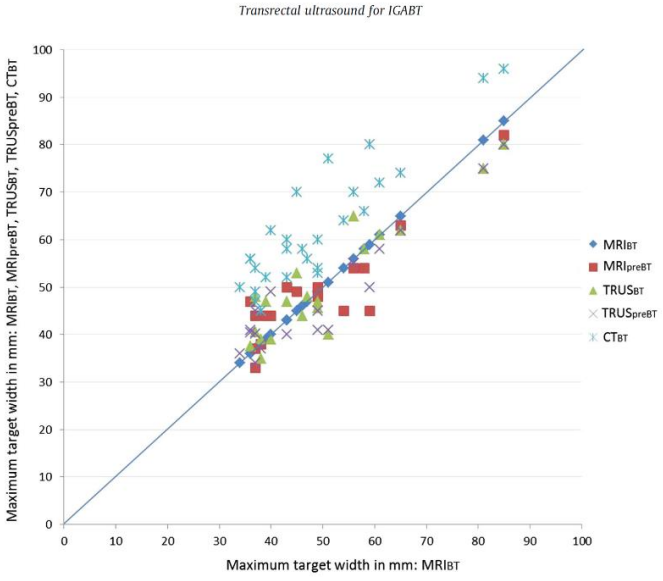

Figure 2.9: Ultrasound-based target delineation in HDR planning for GYN cases correlates well with MRI-based delineation while CT tends to overestimate the target size. Figure (with permission) was taken from Schmid *et al*. 2016.

2.2.2 Process of image-guided brachytherapy

A general scheme of HDR IGBT process is summarized in Figure 2.10. The 3D imaging and image datasets (CT, MRI and/or US) became an essential part of most of these steps including diagnosis, staging, source placement, patient simulation, structures delineation, plan optimization, dose calculation, dose-volume evaluation and pretreatment verification of applicators, needles or seeds positioning. Each imaging modality offered different advantages for the improvement of BT process. For instance, transrectal US (TRUS) was used interactively in guiding the insertion and planning of prostate implants (Wallner *et al*. 1999). Given its availability in most modern radiation oncology clinics, CT greatly improved the planning and pretreatment verification of applicator and/or needles in intracavitary and interstitial procedures such as cervical, prostate, esophageal and breast cancers (Potters *et al*. 2001, Vuong *et al*. 2005, Das *et al*. 2004, Castelnau-Marchand *et al*. 2016). MRI provided enhanced tissue contrast that was shown to be useful beyond diagnosis and staging: during the insertion, planning and pretreatment evaluation of several cancer types (Haie-Meder *et al*. 2005, Pötter *et al*. 2006, Devic 2012, Damato and Viswanathan 2015, Castelnau-Marchand *et al*. 2016, Schmid *et al*. 2020).

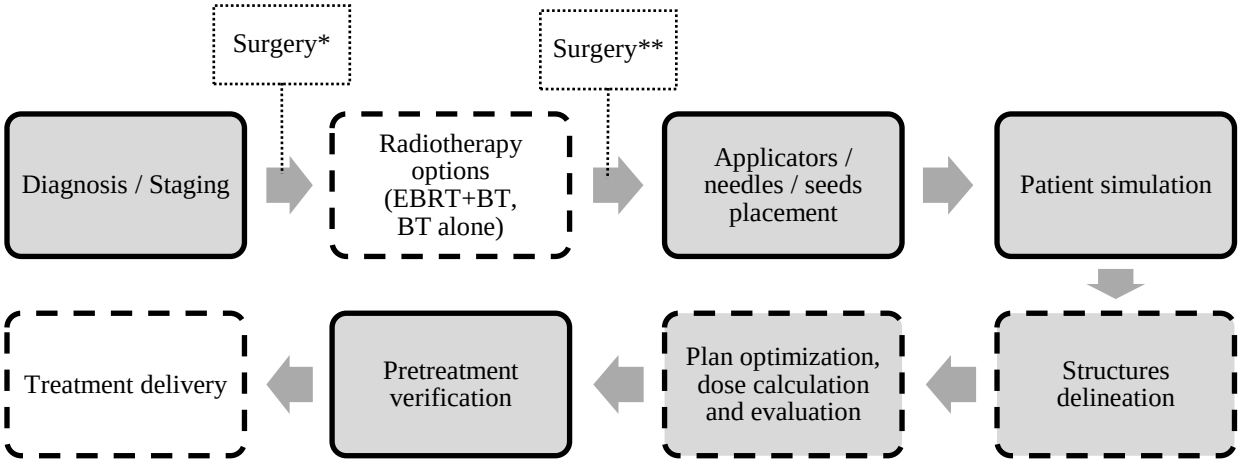

Figure 2.10: A typical treatment process in a contemporary HDR brachytherapy procedure. Steps involving imaging procedures are highlighted in grey and solid lines. Steps involving the use of 3D image datasets are highlighted in grey and dashed lines. *EBRT: External Beam Radiotherapy; HDR: High Dose Rate; BT: Brachytherapy; *: BT given after surgery/EBRT as a boost; **: BT given as preoperative treatment.*

Figure 2.11 and Figure 2.12 show in more detail the involvement of imaging in guiding and verifying different processes during BT treatment. Also they show the main roles of radiation oncologist and medical physicist. In clinical practice, the radiation oncologist performs a procedure under image-guidance to implant catheters or special applicators into or near the target site. After that, an image is taken of the patient using the chosen imaging modality (CT, MR, US) and sent to the planning software. The radiation oncologist contours the target and the OARs and the medical physicist prepares a plan. The definition of the first "dwell" position and the accuracy of the BT device (referred to as the afterloader unit) to execute correct dwell positions and dwell times are the most crucial aspects of the BT delivery process and they are managed by the medical physicist. Afterwards, the dose optimization process takes place in order to give the highest possible dose to the tumor while limiting the dose to the OARs. After plan review and approval by the radiation oncologist, the catheters are connected to the afterloader unit using transfer tubes by the therapist and treatment takes place under image-guidance and supervision by the therapist, medical physicists and radiation oncologist.

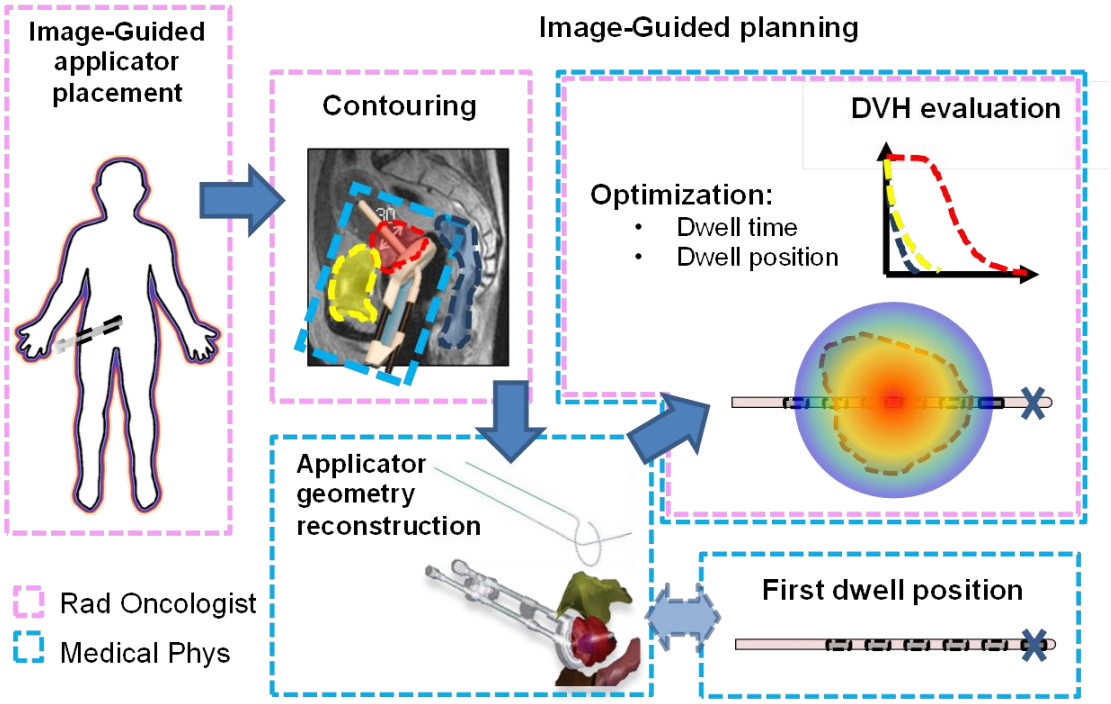

Figure 2.11: Visual illustration of the main steps involved in brachytherapy planning process.

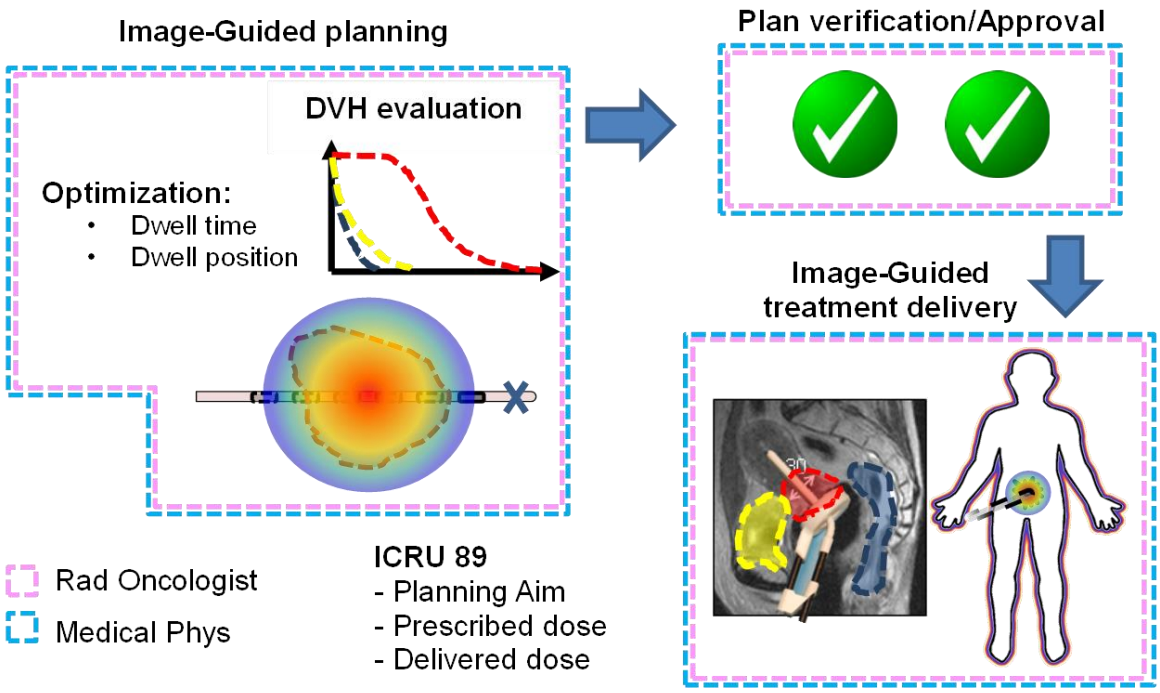

Figure 2.12: Visual illustration of the main steps involved in brachytherapy planning and treatment verification process. Three doses are to be reported as per the ICRU 89: planning aim during planning, prescribed dose as approved by the physician after planning and the actual delivered dose during treatment (requiring in-vivo dosimetry).

2.3 Quality assurance in brachytherapy

2.3.1 Importance of quality assurance

In response to an unfortunate clinical event, the American Brachytherapy Society (ABS) has issued an editorial in 2012 highlighting the importance of proper quality assurance (Horwitz 2012): "…The current Board of the ABS felt that now was the time to include all the relevant sites in which brachytherapy is a principal treatment modality. It was especially important to provide information on proper dosimetric analysis and quality assurance." The American Society for Radiation Oncology (ASTRO) provided a white paper by Thomadsen *et al*. 2014 highlighting "length" failure as one of the most common reported failure types. This included the incorrect applicator length measurements and incorrect definition of distal reference position (or first dwell position). They specifically recommended that vendors should develop new or improved QA equipment and procedures to address these issues.

There are many sources of uncertainty during the BT process (Kirisits *et al*. 2014) and each has its own risk of jeopardizing the quality and/or safety of the treatment (Wadi-Ramahi *et al*. 2016). Some examples of errors that have happened can be found in Palmer *et al*. 2014, World Health Organization 2007 and Bert *et al*. 2016. More recently in 2020, the American Association of Physicists in Medicine (AAPM) presented the report of Task Group 275 (Ford *et al*. 2020) on strategies for effective physics plan and chart review in radiation therapy included a detailed list of 53 failure modes in HDR BT. The "length" related errors were among the highest five risks in HDR BT process highlighting the importance of more-informed QA. Another advantage of proper QA is the minimization of the number of patients required in randomized trials as was found by Pettersen *et al*. 2008, since the risk of under-powering the study is minimized.

2.3.2 Current practice in HDR brachytherapy quality assurance

The standard of care in HDR BT QA is based on the AAPM reports of TG-40 (Kutcher *et al*. 1994), TG-56 (Nath *et al*. 1997), and TG-59 (Kubo *et al*. 1998). The AAPM TG-40 report was the first comprehensive QA protocol in radiation therapy addressing BT as well. The TG-56 report is the AAPM's general code of practice for all types of BT detailing additional issues specific to BT that were not covered in TG-40. For example, these reports detailed the daily, weekly, monthly, quarterly and annual QA requirements that should be performed by the BT medical physicist. Although all of these reports deal with mitigation strategies of systematic and random types of errors, the TG-59 report specifically addressed HDR BT treatment delivery focusing mainly on mitigation of random errors while the TG-56 report provided guidance on reducing systematic errors. Systematic errors are those that would occur in all delivered fractions for all patients. Examples are incorrect source position reconstruction procedure and a malfunctioning imaging modality. Random errors are those specific to each fraction, for example: visibility of catheters and image co-registration quality.

The TG-56 report detailed the goals of the BT QA program and that is to "maximize the likelihood that each individual treatment is administered consistently, that it accurately realizes the radiation oncologist's clinical intent, and that it is executed with regards to safety of the patient and others who may be exposed to radiation during the course of treatment." However, given the variability in practice among different centers, the TG-56 report mentioned that it is difficult to come up with a comprehensive QA program that suits every clinic. Therefore, they

defined end-goals for the QA program, which are: 1) Safety of the patient, the public, and the institution; 2) Positional accuracy; 3) Temporal accuracy; 4) Dose delivery accuracy.

In EBRT, specific QA procedures are well defined for the use of different anatomical imaging modalities: CT (Mutic *et al*. 2003, Bissonnette *et al*. 2012), MRI (Price *et al*. 1990, Lillicrap 2000), and US (Goodsitt *et al*. 1998, Nath *et al*. 1999, Pfeiffer *et al*. 2008). Protocols and QA guidelines also exist for different kinds of BT treatments (Kutcher *et al*. 1994, Nath *et al*. 1997, Kubo *et al*. 1998, Yu *et al*. 1999, Rivard *et al*. 2004, Butler *et al*. 2008, Nath *et al*. 2009, DeWerd *et al*. 2011, Chiu-Tsao *et al*. 2012, Perez-Calatayud J 2012, Beaulieu *et al*. 2012). However, the introduction of image-guidance into BT process must also be associated with an update (Cormack 2008, Tanderup *et al*. 2014b) to current QA protocols taking into account different uncertainties that would affect clinical outcomes (Tanderup *et al*. 2008, Kirisits *et al*. 2014). Advanced QA methodologies that address this issue are required for the use of different modalities (imaging and BT) at different phases of the treatment process. Image-guidance in BT ultimately resulted in better definition of target(s) and smaller CTV margins, and consequently led to much more stringent requirements for precise dose delivery.

2.3.3 Temporal and positional accuracy

While it is true that the introduction of 3D approaches into BT treatment process improved the clinical aspects of target delineation and DVH-based planning, it should not be forgotten that these imaging modalities provide less spatial resolution compared with conventional X-rays. This in turn means that the superior accuracy in reconstruction of the source position based on 2D X-rays may be jeopardized and this justifies the need for more sensitive tests that provide quantitative information about source positioning. Figure 2.11 suggested that the most important elements of BT treatment are the correct determination and verification of dwell positions and dwell times. Therefore, the QA of these two aspects of the afterloader unit is crucial for BT. The aforementioned QA protocols and especially the AAPM TG-56 (Nath *et al*. 1997) and TG-59 (Kubo *et al*. 1998), stressed mainly on the importance of these two aspects in addition to safety and dose delivery accuracy. For example, the Canadian Organization of Medical Physicists (COMP) and the AAPM have both recommended a ±1 mm source positioning accuracy, which is also recognized as a regulation in the US by the Nuclear Regulatory Commission (NRC). To confirm this tolerance clinically, Asgharizadeh *et al*. 2015 introduced intentional shifts (1-5 mm)

on 15 endorectal BT plans and they experimentally found out that no matter what the passing criteria was, all plans shifted by more than 1 mm has significantly failed the QA (See Figure 2.13).

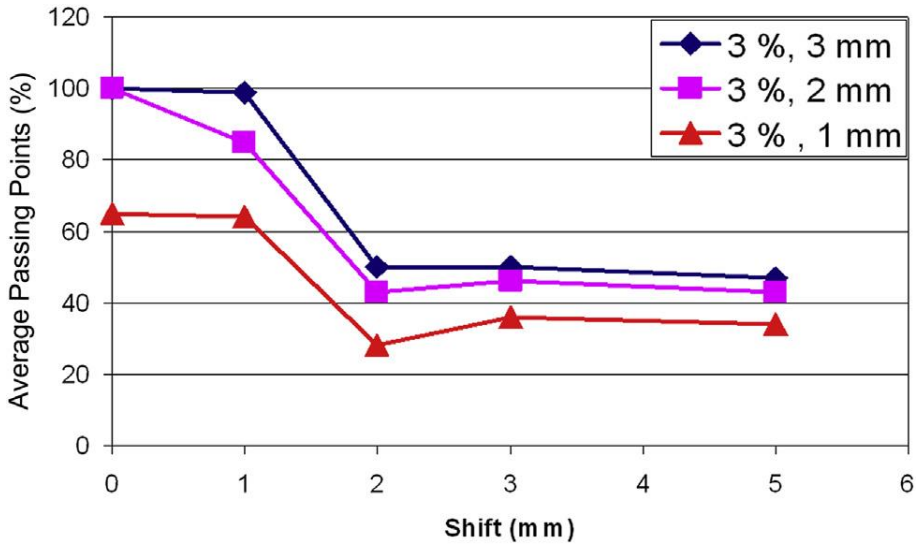

Figure 2.13: Average passing points of 15 endorectal brachytherapy plans based on different passing-rate criteria. Figure (with permission) was taken from Asgharizadeh *et al*. 2015.

2.3.4 HDR source description and absolute dose determination

In this thesis, focus will be on the widely used HDR Iridium 192 (^{192}Ir) source used in a stepping-motor based afterloader unit (microSelectron V2, Elekta, Figure 2.14). The ^{192}Ir source has a half-life of 73.8 days and a spectrum of energies with an effective energy of approximately 380 keV (Nath *et al*. 1995). The current standard for clinical HDR absolute dose determination is based on the source strength (for a given source type and model) calculated from the activity measured with a user well-type ionization chamber (Figure 2.15), having a calibration factor traceable to a primary standard (a primary standard lab's spherical graphite-walled ionization chamber). Both the user well-type ionization chamber as well as the user source must be calibrated as per the AAPM TG-56 report. The assumption is that the source manufacturer provides an identical design to the user and the calibration laboratory (for calibration at the laboratory's well-type chamber). In this way, the user can verify the source strength indicated in the calibration certificate (provided by the source manufacturer) that accompanies every source.

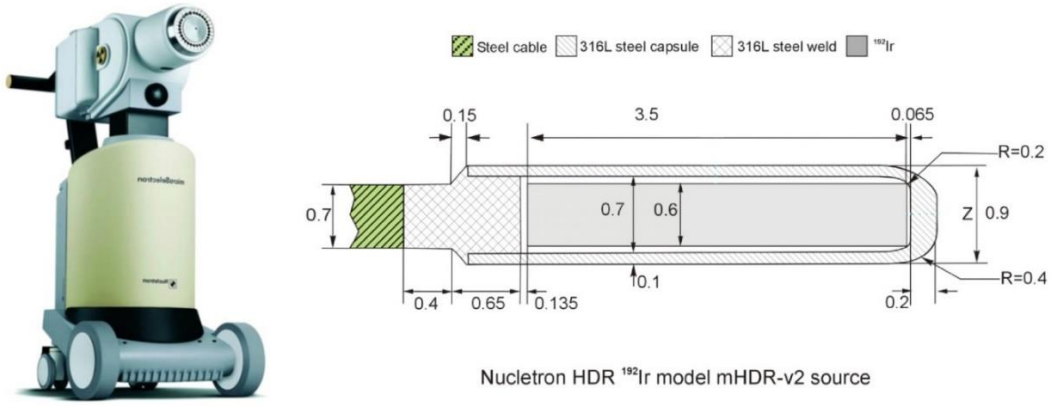

Figure 2.14: Left: the Nucletron microSelectron afterloader unit (Elekta, Sweden). Right: microSelectron b2 source specification (Elekta, Sweden). Source specification is adapted from ref Perez-Calatayud J 2012.

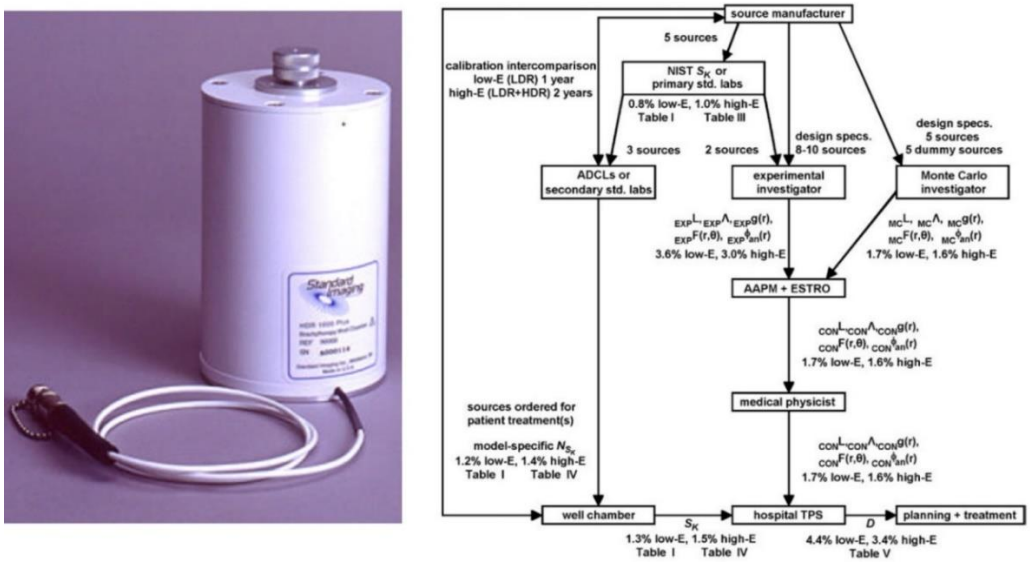

Figure 2.15: Left: well-type ionization chamber used for calibration of BT sources. Right: summary of calibration traceability from source manufacturer to the end user at the clinic. Typical uncertainty in dose determination is provided as well. This figure (with permission) is taken from ref DeWerd *et al*. 2011.

2.3.5 Dose distribution of HDR brachytherapy sources

Since the source is decaying continuously, it is more logical to provide dose distributions based on "dose rates" instead of dose. The most globally used protocol for BT source dosimetry is the AAPM TG-43 and its updates (Nath *et al*. 1995, Rivard *et al*. 2004, Perez-Calatayud J 2012). This protocol provides dose distribution around different source designs relative to a reference point that is 1 cm away from the transverse axis of the cylindrical source. The most important requirement for dose distribution calculated following this protocol is that it assumes full scattering

conditions around the source and every calculation point (i.e. an infinite water phantom). Treatment planning then becomes a 3D superposition of source positions scaled by dwell times. The dose calculation following the TG-43 "recipe" is simple, efficient and fast. The reason is that the protocol provided a single-equation model for all types of BT sources, and a set of published constants and lookup tables (LUTs) specific to each BT source model. The required information account for the source strength, dimensions, geometry, scatter and absorption properties and anisotropy of the distribution around the source. Dose distribution around BT source is given by the following equation:

$$\dot{D}(\mathbf{r},\theta) = S_K \cdot \Lambda \cdot \frac{G_L(\mathbf{r},\theta)}{G_L(\mathbf{r_0},\theta_0)} \cdot g_L(\mathbf{r}) \cdot F(\mathbf{r},\theta) \qquad (2.1)$$

where; $\dot{D}(\mathbf{r},\theta)$ is the dose rate ($\frac{cGy}{hr}$) at any distance $\mathbf{r}$ (cm) from the source center and angle θ (degree) with respect to the source axis (See Figure 2.16); S_K is the source strength ($\frac{cGy \cdot cm^2}{hr}$) provided by source manufacturer and measured by the user as a QA procedure following source installation. All the remaining parameters in Eq. (2.1) are published in the AAPM TG-43 protocol and its updates for different source designs: Λ is the dose rate constant (cm^{-2}) at the reference position ($\mathbf{r_0} = 1\ cm, \theta_0 = 90°$); $G_L(\mathbf{r},\theta)$ is the geometry function accounting for inverse square fluence fall-off; $g_L(\mathbf{r})$ is the radial dose function accounting for tissue scatter and attenuation in the transverse mid-plane only, while $F(\mathbf{r},\theta)$ is the anisotropy function accounting for tissue scatter and attenuation everywhere else.

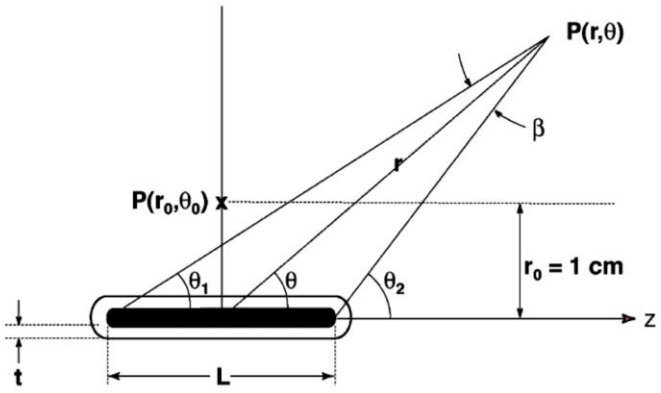

Figure 2.16: Geometry assumptions in the AAPM TG-43 dose calculation formalism. Angle β is that subtended by the active length L at point P. The reference point is represented by $P(r_0, \theta_0)$. Figure (permission not required) is taken from Rivard *et al*. 2004.

2.4 Technological advancement in HDR brachytherapy QA

2.4.1 Dosimetric tools

Different dosimetry systems can be used along different steps of the BT treatment process. Palmer *et al*. 2012 have summarized these systems in Figure 2.17. In another study by the same group, the authors investigated the possibility of performing audits for HDR BT using radiochromic film dosimetry (Palmer *et al*. 2013). Awunor *et al*. 2013 developed a method for source position QA for ring and tandem applicators using XRQA2 radiochromic film. Other relevant systems for BT QA have been investigated including diodes (Jursinic 2014, Espinoza *et al*. 2015), scintillators (Therriault-Proulx *et al*. 2011, Kertzscher and Beddar 2016, 2017, 2019), flat panel detectors (Song *et al*. 2009, Smith *et al*. 2016, 2018), radiographic film (Okamoto *et al*. 2014), radiochromic film (Evans *et al*. 2007, Palmer *et al*. 2012, Awunor *et al*. 2013, Asgharizadeh *et al*. 2015), electromagnetic tracking (Zhou *et al*. 2013, Poulin *et al*. 2015, Kellermeier *et al*. 2017) and magnetic resonance tracking (Wang *et al*. 2015). For patient (*in-vivo*) dosimetry, a summary of currently used detectors can be found in Tanderup *et al*. 2013, which excluded radiochromic film dosimetry.

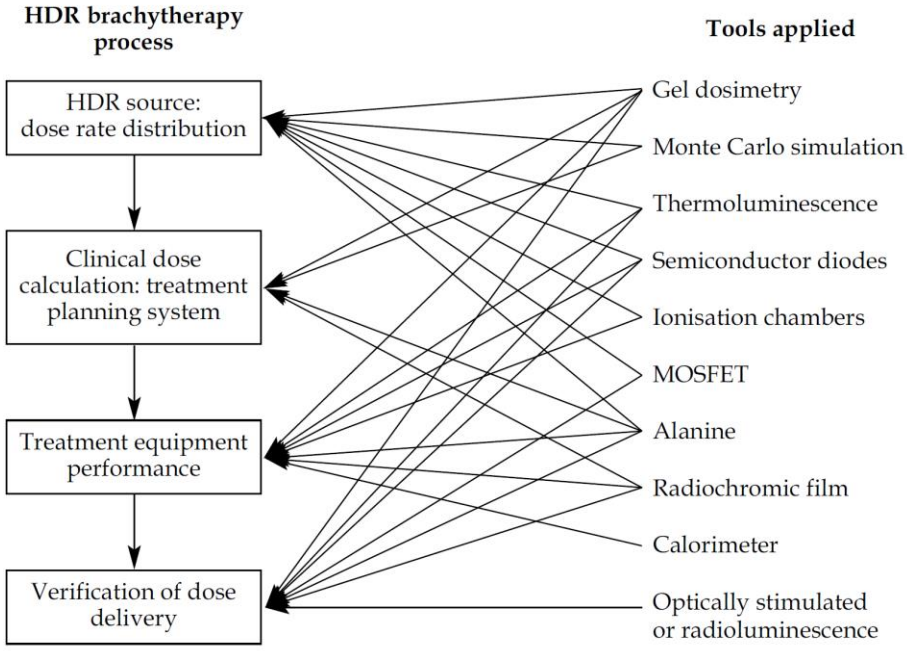

Figure 2.17: Dosimetric tools used for quality assurance at different HDR brachytherapy process. This figure is taken from Palmer *et al*. 2012.

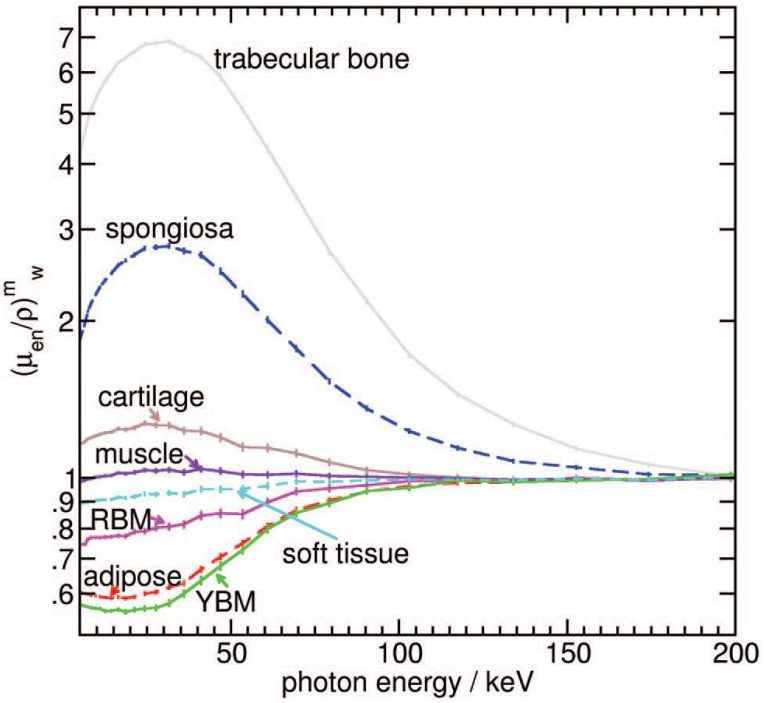

Figure 2.18: Mass energy absorption coefficients for the indicated materials relative to those for water for different energies, calculated with the EGSnrc Monte Carlo simulation code. Figure (with permission) is taken from Beaulieu *et al*. 2012.

2.4.2 Dose calculation and optimization

As mentioned in section 2.3.5, the AAPM TG-43 protocol assumes infinite water around all dose calculation points. This assumption means that tissue heterogeneities, air-tissue interface, BT applicators, and other inserted materials are not taken into account in dose calculation. In the case of high energy photon sources, such as the HDR ^{192}Ir, the impact of tissue heterogeneities is not significant for dose calculation and in fact it is why the TG-43 protocol works well in interstitial and intracavitary BT. However, for the case of surface BT there is an apparent lack of backscatter above the skin and more literature review is discussed about this in Chapter 5. Additionally, as the photoelectric-effect becomes more significant for low energy photon sources tissue heterogeneity is becoming important because of the difference in mass energy absorption coefficients with respect to water, which directly affects dose calculation (See Figure 2.18). To emphasize this, the AAPM TG-186 protocol (Beaulieu *et al*. 2012) reported on model-based dose calculations algorithms (MBDCA) and their potential application to BT. This includes advanced calculation engines such as Monte Carlo (MC) simulations, collapsed-cone (CC) convolution, and

grid-based Boltzmann solver (GBBS). For HDR BT, the application of MBDCAs may be potentially useful for surface BT. There are already some vendors offering MBDCAs such as Varian's ACUROS and Elekta's ACE calculation engines, and other promising calculation engines under research (Chibani and Williamson 2005, Taylor *et al*. 2007, Afsharpour *et al*. 2012, Chibani and Ma 2014, Chamberland *et al*. 2016, Famulari *et al*. 2018, Enger *et al*. 2020, Morcos and Enger 2020, Mao *et al*. 2020).

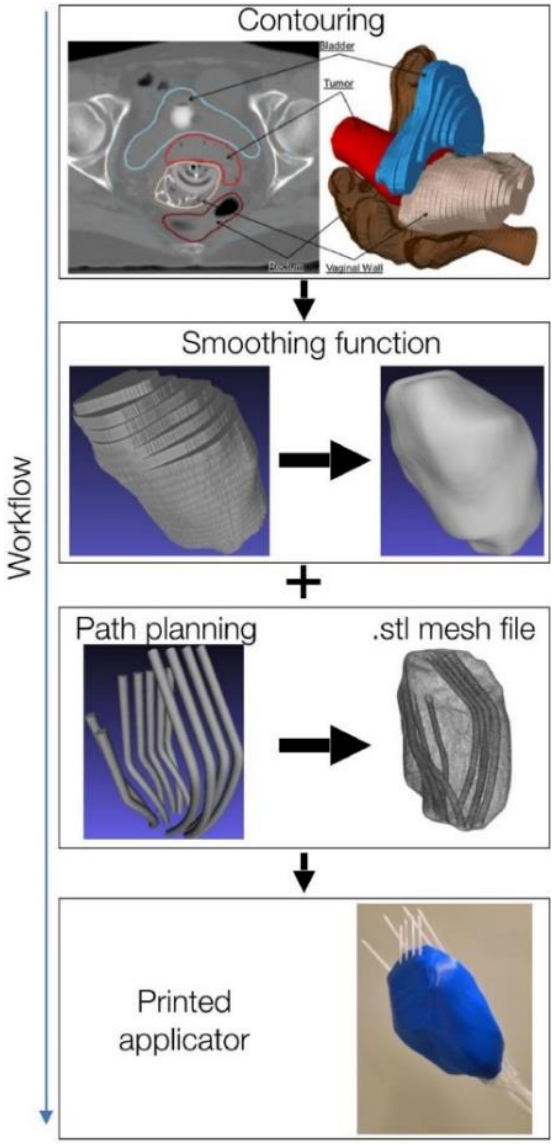

Figure 2.19: Typical 3D printing workflow for HDR brachytherapy. Figure (with permission) is taken from Cunha *et al*. 2020.

2.4.3 Applicator fabrication and customization

Although there are many applicator designs already available commercially for different BT treatment sites, they do not necessarily fit all patient geometries. The evolution in additive manufacturing (AD) in the form of 3D printing (3DP) technology was adopted in BT research because of the ability to customize applicators for specific patient needs. This has the advantage of further dose distribution customized optimization for every patient, which would potentially improve clinical outcomes, simplify the treatment process and facilitate the incorporation of BT around different clinics (Cunha *et al*. 2015, Lindegaard *et al*. 2016, Ricotti *et al*. 2016, Cunha *et al*. 2020). The 3DP also facilitated prototyping and innovation. An example of this is the printing of Freiburg Flap "holders" (Guthier *et al*. 2020). This approach has the advantage of providing reproducible setup between simulation and treatment, as well as an easy applicator positioning procedure, and also provides backscatter material to improve dosimetry accuracy if heterogeneity correction was turned off during dose calculation. Figure 2.19 summarizes the steps in 3DP fabrication of specialized applicators.

2.4.4 Intensity modulation

The goal of this section is to shed some light on the concept of intensity modulated BT (IMBT) which includes directional shielding of the source and thereby modulation of the delivered dose (Webster *et al*. 2013, Dadkhah *et al*. 2015, Seneviratne *et al*. 2018, Safigholi *et al*. 2018, DeCunha and Enger 2018, Famulari *et al*. 2020, Morcos *et al*. 2020). According to Callaghan *et al*. 2019, there are two types of IMBT with respect to the shielding/source movement during delivery: dynamic or static. The shielding could be part of the source or the applicator. Figure 2.20 summarize the current emerging IMBT technologies with the note that these technologies are under development by different research groups. While this thesis concerns only HDR sources, the rest of the technologies seen in Figure 2.20 are provided for completeness.

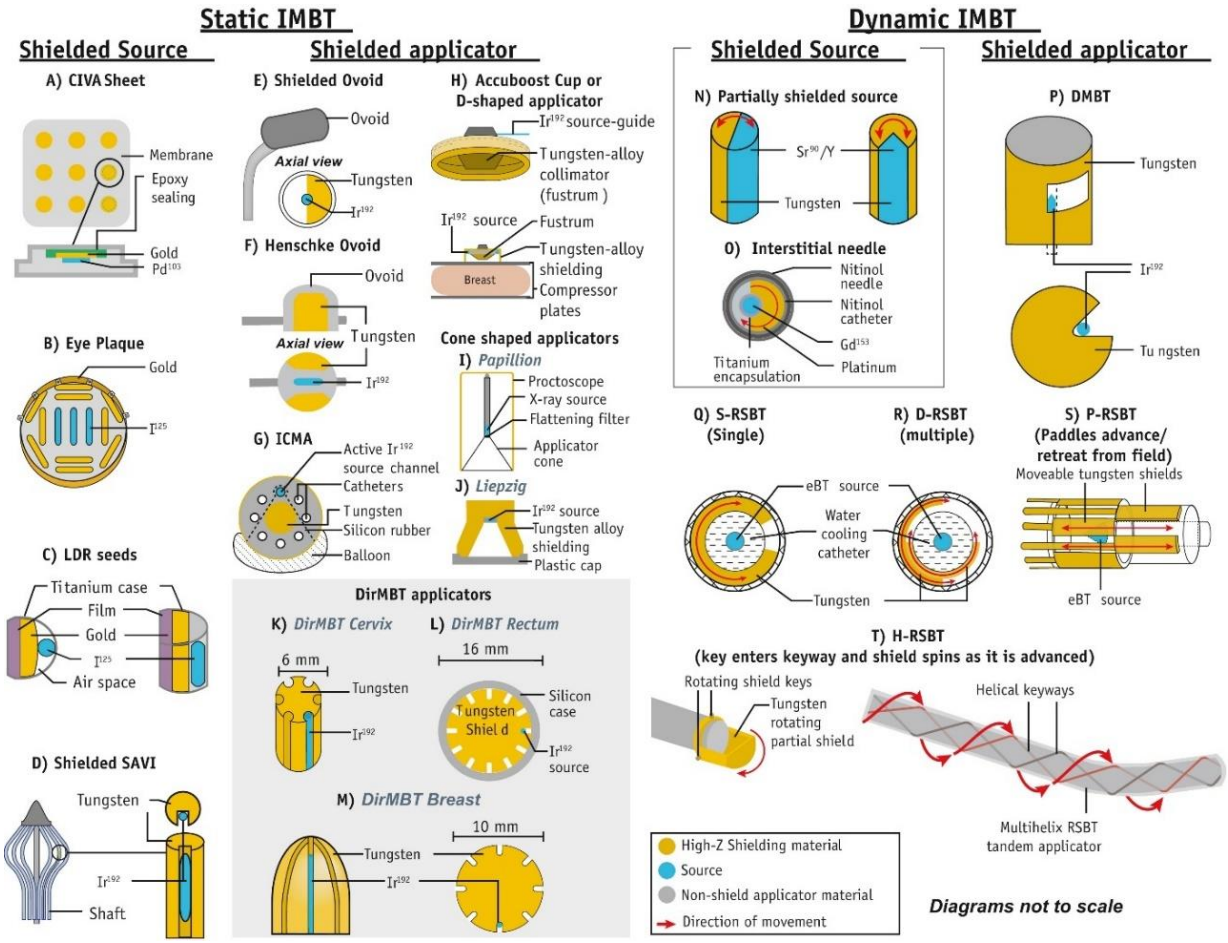

Figure 2.20: Summary of technological advancements in Intensity Modulated Brachytherapy (IMBT) delivery. DirMBT: direction-modulated brachytherapy; DMBT: dynamic modulated brachytherapy; RSBT: rotating-shield brachytherapy; D-RSBT: dynamic RSBT; H-RSBT: multihelix RSBT; P-RSBT: paddle-based RSBT; eBT: electronic brachytherapy; ICMA: intracavitary mold applicator; LDR: low-dose-rate; SAVI: Strut-Adjusted Volume Implant. Figure (with permission) and abbreviations are taken from Callaghan *et al*. 2019.

2.5 Background on radiochromic film dosimetry

This section presents only introductory information about RCF dosimetry since the body of the thesis addresses its different aspects (chapters 3-4) and its application in BT QA (chapters 5-6).

2.5.1 General characteristics

Favorably, RCF dosimetry (McLaughlin *et al*. 1991) offers a 2D high resolution solution that can be applied at different levels of the BT process (Devic 2011). The RCF offers unique properties such as its small thickness, near tissue equivalence and low visible light sensitivity (Devic *et al*. 2016a), dynamic dose range (Devic *et al*. 2009), dose rate independence (Niroomand-Rad *et al*. 1998), and energy independence in clinical beam qualities down to effective energy of 100 keV for EBT1, EBT2 and earlier EBT3 models (Sutherland and Rogers 2010, Arjomandy *et al*. 2010) and down to 40 keV for newer EBT3 film models with an improved active layer composition (Bekerat *et al*. 2014, Hammer *et al*. 2018). Also, the film has been tested widely in the literature in terms of different properties such as absorption spectra (Butson *et al*. 2005, 2009, Devic *et al*. 2010), post irradiation waiting time (Devic *et al*. 2010, Richley *et al*. 2010, Andrés *et al*. 2010, Chang *et al*. 2014), scanning mode and exposure to light (Richley *et al*. 2010, Andrés *et al*. 2010, Park *et al*. 2012), high temperature behavior (Rink *et al*. 2008, Andrés *et al*. 2010), performance in water (Aldelaijan *et al*. 2010), and depth dose measurements (Arjomandy *et al*. 2012). Each EBT model film sheet is 8” by 10” and can be cut conveniently to any desired shape. These properties make it possible to use the film for in-vivo measurements as well (Klassen *et al*. 1997, Zhu *et al*. 1997, Roozen *et al*. 2011, Avanzo *et al*. 2012). Finally, there is a multitude of RCF uses and they are summarized in Figure 2.21.

2.5.2 Definition of radiochromic film dosimetry system

The primary dose-response of RCF is defined as the absorbance and its relation to absorbed dose is not linear. Usually, the film dose-response must be calibrated against a reference dosimetry standard, usually an ionization chamber, to obtain a calibration curve. Furthermore, since the degree of non-linearity is high when using absorbance for film response, scientists looked into different film response functions that would have an improved linearity. Inexpensive document scanners have been used for RCF dosimetry for quite some time now (Devic *et al*. 2004). Depending on the scanning technology and mode used (reflection or transmission), different

response functions were proposed in the literature such as optical density, transmittance and reflectance. The main advantage of these quantities is that they simplify fitting of the response function to dose and therefore decrease uncertainties related to the fitting process.

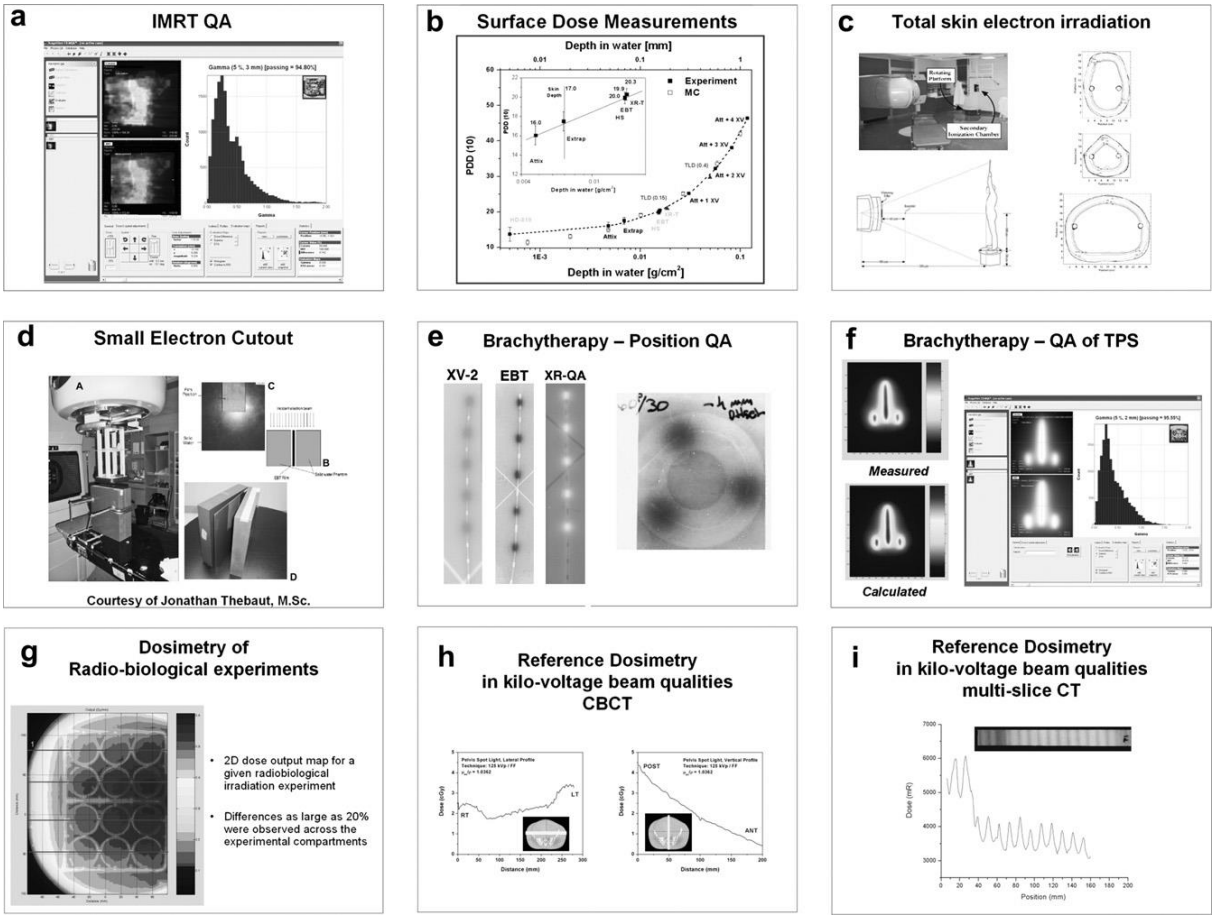

Figure 2.21: Various radiochromic film dosimetry applications. Figure (with permission) was taken from Devic 2011.

Any RCF dosimetry system consists of three essential components: a) the film model, b) the scanner model, and c) the dosimetry protocol (Devic 2011). These components must be clearly defined and maintained during the process of film calibration and measurement. There are different RCF models available nowadays and Figure 2.22 summarize them and their structures. Each of these film models has its own application depending on its sensitivity to the radiation quality and dose. Nowadays, RCFs are scanned with flatbed scanners such as the EPSON models 10000-12000XL which offer transmission and reflection scanning modes. While transmission mode is more frequently used in the literature because of its better overall achievable

dosimetric uncertainty and dose range, reflection model has higher sensitivity and dose contrast since the scanning light passes twice through the film sensitive layer. Lastly, the dosimetry protocol is a reference set of instructions that must be maintained during calibration and measurement phases, as per the AAPM TG-55 recommendations (Niroomand-Rad *et al*. 1998). This includes all the film handling procedures, scanning instructions, image analysis, as well as dose and its associated uncertainty calculation models.

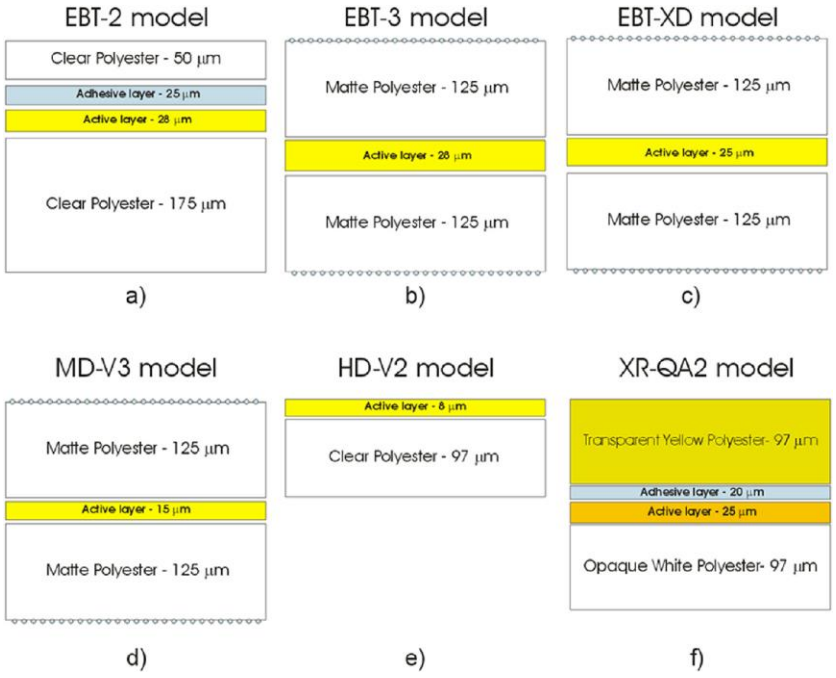

Figure 2.22: Structure and dimensions of different radiochromic film dosimetry models. Figure (with permission) is taken from Devic *et al*. 2016a.

2.5.3 Use of radiochromic film for dosimetry

Before its deployment for dose measurement, RCF response must be calibrated by delivering a range of known doses to different film pieces to establish a calibration curve that relates the film response to dose (See Figure 2.23, top). The film response is a convolution between the scanner light source emission spectrum, the film absorbance spectrum and the sensitivity of the CCD-based light detectors of the scanner. The general outline of the calibration procedure is shown in Figure 2.23: Calibration: a) unboxing and cutting the films, b) scanning before irradiation, c) irradiating films under reference conditions to known doses, d) scanning the films after a fixed

post exposure waiting time (Δt, usually 24 hours), e) establishing the calibration curve and fitting response to dose; Measurements: following the same steps exactly to acquire the response and dose afterwards. The reason there are three colors during the scanning (Red, Green, Blue) is that the films are scanned in tagged image file format (TIFF) which contains these different spectral information. Each color channel offers different dose contrast based on signal reproducibility and therefore the selection of the color channel depends on the desired dose range (Devic *et al*. 2009).

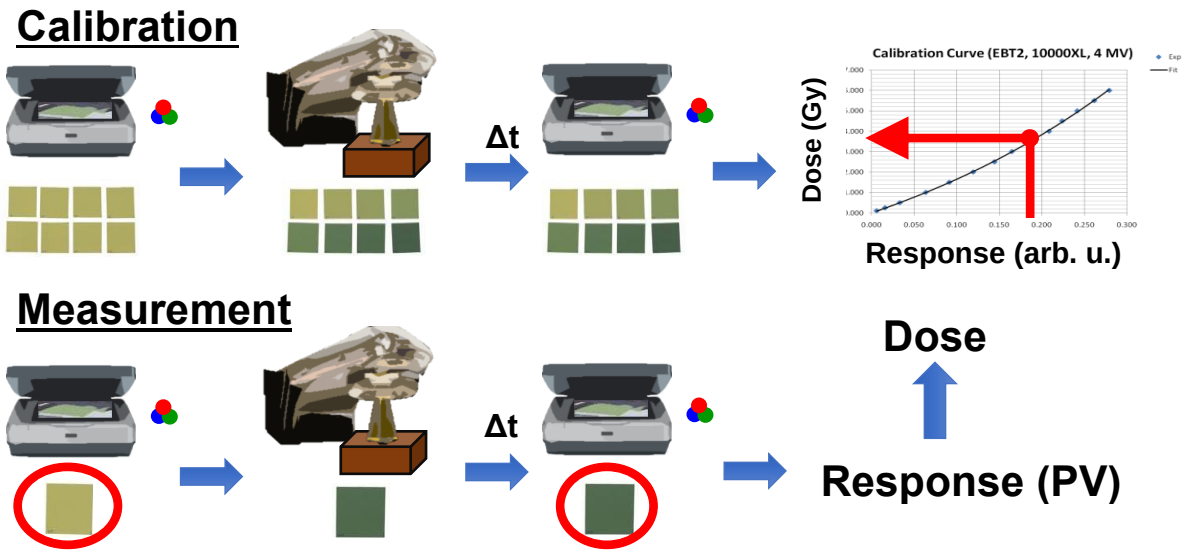

Figure 2.23: Summary of radiochromic film dosimetry protocol showing the calibration and measurement phases. Δt refers to the post exposure waiting time.

2.6 Use of radiochromic film dosimetry for HDR brachytherapy QA

Before we use RCF dosimetry for HDR BT QA, we discuss in chapters 3 and 4 the RCF response and its relation to dose for the EBT3 film model. The protocol that is used in this thesis to measure doses from the RCF is described in detail in chapter 4. Afterwards, we show the use of RCF for HDR BT QA in dosimetry (Chapter 5) and source position QA (Chapter 6). Chapter 5 introduces our first use of the RCF dosimetry protocol for HDR BT dosimetry of surface applicators in a phantom study. Finally, Chapter 6 presents our source tracking algorithm that employs RCF to determine the HDR source positional and rotational information, taking advantage of the RCF's high resolution to improve the source localization accuracy.

CHAPTER 3: Comparison of dose response functions for EBT3 model GafChromic™ film dosimetry system

---

Preface

Any contemporary radiochromic film dosimetry system consists of three main components: the film model (and batch number), the scanner model (and serial number), and a protocol that defines a set of procedures for handling and processing film pieces. The film dose-response primary signal is referred to as the absorbance and it is quantified for flatbed scanners by the quantity "pixel value," which corresponds to the measured light intensity at any point on the scanning bed with respect to the signal measured at the self-calibration area. To facilitate unknown dose measurements, a film response to dose calibration is required. To improve the fitting quality of response to dose, different response functions were proposed in the literature such as optical density, reflectance and transmittance. The use of these quantities depends on the scanning mode (transmission vs. reflection) and also on their response to dose. In this work, we investigate these different quantities as well as a new quantity that we introduced (normalized pixel value), in terms of sensitivity and achievable overall dosimetric uncertainty. We also investigate the need for pre-scanning of the same film piece (double scan protocol) and examine if a general control film piece (single scan protocol) would be sufficient without significantly impacting the achievable dosimetric uncertainty.

This work was has been published in the European Journal of Medical Physics as:

Aldelaijan, Saad and Devic, Slobodan Comparison of dose response functions for EBT3 model GafChromic™ film dosimetry system, *Phys. Med.* 49, 112-118 (2018).

Comparison of dose response functions for EBT3 model GafChromic™ film dosimetry system

Saad Aldelaijan,[1,2,3,4] and Slobodan Devic,[1,2,5]

[1] Radiation Oncology Department, Jewish General Hospital, Montreal, Quebec H3T 1E2, Canada

[2] Medical Physics Unit, McGill University, Montreal, Quebec H4A 3J1, Canada

[3] Biological & Biomedical Engineering Department, Montreal Neurological Institute, Montréal, Québec H3A 2B4, Canada

[4] Biomedical Physics Department, King Faisal Specialist Hospital & Research Centre, Riyadh, Saudi Arabia

[5] Segal Cancer Centre, Jewish General Hospital, McGill University, Montréal, Québec, Canada

Keywords: radiochromic film dosimetry system, response function.

Abstract

Objective: Different dose response functions of EBT3 model GafChromic™ film dosimetry system have been compared in terms of sensitivity as well as uncertainty vs. error analysis. We also made an assessment of the necessity of scanning film pieces before and after irradiation.

Methods: Pieces of EBT3 film model were irradiated to different dose values in Solid Water (SW) phantom. Based on images scanned in both reflection and transmission mode before and after irradiation, twelve different response functions were calculated. For every response function, a reference radiochromic film dosimetry system was established by generating calibration curve and by performing the error vs. uncertainty analysis.

Results: Response functions using pixel values from the green channel demonstrated the highest sensitivity in both transmission and reflection mode. All functions were successfully fitted with rational functional form, and provided an overall one-sigma uncertainty of better than 2% for doses

above 2 Gy. Use of pre-scanned images to calculate response functions resulted in negligible improvement in dose measurement accuracy.

Conclusion: Although reflection scanning mode provides higher sensitivity and could lead to a more widespread use of radiochromic film dosimetry, it has fairly limited dose range and slightly increased uncertainty when compared to transmission scan based response functions. Double-scanning technique, either in transmission or reflection mode, shows negligible improvement in dose accuracy as well as a negligible increase in dose uncertainty. Normalized pixel value of the images scanned in transmission mode shows linear response in a dose range of up to 11 Gy.

3.1 Introduction

If a piece of GafChromic^{TM} film is exposed to ionizing radiation, charged particles will be depositing energy throughout the sensitive layer and will initiate polymerization of a sensitive component (di-acetylene monomers). The irradiated film piece will change its color due to created polymers, which has the highest absorption in the red part of the optical spectrum. While the change in absorbance measured with a spectrophotometer would be the simplest method to evaluate the response of the film to ionizing radiation, use of such a complex instrument even for point dose measurement (let alone two-dimensional ones) would be quite cumbersome and expensive. More than a decade ago, a renaissance of radiochromic film dosimetry emerged with the introduction of the EBT GafChromic^{TM} film model [1-5]. When compared to its predecessors, the new film model was larger in size (8” x 10”), it was less expensive and new film dosimetry protocols were emerging that were using relatively inexpensive flat-bed document scanners [2]. While the film dosimetry in general was performed with various optical devices [6], the use of document scanners became the common practice not only due to its low cost, but also thanks to their straightforward implementation into both clinical and research film dosimetry procedures. Following the previously established film dosimetry protocols with radiographic films, it was somewhat natural to choose optical density as a quantity of choice to describe response of the irradiated film pieces. Optical density change was easily calculated from the transmission images obtained with flat-bed document scanners.

While there were several models of document scanners with transparency scanning options, in 2002 Alva et al. [7] suggested using reflection scanning mode to measure response of irradiated transparent (MD-55-2 model at the time) radiochromic films. In 2008, Kalef-Ezra and Karava [8], reported on comparative dosimetry results when using either reflection or transmission scanning, and reported the reflection mode was superior when used with the MD-55-2 model Gaf-Chromic™ film. Méndez et al. [9] reported on the increased robustness using a novel plan-based method while using the reflection scanned film images.

More recently, Papaconstadopoulos et al. [10] investigated response of EBT3 model Gaf-Chromic™ film in terms of uncertainty and spatial resolution for different color channels in both reflection and transmission mode. While they also found the reflection mode to be superior in terms of sensitivity (particularly at low doses up to 2 Gy based on the red channel), they observed higher uncertainties and lower accuracy that they attributed to signal saturation effects. On the other hand, compared to transmission scanning, they did not observe any loss of spatial resolution despite the additional light scattering (noise) arising from the fact that light was passing twice through the film. Use of reflection scanning mode with transparent films would further extend implementation of radiochromic film dosimetry having in mind much wider abundance and even lower cost of document scanners without transparency option.

Yet another method has been suggested by the film inventor and manufacturer, which is to use only the raw pixel values provided by the document scanner [11, 12]. Commercially available software provided by the film manufacturer was working using pixel values provided by document scanners that correspond to the light that was transmitted through the film piece. In addition, while some reference radiochromic film dosimetry protocols suggest scanning the film pieces before and after irradiation (double-scanning technique) to calculate response as a change in the film's absorbance [2], there are protocols suggesting that only one scan (single-scan technique) of irradiated film piece together with another un-irradiated film piece provides acceptable radiochromic film dosimetry system [12]. In the single-scan method, un-irradiated film piece serves both as a fog (allowing for a change in the response signal to be calculated) and, at the same time, as a control film piece, the latter being suggested [13] to correct for any changes in film absorbance due to environmental conditions (temperature, humidity, UV-light, …).

In this work we investigate the most optimal quantity in terms of sensitivity to be used as a radiochromic film response to radiation for EBT3 GafChromic™ film model based reference film dosimetry system. Pieces of EBT3 model films were irradiated to various doses in the range of up to 11 Gy and reference radiochromic film dosimetry systems were created using twelve different response functions based on film images obtained in both transmission and reflection scanning mode. While the majority of the response functions were already suggested in the literature, for each of response function investigated in this work we defined two variations: one with double-scanning and another one with single-scanning technique. Suitability of different response functions for radiochromic film dosimetry protocol was then assessed by using the error vs. uncertainty analysis.

3.2 Materials and Methods

For this study, we used the EBT3 GafChromic™ film model (Ashland Inc., Wayne, New Jersey), batch number (09071601), which represents an improved version of its predecessor having a symmetric structure and silica particles within polyester layers that led to removal of Newton rings [14, 15]. The readout device used was a flatbed Epson Expression 10000XL document scanner (Epson, Nagano, Japan) that provides 48-bit red, green, and blue (RGB) images. Film pieces were scanned in both transmission and reflection mode before and 24 hours after-irradiation using the EPSON Scan 3.01A software, with maximum OD range and all the imaging filters turned off. Images were scanned with an image resolution of 127 dpi (0.2 mm/pixel).

Eleven film pieces (1” × 2” in size) were irradiated to various dose values of up to 11 Gy. Additionally, an un-irradiated or zero-dose film piece was kept with irradiated set of films at all times. Irradiations were performed in a Solid Water™ (SW) phantom using a 20 cm × 20 cm field size. Film pieces were placed at depth of 10 cm within the phantom, and irradiated with a 18 MV photon beam from a Varian 21EX linear accelerator (Varian, Palo Alto, CA). Output of the linear accelerator was measured using a cross-calibrated chamber (PTW – TN30011) reading based on the AAPM TG-51 reference dosimetry protocol [16]. The same chamber was used as a monitor chamber when irradiating films and it was placed 5 cm below the film plane, and additional 10 cm slabs of SW were added below the monitor chamber to provide full backscatter conditions.

Raw pixel values (PV) were extracted from the scanned TIFF images by sampling six regions of interest (ROI) 2 mm × 2 mm in size (10 pixels × 10 pixels) on every film piece, as indicated in Figure 3.1 (ROI sizes are for illustrative purposes and are not to scale). Average pixel values and corresponding standard deviations were calculated for five ROIs (solid lines in Figure 3.1) using an in-house image manipulation routine written in MatLab™ (MATH Works, Inc.). Average pixel values were then used for calculation of different film response functions to radiation and creation of calibration curves. These five ROIs were sampled around the point on the irradiated film that was placed at the center of the beam, marked by small black ticks indicated on Figure 3.1. The sixth ROI (dashed line) was considered to originate from "unknown" dose and corresponding response quantity was converted into absolute dose using previously established calibration curve for the sake of calculating the absolute dose error for uncertainty vs. error analysis. In this work we used the pixel values from the green channel only, as it was shown previously that green channel provides the most suitable data when working within relatively extended dose range [17]. In addition, we found that average signals for twelve un-irradiated film pieces (total of 60 ROIs) had standard deviation of less than 0.5% for the pixel values originating from the green color channel and 1% for signal coming from the red channel, which is consistent with values reported in the literature [18].

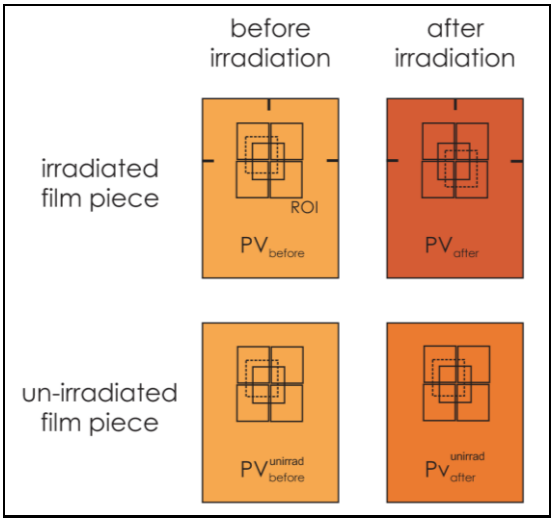

Figure 3.1: Sampling response of irradiated and un-irradiated film piece using both transmission and reflection mode scanned TIFF images from a flat-bed document scanner. (ROI sizes are for illustrative purposes and are not to scale)

According to scanning procedures depicted in Figure 3.2 and based on raw pixel data obtained in accordance with Figure 3.1 we defined total of twelve (12) radiochromic film response functions to radiation. Six functions used single-scan and another six used double-scan method. In order to make this list of functions clear, we will list single- and double-scan method based functions together.

We start with functions constructed from pixel values originating from transmission scans (Figure 3.2.left) and the most common function encountered in the literature is the optical density (OD):

$$\Delta netOD_{trans} = netOD_{trans}^{irrad} - netOD_{trans}^{unirrad} = log\left\{\frac{PV_{before}^{irrad}}{PV_{after}^{irrad}}\right\}_{trans} - log\left\{\frac{PV_{before}^{unirrad}}{PV_{after}^{unirrad}}\right\}_{trans} \quad (3.1)$$

for a double-scan method, and:

$$netOD_{trans} = OD_{trans}^{irrad} - OD_{trans}^{unirrad} = log\left\{\frac{PV_{after}^{unirrad}}{PV_{after}^{irrad}}\right\}_{trans} \quad (3.2)$$

for a single-scan method.

The second quantity that can be defined from transmission data is transmittance:

$$\Delta netT_{trans} = netT_{trans}^{irrad} - netT_{trans}^{unirrad} = \frac{1}{2^{16}}\left\{PV_{before}^{irrad} - PV_{after}^{irrad} - \left[PV_{before}^{unirrad} - PV_{after}^{unirrad}\right]\right\}_{trans} \quad (3.3)$$

for a double-scan, and:

$$netT_{trans} = T_{trans}^{irrad} - T_{trans}^{unirrad} = \frac{1}{2^{16}}\left\{PV_{after}^{unirrad} - PV_{after}^{irrad}\right\}_{trans} \quad (3.4)$$

for a single-scan method.

Finally, as the last response function using transmission data we define a normalized pixel value ($\overline{PV}$) using double-scan method:

$$\Delta\overline{PV}_{trans} = \overline{PV}_{trans}^{irrad} - \overline{PV}_{trans}^{unirrad} = \left\{\frac{PV_{before}^{irrad}}{PV_{after}^{irrad}}\right\}_{trans} - \left\{\frac{PV_{before}^{unirrad}}{PV_{after}^{unirrad}}\right\}_{trans} \quad (3.5)$$

which for single-scan method becomes:

$$\overline{PV}_{trans} = \left\{ \frac{PV_{after}^{unirrad}}{PV_{after}^{irrad}} - 1 \right\}_{trans} \tag{3.6}$$

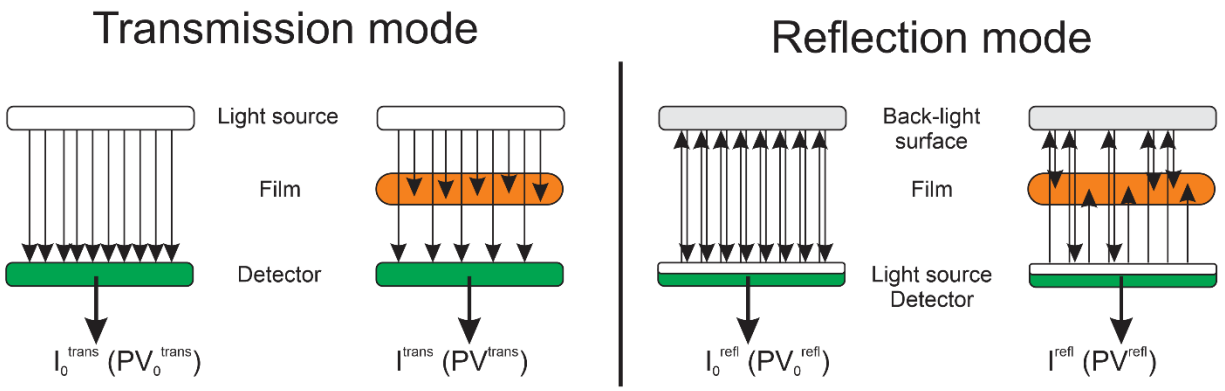

Figure 3.2: Measured "raw" data using flat-bed document scanners in transmission (left) and reflection (right) scanning mode.

The following additional six functions will be defined using pixel values obtained from images acquired in reflection scanning mode. By using raw reflection data (Figure 3.2.right) we start with most commonly encountered function used, the reflectance:

$$\Delta netR_{refl} = netR_{refl}^{irrad} - netR_{refl}^{unirrad} = \frac{1}{2^{16}} \left\{ PV_{before}^{irrad} - PV_{after}^{irrad} - \left[PV_{before}^{unirrad} - PV_{after}^{unirrad} \right] \right\}_{refl} \tag{3.7}$$

for double-scan, and:

$$netR_{refl} = R_{refl}^{irrad} - R_{refl}^{unirrad} = \frac{1}{2^{16}} \left\{ PV_{after}^{unirrad} - PV_{after}^{irrad} \right\}_{refl} \tag{3.8}$$

for single-scan method. It is of note that Eqs. (3.7) and (3.8) are identical to Eqs. (3.3) and (3.4). However, one has to keep in mind that pixel values in Eqs. (3.3) and (3.4) originate from transmission scan while the later come from reflection scan. Furthermore, functions defined by Eqs. (3.3) and (3.4) have a physical meaning of transmission while Eqs. (3.7) and (3.8) do not represent reflectance *per se*, as the measured signal originates from double passage of the light through the sensitive layer and reflection from the back-light surface of the scanner.

The second response function we define might not appear natural for data gathered in a reflection mode but the optical density can be defined in the same way as for transmission scans as:

$$\Delta netOD_{refl} = netOD_{refl}^{irrad} - netOD_{refl}^{unirrad} = log\left\{\frac{PV_{before}^{irrad}}{PV_{after}^{irrad}}\right\}_{refl} - log\left\{\frac{PV_{before}^{unirrad}}{PV_{after}^{unirrad}}\right\}_{refl} \quad (3.9)$$

for double-scan, and

$$netOD_{refl} = OD_{refl}^{irrad} - OD_{refl}^{unirrad} = log\left\{\frac{PV_{after}^{unirrad}}{PV_{after}^{irrad}}\right\}_{refl} \quad (3.10)$$

for single-scan method.

Finally, as in the case of transmission scanning mode, we can define normalized pixel value for the reflection mode:

$$\Delta\overline{PV}_{refl} = \overline{PV}_{refl}^{irrad} - \overline{PV}_{refl}^{unirrad} = \left\{\frac{PV_{before}^{irrad}}{PV_{after}^{irrad}}\right\}_{refl} - \left\{\frac{PV_{before}^{unirrad}}{PV_{after}^{unirrad}}\right\}_{refl} \quad (3.11)$$

which for single-scan method becomes:

$$\overline{PV}_{refl} = \left\{\frac{PV_{after}^{unirrad}}{PV_{after}^{irrad}} - 1\right\}_{refl} \quad (3.12)$$

In Eqs. (3.1-3.12) pixel values were calculated as weighted means:

$$PV_{average} = \sum_{i=1}^{N} \omega_i \cdot PV_i \quad (3.13)$$

with normalized weights calculated as:

$$\omega_i = \frac{1/\sigma_{PVi}^2}{\sum_{i=1}^{N}\left(1/\sigma_{PVi}^2\right)} \quad (3.14)$$

and the corresponding standard deviation on $PV_{average}$ being:

$$\sigma_{PVaverage} = \sqrt{\frac{N}{\sum_{i=1}^{N}\left(1/\sigma_{PVi}^2\right)}} \quad (3.15)$$

where in our case $N = 5$.

For each of the response functions defined by Eqs. (3.1-3.12) we generated calibration curves following previously established reference radiochromic film dosimetry protocol [19]. We successfully fitted all the response functions using rational analytical form:

$$D = \frac{a \cdot \mathcal{F}(D)}{1 + b \cdot \mathcal{F}(D)} \tag{3.16}$$

with Origin 2016 (OriginLab Corp, Northampton, MA) software using the ‘‘Levenberg–Marquardt’’ quasi-Newton minimization method. In Eq. (3.16) the $\mathcal{F}(D)$ represents one of the functions (3.1-3.12), while *a* and *b* are fitting parameters. The uncertainty analysis was performed, following Ref 19, which separates an experimental contribution from the uncertainty contribution due to the calibration curve fit of the film response function. On the other hand, the absolute dose error was calculated as a difference between delivered (assumed to be known) dose and “measured” dose using one of the appropriate response functions given by Eqs. (3.1-3.12) entered into Eq. (3.16), whereby Eqs. (3.1-3.12) were calculated for PV sampled over the sixth ROI (Figure 3.1).

It is important to say that neither the fitting function given by Eq. (3.16) nor the green channel selected represent the most optimal choice for every of the twelve response functions defined. However, our choice of the color channel and the fitting function form was based on the following assumption. In order to make an unbiased comparison, we searched for a function that would provide the same (or at best the similar) uncertainty budget for all the response functions defined. It is also important to stress that the uncertainty budget we performed in this work does not include all the Type A and B uncertainty sources one might consider when establishing a radiochromic film dosimetry system [17]. Examples of these are scanner homogeneity (type B), scanner reproducibility and variability [18] (type A or B), absolute dose calibration (measurements, calibration data, etc…, type B), and monitor chamber reproducibility (type B). However, the uncertainty budget we used for comparison includes the estimates directly related to the response functions (both experimental and fitting) and the two uncertainty sources (when summed in quadrature) have shown to be larger than calculated errors in more than 2/3 of the measurement points. Finally, as we mentioned above, the fog signal of the green channel has shown lower variation (0.5%) when compared to the red channel (1%).

3.3 Results and Discussion

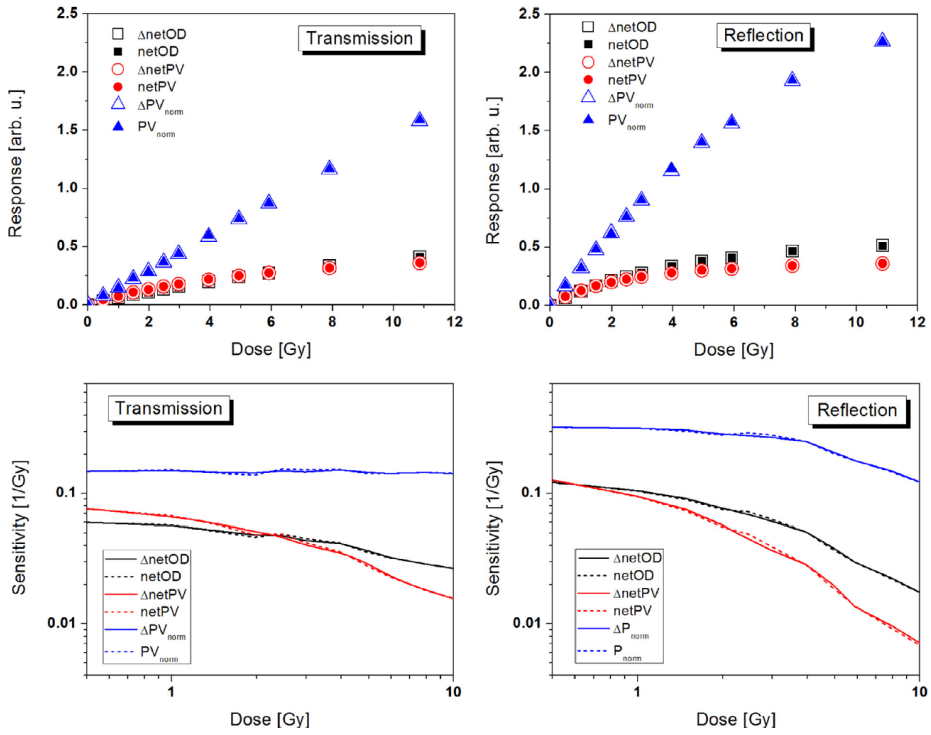

Figure 3.3: Dose response curves for various response functions obtained from transmission (top-left) and reflection (top-right) images; sensitivity curves for various dose response functions from transmission (bottom-left) and reflection (bottom-right) images.

Figure 3.3 shows the dose response curves for various response functions obtained from transmission (top-left) and reflection (top-right) scanned images. Open large symbols correspond to response values obtained using double-scan while the solid small symbols correspond to single-scan values. As emphasized at the bottom of Figure 3.3 the highest sensitivity, defined as the first derivative of the response curves, is associated with the use of "raw" pixel values read-out from the scanner, and as expected, response in reflection mode shows higher sensitivity when compared to transmission mode. It is of note that when using the transmission scanning mode both single- and double-scan normalized pixel value response functions exhibit linear behavior within dose range investigated.

From the results presented in Figure 3.3 one may conclude that the most optimal response function should be normalized pixel value having the highest sensitivity. Yet another important conclusion that emerges from Figure 3.3 is that there is negligible difference in sensitivity between single- and double-scan methods and therefore the scanning of the film pieces prior to irradiation

could be abandoned when designing reference radiochromic film dosimetry system. It is important to point out that the addition of aluminum to the sensitive layer did not only improve the energy response of the EBT3 film model [21] but also resulted in an improved lamination process leading to very uniform thickness of the sensitive layer.[1] Therefore, the unexposed piece of film scanned together with measurement film pieces after exposure serves as both the reference film piece for response change (also known as fog) and the control film piece for eventual environmental impacts on the response of measurement film pieces. This was also demonstrated in this study for the green channel (0.5%) and the red channel (1%), and a similar finding was reported in the literature by [18].

Figure 3.4 represents results of uncertainty vs. error analysis for various dose response functions obtained using transmission images in a dose range up to 11 Gy. Left column corresponds to functions that for their definition require scans of the film pieces prior and after exposure (double-scan method) while the right column corresponds to single-scan method. Both double- (left column) and single-scan (right column) methods provide one sigma uncertainty better than 2% for doses above 2 Gy. It is also of note that single-scan based response functions (right column of Figure 3.4) result in the actual errors that are somewhat higher than in the case of double-scan based response functions (left column of Figure 3.4), as expected. When comparing double-scan based response, unlike the $\Delta netOD$ both pixel value based functions result in errors that are always below the uncertainty estimates in the whole dose region investigated.

Figure 3.5 represents uncertainty vs. error analysis for different dose response functions obtained from reflection images in a dose range up to 5 Gy. Left column corresponds to functions created using double-scanning procedure, while the right column represent functions derived from single-scan method. Unlike transmission mode response functions, reflection mode based responses result in dosimetry systems with higher uncertainty. Increase in uncertainty is mainly governed by the experimental component suggesting that double passage through the sensitive layer does not only increases sensitivity of the response function but also the noise in readout signal of images obtained in reflection scanning mode. The only exception represents single-scan *netOD* response function, where the fitting uncertainty is dominant in the whole dose range investigated. Figure 3.5 also indicates that useful dose range when working in the reflection mode becomes

[1] Dave Lewis, private communication

narrower, and despite the fact the reflection scan based response functions could lead to more widespread use of radiochromic film dosimetry it would come at the expense of somewhat increased uncertainty when compared to response functions based on transmission scans. As in the case of transmission scans, the single-scanning method based response functions result in slightly larger errors.

In both Figure 3.4 and Figure 3.5 one can observe systematically higher uncertainty in double-scanning methods, governed mainly by experimental uncertainty, which is expected as the uncertainties of film pieces before exposure are compounded into the total experimental uncertainty. One can also observe that this increase in uncertainty is accompanied by an increase in accuracy, particularly at low doses.

It is important to emphasize that the choice of using the green channel only in this work was for the sole reason of making an unbiased comparison between the different response functions. Contemporary film dosimetry protocols are incorporating multichannel dosimetry which can furthermore improve the accuracy achieved from film dosimetry without increasing the total uncertainty dramatically since the signals from these color channels are correlated [22-26]. Another important note is that the results of this study were based on the central region of the scanner and therefore they are not affected by the lateral response effect which must be taken into account when performing whole-sheet 2D film dosimetry [27-29].

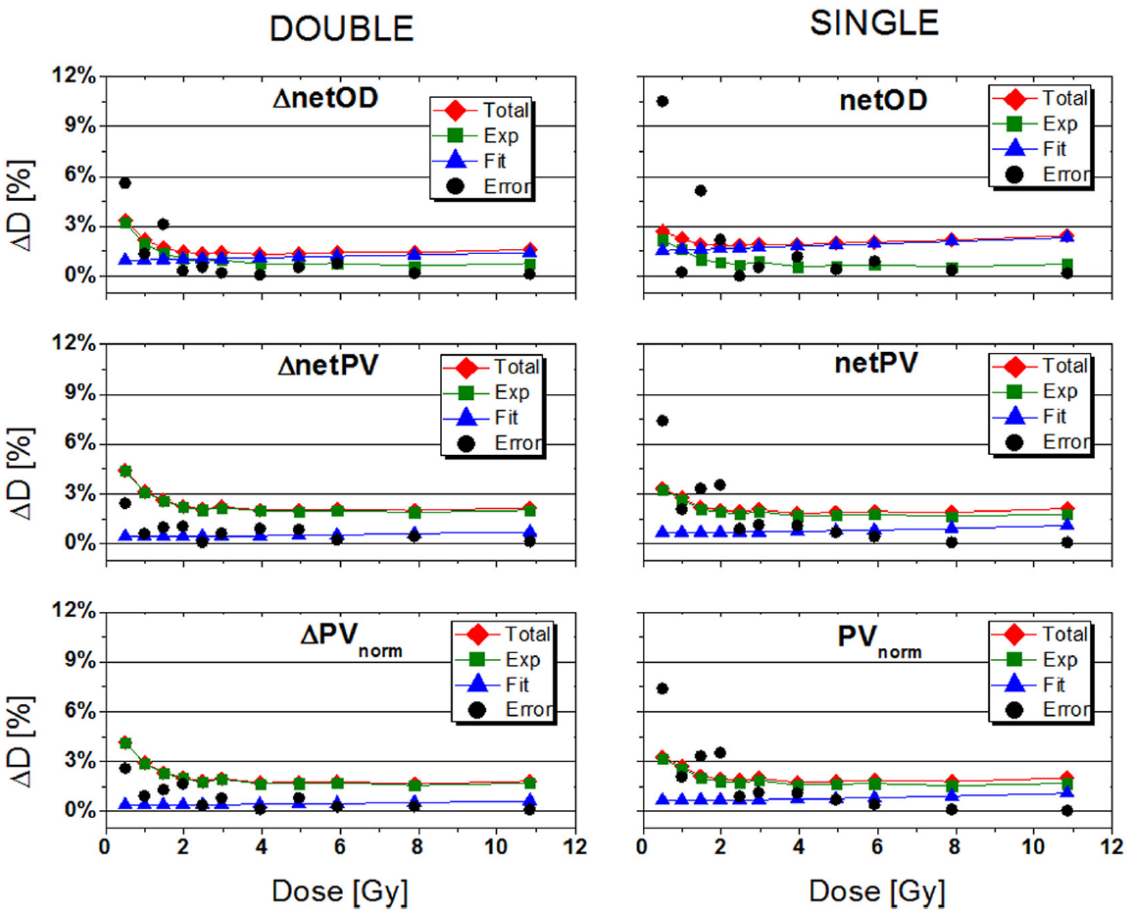

Figure 3.4: Uncertainty vs error analysis for various dose response functions from transmission images in a dose range up to 11 Gy; left column corresponds to double scan functions that for their definition require scan of the film pieces prior to exposure. Right column corresponds to single scan functions.

Taking into account sensitivity results presented in Figure 3.3, as well as uncertainty vs. error analysis given in Figure 3.4 and Figure 3.5 one may conclude that the most optimal response function for reference radiochromic film dosimetry could be the normalized pixel value. Transmission scans appear to provide slightly lower uncertainty than reflection scans, with the later providing slightly better accuracy, but in narrower dose range. Finally, our results suggest that single-scan method based response functions provide the same sensitivity as double-scan methods, with relatively small loss in accuracy, at low doses in particular.

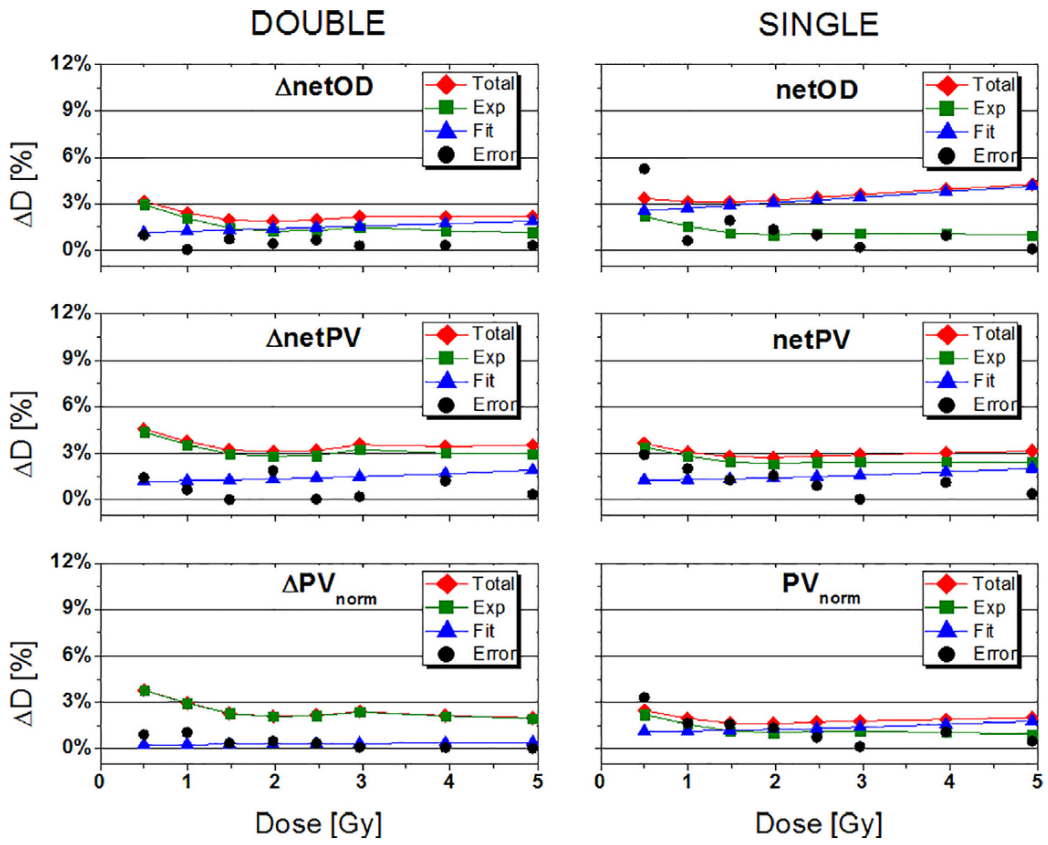

Figure 3.5: Uncertainty vs error analysis for various dose response functions from reflection images in a dose range up to 5 Gy; left column corresponds to double scan functions that for their definition require scan of the film pieces prior to exposure. Right column corresponds to single scan functions.

3.4 Conclusions

Several radiochromic film response functions were compared in terms of dose sensitivity and uncertainty vs. error analysis. While the use of reflection scanning mode provides higher sensitivity and could lead to a more widespread use of radiochromic film dosimetry, it is characterized by limited dose range and increased uncertainty when compared to transmission scanning. We demonstrated that a single-scanning method could be adopted as sufficiently precise for most of clinical and research applications. The unexposed film piece then serves as both background signal definition (fog) as well as the control film piece. Having the highest sensitivity, and the linear dose response in transmission mode, the normalized pixel values could be regarded as the optimal choice of response function for the EBT3 model GafChromic^{TM} film based reference dosimetry system.

3.5 Acknowledgement

This work was supported in part by the Natural Sciences and Engineering Research Council of Canada contract No. 386009. S.A. is a Ph.D. Candidate supported by the scholarship program at King Faisal Specialist Hospital & Research Centre (KFSH&RC). S.A. acknowledges partial support by the CREATE Medical Physics Research Training Network grant of the Natural Sciences and Engineering Research Council (Grant number: 432290).

3.6 References

1. Butson MJ, Cheung T, Yu PK., Absorption spectra variations of EBT radiochromic film from radiation exposure. *Phys Med Biol.* 2005;50:N135-40.
2. Devic S, Seuntjens J, Sham E, Podgorsak EB, Schmidtlein CR, Kirov AS, Soares CG., Precise radiochromic film dosimetry using a flat-bed document scanner. *Med Phys.* 2005;32:2245-53.
3. Rink A, Vitkin IA, Jaffray DA. Characterization and real-time optical measurements of the ionizing radiation dose response for a new radiochromic medium. *Med Phys.* 2005;32:2510-6.
4. Cheung T, Butson MJ, Yu PK. Post-irradiation colouration of Gafchromic EBT radiochromic film. *Phys Med Biol.* 2005;50:N281-5.
5. Chiu-Tsao ST, Ho Y, Shankar R, Wang L, Harrison LB. Energy dependence of response of new high sensitivity radio-chromic films for megavoltage and kilovoltage radiation energies. *Med Phys.* 2005;32:3350-4.
6. Devic S, Seuntjens J, Hegyi G, Podgorsak EB, Soares CG, Kirov AS, Ali I, Williamson JF, Elizondo A. Dosimetric properties of improved GafChromic films for seven different digitizers. *Med Phys.* 2004;31:2392-401.
7. Alva H, Mercado-Uribe H, Rodriguez-Villafuertre M, Brandan ME, The use of a reflective scanner to study radiochromic film response. *Phys Med Biol.* 2002;47:2925–33.
8. Kalef-Ezra J, Karava K. Radiochromic film dosimetry: Reflection vs transmission scanning. *Med Phys.* 2008;35;2308–11.
9. Mendez I, Hartman V, Hudej R, Strojnik A, Casar B. Gafchromic EBT2 film dosimetry in reflection mode with a novel plan-based calibration method. *Med Phys.* 2013;40:11720-9
10. Papaconstadopoulos P, Hegyi G, Seuntjens J, Devic S. A protocol for EBT3 radiochromic film dosimetry using reflection scanning. *Med Phys.* 2014;41:122101.

11. Micke A, Lewis DF, Yu X., Multichannel film dosimetry with nonuniformity correction. *Med Phys.* 2011;38:2523-34.
12. Lewis D, Micke A, Yu X, Chan MF. An efficient protocol for radiochromic film dosimetry combining calibration and measurement in a single scan. *Med Phys.* 2012;39:6339-50.
13. Aldelaijan S, Alzorkany F, Moftah B, Buzurovic I, Seuntjens J, Tomic N, Devic S. Use of a control film piece in radio-chromic film dosimetry. *Phys Med.* 2016;32:202-7.
14. Borca VC, Pasquino M, Russo G, Grosso P, Cante D, Sciacero P, Girelli G, Porta MRL, Tofani S. Dosimetric characterization and use of GAFCHROMIC EBT3 film for IMRT dose verification. *J App Clin Med Phys* 2013;14(2):158-71.
15. Reinhardt S, Würl M, Greubel C, Humble N, Wilkens JJ, Hillbrand M, Mairani A, Assmann W, Parodi K. Investigation of EBT2 and EBT3 films for proton dosimetry in the 4–20 MeV energy range. *Radiat Environ Biophys*, 2015;54(1):71-9.
16. Almond PR, Biggs PJ, Coursey BM, Hanson WH, Huq MS, Nath R, and Rogers DWO. AAPM's TG-51 protocol for clinical reference dosimetry of high-energy photon and electron beams. *Med Phys.* 1999;26:1847–70.
17. Aldelaijan S, Mohammed H, Tomic N, Liang L, DeBlois F, Sarfehnia A, Abdel-Rahman W, Seuntjens J, and Devic S. Radiochromic film dosimetry of HDR ^{192}Ir source radiation fields. *Med Phys.* 2011;38:6074-83.
18. Marroquin EYL, Herrera Gonzalez JA, Camacho Lopez MA, Barajas JEV, García-Garduño, OA. Evaluation of the uncertainty in an EBT3 film dosimetry system utilizing net optical density. *J App Clin Med Phys*, 2016;17(5):1-16.
19. Devic S, Tomic N, Lewis D. Reference Radiochromic Film Dosimetry: Review of Technical Aspects. *Phys Med*. 2016;32:541-56.
20. Lewis D and Devic S, Correcting scan-to-scan response variability for a radiochromic film-based reference dosimetry system, *Med Phys.* 2015;42(10):5692-701
21. Bekerat H, Devic S, DeBlois F, Singh K, Sarfehnia A, Seuntjens J, Shih S, Yu X, Lewis D. Improving the Energy Response of External Beam Therapy (EBT) GafChromic^{TM} Dosimetry Films at Low Energies (≤100 keV). *Med Phys.* 2014;41:022101.
22. Vera-Sanchez JC, Ruiz-Morales C, Gonzalez-Lopez A. Monte Carlo uncertainty analysis of dose estimates in radio-chromic film dosimetry with single-channel and multichannel algorithms, *Phys Med.* 2018;47:11.

23. Ruiz-Morales C, Vera-Sanchez JA, Gonzalez-Lopez A, On the re-calibration process in radiochromic film dosimetry, *Phys Med.* 2017;42:9.
24. Mendez I, Peterlin P, Hudej R, Strojnik A, On multichannel film dosimetry with channel-independent perturbation, *Med Phys.* 2013;41:011705-10.
25. Mendez I, Model selection for radiochromic film dosimetry, *Phys Med Biol*. 2015;60:4089-104.
26. Marrazzo L, Zani M, Pallotta S, Arilli C, Casati M, Compagnucci A, Talamonti C, Bucciolini M. GafChromic® EBT3 films for patient specific IMRT QA using a multichannel approach. *Phys Med*. 2015;31(8):1035-1042.
27. Pérez Azorin JF, Ramos Garcia LI, Ozcoidi DM, Almansa JF. Polarized dosimetry method for Gafchromic EBT3. *Phys Med.* 2016;32(8):972-80.
28. Lewis D and Chan MF. Correcting lateral response artifacts from flatbed scanners for radiochromic film dosimetry. *Med Phys.* 2015;42(1):416-29.
29. Crijns W, Maes F, Van Der Heide UA, Van den Heuvel F. Calibrating page sized Gafchromic EBT3 films. *Med Phys.* 2013;40(1):012102

CHAPTER 4: Dose response linearization in radiochromic film dosimetry based on multichannel normalized pixel value with an integrated spectral correction for scanner response variations

---

Preface

In the previous chapter, we introduced the 'normalized pixel value' response function based on the green color channel of film image scanned in transmission mode, which provided a linear dose response for the EBT3 GAFCHROMIC™ film model for doses of up to 11 Gy. In this work, we introduce the multichannel normalized pixel value dose response to increase the dynamic range of dose-response linearity up to 40 Gy by utilizing all color information available in the RGB images. This is especially useful for measurements of high doses expected in the case of HDR brachytherapy. Additionally, this paper introduced a new spectral correction that is generated from the scanned images themselves to correct for the scanner reading variability and scanner bed inhomogeneities with respect to calibration conditions. With these advancements, a protocol was suggested and verified for a practical, reliable and self-corrected dosimetry procedure with radiochromic films that will be utilized for quality assurance of HDR brachytherapy in the remaining of the thesis.

This work has been published in the AAPM Medical Physics journal:

Aldelaijan, S., Devic, S., Papaconstadopoulos, P., Bekerat, H., Cormack, R.A., Seuntjens, J. and Buzurovic, I.M., Dose–response linearization in radiochromic film dosimetry based on multichannel normalized pixel value with an integrated spectral correction for scanner response variations. Med. Phys., 46: 5336-5349 (2019)

Dose response linearization in radiochromic film dosimetry based on multichannel normalized pixel value with an integrated spectral correction for scanner response variations

Saad Aldelaijan[1-5], Slobodan Devic[3,4], Pavlos Papaconstadopoulos[6], Hamed Bekerat[4], Robert A. Cormack[1], Jan Seuntjens[3], Ivan M. Buzurovic[1]

[1]Department of Radiation Oncology, Dana Farber/Brigham and Women's Cancer Center, Harvard Medical School, Boston, MA, 02115, USA

[2]Department of Biomedical Engineering, Montreal Neurological Institute, McGill University, Montréal, QC, H3A 2B4, Canada

[3]Medical Physics Unit, McGill University, Montréal, QC, H4A 3J1, Canada

[4]Department of Radiation Oncology, SMBD Jewish General Hospital, Montréal, QC, H3T 1E2, Canada

[5]Biomedical Physics Department, King Faisal Specialist Hospital & Research Centre, Riyadh, 12713, Saudi Arabia

[6]Netherlands Cancer Institute, Amsterdam, 1066 CX, Netherlands

Keywords: dosimetry, linearization, multichannel film dosimetry, radiochromic film dosimetry, scanner correction

Abstract

Purpose: To introduce a model that reproducibly linearizes the response from radiochromic film (RCF) dosimetry systems at extended dose range. To introduce a correction method, generated from the same scanned images, which corrects for scanner temporal response variation and scanner bed inhomogeneity.

Methods: Six calibration curves were established for different lot numbers of EBT3 GAFCHROMIC™ film model based on four EPSON scanners (10000XL (2 units), 11000XL, 12000XL) at three different centers. These films were calibrated in terms of absorbed dose to water based on TG51 protocol or TRS398 with dose ranges up to 40 Gy. The film response was defined in terms of a proposed normalized pixel value (nPV_{RGB}) as a summation of first order equations based on information from red, green and blue channels. The fitting parameters of these equations are chosen in a way that makes the film response equal to dose at the time of calibration. An integrated set of correction factors (one per color channel) was also introduced. These factors account for the spatial and temporal changes in scanning states during calibration and measurements. The combination of nPV_{RGB} and this "fingerprint" correction formed the basis of this new protocol and it was tested against net optical density ($netOD_{X=R,G,B}$) single channel dosimetry in terms of accuracy, precision, scanner response variability, scanner bed inhomogeneity, noise, and long term stability.

Results: Incorporating multichannel-features (RGB) into the normalized pixel value produced linear response to absorbed dose (slope of 1) in all six RCF dosimetry systems considered in this study. The "fingerprint" correction factors of each of these six systems displayed unique patterns at the time of calibration. The application of nPV_{RGB} to all of these six systems could achieve a level of accuracy of ±2.0% in the dose range of interest within modeled uncertainty level of 2.0–3.0% depending on the dose level. Consistent positioning of control and measurement film pieces and integrating the multichannel correction into the response function formalism mitigated possible scanner response variations of as much as ±10% at lower doses and scanner bed inhomogeneity of ±8% to the established level of uncertainty at the time of calibration. The system was also able to maintain the same level of accuracy after 3 and 6 months post calibration.

Conclusions: Combining response linearity with the integrated correction for scanner response variation lead to a sustainable and practical RCF dosimetry system that mitigated systematic response shifts and it has the potential to reduce errors in reporting relative information from the film response.

4.1 Introduction

Radiochromic film[1–3] (RCF) has been a dosimeter of choice when high resolution 2D dose measurements are required. Any RCF dosimetry system consists of three essential components: a) the film model, b) the scanner model, and c) the dosimetry protocol.[4] Nowadays, most EBT3 model RCF dosimetry systems utilize linear charge-coupled device (CCD) based flatbed document scanners,[2] and different scanner models may incorporate different light source technologies.[5] These properties affect the film readout since the signal measured by the scanner is a convolution between the light source emission spectrum, the film absorbance properties and the sensitivity of the CCD-based light detectors. Most scanner models used with RCF dosimetry were based on xenon fluorescent lamps (e.g. EPSON Expression 10000XL/11000XL, V700) and different film response functions were well documented in the literature based on transmission or reflection acquisitions using these scanners.[6–8] More recently, LED based scanners (e.g. EPSON 12000XL, V800) were introduced in the market and they are replacing older models. Therefore, it is possible that already-established accuracy levels with the current RCF dosimetry systems may be impacted by such changes and these new scanners must be tested thoroughly. Lárraga-Gutiérrez *et al*[9] evaluated the performance of the V800 LED scanner and compared its use to the 11000XL model. They concluded that the response of the V800 scanner was comparable to the 11000XL but they noted some important spectral differences between the two types of lamps. Although the LED based scanner showed better signal stability, they reported stronger non-uniformity of the scanning bed, which might have an impact when the whole sheets of film are used, such as for larger IMRT/VMAT dose distribution measurements.[10]

The third aspect of RCF dosimetry system is the dosimetry protocol[11] which is a reference set of instructions that must be maintained during calibration and measurement phases, as per the AAPM TG55 recommendations.[3] This includes all the film handling procedures, scanning instructions, image analysis, as well as dose and its associated uncertainty calculation models. The definition of a suitable response function is an important aspect of the dosimetry protocol because it directly affects prospective dose calculation accuracy and precision.[12, 13] Considering transmission scanning, there are three main categories of RCF dosimetry protocols that can be found in the literature: single channel dosimetry based on empirical models,[2] single channel dosimetry based on physical models,[14, 15] and triple channel dosimetry based on empirical models.[16–19] Most of the empirical models were shown to be accurate when used in conditions similar

to the calibration conditions, however, possible changes in the scanner-film states may lead into significant inaccuracies if not accounted for. This in turn lead into the introduction of recalibration protocols[20, 21] which took these changes into account but with the caveat that they require extra irradiation(s) of reference dose(s) to rescale the calibration curve.

In this work, an improved response function based on normalized pixel value[13] of all color channels has been introduced using different scanner models (xenon fluorescent *vs* LED lamps). This response function, referred to as the multichannel normalized pixel value (nPV_{RGB}) has the advantage of reproducibly linearizing the dose response and it allows performing direct per-channel corrections taking into account the spatial and temporal changes between calibration and measurement phases. Also, optimal positioning of control and measurement film pieces on the scanning bed has been discussed. The new protocol has been tested against net optical density ($netOD_{X=R,G,B}$) single channel dosimetry protocol in terms of accuracy, precision, scanner response variability, scanner bed inhomogeneity, noise, and long term stability.

4.2 Materials and Methods

4.2.A Radiochromic film dosimetry system

In this work, six lots of EBT3 GAFCHROMIC™ film model (Ashland Inc, Wayne, NJ) were used together with three different EPSON scanner models: two units of 10000XL (discontinued), one unit of 11000XL (discontinued) and one unit of 12000XL (Epson, Nagano, Japan), available at three different centers at: Montreal (EBT3 lot 1, lot 3 with 10000XL-A and lot 5 with 11000XL), Riyadh (EBT3 lot 2, lot 4 with 10000XL-B), and Boston (lot 6 with 12000XL). More information about the structure and characteristics of the film can be found elsewhere in the literature.[2]

4.2.B Film calibration and irradiation setups

Three different Varian linear accelerators (linacs, Varian, Palo Alto, CA) were used for film calibration under MV photon beams. These linacs and the energy used for calibration were TrueBeam™ (10 MV, Riyadh), Clinac eX (18 MV, Montreal), and Edge® (6 MV, Boston). The beam output was calibrated in terms of absorbed dose to water based on AAPM TG51 protocol[22, 23] (Montreal, Boston) or IAEA TRS398[24] (Riyadh) using reference ion chambers. At all centers, the reference ion chamber was positioned at 10 cm depth within a 30 × 30 × 30 cm^3 Solid

Water™ phantom, and the field size was set to 10 × 10 cm^2 with either a source-to-axis distance (SAD) of 100 cm or a source-to-surface distance (SSD) of 100 cm (TrueBeam™: SSD, Clinac eX: SAD, Edge®: SAD). To generate the calibration curves, film pieces were irradiated in the same phantom (one piece at a time) and they were positioned at 10 cm depth in place of the reference ion chamber. During film calibration the beam was monitored by an ion chamber positioned 10 cm below the film. The six different RCF dosimetry systems used in this work had different dose ranges and approximately the same dose geometric distribution and the maximum delivered dose was 40 Gy.

4.2.C Film scanning and image analysis

Films were scanned in accordance to currently used film protocols[3, 25] 24 hours after irradiation only[13] at 254 dpi (0.1 mm per pixel) in transmission mode by 48-bit EPSON Expression flatbed RGB scanner models: 10000XL, 11000XL and 12000XL as described in section (2.A.). Images were saved as tagged image file format (TIFF) with all color correction features turned off and all RGB color channels were used in this work. For most of the scans (except evaluation of scanner bed inhomogeneity), measurement film pieces were scanned together with control film of the same size at the middle long section of the scanner. The orientations of all film pieces were maintained at all times and the control piece was always placed in the middle of the scanner. A de-noising[26] 2D Wiener filter was applied to all images which was found effective in reducing noise while preserving the true pixel value (PV) information.[2] Since the values of all pixels are determined with respect to the scanner calibration area, any inhomogeneities, deformities, dust particles in that area will appear as horizontal streaks across the film image and it should be accounted for. This "streaks" correction can be applied within any image by making sure to include some space around the films when scanning. For any image of size $i \times j$, the first and last ten pixels of any row n in the image were used to create two average pixel values (PV_{AVG}): one represents the first pixel of the row [$PV_{AVG}(n, 1)$ = Average($PV(n, 1{:}10)$)] and the other, the last pixel [$PV_{AVG}(n, j)$ = Average($PV(n, j\text{-}10{:}j)$)]. The correction along the whole row is then generated by linear interpolation between these two points per row using the following transformation per pixel $PV_{AVG}(1{:}i, 1{:}10 \cup j\text{-}10{:}j)/PV_{AVG}(i, j)$. It is assumed that the first ten pixels and the last ten pixels of every row do not intersect with pixels containing information about the film or any imperfections (dust, fingerprints etc…). After streaks and noise removal, thirty 10 mm by 10 mm

regions of interest (ROIs) were randomly selected within the central 20 mm by 20 mm area of each uniformly irradiated film piece whereas the final mean and standard deviation was calculated as a weighted average of these ROIs.[2]

4.2.D Multichannel normalized pixel value

4.2.D.1 System definition

In a previous work,[13] a dose response function was introduced that is based on normalized pixel values from a green-channel transmission scan (nPV_G). It has the form:

$$nPV_G = \left\{ \frac{PV_{after}^{meas,ctrl}}{PV_{after}^{meas,Dose}} - 1 \right\}_{trans} \tag{4.1}$$

Where $PV_{after}^{meas,ctrl}$ and $PV_{after}^{meas,Dose}$ are the green channel transmission pixel values of the control film piece and the measurement film piece, respectively. The subscript "*after*" means that both film pieces are scanned after irradiation without the need to scan them before exposure since the mean values of several background film pieces was found to be reproducible to within 0.3% in the green channel and confirmed by other studies.[13,27] From this point onward the subscript *"after"* will be omitted assuming that all the pixel values refer to film scans after irradiation. The "– 1" is added to have a response of zero when the film is not irradiated.

The advantage of nPV_G dose response function is that it has a linear response to doses up to 10 Gy.[13] Similarly, for all color channels, one can define:

$$nPV_{X=R,G,B} = \left\{ \frac{PV_X^{meas,ctrl}}{PV_X^{meas,Dose}} - 1 \right\}_{trans} \tag{4.2}$$

Based on the fact that each color channel has an optimal dose response at a specific dose range[27,28] *i.e.* red channel (up to 6-8 Gy), green channel (approximately 6-40 Gy), and blue channel beyond, the concept of nPV was revisited to include a single response function that is weighted by multi-color responses in a way to achieve reproducible linear response from the film including doses higher than 10 Gy. This concept is introduced as an improved multichannel normalized pixel value response based on all color information, nPV_{RGB}, and it can be written as:

$$nPV_{RGB} = \left\{ r \cdot \left(\frac{PV_R^{meas,ctrl}}{PV_R^{meas,Dose}} - 1 \right) + g \cdot \left(\frac{PV_G^{meas,ctrl}}{PV_G^{meas,Dose}} - 1 \right) + b \cdot \left(\frac{PV_B^{meas,ctrl}}{PV_B^{meas,Dose}} - 1 \right) \right\}_{trans} \quad (4.3)$$

From (4.2) and (4.3), one can also write:

$$nPV_{RGB} = r \cdot nPV_R + g \cdot nPV_G + b \cdot nPV_B \quad (4.4)$$

Where *r*, *g*, *b* are weighting factors that determine the overall contribution of specific color channel to the linearized dose response function. These weighting factors can be simply and efficiently found once by fitting the multichannel film response at a given dose range to absorbed dose using multiple regression linear system analysis. However, finding these parameters should be based on minimizing the errors sum of squares at all dose levels. Therefore, care should be taken if the dose step size is different between different dose points. For example the following deemed doses have different step sizes: 0, 50, 100, 200, 300, 400, 500, 800, 1100, 2000, 3000, 4000. The last three points would be less focused on in a robust-type fitting. Therefore, a two-step weighting process for the fit is suggested:

(1.a) find weights (w_D) which give more significance to dose levels with large dose intervals. It has the form:

$$w_{D_i}(D_i) = \frac{D_i - D_{i-1}}{D_{max}} \quad (4.5a)$$

where D_i is the current dose level, D_{i-1} is the precedent dose level and D_{max} is the maximum calibration dose under consideration.

(1.b) find statistical weights (w_S) in a way to give more significance toward dose levels with higher relative standard deviation (corresponding to lower doses), which has the form:

$$w_{S_i}(D_i) = \left(\frac{1}{\sqrt{\left(\frac{\sigma_{i=1}}{PV_i}\right)^2 + \left(\frac{\sigma_i \cdot PV_{i=1}}{{PV_i}^2}\right)^2}} \right) \Big/ \left(\sum_{i=1:n} \frac{1}{\sqrt{\left(\frac{\sigma_{i=1}}{PV_i}\right)^2 + \left(\frac{\sigma_i \cdot PV_{i=1}}{{PV_i}^2}\right)^2}} \right) \quad (4.5b)$$

where the term $\sqrt{\left(\frac{\sigma_{i=1}}{PV_i}\right)^2 + \left(\frac{\sigma_i \cdot PV_{i=1}}{{PV_i}^2}\right)^2}$ is the uncertainty expression of $nPV_{X=R,G,B}$, and σ_i , PV_i are the standard deviation and pixel value of any given color channel calculated over scoring

ROI. Subscript *i*=1 refer to the control film piece. For simplicity, these "dose" weights are picked up from the green channel *PV* information.

(2) The last step is to find the relative combined weights w_C:

$$w_{C_i}(D_i) = n \cdot w_{D_i}(D_i) + (n-1) \cdot w_{S_i}(D_i) \tag{4.5c}$$

where n is found by minimizing the errors sum of squares at all dose levels through providing different proportions (n = 0:1) between w_D and w_S.

Finally, the dose can be written as:

$$Dose(PV_{R,G,B}^{meas}, PV_{R,G,B}^{ctrl}) = d_{lin} \cdot \ nPV_{RGB} \tag{4.6}$$

where d_{lin} is a dose conversion factor that is set to be one at the time of calibration and it can be used as a decay factor for different post exposure times. However, in this study, only 24 hours post exposure time is used in order to showcase the nPV_{RGB} concept and the associated correction protocol.

Based on propagation of error analysis,[29] the uncertainty associated with nPV_{RGB} can be calculated using the following equation: $\sigma_{nPV_{RGB}} =$

$$\sqrt{\sum_{\substack{x=r,g,b \\ X=R,G,B}} \left(\left(\frac{x}{PV_X^{meas}} \right)^2 \cdot \left(\sigma_{PV_X^{ctrl}} \right)^2 + \left(\frac{x.PV_X^{ctrl}}{(PV_X^{meas})^2} \right)^2 \cdot \left(\sigma_{PV_X^{meas}} \right)^2 + \left(\frac{PV_X^{ctrl}}{PV_X^{meas}} - 1 \right)^2 \cdot (\sigma_x)^2 \right)} \tag{4.7}$$

The uncertainty of dose (given by equation 4.6) can be expressed as:

$$\sigma_{Dose} = \sqrt{(d_{lin})^2 \cdot \left(\sigma_{nPV_{RGB}} \right)^2 + (nPV_{RGB})^2 \cdot \left(\sigma_{d_{lin}} \right)^2} \tag{4.8}$$

where $\sigma_{Dose} = \sigma_{nPV_{RGB}}$ at time of calibration since d_{lin}= 1.

4.2.D.2 Introducing the “fingerprint” correction

In order to report the dose correctly based on equation (4.4), the same conditions during calibration and measurement have to be maintained. This is not always the case even if the user followed a specific protocol diligently.[30] The reasons for this are mainly attributed to changes in the film and scanner responses. On one hand, possible changes in film response can be minimized by storing the films properly in places with good temperature history and minimal light exposure and by maintaining the post exposure time as much as possible. On the other hand, the response of the scanner is unpredictable albeit it might be minimal as was shown by Lewis and Devic[31] for the 10000XL model. Since the film signal is often normalized by a background, such as in the cases of optical density and nPV_{RGB}, the readings (per color channel) based on these signals are prone to scanner response changes between exposed and unexposed films. For the case of nPV_{RGB}, it is particularly important to correct for the scanner variability because each of its components ($nPV_{X=R,G,B}$) has a background correction and they are added sequentially. Therefore, a correction methodology is provided that takes into account the spatial and temporal changes in film/scanner responses. The basis of this correction is the assumption that geometric relation between the color channels should be maintained during calibration and measurement phases. A “fingerprint” of the dosimetry system is proposed at the time of calibration and it will be shown that one can acquire a “fingerprint” at another time point and generate a correction (based on measured pixel values only) that takes into account the difference in scanner/film states between the two points in time. Adding color-based scanner response corrections (c_R, c_G, c_B) to $nPV_{X=R,G,B}$ components allows for corrected dose calculation in one step:

$$Dose = nPV_{RGB} = c_R \cdot r \cdot nPV_R + c_G \cdot g \cdot nPV_G + c_B \cdot b \cdot nPV_B \tag{4.9}$$

with c_R, c_G, c_B defined as:

$$c_{X=R,G,B} = \frac{c_{X=R,G,B}^{meas}}{c_{X=R,G,B}^{cal}} = \frac{\frac{PV_X^{meas}}{PV_R^{meas}+PV_G^{meas}+PV_B^{meas}}}{\frac{PV_X^{cal}}{PV_R^{cal}+PV_G^{cal}+PV_B^{cal}}} \tag{4.10}$$

where $c_{X=R,G,B}^{meas}$ and $c_{X=R,G,B}^{cal}$ refer to “fingerprints” at time of measurements and calibration, respectively. The value of $c_{X=R,G,B}$ at the time of calibration is equal to one. At the time of measurement, the value of $c_{X=R,G,B}^{meas}$ can be calculated directly from the measurement image RGB pixel

values, while the correct value of $c_{X=R,G,B}^{cal}$ requires knowledge of the dose *a priori*. To do this, the unknown dose is initially calculated using equation 4.9 with all correction factors (c_R, c_G, c_B) set to one. The resulting calculated dose will then be used to estimate the initial value of $c_{X=R,G,B}^{cal}$ at that particular dose from calibration. For the next iteration, the corrected dose is used to estimate $c_{X=R,G,B}^{cal}$ and the cycle is stopped when the change in the value of $c_{X=R,G,B}^{cal}$ is less than a set threshold (0.5% in our case). The dose is always calculated as the difference between nPV_{RGB} values of measurement and unexposed (control) film pieces. Figure 4.1 demonstrates a timeline showing the application of the "fingerprint" correction.

4.2.D.3 Testing the multichannel normalized pixel value and correction protocol

The multichannel normalized pixel value method was tested for the six RCF dosimetry systems considered in this study. To test the "fingerprint" correction protocol, three common problems related to the scanning process were tested: 1) short term scanner response variability, 2) scanner bed inhomogeneity, and 3) long term verification and stability. For all of these issues the proposed method in this study was compared to single channel dosimetry based on net optical density ($netOD$) responses in red, green and blue color channels, and the reader is referred to Devic *et al* review paper for a comprehensive explanation of this quantity.[2]

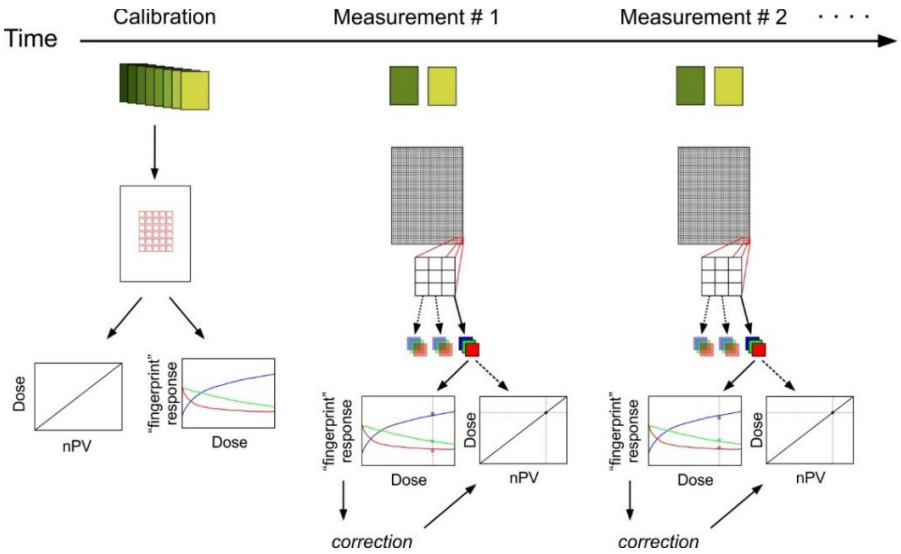

Figure 4.1: Introducing the concept of "fingerprint" correction. At the time of calibration, nPV_{RGB} and the calibration "fingerprint" ($c_{X=R,G,B}^{cal}$) are acquired. At the time of measurement, nPV_{RGB} and $c_{X=R,G,B}^{meas}$ are acquired for each pixel in the image, compared to $c_{X=R,G,B}^{cal}$ (as described in the text), and a correction ($c_{X=R,G,B}$) is generated and re-applied to nPV_{RGB}.

Short term scanner response variability

This issue refers to scan-to-scan variability with respect to the first scan. The 12000XL EPSON scanner was used for evaluation since it is the only scanner out of the three models that we could not find any literature about. A similar approach to Lewis and Devic[31] was followed to evaluate scanner variability: two sets of measurands were scanned at the same time: (a) neutral density (ND) filters (four OD levels: 2, 4, 8, 16), and (b) EBT3 film pieces (0, 0.5, 1, 3, 11 Gy). These sets were scanned 100 consecutive times at 2 minutes intervals between scans and the scanner cover was opened/closed at scans 71-100 while it remained unopened for scans 1-70. In order to test the nPV_{RGB} protocol, four relative quantities were compared in this test (relative to the value of same quantity at scan#1): (1) *PV* of ND filters, (2) *PV* of EBT3 film pieces, (3) Dose converted from nPV_{RGB} of EBT3 film pieces, and (4) Dose converted from $netOD_{X=R,G,B}$ of EBT3 film pieces. For quantities (3) and (4), the difference in results was shown when the control of first scan is used for evaluation (referred to as a global control) versus using a control within the same scan (referred to as scan-specific control).

Scanner bed inhomogeneity

This problem refers to the relative signal at different regions on the scanner bed with respect to the scanner center. The scanning bed of the 12000XL (A3 size) was divided into 25 evaluation regions. Two small film pieces (1" by 2") were scanned each time next to each other within those regions. One was a control (unexposed) film piece while the other was a film exposed to a dose of 8 Gy. In order to test the nPV_{RGB} protocol, three relative quantities were compared in this test (relative to the scanner center): (1) RGB *PV* of EBT3 film pieces, (2) Dose converted from nPV_{RGB} of EBT3 film pieces, and (3) Dose converted from $netOD_{X=R,G,B}$ of EBT3 film pieces. For quantities (2) and (3), the difference in results was shown when the control of the central region is used with measurement film pieces of all other regions (referred to as global control) versus using the control scanned at each region (referred to as region-specific controls).

Long term verification and stability

This issue refers to the accuracy and precision of the dosimetry system sometime after calibration. Here, the results of using nPV_{RGB} with the correction protocol will be shown and compared to regular single channel RGB net optical densities at three points in time: at calibration, after 3

months and after 6 months. Films (lot 6 and 12000XL) were irradiated under the same conditions as described in section (4.2.B) and the doses to films were adjusted according to the daily output measurement for the day experiment was performed and the response of the monitor chamber. At calibration, more dose levels were used to generate the calibration curve while for the verification irradiations (after 3 and 6 months, respectively) the nominal dose levels delivered to the film sets were: 1, 2, 3.5, 5, 7.5, 10, 20 Gy. Since the RCF dosimetry systems should be evaluated as a whole, the average error calculated from dose error at each dose level will be reported even though some influence from lower doses (1 Gy or less) is expected to impact this statistical evaluation.

4.3 Results

4.3.A Multichannel normalized pixel value

Figure 4.2(a) shows the concept of dose-response linearization when using the multichannel normalized pixel value response and highlights the "unity" response with dose (nPV_{RGB} = dose). Figure 4.2(b) shows the sensitivity of nPV_{RGB} and $nPV_{X=R,G,B}$ curves at different dose levels. For this specific batch of film together with the 10000XL scanner, a drop of sensitivity can be seen in the red channel while blue channel sensitivity remains relatively unchanged although some variability can be seen between 1 Gy and 10 Gy. The green channel showed an increase in sensitivity (when viewed in normalized pixel value form) after 6-8 Gy which was advantageous for the linearization process.

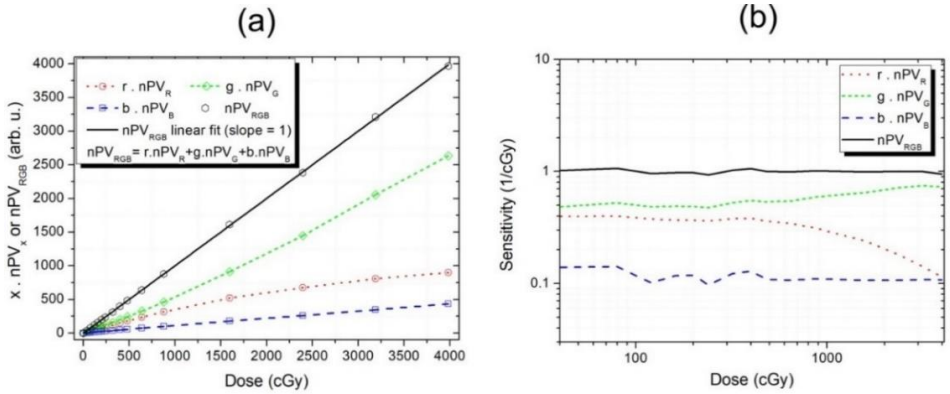

Figure 4.2: Concept of dose-response linearization based on multichannel normalized pixel value response (nPV_{RGB}). (a) nPV_{RGB} response and its constituent terms $r \cdot nPV_R$, $g \cdot nPV_G$ and $b \cdot nPV_B$ representing individual responses in red, green and blue color channels. (b) sensitivity curves of nPV_{RGB} and its constituents.

Figure 4.3(a) shows the modeled 1-σ and 2-σ dose uncertainties at different dose levels of the same calibration presented in Figure 4.2(a) calculated using equation 4.8. The average error of the mean values of thirty ROIs per dose level seems to be within the modeled one sigma uncertainty level down to 1 Gy. Figure 4.3(b) shows the same data in 4.3(a) but with a maximum dose of 10 Gy (the change is in the view settings only *i.e.* the fitting process was still done with a dose range of 0 – 40 Gy). In comparison to Figure 4.3(b), Figure 4.3(c) shows a re-fit considering only the dose range 0 – 10 Gy and it shows the gain in accuracy at lower dose values. It also shows that irrespective of this gain in accuracy, the uncertainty level remains the same. Depending on the dose range, the accuracy was also found to be impacted at the higher dose end of the calibration curve. Figure 4.3(d) shows what happens to linearity if the maximum calibration dose was exceeded. This result indicates that linearity should not be assumed for doses outside the maximum calibration dose and this is expected given the drop of RGB dose sensitivities observed in Figure 4.2(b).

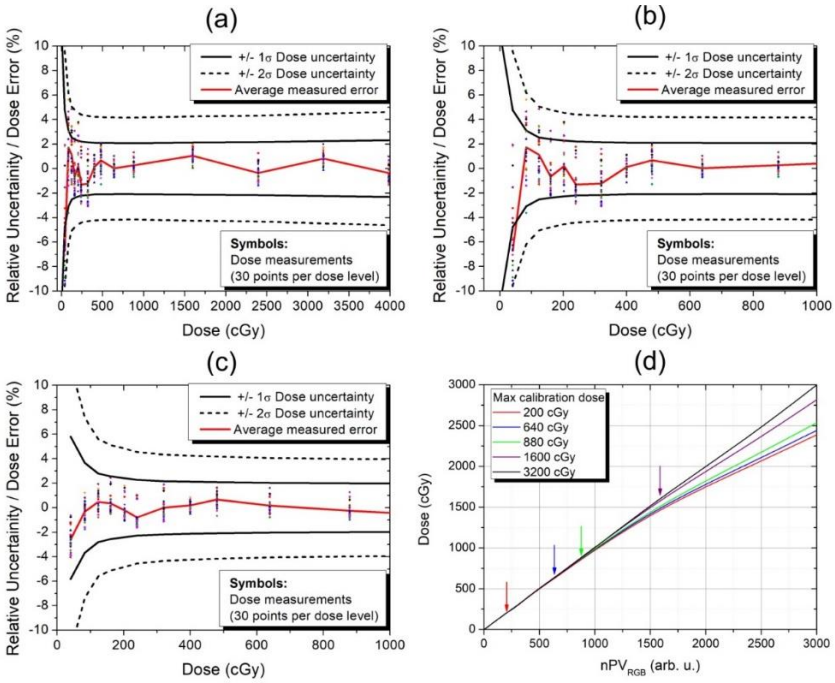

Figure 4.3: The impact of dose range on dose uncertainty and error analysis of one of the EBT3 GAFCHROMIC™ film dosimetry systems used in this work (lot#1, 10000 XL). (a) Uncertainty/error analysis for the dose range 0 – 40 Gy, (b) 0 – 10 Gy focused view of the same figure in (a), (c) Uncertainty/error analysis for the dose range 0 – 10 Gy when the system was re-fit to maximum dose of 10 Gy (instead of 40 Gy), and (d) the impact of dose range (maximum calibration dose, indicated by the arrows) on linearity of the dose-response.

Figure 4.4(a) shows the result of using nPV_{RGB} as a response function for six different lot numbers of EBT3 films calibrated at three different centers and scanned with different EPSON scanner models. Figure 4.4(b) shows the mean error of thirty ROIs per dose level for each of the six RCF dosimetry systems. Results show that the accuracy level of ±2% is achievable with this response function for doses higher than 1 Gy.

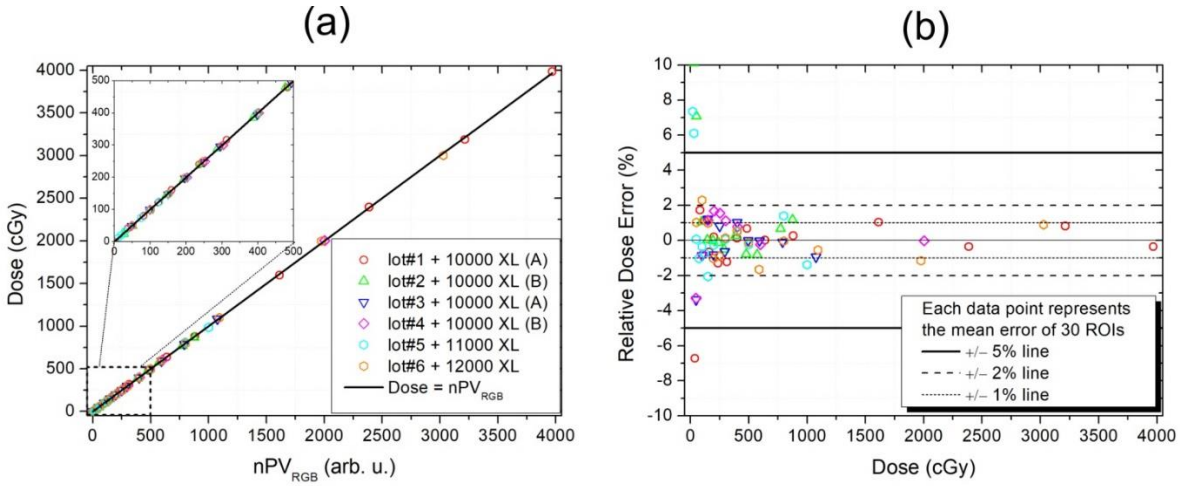

Figure 4.4: Applying the concept of nPV_{RGB} to six different EBT3 GAFCHROMIC™ film dosimetry systems used in this work. (a) Linearization of the dose-response and comparison to the unity curve, and (b) Achievable accuracy represented as the percentage relative dose error at different dose levels.

4.3.B Testing the multichannel normalized pixel value and correction protocol

4.3.B.1 Fingerprint correction protocol

Figure 4.5 shows the "fingerprint" at the time of calibration ($c_{X=R,G,B}^{cal}$). Each system had a unique pattern for the relative contribution of each color channel to a specific dose (hence justifying the naming; "fingerprint") and it is postulated that this relation must be maintained for correct interpretation of the calibration equation at the time of measurement for a given combination of the film batch and scanner.

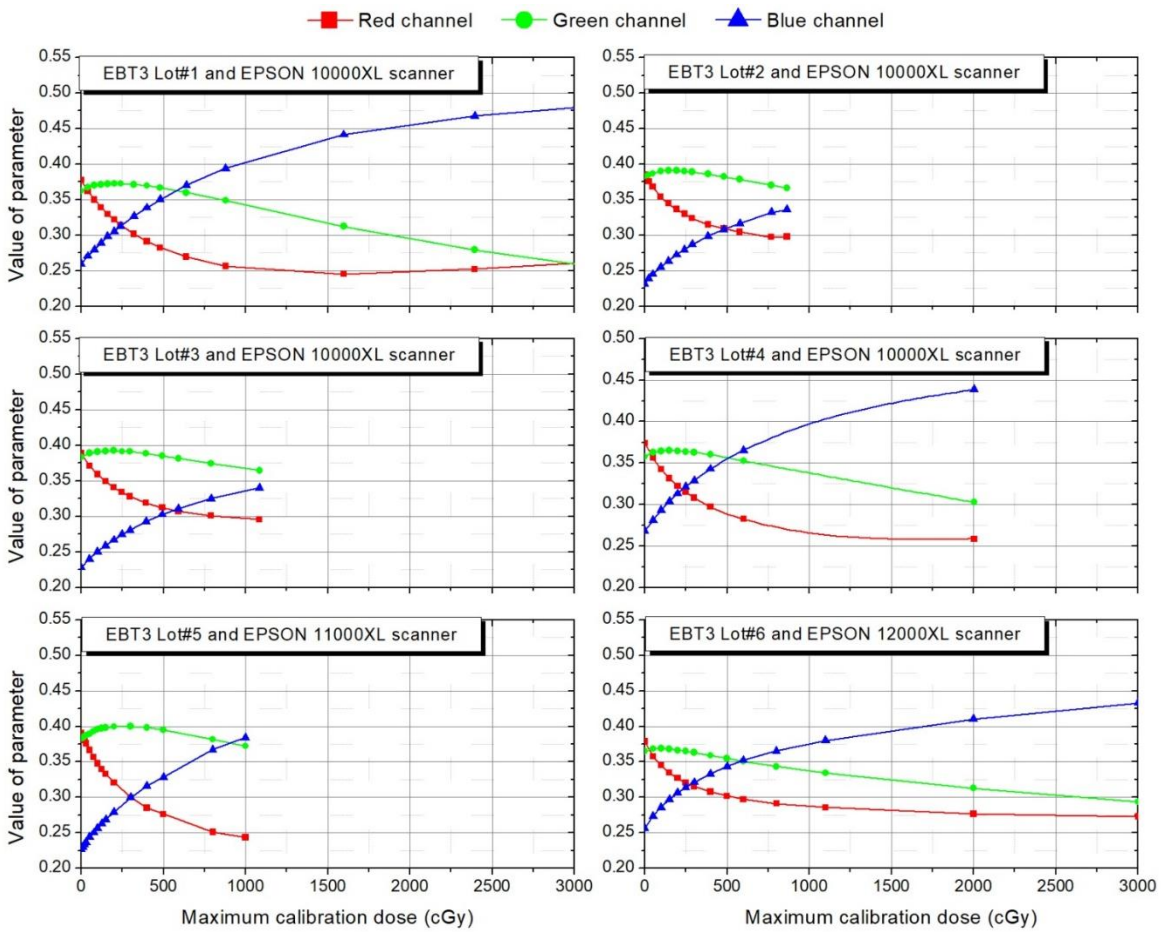

Figure 4.5: Visualization of the "fingerprint" at the time of calibration ($c^{cal}_{X=R,G,B}$) for the six EBT3 GAF-CHROMIC™ film dosimetry systems used in this work.

4.3.B.2 Short term scanner response variability

Figures 4.6 and 4.7 show the scan-to-scan response variability of the 12000XL scanner. Pixel values of both ND filters and EBT3 film show sudden systematic changes in response. The difference in variability levels between ND filters and EBT3 film can be attributed to their color, purity and absorption properties. It is also noticeable that the response of ND filters does not have any increasing or decreasing spread like the EBT3 response. This can be an indication of effects from the scanning medium on the film signal. Figure 4.7 shows the relative dose readouts when using nPV_{RGB} or $netOD$ as a response function. It can be seen that the use of a global control film *i.e.* at a different scan (always scan#1 in this case) can be detrimental in both responses since some significant unpredictable changes were observed. The use of a scan-specific control seems to effectively avoid these large changes in response in both signals. However, the shifts in

response affected the dose converted from $netOD$ of the red channel more than the other two channels. The use of the three channels in nPV_{RGB} response seems to approximately average these changes in the scanner response and the use of the "fingerprint" correction reduced the scanner variation consistently at all examined dose levels. Another observation was the systematic change in response in scan#70 (when the scanner cover was opened and closed until scan#100) but it is difficult to conclude that opening and closing the scanner cover caused larger variations in scanner response in comparison to the first 70 scans.

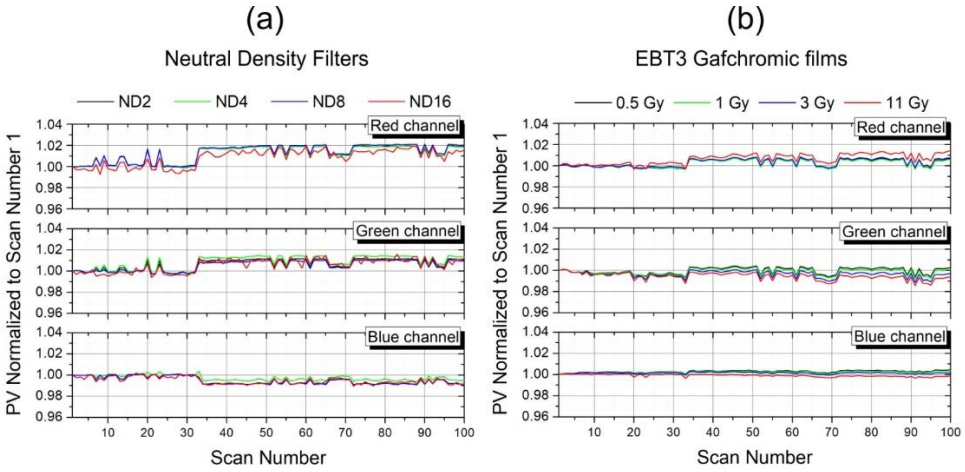

Figure 4.6: EPSON 12000XL scanner response variability in terms of pixel values relative to the 1st scan. (a) for neutral density filters, and (b) for EBT3 GAFCHROMIC™ film.

4.3.B.3 Scanner bed inhomogeneity

Figure 4.8 shows the EPSON 12000XL scanner bed signal inhomogeneity with respect to the scanner center using different response signals. The RGB relative response maps in *PV* of control and 8 Gy exposed film pieces (first and second rows of Figure 4.8, respectively) showed a higher degree of inhomogeneity when using the red channel (in the order of 10% at the top and bottom parts of the scanner). The green channel showed better homogeneity than the red channel where the maximum inhomogeneity was in the order of 4% at the top of the scanner where the cover hinges are located. The blue channel showed a reproducible response in both film pieces, however, this might be attributed to its known signal insensitivity. A similar trend was seen in all color channels when the dose is acquired through $netOD_{X=R,G,B}$ (specific controls, row number 4 in Figure 4.8) albeit the value of changes are different since the relation between the dose and raw *PV* is not linear. Using a global control produced worse homogeneity maps at all color

channels (row number 3 of Figure 4.8). A similar behavior was seen when using nPV_{RGB} with global and specific controls. The corrected nPV_{RGB} produced a scanner inhomogeneity map with a maximum of 2.97% change at only a specific region of the scanner bed (top left, near the calibration area) while the average homogeneity of the signal elsewhere was 100.86% ± 0.72% which is within the dosimetric uncertainty expected from film dosimetry (See Figure 4.3).

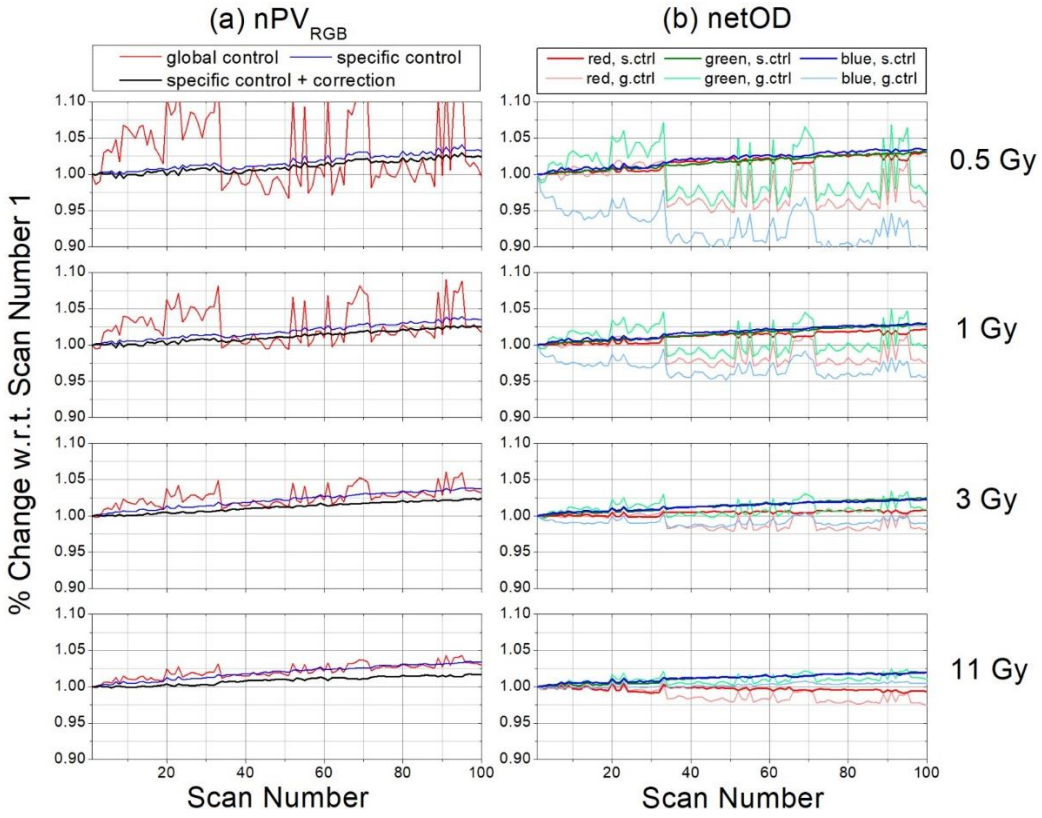

Figure 4.7: EPSON 12000XL scanner response variability in terms of dose relative to the 1st scan. (a) using nPV_{RGB} with and without correction, and (b) using $netOD_{X=R,G,B}$. Global control refer to the use of control film from scan#1 image in all subsequent measurement film images while specific control means using the control film from the same scanned image as the measurement film. (s.ctrl: specific control, g.ctrl: global control).

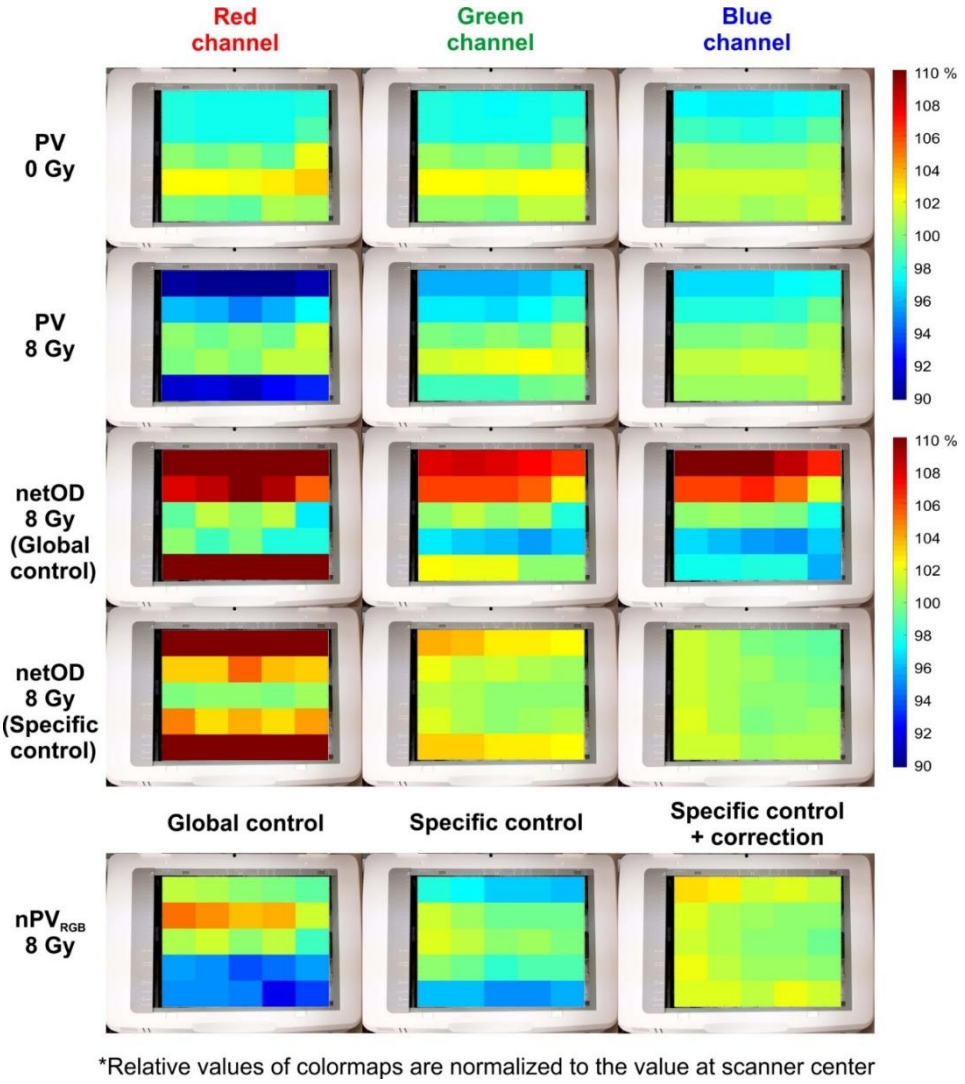

Figure 4.8: EPSON 12000XL scanner bed inhomogeneity with respect to the scanner center. First and second rows show the RGB relative responses in pixel values (PV) for a control and an exposed film piece (8 Gy). Third and fourth rows show the RGB dose conversion based on $netOD_{X=R,G,B}$, when using a global or specific controls. Fifth row shows the use of nPV_{RGB} with global control, specific control (no correction) and specific control (with correction).

4.3.B.4 Long term verification and stability

Figure 4.9 shows a chronological box plot demonstrating the performance of different RCF dosimetry systems considered in this work, and those are nPV_{RGB} and $netOD_{X=R,G,B}$. Here, performance is defined as the accuracy and precision of the dosimetry system sometime after the calibration time. For all signals, figures 4.9(a) and 4.9(b) show generally higher accuracy and better

reproducibility when the fitting covered smaller dose range (0 – 10 Gy vs 0 – 40 Gy). The nPV_{RGB} combined with the correction seemed to provide a reproducible response throughout the 6 months period. The $netOD_G$ dose response also provided good performance if used to measure doses larger than 1 Gy. The blue channel had the least favorable performance and its sole use appears to lead to severe inaccuracies. The red channel showed slight systematic changes in response after 3 and 6 months (Figures 4.9(c) and 4.9(d)).

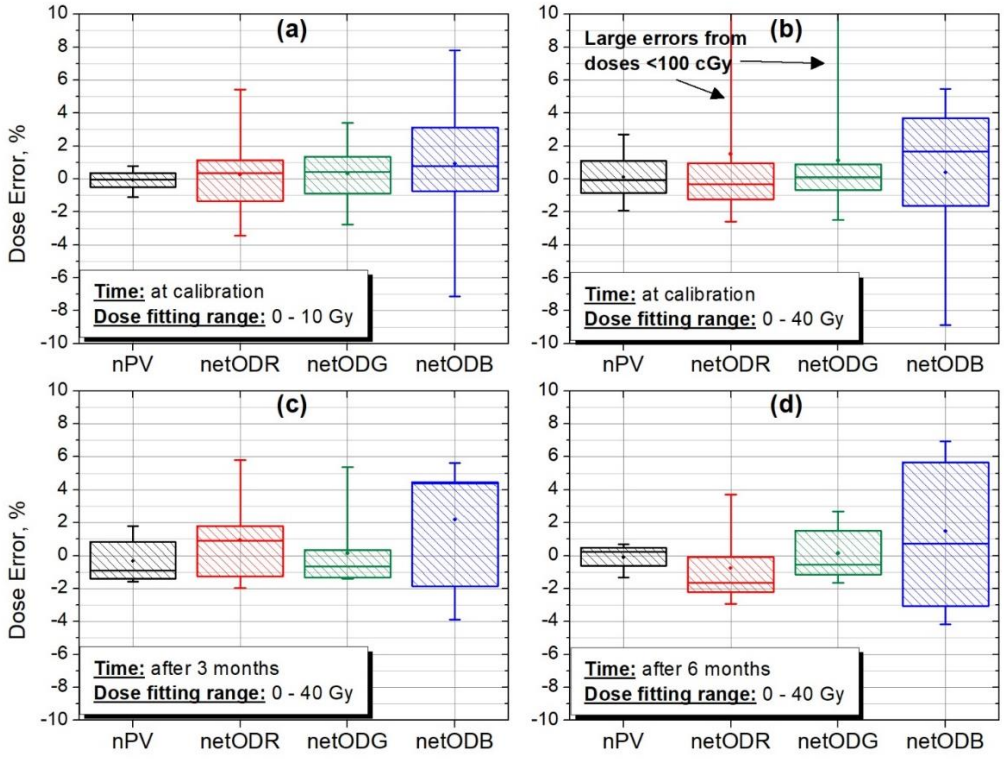

Figure 4.9: Box plot demonstration of the accuracy and precision of RCF dosimetry at different time points and using different response signals. (a) at the time of calibration, using 0 – 10 Gy fit, (b) at the time of calibration, using 0 – 40 Gy fit, (c) three months after calibration, using 0 – 40 Gy fit, and (d) six months after calibration, using 0 – 40 Gy fit.

4.3.B.5 Limitation of the linearization process

Figure 4.10 summarizes the limitation of the fitting process that leads into linearization of the film multichannel response. As can be seen, the values of the fitting parameters change with dose level, demonstrating dose range dependence even though five out of these six systems showed

consistent values of fitting parameters. These changes suggest that it is not feasible yet to find "global" fitting parameters which necessitate the process of calibration.

4.4 Discussion

4.4.A Advantages and limitations of linearization

In this work a radiochromic film dosimetry protocol based on multichannel normalized pixel value (nPV_{RGB},) was described. The main advantages of this system are: (a) it provides a linearized response based on all color channel information available in each pixel of the image and (b) it allows per-color correction that takes into account the difference in scanning states between the times of calibration and measurement. The nPV_{RGB} response function is also determined from pixel value information extracted from transmission-scanned image(s) of two film pieces: measurement film and control film and it does not require pre-scan of the same measurement film piece. Also all corrections described in this work ("fingerprint", filtration, streaks) are generated and applied based on the same measurement images.

Furthermore, the calibration process is considered to be simple since equation 4.4 can be directly solved using multiple regression analysis. The intercept values of these equations (one per color channel) were set to zero because the dose should be equal to zero when the value of response is equal to zero. However, the values of *r*, *g*, *b* fitting parameters are not always positive (as in the case of Figure 4.2) and this is attributed to signal saturation at higher doses. Therefore, it is expected to see negative slopes for different batch numbers. Also, as demonstrated in Figure 4.3(d), the dose range has an impact on the accuracy and precision of this protocol, and this in turn, affects the values of the fitting parameters too. Figure 4.10 shows these two aspects of the fitting process (negative slopes and dose range effect), for the six RCF dosimetry systems considered in this work.

While some systems showed similar trend in the fitting parameters when using the 10000XL scanner, Figure 4.10 in fact shows that it is difficult to have "global" parameters to enable linearization without the need of calibration. This can be considered as a drawback for this method; however, as was shown in previous works,[13,32] linearization without calibration is possible with the use of different functional forms (equation 4.1). However, there is no guarantee that these observations would hold true for all combinations of RCF dosimetry systems. Interestingly,

and when used for doses less than 10 Gy, nPV_G was able to linearize the response of five out of the six RCF dosimetry systems considered in this study with residuals less than 3% where the system that had high value of residuals (up to 10%) was the EBT3 model (purchased on October 2018) and scanned using the 12000XL LED scanner. Therefore, utilizing all color channels would be a more robust approach to compensate any differences in response caused by film composition or scanner model.

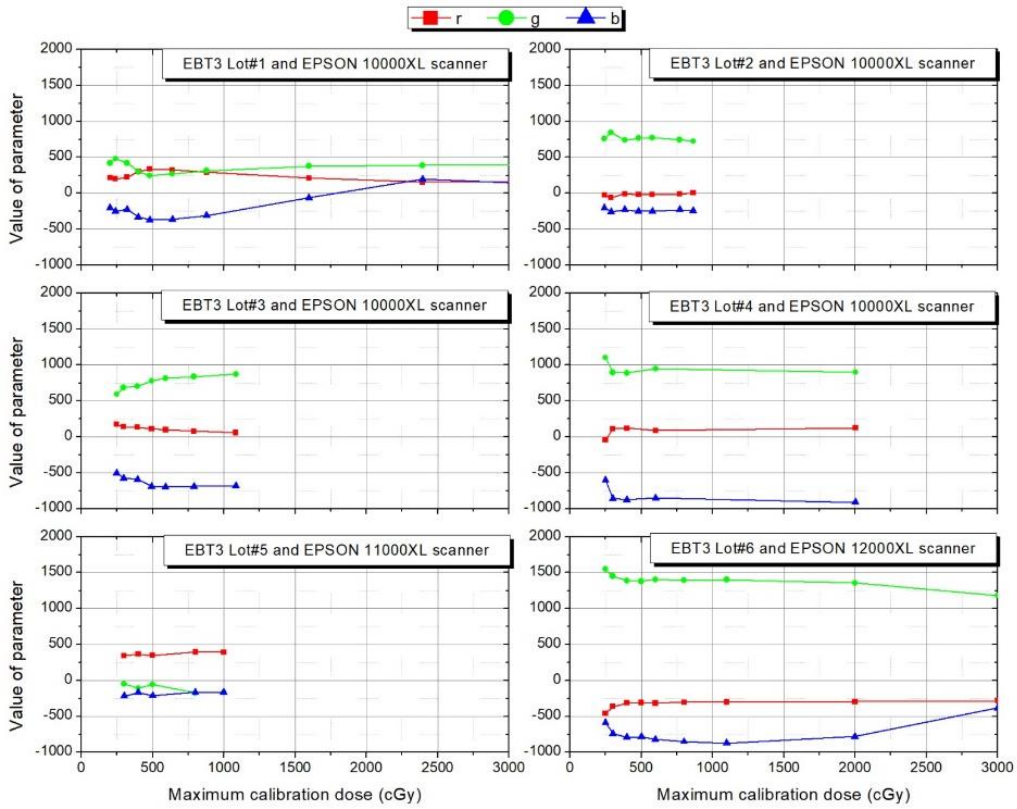

Figure 4.10: Changes in the values of *r*, *g*, *b* fitting parameters (equation 4) among the six GAFCHROMIC™ film dosimetry systems used in this work. The figure shows that each system has its own unique pattern of these parameters and that the values of parameters depend on the maximum calibration dose.

Another important aspect was the determination of weights for the fitting process. It was found that the application of set of equations 4.5(a-c) demonstrated similar accuracy level for the whole dose range under consideration while sole use of statistical fitting (equation 4.5b) can result in increased accuracy for most of the dose points, however, it can also result in lower accuracies (>4%) for some dose points.

4.4.B The fingerprint correction protocol

Although nPV_{RGB} provided a robust and reproducible system for linearizing the RCF dosimetry system response, the nature of this response function that is the summation of the signals also brings unwanted features. One example is the signal sensitivity that limited the dose range (as mentioned earlier), and another example is the inaccuracies associated with the blue channel (Figure 4.9 and Ref 33). Assigning the slopes to the nPV response per color does not take into account the dosimetric accuracy and precision expected from that color response. Therefore, the blue channel will compile its inaccuracies into nPV_{RGB} as a form of increased noise and that is another reason why the correction protocol is necessary. The "fingerprint" correction protocol not only corrects for differences between the calibration and measurement states, but it also mitigates this added "blue noise". This is an advantage in terms of spatial and temporal consistency but also a limitation since the method does not guarantee less noise but rather similar noise level to single channel dosimetry. However, in addition to the "fingerprint" correction, the methodology described in section 4.2.C, that is, the use of a de-noising filter as recommended by Vera-Sanchez *et al*[26] and Devic *et al*[2] for resolutions higher than 150 dpi, together with the removal of horizontal streaks, significantly decreased the noise levels achievable with nPV_{RGB}. At 3 Gy, the reductions in noise levels after application of the three corrections (fingerprint, streaks, filtration), for nPV_{RGB} and ($netOD$) were from 4.4% (3.2%) to 1.59% (2.01%). At 5 Gy, the reductions were 3.57% (2.3%) to 1.19% (1.12%). It was noted that the approximate relative contribution of each of these corrections to noise reduction was 10%, 3% and 87%, respectively. The model uncertainty given by equations 4.7 and 4.8 (and demonstrated in Figure 4.3) was established during the calibration process at the time when the "fingerprint" correction was set to unity. Figure 4.3 clearly demonstrates that calculated dose uncertainties are always larger than the actual dose errors (available only during calibration process) justifying the proposed reference radiochromic film dosimetry system. When performing dose measurements at a later date with the "fingerprint" correction, dose error will become smaller, while the uncertainty, given by equation 4.7, will remain the same. Addition of the "fingerprint" correction factor uncertainties to equation 4.7, albeit insignificant (0.3-0.7% for all channels), would only make the overall dose uncertainty of the method unnecessarily larger, and could be ignored.

4.4.C Short term scanner response variability

In this study, only results from the 12000XL scanner were reported since other studies already addressed xenon fluorescent lamp-based scanners.[9, 10, 21, 26, 30, 31] The changes seen in Figure 4.7 between the 1st and 20th scan were less than 1% at all dose levels when using single channel dosimetry and almost negligible when using nPV_{RGB}. In comparison to the 10000XL scanner, the single channel dosimetry results in this study seem to agree with results from Vera Sánchez *et al*[26] where they examined the use of multichannel algorithms[17, 20] in characterizing the response variability for 20 scans, in terms of relative dose as well as PV which was shown to be less than 1%. Lewis and Devic[31] and Ferreira *et al*[10] showed that 10000XL scanner warmup up can take up to 20 scans but the variations are minimal afterwards (less than 1% in PV). When converted to dose, they showed that the Mayer *et al*[17] method lead to variabilities in the order of 6 – 10%, while the Lewis *et al*[20] method lead to significantly less variabilities (in the order of 1 – 3%). This amount of variation was not seen when using any of the response functions included in this study for the 12000XL scanner. For this reason the recalibration protocols have surfaced in the literature.[20, 21] Ruiz-Morales *et al*[21] reported the variability of 20 scans from the 10000XL scanner and showed that recalibration methods accounted for it (less than 0.2% variation after the 20th scan) while control film piece protocol could not (at all color channels), where the maximum deviation was 1% in the green channel. The results in Figure 7 indicates that this depends on whether the control was included in the same scan (specific control) or not (global control), and on their relative position within the scanner as well (Figure 8).

The most important observation from Figure 7 is the use of a global or specific control film piece. Results showed that the use of a specific control mitigated the high variation seen with the global control. This observation agreed with conclusions from Lewis and Devic[31] and Mendez *et al*[30] where they recommended the inclusion of a reference material during any scan. Furthermore, nPV_{RGB} with the "fingerprint" correction protocol was shown to reduce the scanner variation consistently at all examined dose levels, which could be an indication for the potential effect of continuous scanning medium on the film signal. Lárraga-Gutiérrez *et al*[9] compared the use of an LED scanner (EPSON V800) to that of a xenon fluorescent lamp (EPSON 11000 XL). They reported no significant changes for both scanners after the 5th scan when used to scan EBT3 films model, which is not in full disagreement with results of this study since most

"appreciable" changes started to appear approximately after scan#40 in this study to a level of 2.0-2.5% after 100 scans (after correction).

4.4.D Scanner bed inhomogeneity and recommended film positioning

The relative inhomogeneity maps in Figure 8 visually summarize the bed homogeneity seen with EBT3 film and 12000XL RCF system. The dose dependence (control vs 8 Gy film) was confirmed as well as the dependence on positioning of the control film. The use of a global control at the center of the scanner lead to larger deviations at the top and bottom of the scanner but it worked well with the central long region of the scanner.[2] The use of a specific control improved the response elsewhere. Therefore, it is always strongly recommended to use a control film piece within the same scan and around the same position as the measurement film piece. When more than one film piece is needed to be scanned, the control should be at the center while the other pieces should be positioned to the left and right of the control piece. This is important since the control is by definition included mathematically into all responses. For the case of whole sheet scanning, the control could only be scanned in another scan and the scanner variability will limit the uncertainty achievable this way. It is also important to note that out of all the maps presented in Figure 8, only three maps showed good homogeneity level (within 2%) for a whole sheet scanning: nPV_{RGB}, $netOD_G$ and $netOD_B$, although, the use of $netOD_B$ is discouraged because of its inaccuracy. The red channel especially showed strong spatial dependency which agrees with the work of Lárraga-Gutiérrez *et al*[9] with an LED-based scanner (although to a less extent, 8%). It is important to mention that most of the available literature on lateral scan correction[9, 10, 34–37] are based on xenon fluorescent lamps so comparison to them would not be meaningful especially that the dose levels are different. However, quantitatively, results of this study support the conclusion that the lateral scan correction seems to be more severe for LED based scanners in the red channel only, since it was shown that for the green and blue channels, it is correctable with the use of specific control.

4.4.E Long term verification and stability

The stability of the RCF dosimetry system over longer periods of time is definitely a desirable feature. However, the inaccuracies seen in scanner variability prompted the use of recalibration protocols[20, 21] to seek more reliable dosimetry systems. In this study, nPV_{RGB} was shown to

provide the same dosimetric performance seen during calibration, at later time points (Figure 9). This is an important observation because unlike recalibration procedures, this protocol does not require any additional irradiations and it uses the information contained within the same measurement images to spatially relate the position of each pixel to the center of the scanner and deduce final dose values under the same conditions during calibration (Figure 1). In comparison, Ruiz-Morales *et al*[21] investigated three different methods for film recalibration: Lewis *et al*[20], parameter escalation, axis escalation, and compared them to the use of control film piece[25, 38] and the case of no correction. Their results showed comparable levels of accuracy when using red/green single channel dosimetry techniques (control film, axis escalation, and parameter escalation). Palmer *et al*[39] showed that fail rates of plans with high doses actually increased when the quality assurance is done with triple channel dosimetry using EBT3 film model. They also show that single channel dosimetry lead to better results at high doses. This might be explained by the increased uncertainty level above 4 Gy when the triple channel dosimetry method was used.[33]

4.5 Conclusion

While the use of multichannel information, dose linearization, normalized pixel value, control film, and scanner response correction are all features that were individually investigated by different research groups, a formalism that combines them into a single protocol is lacking. In this study, a new formalism based on all of these features was introduced. It provided a linearized dose response for six tested EBT3 film dosimetry systems, and it was shown to be self-corrected for scanner variation issues in a sustainable way. A pixel-by-pixel “fingerprint” correction, based on the relative contribution of each color channel at different dose levels, was proposed and it provided a link between the film-scanner states at the time of calibration and measurements, respectively, based on measured pixel values only. It was shown that this protocol can correct for spatial and temporal changes of the scanner/film states, providing long term stability without jeopardizing dosimetric accuracy. These features will add sustainability to film dosimetry which is going through renaissance as a quality assurance tool for contemporary radiotherapy applications.

4.6 Acknowledgment

The authors have no conflicts to disclose. This work was supported in part by the Natural Sciences and Engineering Research Council of Canada contract No. 386009. S.A. is a Ph.D. Candidate supported by the scholarship program at King Faisal Specialist Hospital & Research Centre (KFSH&RC). S.A. acknowledges partial support by the CREATE Medical Physics Research Training Network grant of the Natural Sciences and Engineering Research Council (Grant number: 432290).

4.7 References

1. W.L. McLaughlin, C. Yun-Dong, C.G. Soares, A. Miller, G. Van Dyk, and D.F. Lewis, Sensitometry of the response of a new radiochromic film dosimeter to gamma radiation and electron beams, Nucl. Inst. Methods Phys. Res. A **302**(1), 165–176 (1991).
2. S. Devic, N. Tomic, and D. Lewis, Reference radiochromic film dosimetry: Review of technical aspects, Phys. Medica **32**(4), 541–556 (2016).
3. A. Niroomand-Rad, C.R. Blackwell, B.M. Coursey, *et al.*, Radiochromic film dosimetry: Report No. 63, Radiat. Meas. **25**(63), (2006).
4. S. Devic, Radiochromic film dosimetry: Past, present, and future, Phys. Medica **27**(3), 122–134 (2011).
5. S. Devic, J. Seuntjens, G. Hegyi, *et al.*, Dosimetric properties of improved GafChromic films for seven different digitizers, Med. Phys. **31**(9), 2392–2401 (2004).
6. A.S. Aydarous, P.J. Darley, A. De Puysseleyr, and R.P. Srivastava, Physics in Medicine & Biology The use of a reflective scanner to study radiochromic film response, (2002).
7. J. Kalef-Ezra and K. Karava, Radiochromic film dosimetry: Reflection vs transmission scanning, Med. Phys. **35**(6), 2308–2311 (2008).
8. P. Papaconstadopoulos, G. Hegyi, J. Seuntjens, and S. Devic, A protocol for EBT3 radiochromic film dosimetry using reflection scanning, Med. Phys. **41**(12), (2014).
9. J.M. Lárraga-Gutiérrez, O.A. García-Garduño, C. Treviño-Palacios, and J.A. Herrera-González, Evaluation of a LED-based flatbed document scanner for radiochromic film dosimetry in transmission mode, Phys. Medica **47**(March), 86–91 (2018).
10. B.C. Ferreira, M.C. Lopes, and M. Capela, Evaluation of an Epson flatbed scanner to read Gafchromic EBT films for radiation dosimetry, Phys. Med. Biol. **54**(4), 1073–1085 (2009).

11. W.L. Mclaughlin and M.F. Desrosiers, Dosimetry systems for radiation processing, Radiat. Phys. Chem. **46**(4-6 PART 2), 1163–1174 (1995).

12. I. Méndez, Model selection for radiochromic film dosimetry, Phys. Med. Biol. **60**(10), 4089–4104 (2015).
13. S. Aldelaijan and S. Devic, Comparison of dose response functions for EBT3 model GafChromic^{TM} film dosimetry system, Phys. Medica **49**, (2018).
14. F. Del Moral, J.A. Vázquez, J.J. Ferrero, *et al.*, From the limits of the classical model of sensitometric curves to a realistic model based on the percolation theory for GafChromic EBT films, Med. Phys. **36**(9), 4015–4026 (2009).
15. C. Rodríguez and L.C. Martínez, Radiochromic EBT2 and EBT3 sensitometry based on growth of two color phases of the polymer, Med. Phys. **46**(4), 1896–1904 (2019).
16. A. Micke, D. Lewis, and X. Yu, Multichannel film dosimetry with nonuniformity correction, Med. Phys. **38**(5), 2523–2534 (2011).
17. R.R. Mayer, Y. Chen, R.I. Miller, *et al.*, Enhanced dosimetry procedures and assessment for EBT2 radiochromic film., Med. Phys. **39**(4), 2147–55 (2012).
18. I. Méndez, P. Peterlin, R. Hudej, A. Strojnik, and B. Casar, On multichannel film dosimetry with channel-independent perturbations, Med. Phys. **41**(1), (2014).
19. J.F. Pérez Azorín, L.I. Ramos García, and J.M. Martí-Climent, A method for multichannel dosimetry with EBT3 radiochromic films, Med. Phys. **41**(6), (2014).
20. D. Lewis, A. Micke, X. Yu, and M.F. Chan, An efficient protocol for radiochromic film dosimetry combining calibration and measurement in a single scan, Med. Phys. **39**(10), 6339–6350 (2012).
21. C. Ruiz-Morales, J.A. Vera-Sánchez, and A. González-López, On the re-calibration process in radiochromic film dosimetry, Phys. Medica **42**(2017), 67–75 (2017).
22. P.R. Almond, P.J. Biggs, B.M. Coursey, *et al.*, AAPM's TG-51 protocol for clinical reference dosimetry of high-energy photon and electron beams, Med. Phys. **26**(9), 1847–1870 (1999).
23. M. McEwen, L. DeWerd, G. Ibbott, *et al.*, Addendum to the AAPM's TG-51 protocol for clinical reference dosimetry of high-energy photon beams., Med. Phys. **41**(4), 041501 (2014).

24. IAEA International Atomic Energy Agency, TRS 398: Absorbed Dose Determination in External Beam Radiotherapy, At. Energy Agency 1–229 (2000).
25. S. Devic, J. Seuntjens, E. Sham, *et al.*, Precise radiochromic film dosimetry using a flat-bed document scanner, Med. Phys. **32**(7), 2245–2253 (2005).
26. J.A. Vera Sánchez, C. Ruiz Morales, and A. González López, Characterization of noise and digitizer response variability in radiochromic film dosimetry. Impact on treatment verification, Phys. Medica **32**(9), 1167–1174 (2016).
27. E.Y. León Marroquin, J.A. Herrera González, M.A. Camacho López, J.E. Villarreal Barajas, and O.A. García-Garduño, Evaluation of the uncertainty in an EBT3 film dosimetry system utilizing net optical density, J. Appl. Clin. Med. Phys. **17**(5), 466–481 (2016).
28. S. Devic, N. Tomic, C.G. Soares, and E.B. Podgorsak, Optimizing the dynamic range extension of a radiochromic film dosimetry system, Med. Phys. (2009).
29. D.K.R. Philip R. Bevington, *Data Reduction and Error Analysis for the Physicsal Sciences, 3rd ed*, 1–320 (2003).
30. I. Méndez, Šljivić, R. Hudej, A. Jenko, and B. Casar, Grid patterns, spatial inter-scan variations and scanning reading repeatability in radiochromic film dosimetry, Phys. Medica **32**(9), 1072–1081 (2016).
31. D. Lewis and S. Devic, Correcting scan-to-scan response variability for a radiochromic film-based reference dosimetry system, Med. Phys. **42**(10), 5692–5701 (2015).
32. S. Devic, N. Tomic, S. Aldelaijan, *et al.*, Linearization of dose-response curve of the radiochromic film dosimetry system, Med. Phys. **39**(8), (2012).
33. J.A. Vera-Sánchez, C. Ruiz-Morales, and A. González-López, Monte Carlo uncertainty analysis of dose estimates in radiochromic film dosimetry with single-channel and multichannel algorithms, Phys. Medica **47**(September 2017), 23–33 (2018).
34. L. Paelinck, W. De Neve, and C. De Wagter, Precautions and strategies in using a commercial flatbed scanner for radiochromic film dosimetry, Phys. Med. Biol. **52**(1), 231–242 (2007).
35. A.A. Schoenfeld, S. Wieker, D. Harder, and B. Poppe, The origin of the flatbed scanner artifacts in radiochromic film dosimetry - Key experiments and theoretical descriptions, Phys. Med. Biol. **61**(21), 7704–7724 (2016).

36. D. Lewis and M.F. Chan, Correcting lateral response artifacts from flatbed scanners for radiochromic film dosimetry, Med. Phys. **42**(1), 416–429 (2015).
37. S. Devic, Y.Z. Wang, N. Tomic, and E.B. Podgorsak, Sensitivity of linear CCD array based film scanners used for film dosimetry, Med. Phys. **33**(11), 3993–3996 (2006).
38. S. Aldelaijan, F. Alzorkany, B. Moftah, *et al.*, Use of a control film piece in radiochromic film dosimetry, Phys. Medica **32**(1), (2016).
39. A.L. Palmer, A. Dimitriadis, A. Nisbet, and C.H. Clark, Evaluation of Gafchromic EBT-XD film, with comparison to EBT3 film, and application in high dose radiotherapy verification, Phys. Med. Biol. **60**(22), 8741–8752 (2015).

CHAPTER 5: Dose comparison between TG-43 based calculations and radiochromic film measurements of the Freiburg flap applicator used for high-dose-rate brachytherapy treatments of skin lesions

---

Preface

This paper introduced the use of radiochromic film dosimetry in quality assurance of surface brachytherapy treatment accuracy. The current standard of care in dose calculation of skin treatment with HDR brachytherapy is based on the AAPM TG-43 datasets which assume full backscatter conditions. For skin treatments with the Freiburg flap (FF) applicator, this represents a setup different than the actual clinical situation where contributions of backscatter originating above the applicator and air gaps between the applicator spheres are missing. The aims of this work are twofold: to experimentally evaluate the treatment planning dose calculation accuracy during surface treatments with the FF applicator at different depths, and to evaluate means of improving the delivered dose accuracy in light of experimental results.

This work has been published in the ABS Brachytherapy Journal:

Aldelaijan, S., Bekerat, H., Buzurovic, I.M., Devlin, P.M., DeBlois, F., Seuntjens, J. and Devic, S., Dose comparison between TG-43–based calculations and radiochromic film measurements of the Freiburg flap applicator used for high-dose-rate brachytherapy treatments of skin lesions. *Brachytherapy*, 16(5): 1065-1072 (2017)

Dose comparison between TG-43 based calculations and radiochromic film measurements of the Freiburg flap applicator used for high-dose-rate brachytherapy treatments of skin lesions

Saad Aldelaijan,[1,2,3,4,*] Hamed Bekerat,[2,3] Ivan Buzurovic,[5] Phillip Devlin,[5] Francois DeBlois,[2,3] Jan Seuntjens,[2] Slobodan Devic[2,3]

[1]Biological & Biomedical Engineering Department, Montreal Neurological Institute, Montréal, Québec, Canada

[2]Medical Physics Unit, McGill University, Montréal, Québec, Canada

[3]Department of Radiation Oncology, Jewish General Hospital, Montréal, Québec, Canada

[4]Biomedical Physics Department, King Faisal Specialist Hospital & Research Centre, Riyadh, Saudi Arabia

[5]Department of Radiation Oncology, Dana-Farber/ Brigham and Women's Cancer Center, Harvard Medical School, Boston, MA, USA

Keywords: Freiburg flap, HDR brachytherapy, radiochromic film dosimetry, skin treatment

Abstract

Purpose: Current HDR brachytherapy skin treatments with the Freiburg flap (FF) applicator are planned with treatment planning systems based on AAPM TG-43 datasets which assume full backscatter conditions in dose calculations. The aim of this work is to describe an experimental method based on radiochromic film dosimetry to evaluate dose calculation accuracy during surface treatments with the FF applicator at different depths and bolus thicknesses.

Methods: Absolute doses were measured using a reference EBT3 radiochromic film dosimetry system within a Solid Water™ phantom at different depths (0, 0.5, 1, 2 and 3 cm) with respect to the phantom surface. The impact of bolus (up to 3 cm thickness) placed on top of the applicator

was investigated for two clinical loadings created using Oncentra MasterPlan™: 5 cm × 5 cm, and 11 cm × 11 cm.

Results: For smaller loading and depths beyond 2 cm and for larger loading and depths beyond 1 cm, the dose difference was less than 3% (±4%). At shallower depths, differences of up to 6% (±4%) at the surface were observed if no bolus was added. The addition of 2 cm bolus for the smaller loading and 1 cm for larger loading minimized the difference to less than 3% (±4%).

Conclusions: For typical FF applicator loading sizes, the actual measured dose was 6% (±4%) lower at the skin level when compared to TG-43. Additional bolus above the FF was shown to decrease the dose difference. The consideration of change in clinical practice should be carefully investigated in light of clinical reference data.

5.1 Introduction

Treatment of skin lesions with high-dose-rate (HDR) brachytherapy evolved over the years using either Leipzig (1, 2) or the Valencia (3, 4) applicators (Elekta, Veenendaal, The Netherlands) for relatively small treatment areas, less than 3 cm in diameter (5). The Freiburg flap (FF) applicator (Elekta, Veenendaal, The Netherlands) can be used for small and large surface lesions as well as intra-operative treatments (6, 7). One of the main advantages of the FF applicator is that it can easily conform to most surface target shapes while preserving its geometry in relation to the surface (8, 9). The FF applicator represents a mesh mold consisting of 1 cm diameter silicon spheres with flexible catheters channeled through in one direction.

As the current (TG-43 based (10, 11, 12)) treatment planning system(s) (TPS) assume the full water phantom approximation in dose calculations, the apparent lack of full scattering (backscatter from above the applicator and air gaps between spheres) raises the question about dose precision in the current clinical practice while implementing this type of applicator (13,14,15). Recent developments in advanced methodologies in dose calculation and computational power have paved the way towards model-based brachytherapy dose calculation algorithms (16). These algorithms employ different approaches in scatter integration into dose calculation in heterogeneous media including tissue and applicators. For HDR ^{192}Ir brachytherapy, numerous solutions were explored such as analytical or semiempirical solutions (17,18), collapsed-cone superposition/convolution (19), stochastic (20,21) and deterministic (22,23,24,25,26) solutions to the

linear Boltzmann transport equation. For skin dose during breast implants, Lymperopoulou *et al* (27) and Poon *et al* (28) showed that the difference between Monte Carlo (MC) simulations and TG-43 calculated dose is in the order of 5%. For superficial treatments, Granero *et al* (15) showed the same difference was within 3% and 2% for superficial mould mesh and catheter in contact with skin, respectively using GEANT4 MC simulations. For the FF, Vijande *et al* (13) found the differences between PENELOPE simulations and TG-43 to be less than 5% for typical clinical loadings. Raina *et al* (14) used a linear ionization chamber array positioned just under the FF for their measurements and concluded that the difference between a measurement under full scattering conditions (15 cm added bolus material) and one without bolus material depended on the prescription depth and it reached 8.5%, 12.5%, and 15% for prescription depths of 0.5 cm, 1.0 cm, and 1.5 cm, respectively.

Additional experimental determination of the difference between delivered dose and TG-43 is desirable and radiochromic film dosimetry provides appealing properties for skin dose measurements (29). These properties include the small physical thickness, tissue equivalence (30, 31) and low energy dependence down to effective energy of 100 kV for EBT, EBT2 and earlier EBT3 models (Ashland Inc., Wayne, NJ, 32,33) and down to 40 kV for newer EBT3 film models with improved active layer (34). In this work, the absolute dose was measured using a reference radiochromic film dosimetry system within a Solid Water™ (SW) phantom, at different depths (down to 3 cm depth), with a FF applicator placed on top of such phantom. The impact of additional bolus (up to 3 cm thickness) placed on top of the applicator was investigated for two treatment plans: one with 5 cm × 5 cm loading, and another one with 11 cm × 11 cm loading. The measured dose values were compared to the calculated ones for each experimental setup and depth in terms of dose ratio between film measurement and calculation by a commercially available TPS.

5.2 Methods and materials

5.2.1 Radiochromic film dosimetry system

The radiochromic film dosimetry system used in this study has been described in detail elsewhere (31,35). GafChromic™ EBT3 film was used in this study and has three main performance improvements over the previous (EBT2) film model. The EBT3 radiochromic film model had a unique polyester substrate with small silica particles that prevented the formation of Newton's

Rings interference patterns in images acquired using flatbed document scanners. Moreover, as opposed to the EBT2 film model, that had an asymmetric layer structure, the EBT3 film model has a 30 μm thick active layer sandwiched between two matte 125 μm thick polyester sheets. Finally, the sensitive layer of the latest batch numbers of EBT3 film model contains aluminum (36) improving the energy response down to 40 kV (34).

The reference radiochromic film dosimetry system used in this work consisted of an Epson Expression 10000XL flatbed document scanner (Epson, Nagano, Japan) and both the calibration and measuring EBT3 model film pieces taken from the same batch number (A05151202). The scanner provided 48-bit red, green, and blue (RGB) images scanned in transmission mode with all filters and image enhancement options turned off. Although it was shown previously (37) that the green color channel is the most optimal for dose measurements in the vicinity of brachytherapy sources exhibiting high dose gradients, in this work, it was decided to use the red color channel instead. The rationale for this decision is based on the main motivation of this study to investigate dose deposition at different depths (from surface to 30 mm), avoiding very high dose gradients in direct proximity to the source (first measurement point is 5 mm from the source position). In addition, by expecting relatively low doses at relatively deep measurement points, the red color channel (being more sensitive than green color channel) was assumed to be more suitable for the measurements. Measurements were extended to 30 mm depth to show the mitigation of dose difference between them and TG-43 dose calculation.

Ten calibration film pieces (2” × 2.5”) were scanned with a 127 dpi resolution (0.2 mm/pixel) prior to and 24-hours after exposure to various doses ranging from 50 to 1000 cGy. Calibration film pieces were irradiated within a SW phantom at a depth of 10 cm with 18 MV photon beam in a 100 cm source-to-surface distance (SSD) setup using a 20 cm × 20 cm field defined at the isocentre of a Varian Clinac eX linear accelerator (Varian Medical Systems, Palo Alto, CA). As shown earlier, response of the initial EBT3 film model showed minimal energy dependence down to 100 kV (similar sensitive layer to EBT1 and EBT2 film models (32,33,34,38). However, the latest EBT3 film model showed minimal under-response down to 40 kV effective photon energy (34). Ten centimeters below the plane where the films were positioned, a monitor chamber was placed, below which additional 10 cm SW slab was added to provide consistent and reproducible scattering geometry for monitor chamber readings. The use of 18 MV photon beam

has the advantage of less number of monitor units to deliver the same dose using a 6 MV beam and also the less backscatter effect from the monitor chamber to the film level. The scanner-film response (39) during calibration and measurement was monitored using a control film piece in accordance with our previous work (40).

5.2.2 Experimental setup

Figure 5.1 represents the experimental setup used in this work. Five 30 cm × 30 cm slabs of SW positioned below the FF applicator were indented (in-house to 280 microns depth) in the middle to accommodate 1" × 2" pieces of EBT3 film model. This was done order to alleviate any impact of air gaps between SW slabs on dose measurement precision. In addition, a 5 cm slab of SW (of the same size) was placed below the last measurement point (3 cm phantom depth) in order to provide sufficient backscattering material. A removable marker was used to place reference marks on the topmost slab of SW and on the applicator itself, in order to assure precise positioning of the applicator with respect to the phantom, and the measuring film pieces. Five (5) film pieces were irradiated at the time within the phantom with one of the two treatment plans, created using Oncentra MasterPlan™ (version 4.1, Elekta, Veenendaal, The Netherlands): one with 5 cm × 5 cm loading, and another one with 11 cm × 11 cm loading. Both plans had a 2.5 mm step size and were optimized using the distance-based dose optimization method in order to prescribe an absolute dose of 6 Gy at prescription depth chosen for this study to be at 1 cm. The choice of prescription dose and depth was based on the uncertainty analysis of the reference radiochromic film dosimetry system, established during the film calibration process which will be discussed below. It has to be pointed out that typical prescription depth in skin surface brachytherapy is 5 mm from the skin surface (to avoid overdosing the skin surface) where prescription depth ranged from 1 to 10 mm as reported in the recent survey results of Likhacheva *et al* (41) and ABS recommendations on aspects of dosimetry and clinical practice of skin brachytherapy (42).

Five irradiations were delivered for both plans each one under different scattering conditions depending on the amount of bolus material (SW) placed on top of the FF applicator: 0, 0.5, 1, 2, and 3 cm. Figure 5.1 also depicts the measurement setup in which the 3 cm bolus material is added on top of the applicator. The measurement setup with 0 cm bolus material thickness directly corresponds to the most commonly encountered clinical practice, whereby no bolus material is placed on the surface of the FF applicator. The same TPS used to generate treatment plans was

employed to register absolute dose values in the center of the treatment plans at each depth where the film pieces were positioned. The difference between calculated dose (by the TPS) and measured dose (by the film) was reported as the dose ratio between measurement and calculation for all depths and setups used in this study.

5.2.3 Image processing

Scanned images were saved as tagged image file format (TIFF) and as mentioned before, they were acquired with a 127 dpi resolution (0.2 mm/pixel) and the red channel was used for dosimetry in this work. The location of region-of-interest (ROI) on films irradiated by the HDR source was determined using a semi-automatic localization based on Gaussian fitting as described in our previous work (37). An ROI size of 2 mm × 2 mm was used and the mathematical model we used to convert the film signal to dose was described thoroughly elsewhere (36, 37).

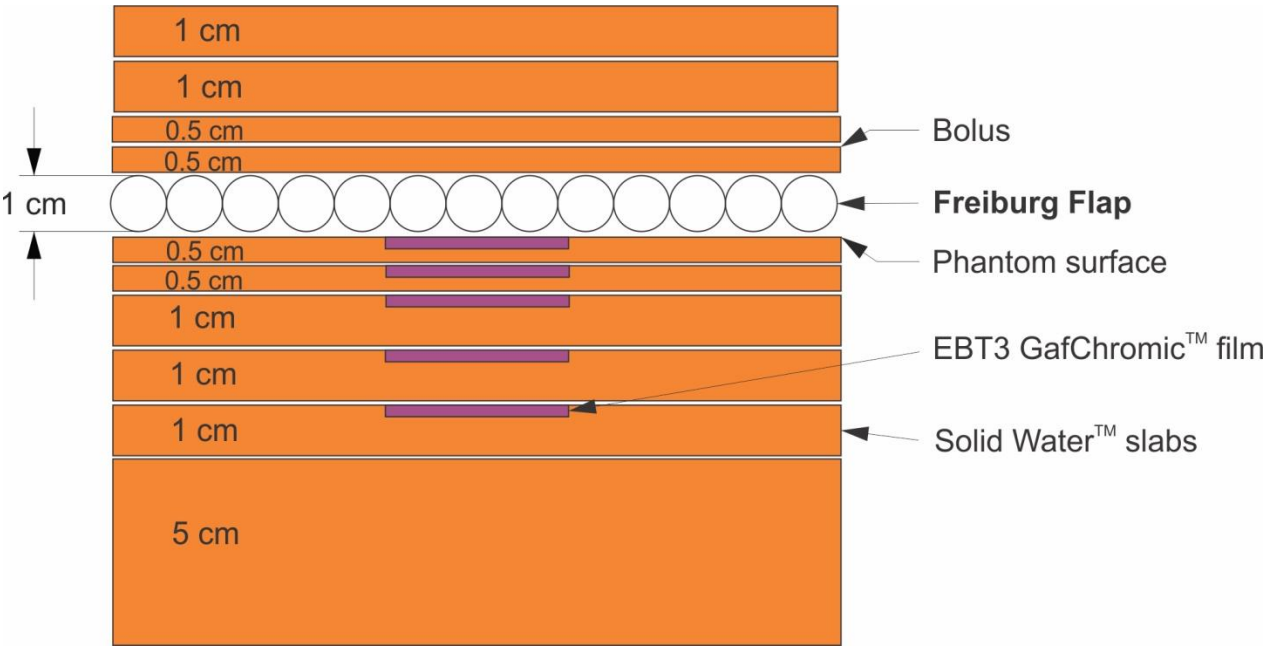

Figure 5.1: Experimental setup (with 3 cm bolus on top of the Freiburg Flap). Solid Water™ slabs are 30 cm × 30 cm in size. Dimensions are not to scale.

5.3 Results

Figure 5.2 shows the calibration curve (subfigure 5.2A), uncertainty analysis (subfigure 5.2B) as well as the uncertainty vs. error analysis (subfigure 5.2C) for the reference radiochromic film dosimetry system used in this work. The line in figure 5.2A represents the calibration fit while the closed circle symbols represent the experimental data. In subfigure 5.2B, the thick line with closed circle symbols represents the total uncertainty which is the quadrature sum of the fit (thin line, open square symbols) and experimental (thin line, open diamond symbols) uncertainties. The line in subfigure 5.2C represents the total dose uncertainty while the close circle symbols represent the dose error. As expected, dose errors (calculated as the absolute difference between known and calculated doses) and dose uncertainties (sum of experimental and fitting uncertainties (36) are higher at lower dose levels. Figure 5.2 suggests that the radiochromic film dosimetry system used in this work and defined by the protocol described in Materials section can measure dose with an uncertainty better than 3% for doses larger than 2 Gy. In this regard, the plans created for this investigation were tailored in such a way so that the delivered dose measured by the film pieces should have been in the range between 2 and 10 Gy.

Figure 5.3 summarizes results of investigations into the impact of additional bolus material on top of the FF applicator on dose calculation precision using contemporary brachytherapy treatment planning systems. Subfigures 5.3A and 5.3B show the dose distributions for the two loading patterns 5 cm × 5 cm (5.3A) and 11 cm × 11 cm (5.3B) at the plane containing the central silicon sphere (placed at the center of the coordinate system). The vertical axis represents direction (downwards) along which the dose values were calculated and measured at five different depths. The corresponding isodose lines at five depths (i.e., 0, 0.5, 1, 2 and 3 cm) have been presented for the two plans as well. It is apparent from subfigures 5.3A and 5.3B that the isodose distribution for the 11 cm × 11 cm plan is more uniform when compared with the plan with a smaller number of dwell positions. It was observed that for the larger treatment fields (and by engaging plans with more dwell positions) dwell weight could be more equally distributed resulting in more uniform dose distributions. Since the FF applicator is commonly used for larger treatment lesions, it was decided to examine the 5 cm × 5 cm plan as the smallest size in this study. Subfigures 5.3C and 5.3D depict the influence of bolus thickness on dose ratio between measurements and treatment

planning system for two experimental setups: dwell positions at 5 cm × 5 cm (subfigure 5.3C), and 11 cm × 11 cm (subfigure 5.3D).

Table 5.1 shows the uncertainty budget of overall dose calculation and measurement of a single point (film ROI of 2 mm by 2 mm) at the level of prescription depth of 1 cm from the phantom surface, below the central sphere of the Freiburg flap for an 11 cm × 11 cm loading area.

Table 5.1: Uncertainty budget example of overall dose calculation and measurement at depth of 1 cm from the phantom surface for an 11 cm × 11 cm loading area.

Source of uncertainty	***Uncertainty (%)***	***Evaluation Type****	***Remark***
Dose calculation			
Source strength measurement	*1.5*	*A*	*Sources: AAPM TG-138 (43), Kirisits et al (44)*
TG-43 Cons data	*1.6*	*B*	
TPS interpolation	*2.6*	*B*	
Combined dose calculation uncertainty	***3.4***		*k=1*
Expanded dose calculation uncertainty	***6.8***		*k=2*
Dose measurement			
Absolute dose calibration (measurements, calibration data, influence quantities)	*1.5*	*B*	*Source: AAPM TG-51 addendum (45)*
Monitor chamber reproducibility	*0.5*	*B*	
Film scanner homogeneity	*0.2*	*B*	*Source: Aldelaijan et al 2010 (37)*
Film scanner reproducibility	*0.2*	*A*	
Film calibration curve fitting	*2*	*B*	*Figure 2, prescription of 6 Gy at 1 cm depth*
Film netOD measurement reproducibility	*0.2*	*A*	
Source-film positioning	*1*	*B*	*At 15 mm from the source and includes a combined uncertainty from FF sphere, Solid Water™, and film thickness measurements with a digital caliper (±0.01 mm) and the TPS ruler tool (±0.1 mm).*
Solid Water™ to water dose conversion at ^{192}Ir	*0.07*	*B*	*Source: Aldelaijan et al 2010 (37)*
Combined dose measurement uncertainty	***2.8***		*k=1*
Expanded dose measurement uncertainty	***5.5***		*k=2*

** Evaluation types A/B are based on the JCGM100:2008 Guide to the expression of uncertainty in measurements (46)*

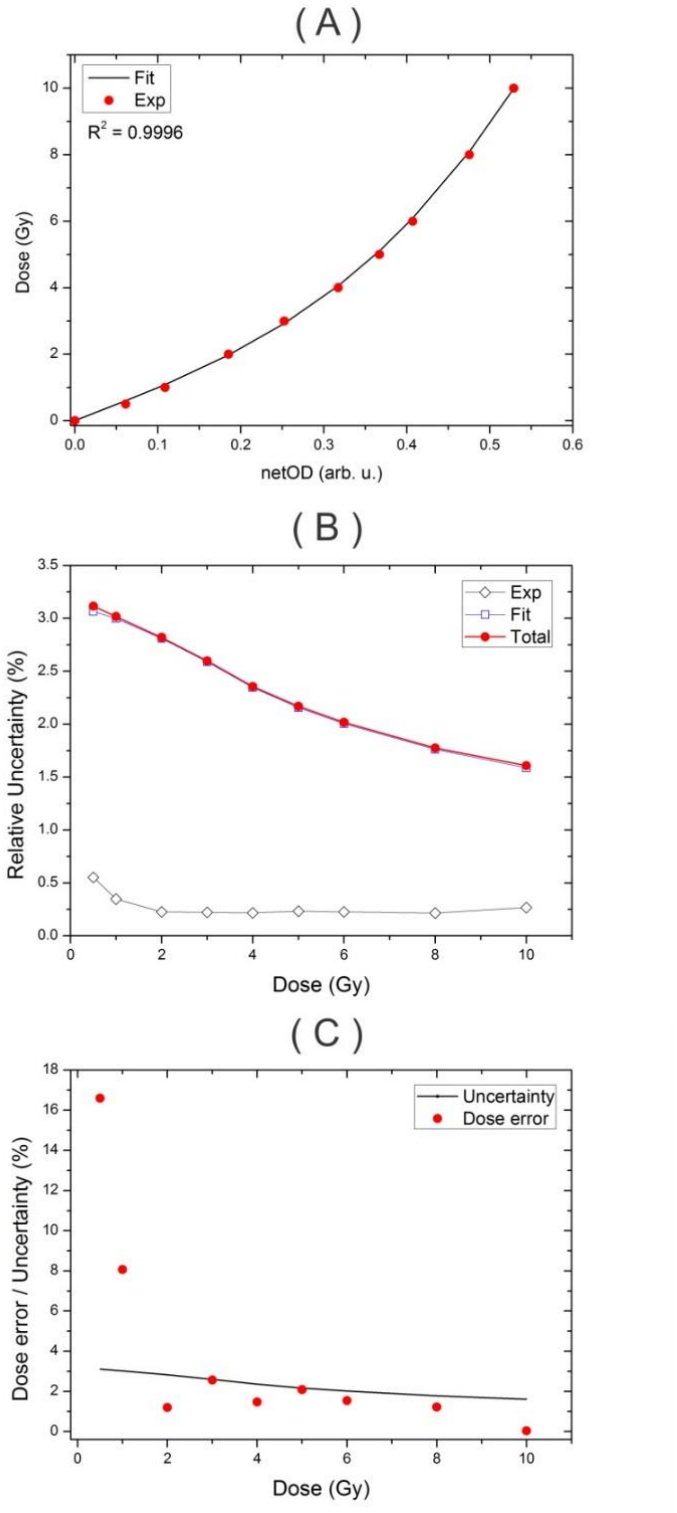

Figure 5.2: Reference radiochromic film dosimetry system used: calibration curve (5.2A); two-component (experimental and fit) relative uncertainty (5.2B); and error vs. uncertainty assessment (5.2C).

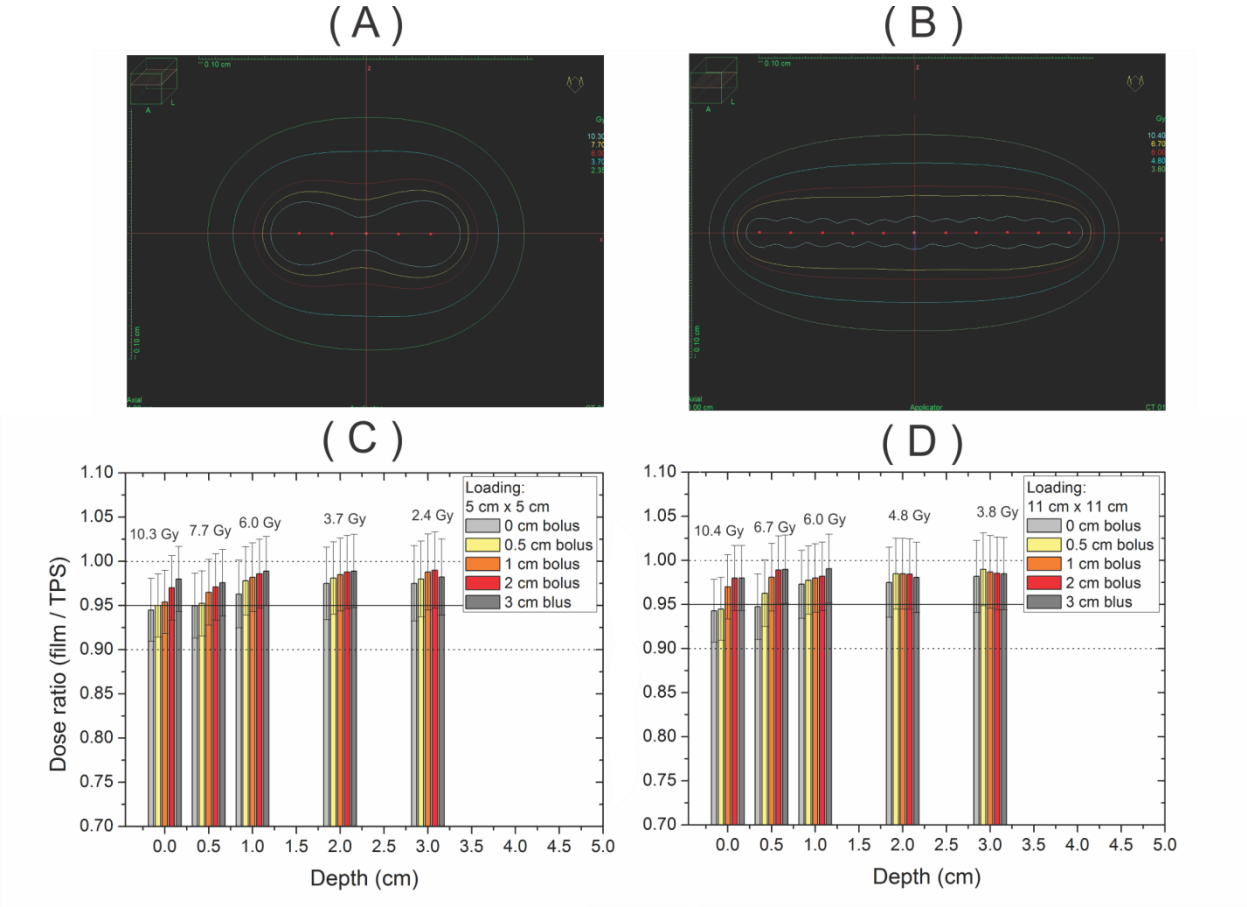

Figure 5.3: The impact of bolus thickness on absolute dose ratio between measurements (using radiochromic film based reference dosimetry system) and treatment planning system (Oncentra - MasterPlan™) at the downward vertical plane to the central sphere of the Freiburg flap for two experimental setups: dose distributions for 5 cm × 5 cm loading (5.3A), and 11 cm × 11 cm loading (5.3B); dose ratio histograms with numbers above representing dose values calculated by TPS at corresponding depths for 5 cm × 5 cm loading (5.3C), and 11 cm × 11 cm loading (5.3D). Error bars include the uncertainty in dose calculation and measurement per dose level.

5.4 Discussion

Subfigures 5.3C and 5.3D showed that the dose ratio between measured and calculated dose values were always positive, meaning that TPS systematically overestimated the actual delivered dose. This result is expected as the TPS-calculated dose assumes full scattering conditions that are not usually met in clinical practice. In addition, subfigures 5.3C and 5.3D showed that for depths of 2 cm (for smaller targets) and 1 cm (for larger targets) and beyond, the actual dose difference is less than 3% (±4%). At shallower depths, the addition of 2 cm bolus material for smaller lesions as

well as 1 cm bolus material for larger lesions provided a dose difference (between calculated and measured) of less than 3% (±4%). It is of note that the quoted uncertainty (±4%) is calculated for the dose ratio between measured and calculated doses and therefore it is dominated by the TPS dose calculation uncertainty (see Table 5.1). The uncertainty in film measurement is mostly affected by the dose level (Figure 5.2C) and the difference in source-film distance between planning and measurements (Table 5.1). To analyze the difference in source to film distance between measurement and planning, we measured individual thicknesses (FF spheres, SW and films) and evaluated their uncertainties using a digital caliper (±0.01 mm precision). The total difference between source-film distance during measurements and planning was 0.16 mm which corresponds to a systematic error in dose of 0.5% as determined with TG-43, that is taken into account.

Measurement-based results in Figure 3 for the 5 cm × 5 cm plan without bolus material are slightly higher than previously published MC simulation-based results by Vijande *et al* (13), who reported 1–5% difference at the skin surface and 3–5% at 0.5 cm depth. This might be attributed to the difference in geometries and loading patterns between this study and theirs. On the other hand, in comparison to Raina *et al*'s (14) work, our results in Figure 3 show a lower deviation between TG-43 and measurements. When comparing phantom surface doses (1 cm prescription depth) without and with bolus thickness of 0.5, 1, 2 and 3 cm, Raina *et al* report differences as high as 9% for loading areas similar to our work (4 cm × 4 cm and 12 cm × 12 cm). These differences might again be attributed to difference in geometries and loading patterns, where it is of note that Raina *et al* used FF sizes that were cut and fitted within tissue-equivalent material to mimic intraoperative procedures while in our work the FF size was the same for different loading sizes.

The importance of these experimental results stems from the precision of the radiochromic film dosimetry system used in this study. The film has the convenience of small physical size, tissue equivalence and low energy dependence as described in Materials and methods section. The advantage of calibrating film under a megavoltage beam quality instead of calibrating it under HDR ^{192}Ir is the avoidance of TG-43-associated uncertainties in dose calculation (See top section of Table 5.1). The film energy dependence (between megavoltage and ^{192}Ir beam qualities) was found to be minimal as shown by Sarfehnia *et al* (47) for the EBT1 film. They calibrated the film under 6 MV and calculated a 0.9971 (1σ=0.1%) dose scaling factor to account for the energy difference. As discussed earlier, Bekerat *et al* (34) showed that new batches of EBT3 films (with

improved response), resulted in a refined energy response in comparison to EBT1 film. In our previous study (37), it was shown using MC simulations that the difference between dose to film in SW and dose to film in water was minimal (0.9941 (1σ=0.07%)). Schoenfeld *et al* (48) also analyzed the use of water equivalent phantoms for ^{192}Ir brachytherapy and found that the maximum deviations of absorbed dose to water between SW and water for phantoms with 5 cm and 10 cm radii were -0.29% and -0.76%, respectively.

As was shown in subfigures 5.2B and 5.2C, the radiochromic film dosimetry system used in this work has a limit of 3% uncertainty at doses lower than 2 Gy and this was the rationale we prescribed a high dose (6 Gy at 1 cm depth) *i.e.* to lower the uncertainty in dose determination. Figure 5.2C showed that the dose error resulting from using this system is within the uncertainty limit except for doses lower than 2 Gy, which is not of interest in this work. On the other hand, the lower portion of Table 5.1 summarizes the overall uncertainty achievable using this system at a prescription depth of 1 cm. Viewing these results with subfigure 5.2C reveals that the uncertainty is indeed dose-dependent (or depth-dependent in this case). It is also of note that the uncertainty provided by this system is well within the recommendations of AAPM TG-138 that the overall expanded uncertainty associated with single-photon-emitting brachytherapy sources (from calibration in a primary standards laboratory to the clinic) should be less than 10% (k=2).

The results of Figure 3 are similar to Vijande *et al*'s simulations (13) within the achievable measurement precision. However, irrespective of the variability of reported values among different studies (this study, 13, 14), they mainly show that the deviation between TG-43 and delivered doses is positive and the magnitude of the difference has to be analyzed locally. It is also anticipated that modern model-based brachytherapy calculations would provide (ultimately) more accurate dose distributions, and since the current dose prescriptions are rather evidence-based (41), this work shows that the switch from the old calculations (TG-43 based) and even more importantly dose prescriptions should be implemented in a cautious way. This conclusion is in line with the recommendation of AAPM TG-186 report (16) that TG-43 formalism remains the standard of practice for dose calculation until sufficient clinical data become available (section VI.C. of TG-186). Finally, these experimental results justify the need for the more accurate (model-based) dose calculations in brachytherapy in general, and for the surface brachytherapy in particular. However, as the new, more accurate, calculation methods become clinically

available, any change in prescription must be weighed against current evidence-based prescribed doses for each treatment site separately.

5.5 Conclusions

This work experimentally investigated the impact of lack of full backscatter conditions on the use of FF applicator for HDR brachytherapy skin treatment. For depths of 2 cm and beyond, the dose difference between measured and calculated dose distributions was below 3% (±4%) for plans used in the treatment of small lesions. For the larger lesions, the same level of dose difference was observed for depths of 1 cm and beyond. It was also observed that adding a 2 cm slab of bolus material for smaller targets as well as 1 cm bolus material for larger regions, would bring the dose difference to less than 3% (±4%) even at the surface and at 0.5 cm depth which is frequently used for dose prescription in patients treated with FF applicator. It is not the intent of this work to provide recommendations on policies to mitigate the difference between current TPS dose calculations (which are mostly based on TG-43), but rather to present a dosimetry system based on the radiochromic film that provided a convenient way for local establishment of dose difference between TG-43 and actual delivered dose.

5.6 Acknowledgement

This work was supported in part by the Natural Sciences and Engineering Research Council of Canada contract No. 386009. S.D. is a Research Scientist supported by the Fonds de Recherche en Santé du Québec (FRSQ). S.A. is a Ph.D. Candidate supported by the scholarship program at King Faisal Specialist Hospital & Research Centre (KFSH&RC). S.A. acknowledges partial support by the CREATE Medical Physics Research Training Network grant of the Natural Sciences and Engineering Research Council (Grant number: 432290).

5.7 References

1. Perez-Calatayud J, Granero D, Ballester F, *et al*. A dosimetric study of Leipzig applicators. *Int J Radiat Oncol Biol Phys* 2005;62:579-584.
2. Niu H, Hsi WC, Chu JC, *et al*. Dosimetric characteristics of the Leipzig surface applicators used in the high dose rate brachy radiotherapy. *Med Phys* 2004;31:3372-3377
3. Granero D, Perez-Calatayud J, Gimeno J, *et al*. Design and evaluation of a HDR skin applicator with flattening filter. *Med Phys* 2008;35:495-503

4. Guix B, Finestres F, Tello J *et al*. Treatment of skin carcinomas of the face by high-dose-rate brachytherapy and custom-made surface moulds. *Int J Radiat Oncol Biol Phys* 2000; 47: 95-102.
5. Delishaj D, Laliscia C, Manfredi B, *et al*. Non-melanoma skin cancer treated with high-dose-rate brachytherapy and Valencia applicator in elderly patients: a retrospective case series. *J Contemp Brachytherapy* 2015 Dec 1;7(6):437-44.
6. Moningi S, Armour EP, Terezakis SA, *et al*. High-dose-rate intraoperative radiation therapy: the nuts and bolts of starting a program. *J Contemp Brachytherapy*. 2014 Mar;6(1):99.
7. Lloyd S, Alektiar K M, Nag S, *et al*. Intraoperative high-dose-rate brachytherapy: An American Brachytherapy Society consensus report. *Brachytherapy* 2017; in press.
8. Gao S, Delclos ME, Tomas LC, *et al*. High-dose-rate remote afterloaders for intraoperative radiation therapy. *AORN*. 2007;86:827–836
9. Devlin PM, *editor*, Cormack RA, Holloway CL, Stewart AJ, Brachytherapy: applications and techniques, *2nd ed., Demos Medical Publishing*, ISBN 9781620700822, 2016
10. Nath R, Anderson L, Luxton G, *et al*. Dosimetry of interstitial brachytherapy sources: Recommendations of the AAPM Radiation Therapy Committee Task Group No. 43, *Med. Phys.* 1995;22, 209–234
11. Rivard MJ, Coursey BM, DeWerd LA, *et al*. Update of AAPM Task Group No. 43 Report: A revised AAPM protocol for brachytherapy dose calculations, *Med. Phys.* 2004;31, 633–674
12. Daskalov GM, Lo¨ffler E, and Williamson JF, Monte Carlo-aided dosimetry of a new high dose-rate brachytherapy source, *Med. Phys.* 1998;25, 2200–2208
13. Vijande J, Ballester F, Ouhib Z, *et al*. Dosimetry comparison between TG-43 and Monte Carlo calculations using the Freiburg flap for skin high-dose-rate brachytherapy *Brachytherapy* 2012;11:528-535
14. Raina S, Avadhani J S, Oh M, *et al*. Quantifying IOHDR brachytherapy underdosage resulting from an incomplete scatter environment. *Int J Radiat Oncol Biol Phys* 2005;61:1582-1586
15. Granero D, Perez-Calatayud J, Vijande J, *et al*. Limitations of the TG-43 formalism for skin high-dose-rate brachytherapy dose calculations *Med. Phys.* 2014; 41;021703-1

16. Beaulieu L, Carlsson Tedgren Å, Carrier J F, *et al*. Report of the Task Group 186 on model-based dose calculation methods in brachytherapy beyond the TG-43 formalism: Current status and recommendations for clinical implementation *Med. Phys.* 2012;39,6208-36
17. Rivard M J, Melhus C S, Granero D, *et al*, An approach to using conventional brachytherapy software for clinical treatment planning of complex, Monte Carlo-based brachytherapy dose distributions. *Med. Phys.* 2009;36(6),1968-1975.
18. Poon E and Verhaegen F, A CT-based analytical dose calculation method for HDR 192Ir brachytherapy. *Med. Phys.*, 2009;36(9),3982-3994.
19. Carlsson Tedgren Å K and Ahnesjö A, Accounting for high Z shields in brachytherapy using collapsed cone superposition for scatter dose calculation. *Med, Phys.*, 2003;30(8),2206-2217.
20. Yegin G and Rogers D, A fast Monte Carlo code for multi-seed brachytherapy treatments, including inter-seed effects. *Med. Phys.*, 2004;31(6),1771.
21. Chamberland M J, Taylor R E, Rogers D W O and Thomson R M, egs_brachy: a versatile and fast Monte Carlo code for brachytherapy. *Phys. Med. Biol.*, 2016;61(23), 8214.
22. Daskalov G M, Baker R S, Rogers D W O and Williamson J F, Dosimetric modeling of the microselectron high-dose rate ^{192}Ir source by the multigroup discrete ordinates method. *Med. Phys.*, 2000;27(10),2307-2319.
23. Gifford KA, Price MJ, Horton JL, *et al*, Optimization of deterministic transport parameters for the calculation of the dose distribution around a high dose-rate ^{192}Ir brachytherapy source. *Med Phys*, 2008;35(6),2279-2285.
24. Mikell JK and Mourtada F, Dosimetric impact of an ^{192}Ir brachytherapy source cable length modeled using a grid-based Boltzmann transport equation solver. *Med Phys*, 2010;37(9), 4733-4743.
25. Zourari K, Pantelis E, Moutsatsos A, *et al*, Dosimetric accuracy of a deterministic radiation transport based ^{192}Ir brachytherapy treatment planning system. Part I: Single sources and bounded homogeneous geometries. *Med Phys*, 2010;37(2),649-661.
26. Petrokokkinos L, Zourari K, Pantelis E, *et al*, Dosimetric accuracy of a deterministic radiation transport based ^{192}Ir brachytherapy treatment planning system. Part II: Monte Carlo and experimental verification of a multiple source dwell position plan employing a shielded applicator. *Med Phys*, 2011;38(4),1981-1992.

27. Lymperopoulou G, Papagiannis P, Angelopoulos A, *et al*,. A dosimetric comparison of ^{169}Yb and ^{192}Ir for HDR brachytherapy of the breast, accounting for the effect of finite patient dimensions and tissue inhomogeneities. *Med Phys*, 2006;33(12), 4583-4589.
28. Poon E and Verhaegen F, Development of a scatter correction technique and its application to HDR ^{192}Ir multicatheter breast brachytherapy. *Med Phys*, 2009;36(8), 3703-3713.
29. Devic S, Seuntjens J, Abdel-Rahman W, *et al*, Accurate skin dose measurements using radiochromic film in clinical applications. *Med Phys*, 2006;33(4), 1116-1124.
30. McLaughlin WL, Chen YD, Soares CG, et al. Sensitometry of the response of a new radiochromic film dosimeter to gamma radiation and electron beams Nucl. Instrum. Methods Phys. Res. 1991;A302:165–176.
31. Devic S, Radiochromic film dosimetry: Past, present, and future Phys. Med. 2011;27:122–134.
32. Sutherland JGH and Rogers DWO, Monte Carlo calculated absorbed-dose energy dependence of EBT and EBT2 film, Med. Phys. 2010;37:1110–1116.
33. Arjomandy B, Tailor R, Anand A, et al. Energy dependence and dose response of Gafchromic EBT2 film over a wide range of photon, electron, and proton beam energies, Med. Phys. 2010;37:1942–1947.
34. Bekerat H, Devic S, DeBlois F, et al. Improving the energy response of external beam therapy (EBT) GafChromic^{TM} dosimetry films at low energies (≤ 100 keV). Med. Phys. 2014;41:022101.
35. Devic S, Seuntjens J, Sham E, *et al*. Precise radio-chromic film dosimetry using a flat-bed document scanner *Med. Phys.* 2005;32:2245–2253
36. Devic S, Tomic N, Lewis D, Reference radiochromic film dosimetry: Review of technical aspects *Phys. Med.* 2016;32:541-556
37. Aldelaijan S, Mohammed H, Tomic N, *et al*. Radiochromic film dosimetry of HDR ^{192}Ir source radiation fields *Med. Phys.* 2011;38,6074–6083
38. Rink A, Vitkin I A and Jaffray D A Energy dependence (75kVp to 18MV) of radiochromic films assessed using a real-time optical dosimeter. *Med. Phys.* 2007;34(2),458-463.
39. Lewis D and Devic S, Correcting scan-to-scan response variability for a radiochromic film-based reference dosimetry system. *Med. Phys.* 2015;42(10),5692-5701

40. Aldelaijan, S., Alzorkany, F., Moftah B, *et al* Use of a control film piece in radiochromic film dosimetry. *Phys. Med.* 2016;32(1),202-207.
41. Likhacheva A O, Devlin P M, Shirvani S M, *et al* Skin surface brachytherapy: A survey of contemporary practice patterns *Brachytherapy* 2017;16:223-229
42. Ouhib Z, Kasper M, Calatayud J P, *et al* Aspects of dosimetry and clinical practice of skin brachytherapy: The American Brachytherapy Society working group report. *Brachytherapy* 2015;14,840-858
43. DeWerd LA, Ibbott GS, Meigooni AS, *et al*. A dosimetric uncertainty analysis for photon-emitting brachytherapy sources: report of AAPM Task Group No. 138 and GEC-ESTRO. *Med Phys.* 2011;38(2),782-801.
44. Kirisits C, Rivard MJ, Baltas D, *et al.* Review of clinical brachytherapy uncertainties: analysis guidelines of GEC-ESTRO and the AAPM. *Radiother Oncol.* 2014;110(1),199-212.
45. McEwan M, DeWerd L, Ibbot G, *et al*. Addendum to the AAPM's TG-51 protocol for clinical reference dosimetry of high-energy photon beams, *Med. Phys.* 2014;41,041501-1-20
46. JCGM 100:2008 Evaluation of measurement data — Guide to the expression of uncertainty in measurement 1st Edition, 2008
47. Sarfehnia A, Kawrakow I and Seuntjens J, Direct measurement of absorbed dose to water in HDR ^{192}Ir brachytherapy: Water calorimetry, ionization chamber, Gafchromic film, and TG-43. Med. Phys. 2010;37,1924-1932.
48. Schoenfeld A A, Harder D, Poppe B and Chofor N Water equivalent phantom materials for ^{192}Ir brachytherapy. *Phys Med Biol.* 2015;60(24),9403.

CHAPTER 6: Positional and angular tracking of HDR ^{192}Ir source for brachytherapy quality assurance using radiochromic film dosimetry

---

Preface

In chapter 5, the radiochromic film dosimetry protocol (chapters 3, 4) was employed for reference dosimetry of surface HDR brachytherapy. This paper highlights the unique physical advantage of using radiochromic film to perform HDR source quality assurance; that is the high two-dimensional (2D) resolution. A tracking model was described to track the source positional and angular information based on a measured 2D dose map. The source tracking model is based on the fact that each isodose line away from the source has unique 2D features that are obtainable from "blob" analysis. Combined with the dosimetry protocol, high resolution EBT3 radiochromic films was able to capture these 2D dose maps, retrieve the relative isodose lines and compare them to a reference library of features to estimate the most probable source coordinates. This technique offers a novel multidimensional source localization methodology and has the potential to be used for quality assurance of commercial and customized applicators.

This work has been accepted for publication in the AAPM Medical Physics journal:

Aldelaijan, S., Devic, S., Bekerat, H., Papaconstadopoulos, P., Schneider, J., Seuntjens, J., Cormack, R.A. and Buzurovic, I.M. Positional and angular tracking of HDR ^{192}Ir source for brachytherapy quality assurance using radiochromic film dosimetry. *Med. Phys.* Accepted Author Manuscript, https://doi.org/10.1002/mp.14540 (2020)

Positional and angular tracking of HDR ^{192}Ir source for brachytherapy quality assurance using radiochromic film dosimetry

Saad Aldelaijan[1-5], Slobodan Devic[3,4], Hamed Bekerat[4], Pavlos Papaconstadopoulos[6], James Schneider[4], Jan Seuntjens[3], Robert A. Cormack[1], Ivan M. Buzurovic[1]

[1]Department of Radiation Oncology, Dana Farber/Brigham and Women's Cancer Center, Harvard Medical School, Boston, MA, 02115, USA

[2]Department of Biomedical Engineering, Montreal Neurological Institute, McGill University, Montréal, QC, H3A 2B4, Canada

[3]Medical Physics Unit, McGill University, Montréal, QC, H4A 3J1, Canada

[4]Department of Radiation Oncology, Jewish General Hospital, Montréal, QC, H3T 1E2, Canada

[5]Biomedical Physics Department, King Faisal Specialist Hospital & Research Centre, Riyadh, 12713, Saudi Arabia

[6]Netherlands Cancer Institute, Amsterdam, 1066 CX, Netherlands

Abstract

Purpose: To quantify and verify the dosimetric impact of HDR source positional uncertainty in brachytherapy, and to introduce a model for 3D position tracking of the HDR source based on a 2D measurement. This model has been utilized for development of a comprehensive source quality assurance method using radiochromic film dosimetry including assessment of different digitization uncertainties.

Methods: An algorithm was developed and verified to generate 2D dose maps of the mHDR-V2 ^{192}Ir source (Elekta, Veenendaal, Netherlands) based on the AAPM TG-43 formalism. The limits of the dosimetric error associated with source (0.9 mm diameter) positional uncertainty were evaluated and experimentally verified with EBT3 film measurements for 6F (2.0 mm diameter) and 4F (1.3 mm diameter) size catheters at the surface (4F, 6F) and 10 mm further (4F only). To

quantify this uncertainty, a source tracking model was developed to incorporate the unique geometric features of all isodose lines (IDL) within any given 2D dose map away from the source. The tracking model normalized the dose map to its maximum, then quantified the IDLs using blob analysis based on features such as area, perimeter, weighted-centroid, elliptic orientation, and circularity. The Pearson correlation coefficients (PCC) between these features and source coordinates (x, y, z, θ_y, θ_z) were calculated. To experimentally verify the accuracy of the tracking model, EBT3 film pieces were positioned within a Solid Water® phantom above and below the source and they were exposed simultaneously.

Results: The maximum measured dosimetric variations on the 6F and 4F catheter surfaces were 39.8% and 36.1%, respectively. At 10 mm further, the variation reduced to 2.6% for the 4F catheter which is in agreement with the calculations. The source center (x, y) was strongly correlated to the low IDL-weighted centroid (PCC=0.99), while the distance to source (z) was correlated with the IDL areas (PCC=0.96) and perimeters (PCC=0.99). The source orientation θ_y was correlated with the difference between high and low IDL-weighted centroids (PCC=0.98), while θ_z was correlated with the elliptic orientation of the 60-90% IDLs (PCC=0.97) for a maximum distance of z = 5 mm. Beyond 5 mm, IDL circularity was significant, therefore limiting determination of θ_z (PCC≤0.48). The measured positional errors from the film sets above and below the source indicated a source position at the bottom of the catheter (-0.24±0.07 mm).

Conclusions: Isodose line features of a 2D dose map away from the HDR source can reveal its spatial coordinates. Radiochromic film was shown to be a suitable dosimeter for source tracking and dosimetry. This technique offers a novel source quality assurance method and has the potential to be used for quality assurance of commercial and customized applicators.

6.1 Introduction

According to the American Association of Physicists in Medicine (AAPM) task groups TG-40,[1] TG-56,[2] and TG-59,[3] the source strength of new brachytherapy sources must be verified before deployment into clinical use. The current standard for clinical high-dose-rate (HDR) ^{192}Ir absolute dose determination is based on a user well-type ionization chamber measurement with a calibration traceable to a primary standard.[4] The uncertainty in the distance between the source and detector planes plays a large role in why a 4π well-type ionization chamber was chosen to verify

the source strength. AAPM TG-138 report[4] addressed the source-to-detector positional uncertainty for other detectors including radiochromic film (RCF) dosimetry. Specifically, the report provided recommendations on how to properly verify the TG-43 datasets[5–8] with measurements and addressed different types and limits of uncertainty. However, if the problem of positional uncertainty and source orientation can be solved, then in principle, accurate verification of the source strength and dose rate distribution could be achieved without 4π geometry based measurement.

RCF dosimetry has a strong potential to address the source positional uncertainty problems in HDR brachytherapy quality assurance (QA). Favorably, RCF dosimetry[9] is a high resolution 2D solution that can be applied at different stages of the brachytherapy process.[10] RCF has unique properties such as its small thickness, near tissue equivalence and lower light sensitivity,[11] dynamic dose range,[12] dose rate independence,[13] and energy independence in clinical beam qualities down to an effective energy of 100 keV for EBT1, EBT2 and earlier EBT3 models[14,15] and down to 40 keV for newer EBT3 film models with an improved active layer composition.[16,17] Each film sheet is 8” by 10” and can be cut conveniently to any desired shape. These properties make it possible to use the film in many aspects of HDR brachytherapy QA.[18,19] Awunor *et al*[20] developed a method for source position QA for ring and tandem applicators using XRQA2 RCF. Palmer *et al*[21] investigated the possibility of performing audits for HDR brachytherapy using RCF. They also provided a summary of other dosimetry systems as well.[22] Other systems used for brachytherapy QA have been investigated including diodes,[23,24] scintillators,[25,26] flat panel detectors,[27,28] radiographic film, electromagnetic tracking[30–32] and magnetic resonance tracking.[33] These systems showed promise mainly in source position QA; however full tracking of the HDR source positional information including its orientation is still an open topic. Full knowledge of the seed-like source positional information (position of the source center and angular orientation) enables QA of the brachytherapy catheters and QA of both standard and customized applicators as well.

In this work, an HDR ^{192}Ir source tracking model is presented for 3D spatial position and orientation detection based on a 2D plane measurement. The main aim of this work is to quantitatively use the RCF to determine the source position with high accuracy. Firstly, an algorithm is described and verified for the generation of TG-43-based relative dose rate maps. Then, the

source positional uncertainty of a single dwell position is evaluated based on this algorithm and EBT3 GAFCHROMIC™ film model dose measurements. Afterwards, the impact of the source positional uncertainty is investigated for a clinical case with multiple dwell positions. Once the positional uncertainties have been studied, the source tracking model is introduced based on 1D and 2D approaches. Blob analysis[34] was used to relate different features of the measured isodose lines to a library of reference features based on TG-43 formalism. Also, digitization issues that might affect dosimetry in the presence of high dose gradients are addressed. Finally, the application of the source tracking model is presented for RCF dosimetry discussing its possible advantages and limitations.

6.2 Materials and Methods

6.2.A HDR source positional uncertainty

The dosimetric effect of source positional uncertainty was quantified and verified for different catheter sizes typically used in superficial and interstitial HDR brachytherapy. The source used throughout this study is the mHDR-V2 HDR Iridium 192 (^{192}Ir) controlled by a microSelectron V3 after-loader unit (Elekta, Veenendaal, Netherlands). The source positional uncertainty in this case refers to the possible variation of the actual source position with respect to the nominal central source position that is assumed in the treatment planning process. First, in order to estimate the dose rate variation at a plane away from the source, a coordinate system is defined (Sec 6.2.A.1). Then, according to this coordinate system, an algorithm is described to generate dose rate distributions based on AAPM TG-43 formalism which was used to estimate the dosimetric impact of source positional uncertainty for different catheter sizes (Sec 6.2.A.2). This dosimetric impact is then verified experimentally with EBT3 RCF dosimetry for a single source dwell position (Sec 6.2.A.3), and for multiple dwell positions of a clinical case (Sec 6.2.A.4).

6.2.A.1. Coordinate system definition

In this work, two coordinate systems were defined for the purpose of establishing the tracking model and for measurements (See Figure 6.1a). The first system is the source coordinate system (x', y', z') where the source center represents the origin of the system. This is used mainly to calculate TG-43 dose rate maps away from the source where the distance between the origin and

each pixel in the calculation plane is known. The second one is the phantom coordinate system (x, y, z) where the origin is at the nominal first dwell position within the catheter. This system is mainly for the measurement setups. For simplicity, both systems were defined using the Cartesian coordinate system. The source is assumed to be in full scattering conditions, as per the TG-43 report, and the phantom shape is assumed to be cubical. For both systems, the x- or x'- axis is the axis of the catheter or the source with the positive direction as the direction away from the after-loader unit; the positive y- or y'- axis refers to the transverse bisector of the nominal first dwell position or the source in a plane parallel to the phantom "coronal" plane; the positive z- or z'- axis refers to the transverse bisector of the nominal first dwell position or the source in a plane parallel to the phantom "sagittal" plane. Depending on the coordinate system, the 3D source orientation is defined by $\theta_{x'}$, $\theta_{y'}$, $\theta_{z'}$ (or θ_x, θ_y, θ_z) where these are the rotations around the x'-, y'-, z'- (or x-, y-, z-) axes, respectively. The unit of both systems is "mm" and the default orientation is when the source is at the first dwell position within the catheter meaning that both origins are aligned *i.e.* $x = x'$, $y = y'$, $z = z'$ and all rotations are zero.

6.2.A.2. TG-43 model calculation

In order to estimate limits of possible dosimetric error associated with the source positional uncertainty, the spatial limits within typical clinical catheters should be determined. Three plastic catheter models (Elekta, Veenendaal, Netherlands) were included in this study: the 4F OncoSmart catheter, the 6F ProGuide needle, and the 6F Flexible catheter (Figure 6.1b, F: French where 3 French corresponds to 1 mm diameter). The inner dimension of each catheter was determined by fitting known-size industrial drill bits and the outer dimension was measured using a digital caliper. The dosimetric error limits at any distance away from the source (along z'-axis), were identified as the dose rate difference when the source is at the top or bottom sides with respect to the dose rate at the center of the catheter.

The 2D dose rate map at any plane away from the source was calculated using a script written in MATLAB (v.9.7, R2019b, Natick, MA) based on the AAPM TG-43 formalism. The source model fixed inputs, namely; the dose rate constant (Λ), the active length of the source (L), the radial dose function ($g(r)$), and the anisotropy function ($F(r, \theta)$), were imported from published consensus data of the mHDR-V2 HDR source.[7,8,35] Since the TG-43 model is based on polar coordinates, it requires knowledge of the distance to the source ($r_{i,j}$), in cm, and the

corresponding angle with respect to the source axis ($\theta_{i,j}$), in degrees, where i and j are the pixel indices of any given map and their values are $i, j \in \mathbb{Z}$ so that 0,0 represents the map center ($x' = 0$, $y' = 0$). To calculate the 2D dose rate map ($\frac{\text{cGy}}{\text{h}}$) of any plane away from the source based on the source coordinate system defined in Sec 6.2.A.1, $r_{i,j}$ and $\theta_{i,j}$ of each pixel must be calculated. To do this, some information must be set *a priori*. This includes the required map dimensions (mm), the spatial resolution (*res*, in mm/pixel), $r_{0,0}$ (cm), $\theta_{x'}$, $\theta_{y'}$, $\theta_{z'}$ (degree) and the source strength (S_k, $\frac{\text{cGy}\cdot\text{cm}^2}{\text{h}}$). The 3D rotation transformation $R_{x'y'z'}$ is applied to the required map plane rather than the source, and it consists of the following:

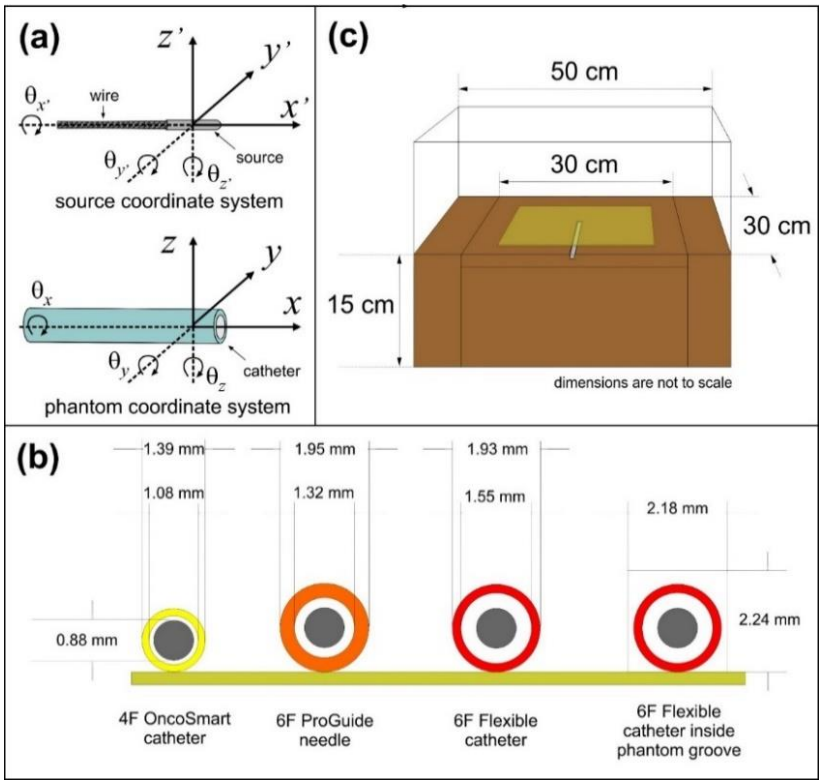

Figure 6.1: Geometric coordinate systems and setups. Dimensions are not to scale. a) coordinate systems used for this work: source coordinate system is used mainly for TG-43 calculations, and phantom coordinate system is used to describe the location of the film and the tracked source position for experimental setups. The default orientation is when the origins of both systems are aligned (source at nominal first dwell position) , b) sectional dimensions of different HDR brachytherapy catheters that are typically used in the clinic seen at the default orientation. Different Solid Water® (SW) slabs were grooved for 6F and 4F catheters in order to mitigate catheter movement, c) the SW phantom (30 × 50 × 30 cm^3) designed to satisfy TG-43 full scattering conditions for all dosimetry points of the EBT3 GAFCHROMIC™ film.

$$R_{x'y'z'} = R_{x'} * R_{y'} * R_{z'} \tag{6.1}$$

Where $R_{x'}$, $R_{y'}$, $R_{z'}$ are axis-specific rotations and they are defined as:

$$R_{x'} = \begin{bmatrix} 1 & 0 & 0 \\ 0 & \cos(\theta_{x'}) & -\sin(\theta_{x'}) \\ 0 & \sin(\theta_{x'}) & \cos(\theta_{x'}) \end{bmatrix}, R_{y'} = \begin{bmatrix} \cos(\theta_{y'}) & 0 & \sin(\theta_{y'}) \\ 0 & 1 & 0 \\ -\sin(\theta_{y'}) & 0 & \cos(\theta_{y'}) \end{bmatrix}, R_{z'} = \begin{bmatrix} \cos(\theta_{z'}) & -\sin(\theta_{z'}) & 0 \\ \sin(\theta_{z'}) & \cos(\theta_{z'}) & 0 \\ 0 & 0 & 1 \end{bmatrix} \tag{6.2}$$

where θ is converted to radians. The 3D rotation matrix is then applied to the *x'*-, *y'*-, *z'*- coordinates of the required map. These coordinates are defined in cm (for the purpose of TG-43 calculation only) as $x'_{i,j}, y'_{i,j}, z'_{i,j}$ where $x'_{i,j} = \frac{i \,.\, res}{10}$ (cm), $y'_{i,j} = \frac{j \,.\, res}{10}$ (cm), $z'_{i,j} = r_{0,0}$ (cm). The value of each pixel in $r_{i,j}$ and $\theta_{i,j}$ can now be calculated as:

$$r_{i,j} = \left\| R_{x'y'z'} * \begin{bmatrix} x'_{i,j} \\ y'_{i,j} \\ z'_{i,j} \end{bmatrix} \right\| \tag{6.3}$$

$$\theta_{i,j} = \cos^{-1} \frac{x'_{i,j}}{r_{i,j}} \tag{6.4}$$

At this point, all the inputs to the TG-43 model are known and the dose rate at each pixel can be efficiently computed in vectorized form.

6.2.A.3. Radiochromic film measurements

Radiochromic film dosimetry system

The RCF dosimetry system consisted of: (1) EBT3 GAFCHROMIC™ film model lot# 06181801 (Ashland Inc, Wayne, NJ), (2) EPSON scanner model 12000XL (Epson, Nagano, Japan), and (3) the dosimetry protocol developed in our previous work[36] including film handling procedures, calibration, scanning instructions, image analysis, dose and uncertainty calculation models. The film was calibrated in a 6 MV beam instead of calibrating it at HDR ^{192}Ir beam quality directly to a maximum dose of 40 Gy. The advantage of this approach is the avoidance of TG-43-associated uncertainties in dose calculation (3.4%, Table V, TG-138)[4] and positioning.[37] The film energy dependence (between megavoltage and ^{192}Ir beam qualities) was found to be negligible as was shown by Sarfehnia *et al*[38] for the EBT1 film model and Bekerat *et al*[16] for the EBT3 film model.

Phantom design

To experimentally verify the estimated dose rate variability in Sec 6.2.A.2, a phantom was constructed consisting of a 1 cm thick 30 × 30 cm^2 Solid Water™ (SW) slab with a 20 cm long groove at the center of the phantom. Two designs were implemented: one fitting the 4F OncoSmart catheter and the other for the 6F Flexible catheter. Although testing relative reproducibility does not require a TG-43-compliant geometry, the phantom was supported by at least 15 cm of SW around the source and any dosimetry point.[39] The final size of the phantom was 30 × 50 × 30 cm^3 (See Figure 6.1c). In a previous study,[37] it was shown using Monte Carlo simulations that the difference between dose-to-film (EBT2 film model) in SW and in water was minimal (0.9941 (1σ=0.07%)). Schoenfeld *et al*[40] also analyzed the use of water equivalent phantoms for ^{192}Ir brachytherapy and found that the maximum deviations of absorbed dose-to-water between SW and water for phantoms with 5 cm and 10 cm radii were -0.29% and -0.76%, respectively. Since these differences are small, the phantom was deemed TG-43-compliant, and we also assumed that the dosimetric differences between EBT2 and EBT3 film models for dosimetry in water and SW are insignificant since their elemental compositions are similar.

Film irradiation

Nine measurements were collected per catheter model with a single dwell position and a fixed dwell time. During these measurements, the film was positioned directly under the catheter so that the nominal distances between the source center (at the default orientation) and the film are 0.84 mm and 1.14 mm for the 4F and 6F catheters, respectively. Another set of five measurements were conducted at distance of 10 mm below the catheter using the 4F phantom only to evaluate the signal reproducibility. Since RCF is a passive dosimeter, one has to interpret the source positional uncertainty in light of other embedded uncertainties such as the timer uncertainty and the achievable dosimetric uncertainty of the film itself. The timer linearity and dwell time uncertainty were evaluated in a well-type ionization chamber (HDR-1000 plus, Standard Imaging, WI) at the position of maximum measured signal for three dwell times: 2 sec, 5 sec, and 10 sec; ten measurements were taken for each dwell time.

6.2.A.4. Clinical impact of HDR source positional uncertainty

The dosimetric impact of source positional uncertainty for a typical clinical case with multiple dwell positions and channels may be overestimated when evaluated in lieu of a single dwell position. For completeness, a more realistic clinical evaluation of this uncertainty was conducted. One selected case of Freiburg Flap (FF) based surface brachytherapy (17 catheters, 9 cm × 8 cm loading, 171 dwell positions) was delivered five times in a SW phantom. One EBT3 film sheet was positioned right below the FF (5 mm nominal distance to source) and another sheet was positioned 3 mm below the FF (8 mm nominal distance to source). For the repeats, care was taken during the positioning of the film sheets to make sure they were always placed at the same location within the phantom with respect to the applicator. Specifically, point marks were drawn on each corner of the film sheet and they were reproduced at the same positions for all film sheets. These point marks helped in image registration of the repeats. The corners of the film sheet were also marked on the phantom at 5 mm distance from the source to reproducibly place the films on the same position within the phantom. These marks were matched at 8 mm distance to source as well with respect to the phantom edges. Finally, marks to relate the applicator to the phantom were also drawn on the phantom surface and all SW pieces were aligned using a plastic base with four edges that tightly keeps the SW in place.

6.2.B Source tracking model

If the spatial and temporal information of the source are known, then an accurate 2D dose measurement at any plane away from the source can accurately recover its strength (S_k) and confirm its dose rate distribution with respect to TG-43 data. The idea of the source tracking is based on the fact that each dose rate map away from the source has unique features that are specific to a single source positional and orientational information (x', y', z', $\theta_{y'}$, $\theta_{z'}$). These features will be defined and exploited so that a model can be created based on TG-43 calculations for source tracking. The use of this model for tracking the source with RCF (*i.e.* determining x, y, z, θ_y, θ_z) would be based on the measured version of these features. Since the source is assumed to be cylindrically symmetric in the TG-43 formalism, $\theta_{x'}$ can be chosen arbitrarily (e.g., $\theta_{x'} = 0$, which makes $R_{x'}$ the unit matrix). In this section, two approaches will be discussed: (1) 1D approach where some features of a dose rate profile could be used for source tracking, and (2) 2D approach utilizing different features of a dose rate map.

6.2.B.1 Features of a 1D dose rate profile

The TG-43-based MATLAB script described in 6.2.A.2 was used to generate *x'*- profiles at different distances away from the source. Different fitting models (*Gauss*, *Lorentz*, *Pearson VII*) were examined to fit these profiles at *z'*={2, 5, 10, 20, 40} mm. After these fits were obtained, the distance to the source was plotted as function of the full width at half maximum (FWHM) of the TG-43-profiles and a mathematical relationship was derived between them.

6.2.B.2 Features of a 2D dose rate map

As indicated in Sec 6.2.A.2, any 2D dose rate map (or simply, a map) away from the source can be calculated using the TG-43-based MATLAB script. After the map is obtained, the first step is to find the maximum dose rate position and to normalize the map to it. Once this is done, different relative "isodose" lines (IDLs) can be identified. It is the shape and measurements (blob analysis) of these contours that form the basis of the "source features" in this study. For any IDL at a given x', y', z', $\theta_{x'}$, $\theta_{y'}$, $\theta_{z'}$, this includes: *area*, *perimeter*, *centroid*, *orientation*, and *circularity*. *Orientation* refers to the angle between the major axis of an ellipsoid that can be fit within the IDL contour and the *x'*-axis. *Circularity* is defined as $\frac{4 \cdot area \cdot \pi}{perimeter^2}$. *Centroid* refers to the IDL center of mass. Two additional *centroid*-based features were defined: a high-IDL weighted *centroid* ($centroid_H$) and a low-IDL weighted centroid ($centroid_L$). Afterwards, the Pearson correlation coefficients (PCC) between these features and each source coordinates (x', y', z', $\theta_{y'}$, $\theta_{z'}$) are computed. For each significant correlation (PCC>0.95), a mathematical model is used to best fit the relationship between the IDL feature and the deemed positional parameter.

For the purpose of model development, it is assumed that the TG-43-based MATLAB model produces "noise-free" maps and therefore no noise-filtration is required at this stage. Therefore, the position of the maximum dose rate pixel can be taken as-is. Each IDL is selected through a process of thresholding and binarization based on connected pixels that has the same integer pixel values. After the IDL is identified, the image is cropped to fit only the IDL and the "region properties" function of the MATLAB Image Processing tool box (9.7.0.1261785 (R2019b) Update 3) is used to get the sought features. To increase the time efficiency, the size of the map was always modified to get the IDL contours down to 1%. The maximum *z'* set for this evaluation was 30 mm. Based on geometry of a 6F catheter and the source dimensions, the

maximum possible values for $\theta_{y'}$ are between -15 to +15 degrees and therefore its value was limited between these angles.

6.2.C Source distribution digitization uncertainties

HDR brachytherapy retains its dosimetric uniqueness because of the high-dose-gradient that can be achieved near the source.[41] For measurements with RCF, the digitization choices such as scanning resolution, size of region-of-interest (ROI), as well as image processing choices such as the noise-filtration method and its size might be impacted by this high-dose-gradient. Therefore, in this section, the TG-43-based MATLAB script described in Sec. 6.2.A.2 is used to characterize the effect of resolution, ROI size and noise-filtration on the reported dose rate maps.

6.2.C.1 Resolution and Size of Region-of-Interest (ROI)

As indicated in Sec 6.2.A.2, the resolution can be set by the user in the model. In this study, the selected resolutions reflect typical scanning resolutions used in our RCF dosimetry protocol including resolutions of 127 dpi and 254 dpi which correspond to 0.2 mm/pixel and 0.1 mm/pixel, respectively. For each resolution, maps were created at z'={2, 5, 10, 20} mm distances to source. The effect of digitization resolution on reported dose was checked in two ways: 1) when selecting an ROI of a certain size rather than a "pixel" to report the reading corresponding to the source center, and 2) when selecting size of the noise-filter, as will be explained in Sec 6.2.C.2.

6.2.C.2 Noise and filtration

The tracking model explained in Sec. 6.2.B. should be tested at realistic noise levels. Typical noise associated with RCF dosimetry was estimated to be *Gaussian*.[42] Therefore, the use of a Wiener filter (0.5×0.5 mm^2) was shown to be effective in removing the noise while preserving the pixel value information.[11] The goal in this section is to evaluate the combined effects of high-dose-gradient and the choice of filter size. For different filter sizes (W={3, 5, 7, 9, 11, 13, 15} pixel) and different distances to the source (z'={2, 5, 10, 20} mm), the maximum dose rate from the filtered image will be normalized to the maximum dose rate from the noise-free image. This will be tested at different resolutions (*res*={0.1, 0.2} mm/pixel). The noise is assumed to be *Gaussian* and it is added to the noise-free calculated images. For the selected resolution and filter

size, a profile comparison will be made at different *z* between the noise-free, added noise, and filtered profiles.

6.2.D Source tracking with radiochromic film dosimetry

Using the same SW phantom described in Sec 6.2.A.3, six EBT3 model film pieces were exposed simultaneously using a single dwell position that was delivered at the center of the phantom. Three of the film pieces were below and other three pieces were above the catheter. The thicknesses of the SW slabs were measured by a digital caliper taking into account the catheter groove dimensions as well as the film thickness. The film nominal positions were: *z* = {-19.98, -14.70, -9.42, 6.43, 11.71, 22.27} mm. After the relative IDL maps were recovered from these films, the tracking model was applied to estimate the distance between the films and the source.

6.3 Results

6.3.A HDR source positional uncertainty

6.3.A.1 Verification of the TG-43 model implementation

Figure 6.2 shows 2D maps of the distance to source ($r_{i,j}$), the angular distribution ($\theta_{i,j}$), and the resulting relative TG-43 dose rate distribution from the MATLAB script. Two different distances to the source (z={1,10}mm) and source angles (θ_y={0,15}deg) were chosen to visually illustrate their effect on the corresponding maps.

6.3.A.2 Source positional uncertainty: TG-43 calculations and film measurements of single dwell position

For different catheter sizes, Figure 6.3 summarizes the source positional uncertainty of a single dwell position using the MATLAB script of TG-43 formalism at different distances to the source (Figure 6.3a) and repeated EBT3 model film measurements at the catheter surface (i.e. distance to the film center, Figure 6.3b). The maximum recorded dosimetric variations in the RCF measurements at the surface of the 4F catheter and at the distance-to-source of 10 mm were 36.1% and 2.6%, respectively. Figure 6.3c shows the dose gradient at the surface of the catheters. The total uncertainties in the RCF dosimetry system and the timer accuracy were 2.0% and 1.1%, respectively.

6.3.A.3 Clinical impact of HDR source positional uncertainty

The average dose measured by the EBT3 film model is displayed in the left panel of Figure 6.4 for the two selected distances to the source. The per-pixel relative standard deviation of the five repeated measurements normalized to the maximum dose within the image is shown in the middle panel. For the highlighted dwell position (red square, left panel), the right panel shows the 80% IDL (normalized to max per image) of each film set. Table 6.1 shows the dwell position accuracy and the IDL measurements (perimeter and area) with respect to the first film which is taken as a reference (Set #1).

Table 6.1: Dimensions of the 80% isodose line (IDL) of each blob in right panel of Figure 6.4.

Distance to source (mm)	Set #	Centroid displacement from the 80% IDL centroid of Set #1 (mm)	Area of the 80% IDL (mm^2)	Perimeter of the 80% IDL (mm)
5	1	0.00	21.19	16.22
	2	0.46	19.07	15.42
	3	0.23	21.67	16.37
	4	0.67	23.12	16.98
	5	0.16	21.16	16.31
8	1	0.00	109.68	43.07
	2	1.06	81.61	33.96
	3	0.46	105.78	41.51
	4	0.97	103.70	39.36
	5	1.08	115.05	45.67

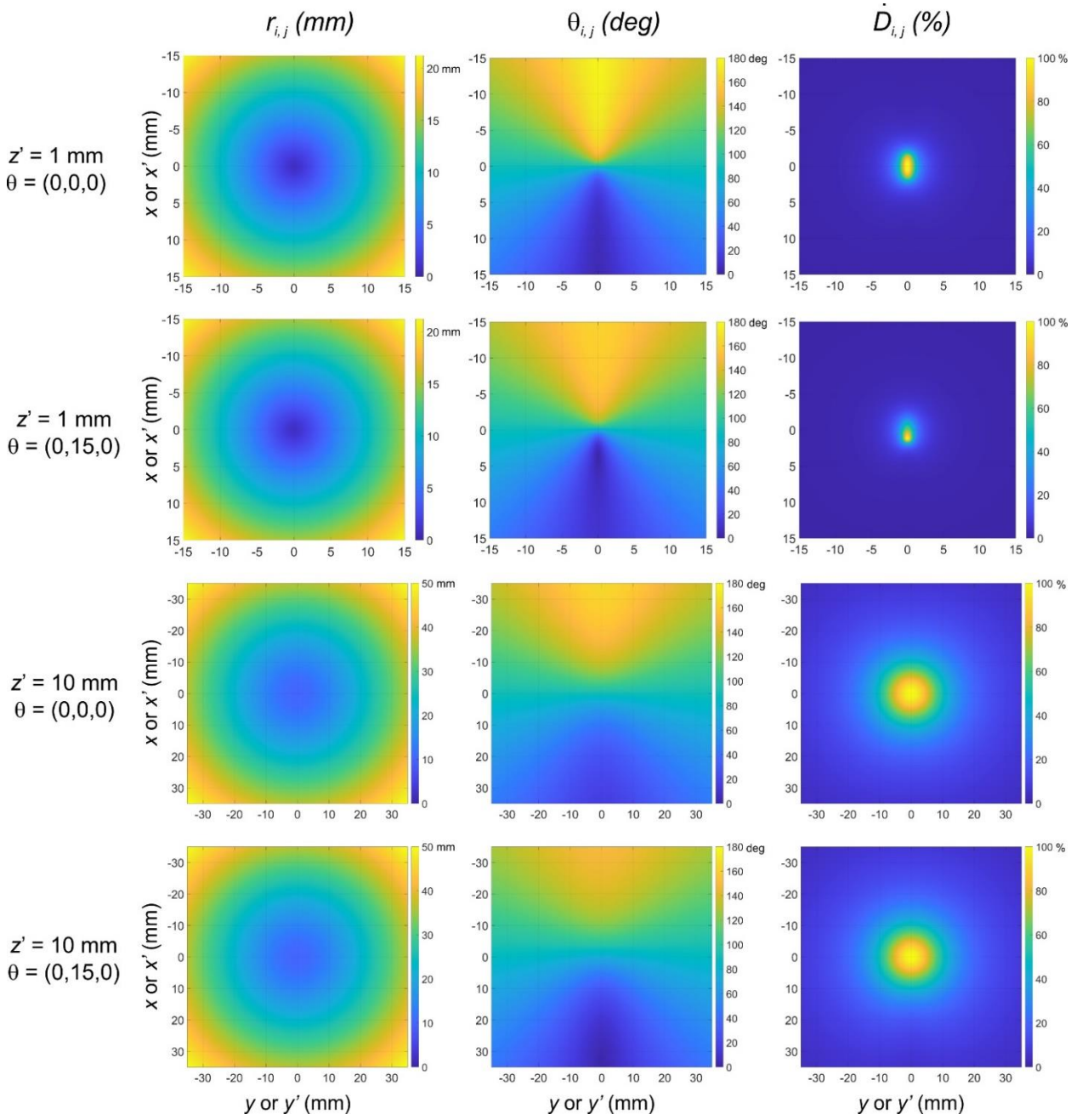

Figure 6.2: The AAPM TG-43 protocol implementation in MATLAB. Left panels show the distance to source ($r_{i,j}$), middle panels show the angular distribution ($\theta_{i,j}$), and right panels show the relative dose rate distributions ($\dot{D}_{i,j}$). Four different geometries are shown to highlight the impact on the individual 2D maps. Pixel size for all maps is 1 by 1 mm^2. The unit of the abscissas and ordinates of all images are "mm" and the units of the pixels are "mm", "deg", or "%" for the left, middle or right panels, respectively.

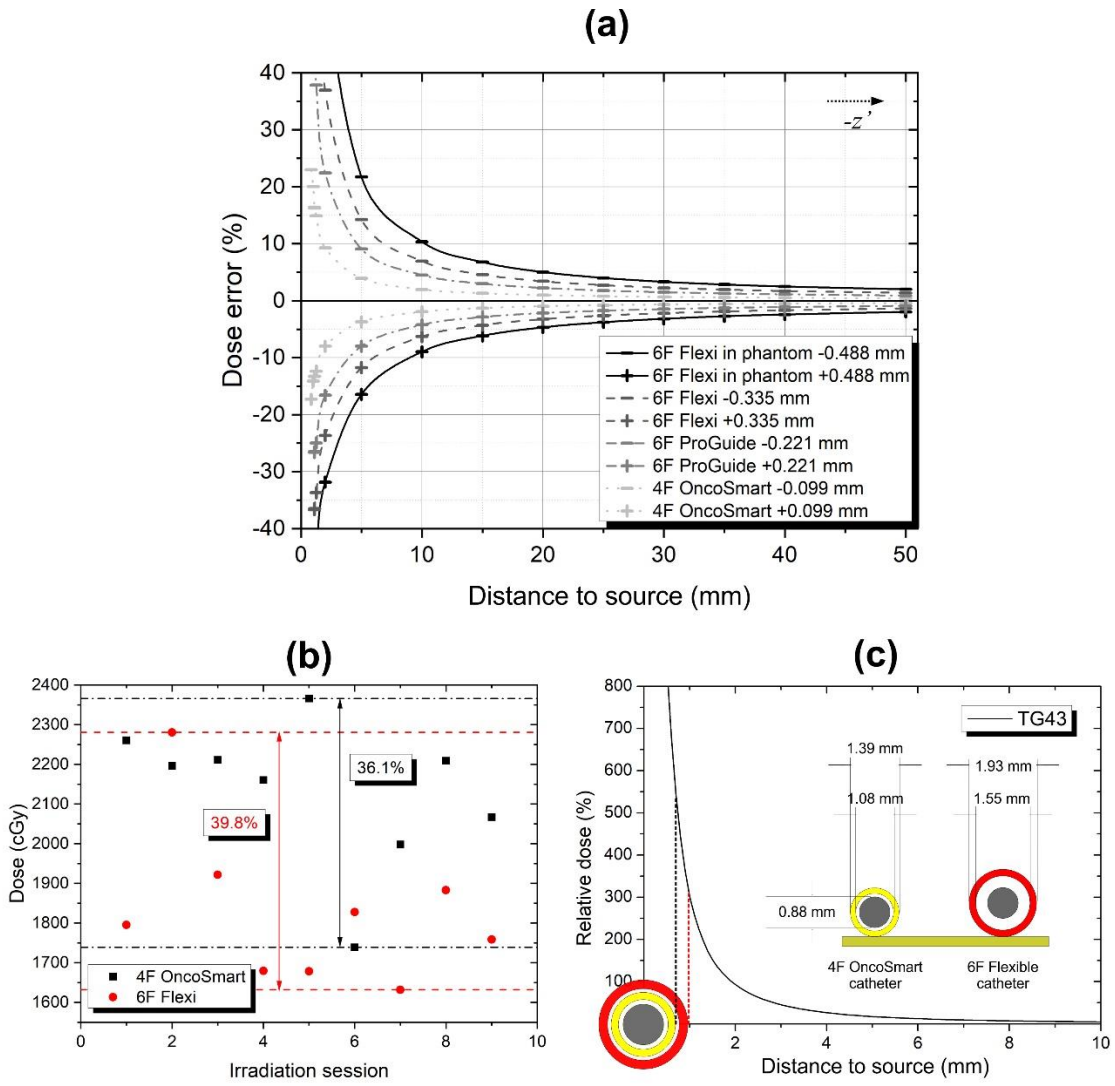

Figure 6.3: The HDR Ir^{192} source positional uncertainty of a single dwell position. (a) limits of the dosimetric error based on the AAPM TG-43 protocol calculations for different catheter geometries, (b) experimental confirmation of source positional uncertainty of a single dwell position repeated nine times, (c) demonstration of the surface dose gradient difference between the 4F and 6F catheters.

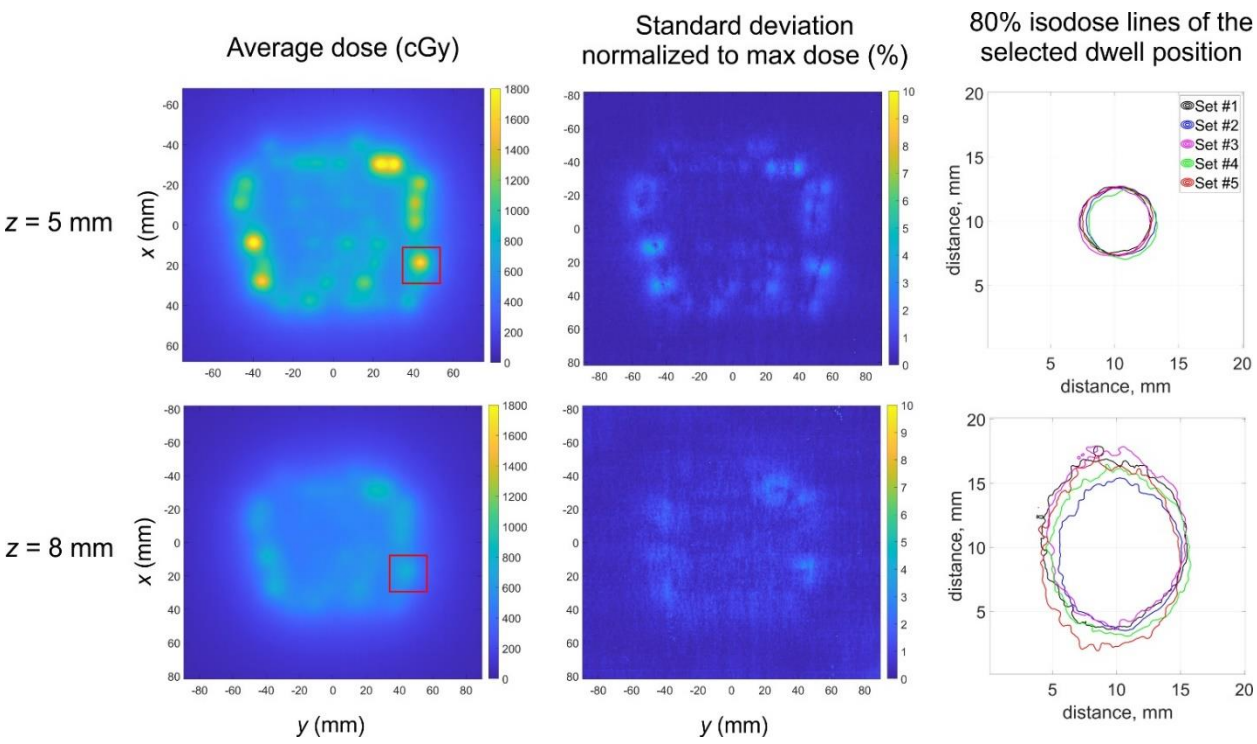

Figure 6.4: Impact of HDR ^{192}Ir source positional uncertainty on a clinical surface brachytherapy case. At two different distances to source (5 mm and 8 mm, exposed simultaneously): the left panel shows the average dose map of five repeated EBT3-film based dose measurements, middle panel shows the per-pixel standard deviation of these repeats normalized to the maximum dose within the image, left panel shows the 80% isodose lines of a selected dwell position (red squares, right panel) from the five film images.

6.3.B Source tracking model

6.3.B.1 Features of 1D dose rate profile

Figure 6.5 shows the results of fitting different models (6.5a: *Gauss*, 6.5b: *Lorentz*, 6.5c: *Pearson VII*) to the TG-43 reference data as extracted by the MATLAB script. Figure 6.5d shows that the relationship between the distance to source and the FWHM is linear. This linear model has the form [depth (mm) = 0.524 × FWHM (mm) - 0.322] and can be used to predict the distance between the source center and the measurement plane based on the FWHM which can be used in source tracking.

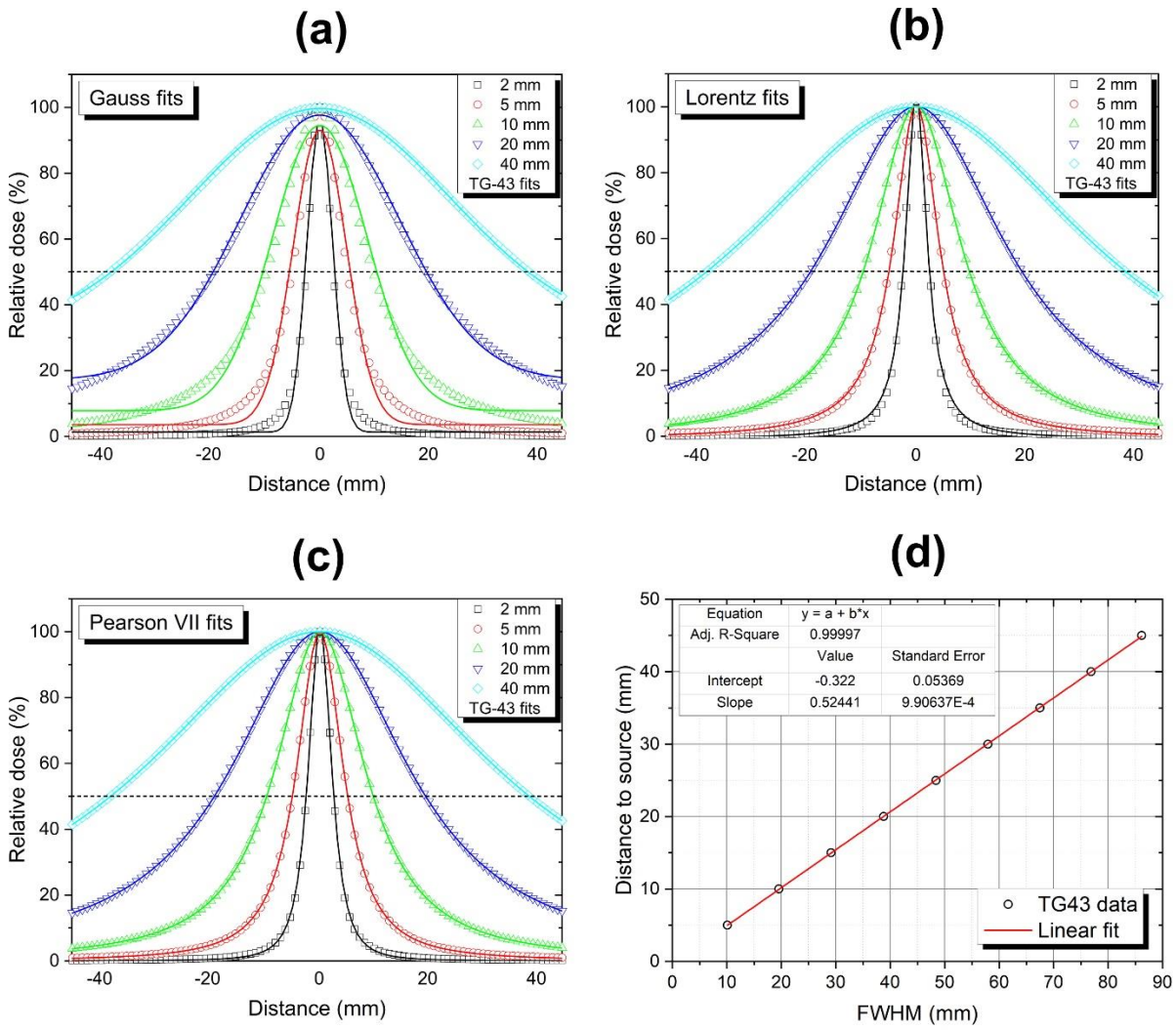

Figure 6.5: Relative dose profiles at different distances away from the HDR source based on the AAPM TG-43 protocol data of the mHDR-V2 source: (a), (b) and (c) show data fitting with different models: *Gauss*, *Lorentz* and *Pearson VII*, respectively. (d) Linear fit of the distance to source as a function of the full width at half maximum (FWHM).

6.3.B.2 Features of 2D dose rate map

Isodose line dimensions and shapes

Based on the TG-43 MATLAB model, Figure 6.6 demonstrates the IDL dimensions and shapes at two different distances to the source (z={1,10}mm) and source angles (θ_y={0,15}deg). The dimensions of these IDLs are significantly different and they can be used to determine the source positional information. Figure 6.7 shows the results of analyzing the IDL features. In particular,

left panel of Figure 6.7 shows the area, perimeter and circularity of these IDLs at (θ_y= 0 deg), while the right panel shows the same information for (θ_y= 15 deg).

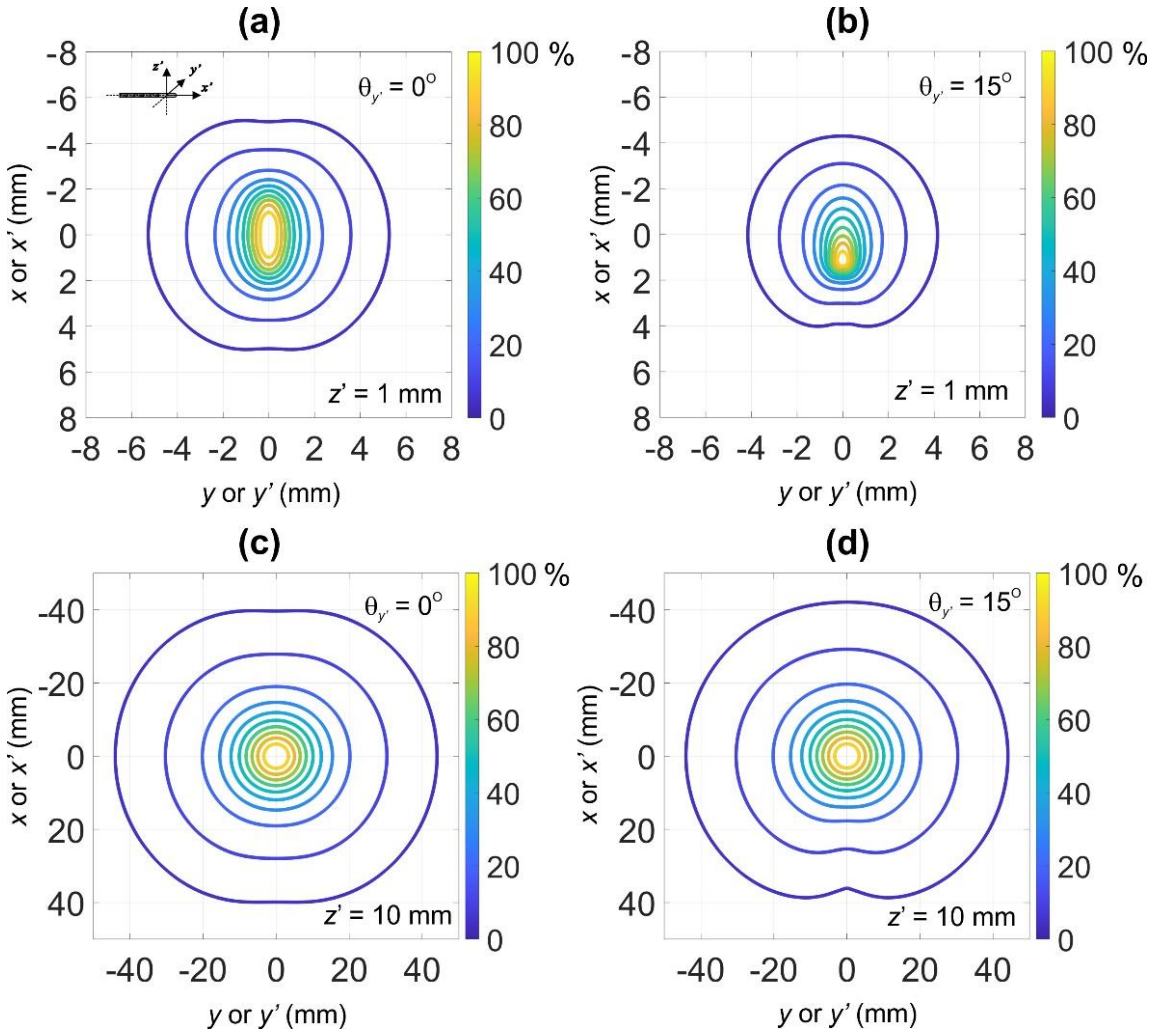

Figure 6.6: Dimensions and shapes of the HDR source isodose lines at different distances away from the HDR source based on the AAPM TG-43 protocol data for the mHDR-V2 source.

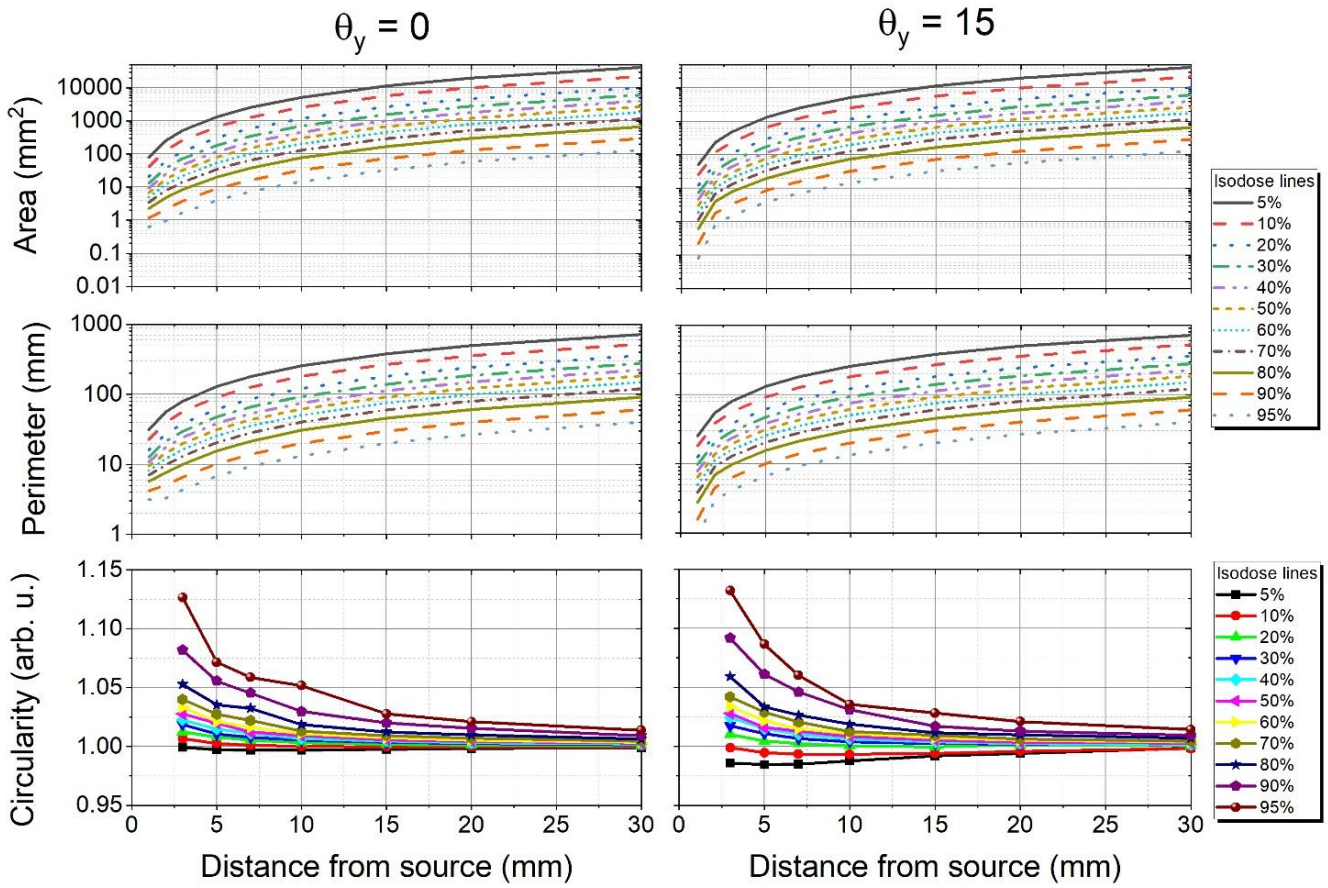

Figure 6.7: Variation of 2D features of the HDR source isodose lines: area, perimeter and circularity, with respect to the distance to the source for θ_y= 0 deg (left panel) and θ_y= 15 deg (right panel).

Tracking the source center and orientation

Different metrics were used to determine the source center (*x, y*). Figure 6.8 shows the localization performance of these metrics for different source angles (θ_y) and distances to source in a noise-free environment. The performance is evaluated in terms of the localization error i.e. the displacement between the actual source center and the predicted one based on the given metric. Figure 6.9 shows the impact of different noise levels on the performance of these metrics in localizing the source center. Figure 6.10 on the other hand, shows the source orientation prediction (θ_z) accuracy based on the shape of different IDLs. The data shows that beyond 5 mm, the source orientation is difficult to obtain because of the increased IDL circularity.

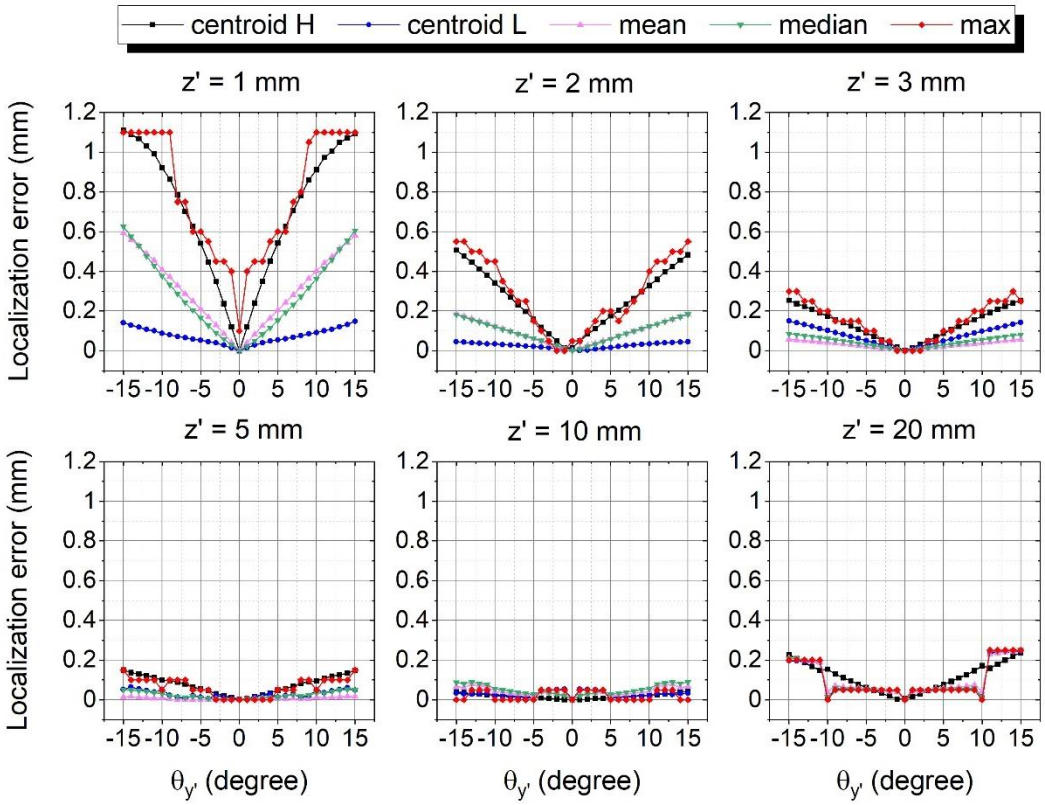

Figure 6.8: Finding the HDR source center (*x*, *y*) at different distances to source based on different dose distribution features: weighted centroids (H for high isodose lines, L for low isodose lines), mean dose, median dose, and max dose.

6.3.C Source dose distribution digitization uncertainties

6.3.C.1 Resolution and Size of Region of Interest (ROI)

Dose profiles closer to the source have higher dose gradients as seen in Figure 6.5. When selecting an ROI around the source center, the size of the ROI was found to have a significant impact on reported dose. This is demonstrated in Figure 6.11 at two different resolutions that are typically used by our lab in RCF dosimetry (127 dpi or 0.2 mm/pixel and 254 dpi or 0.1 mm/pixel). The effect of the resolution seems to be minimal in this geometry.

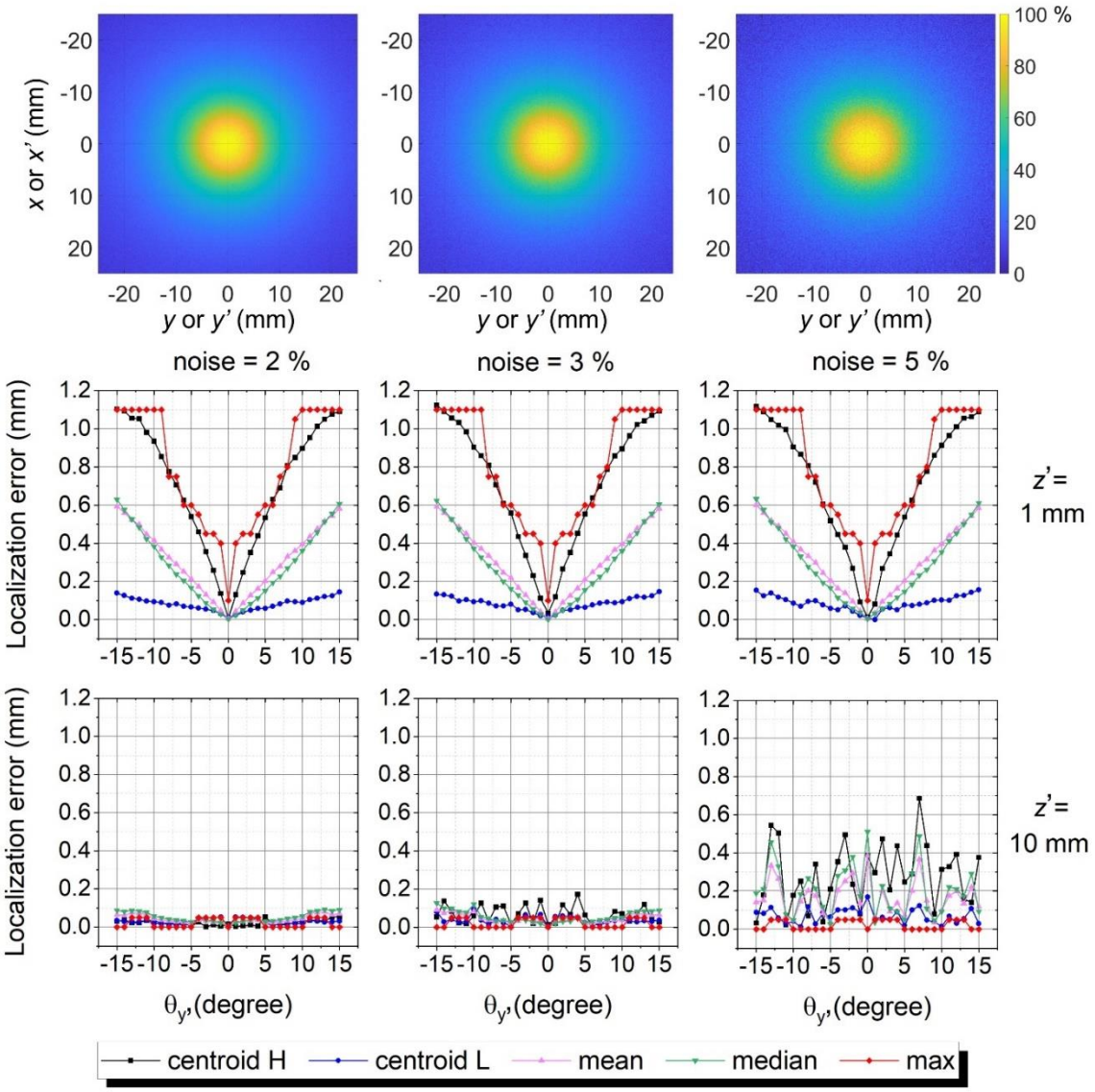

Figure 6.9: Effect of noise on the accuracy of the source center determination at three different noise levels: 2% (left panel), 3% (middle panel), and 5% (right panel). Top figures are dose maps at z=10 mm and they are provided to visualize the noise only.

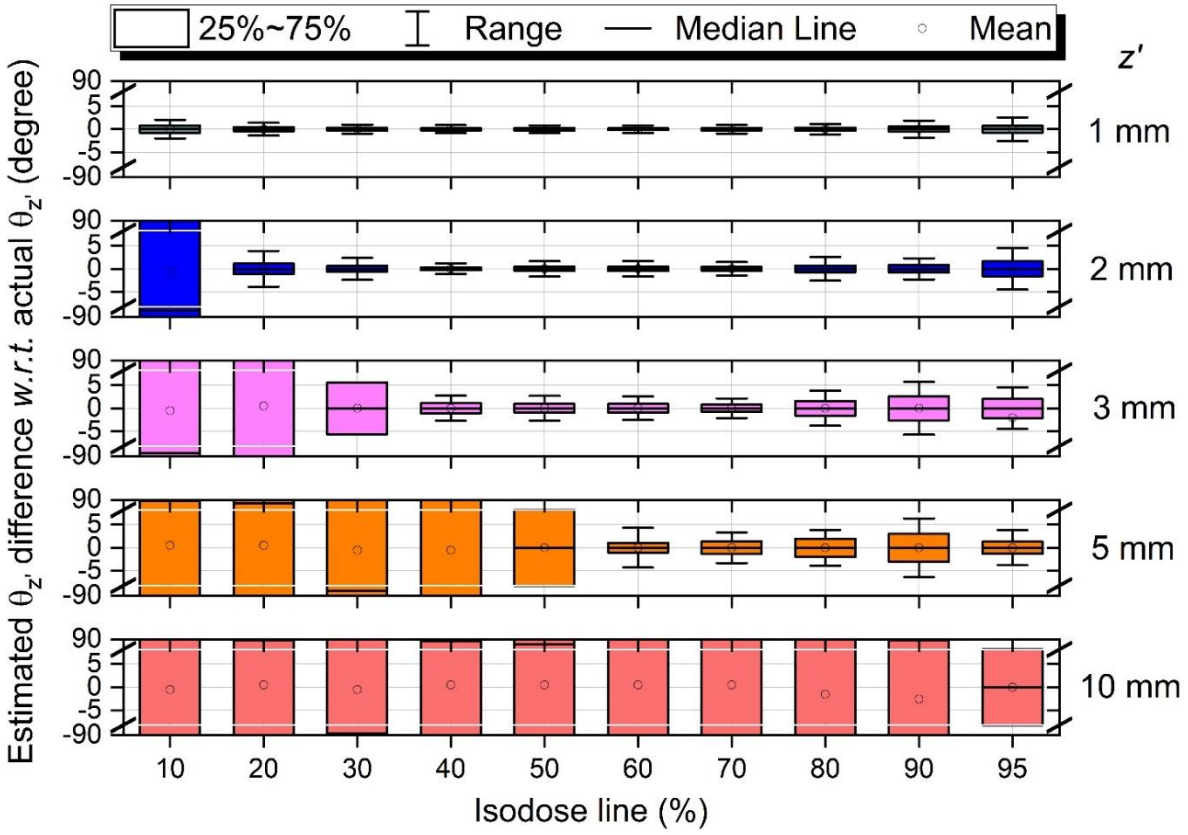

Figure 6.10: Model performance in finding the source orientation θ_z from different isodose line levels, at different distances to the source. Beyond 5 mm, it is not possible to determine the orientation of the source irrespective of the IDL level.

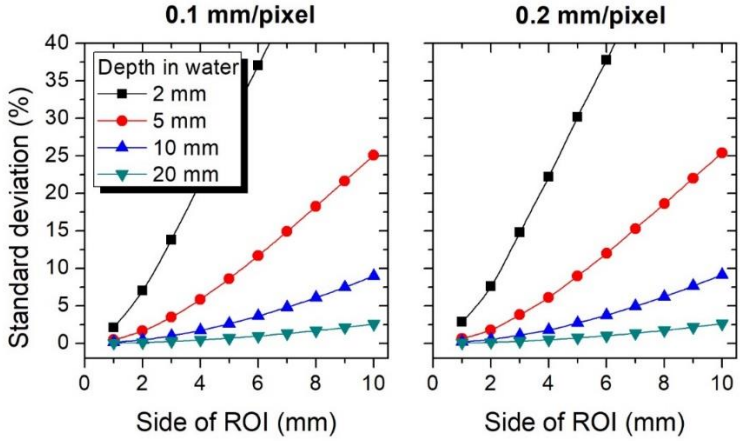

Figure 6.11:Effect of choosing different size regions of interest (ROI) on the standard deviation of dose within the ROI. Data are shown for different distances to the HDR source and digitizing resolutions. The data are generated from the AAPM TG-43 protocol based MATLAB model.

6.3.C.2 Noise and filtration

The effect of the Wiener filter size on the reported dose at different dose gradients (i.e. distances to source) is reported in Figure 6.12 (left panel). Right panel shows the effectiveness of the filter in removing intentionally-added noise. For a selected filter size (5 by 5 pixel^2) and resolution of 0.1 mm/pixel (corresponding to 0.5 by 0.5 mm^2), Figure 6.13 shows that this filter size effectively recovers the dose profiles at different distances from the source.

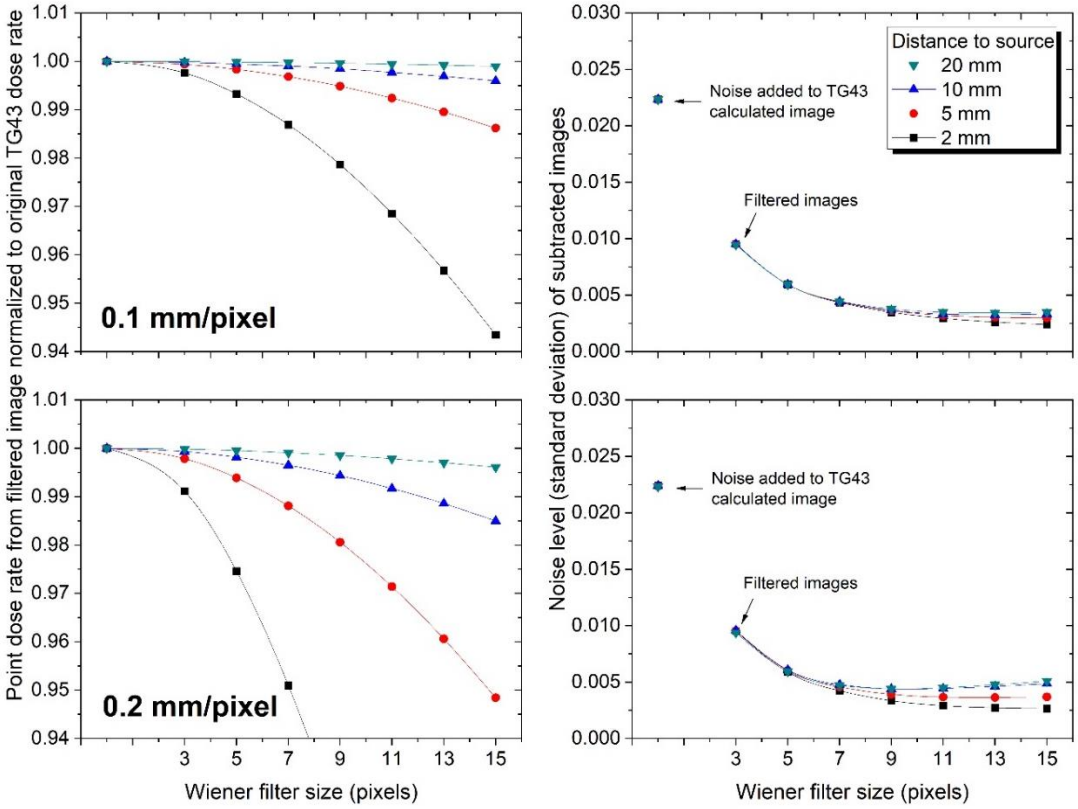

Figure 6.12: Effect of Wiener filter size on the dose reading in noise-free data (left panel), and on noise reduction in data with added noise (right panel). Data are shown for different distances to source and digitizing resolutions. The noise-free data are generated from the AAPM TG-43 protocol based MATLAB code.

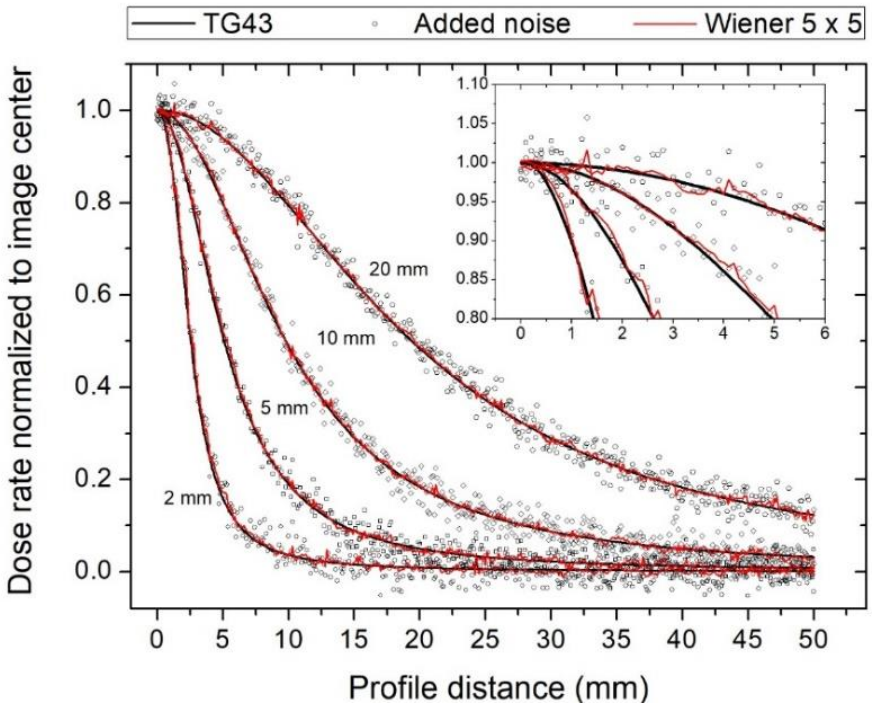

Figure 6.13: Noise reduction performance of a 5 by 5 pixel^2 Wiener filter applied to noisy dose rate profiles (red lines). Symbols show the noise added to the noise-free profiles (black lines). Data are shown for different distances to source. The digitizing resolution is 0.1 mm/pixel.

6.3.D Source tracking with radiochromic film dosimetry

Figure 6.14a shows the results of using the EBT3 RCF model in obtaining the 2D dose maps with acceptable noise level (compare to Figure 6.9). The relative IDL of this 2D dose map is converted into a curve and compared with the TG-43 reference library (Figure 6.14b). The example here shows the results of the film piece that is nominally 6.43 mm away from the catheter center. For the other film pieces, the differences between the estimated distance to the source and the nominal distances were Δz = {-0.35,-0.27, -0.22, 0.15, 0.18, 0.25} mm. Interestingly, both film sets i.e. below and above the catheter, indicated a source position within the catheter that is at the bottom (on average, -0.24 mm from the nominal center). The measured positional errors (*w.r.t.* center of the catheter) from the film sets below and above the source were 0.29 mm and -0.19 mm, respectively.

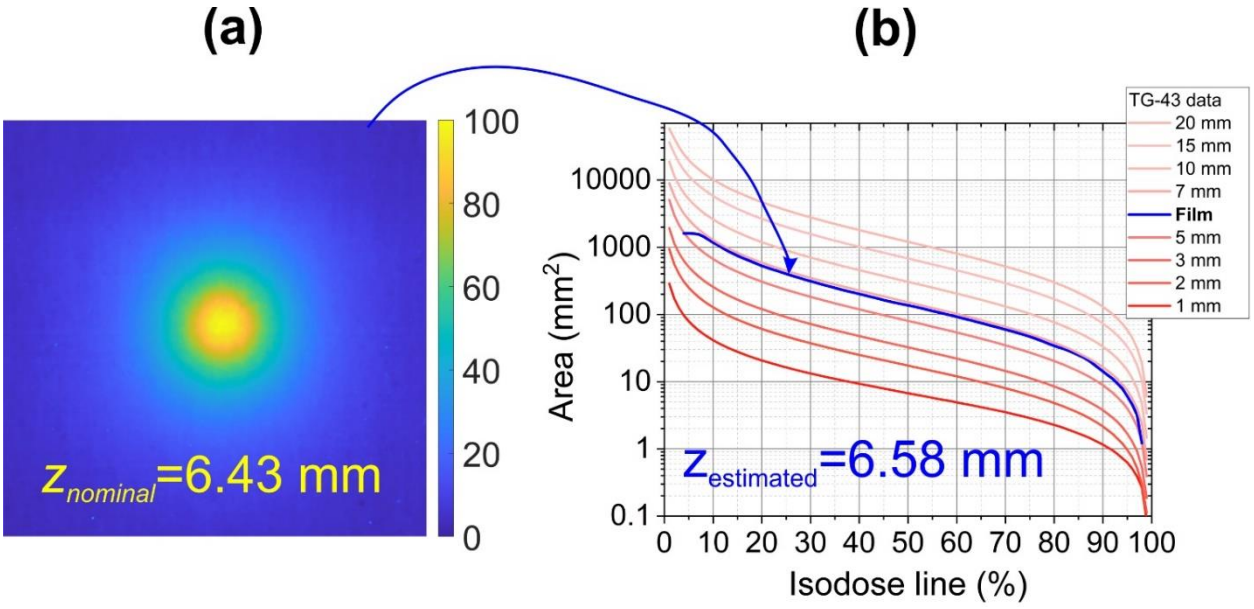

Figure 6.14: Using the source tracking model with a dose map measured by the EBT3 GAFCHROMIC™ film model. The measured dose map (a) is converted to a curve (b) and compared to the AAPM TG-43 protocol reference library of the isodose lines area in this example.

6.4 Discussion

6.4.A Impact of source positional uncertainty

In order to quantify the limits of the source positional uncertainty, a reliable and fast routine should be developed to generate 2D dose maps at any given source-to-detection plane geometry. Therefore, a validation is necessary of the inputs and the mechanics of this model since the data generated from it provide the basis of the source positional uncertainty estimation and the source tracking model as well. Figure 6.2 presented some examples of this vectorized routine at different geometries. Since this model is based on TG-43 data and formalism, the routine output was revised and verified against hand calculations of the reference data at many other geometries (spot-checks). It is also important to mention that the interpolation/extrapolation of the TG-43 datasets was carried out according to the High Energy Brachytherapy Source Dosimetry (HEBD) Working Group recommendations (Table III).[8] Additionally, it has to be noted that the routine does not take into account the material of the catheters, which was investigated in the literature and found not to have a significant effect on the calculation accuracy for plastic catheters.[43]

Although the major component of the source positional uncertainty seen in Figure 6.3a originates from the inverse square law, the use of line-source geometry over a point-source approximation in TG-43 calculation provides more accurate estimation of this uncertainty. Nevertheless, these results should be viewed in line with the uncertainties associated with TG-43 dose calculation (3.4%, Table V, TG-138)[4]. This figure shows that the impact of source positional uncertainty is significantly high at the surface of the catheters irrespective of the catheter size. The dosimetric error was demonstrated to be around 40% when close to the source. This was verified experimentally with EBT3 RCF dosimetry at the surface of the 4F and 6F catheters as was seen in Figure 6.3b. The maximum detected variation was 36.1% for the 4F catheter while it was 39.8% for the 6F Flexi catheter. The experimental results matches well with the calculations in Figure 6.3a. This also confirms that the source could be anywhere within the catheter diameter because of the competing effects of the gravity and the stiffness of the source-to-cable connection. While the dosimetric error from the source positional variation was expected to be less for the 4F catheter, the higher dose gradient (shown in Figure 6.3c) explains the persisting dose variation since the distance between the source and the film is smaller. The impact of source position variation within different catheter sizes was found to be significant (>5%) for depths of less than 5 mm and 10 mm for 4F and 6F catheters (all configurations in Figures 6.1b, 6.3a), respectively.

The reported results in Figure 6.3 were for a single dwell position and it can be argued that the dosimetric effect of the source positional uncertainty maybe exaggerated in a clinical setting with multiple dwell positions. Although the dosimetric impact of this positional uncertainty may be minimal for interstitial applications, it may have an impact on the dosimetric accuracy of surface brachytherapy. To answer this question, Figure 6.4 shows that such uncertainty is still considered to be acceptable (middle panel). The standard deviation was normalized to the global maximum dose in a similar manner to typical patient specific quality assurance of intensity modulated radiation therapy plans. Additionally, a histogram of the differences between the per-pixel recorded dose of film#1 and the dose of the same pixel location of the other repeat films normalized to the global max dose showed that the percentage variation is well within ±2.5% at the 95% confidence level at both distances to source (5 mm and 8 mm). The results of Figure 6.4 are highly dependent on the quality of dose image registration between the five repetitions. To demonstrate this, the right panel of Figure 6.4 shows the 80% IDLs of a selected dwell position from five images. The centroid of these IDLs seems to be well within 1 mm with respect to

film#1 at the distance of 5 mm (Table 6.I). One film set (#2) showed significantly smaller IDL dimensions in terms of area and perimeter at both distances to source indicating that the source may have been slightly further in this case. The results in Table 6.I for 8 mm are provided for completeness only because the centroid positions were highly affected by the dose components of the preceding and following dwell positions.

6.4.B Performance of the source tracking models

Two approaches, 1D and 2D, were discussed in this work for source tracking. Different features of dose profiles (1D approach) and isodose lines (2D approach) were exploited to set the basis of the tracking models. The FWHM of a dose profile was found to be in linear relationship with the distance to the source center and acquiring the dose profile was the only requirement for this technique (Figure 6.5). Film dosimetry seems to be the natural choice for such task and, in order to avoid the effect of noise and spikes on the correct recovery of dose profiles, it was found that a Pearson VII model can be used to fit the measured data in order to acquire the FWHM. For example, a film exposed at a caliper-measured distance of 10.93 mm away from the source reported a dose profile with a FWHM of 21.49 mm (film data) and 21.41 mm (fitted data) which correspond to 10.94 mm and 10.90 mm, respectively. Although the source tracking model with the 1D profile seems to yield accurate distances to source, its performance is limited to finding "z" only. Strictly, even determining the value of z is dependent on the noise level and the fact that the profile actually passed through the dose distribution center. Therefore, a 2D approach would be more reliable and logical.

The dimensions and shapes of the isodose lines were found to be sensitive to the distance to the source. Instead of utilizing the FWHM only (50% IDL in 2D), most of the IDLs could be utilized for the purpose of source tracking. The requirement in this case is that the dose map is normalized to the maximum value within the map. In that way, the measured IDLs features could be compared to the reference TG-43 library of a wide range of possible source geometries. Examples of these libraries were given in Figures 6.6, 6.7 and 6.10. Analysis of the measured features of these IDLs with respect to the reference library yielded the most probable 3D coordinates of the source center with respect to the measurement plane. This was demonstrated in Figure 6.14 with the "IDL area" feature for finding the distance to source (z). To find the source center (x, y), the performance of five different measures to localize the source center was

evaluated. These are the low and high IDL-weighted centroids, the max, the mean and the median (of a 1 by 1 mm^2 region centered around the maximum). It can be seen from Figures 6.8 and 6.9 that the low IDL-weighted centroid can better localize the source center because of the increased circularity of these IDLs (See Figure 6.7). Beyond z = 5 mm, all of these measures could be representative of the source center. Additionally, the increased IDL circularity beyond 5 mm, made it difficult to estimate the source orientation around the *z* axis (θ_z, See Figure 6.10). On the other hand, when the measurement plane is too close to the source; a maximally tilted source around the *y* axis (θ_y= ±15° for a 6F catheter, See Figure 6.6), can shift the maximum point position to up to 1.10 mm in the worst case scenario (at *z* = 1 mm away from the source). Although this situation may seem unlikely because the source is welded to a wire, more specific experimental work is needed to determine the most probable θ_y range.

It is difficult to experimentally estimate the uncertainty in source orientation based on described tracking model because it is not possible to establish the actual source orientation during an experiment described in this work. Also, multiple 2D features showed promise in tracking the source, but there are also other features that can be studied. The aim of this work is to introduce the concept of IDL blob analysis for source tracking. The verification of the tracking performance requires significant amount of work and is left for future projects. Instead, we present the most correlated features with the source 3D coordinates. The source center (*x*, *y*) was significantly correlated with the low IDL-weighted centroid (PCC=0.99), while the distance to source (*z*) was correlated with the IDL areas (PCC=0.96) and perimeters (PCC=0.99). The area is preferred to the perimeter as a feature because of the possible inaccuracies in determining the perimeter of very small ROIs[44] as in the case with high IDLs. The source orientation θ_y was correlated with the difference between high and low IDL-weighted centroids (PCC=0.98), while θ_z was correlated with elliptic orientation of the 60-90% IDL (PCC=0.97) for a maximum distance of *z* = 5 mm. Beyond 5 mm, IDL circularity was significant, therefore limiting the determination of θ_y (PCC≤0.48).

6.4.C Source dose distribution digitization uncertainties

The digitization of RCF exposed to the HDR source with different recorded dose gradient levels can impact the accuracy of the reported doses. The size of the selected ROI must be small

enough if the film was too close to the source. For example, if we consider placing pieces of film at a distance of 10 mm from the source, Figure 6.11 shows that dose inhomogeneity will be less than 2.5% if the chosen ROI size was less than 5 mm × 5 mm. It was also seen that a higher scanning resolution (254 dpi or 0.1 mm/pixel) was preferred over the 127 dpi (0.2 mm/pixel) in order to avoid the dose averaging effects at high dose gradients. A higher scanning resolution introduces more noise,[42] and therefore the application of a noise removal filter is recommended. However, the size of the filter must be chosen carefully in order to avoid dose underestimation around high dose gradient regions (Figure 6.12). Although the performance of the filter seems more aggressive with the lower scanning resolution, the mm size of the filter is double that of the 0.1 mm/pixel resolution. The filter size was still presented with respect to pixels instead of mm on the *x*-axis, because we believe it is more relatable in programming since the filter size is usually set by number of pixels. In summary, a scanning resolution of 0.1 mm/pixel, with a Wiener filter size of 5 by 5 pixel^2 was found to correctly recover dose profiles from noisy datasets (See Figure 6.13).

6.4.D Source tracking with radiochromic film dosimetry versus other systems

The accuracy of the source tracking model was tested by having two film sets at opposing directions from the source. The hypothesis of this experiment was if the tracking method was sensitive enough, both film sets should report the same source position within the catheter. Set #1 which was above the source reported a position that is at the bottom of the catheter (-0.19±0.05 mm) while Set #2 which was below the source reported a position that was also at the bottom of the catheter (-0.28±0.07 mm). Both sets reported a position that is -0.24±0.07 mm at the bottom of the catheter. This means that this method has a potential accuracy in determining the source position in the *z*-direction of 0.1 mm (since the actual source position cannot be verified inside the SW). Additionally, there seems to be a small systematic error in the method since there is a correlation between the distance to the source and the reported position within the catheter but this is taken into account within the uncertainty estimation.

The tracking model in this study was shown to be able to retrieve source positional information in the "z" direction in addition to "*x, y*", while most of the tracking methods available in the literature are focused on the source positioning accuracy in the "*x*" or "*x, y*" directions.[20,23,24,28,29,45–50] An exception is the study by Johansen *et al*[48] where they reported errors in

the radial direction (distance between the detector and the source) based on geometry of multiple dwell positions (0.2±1.1 mm). However, the main aim of this study is to establish an accurate source quality assurance method while most of the cited studies focused on possibility of real-time source detection pre- or during treatment.

6.4.E Practical aspects, limitations and summary of the tracking algorithm

Based on the results shown in this study, the source tracking model shows potential promise in providing a quantitative HDR source localization method. Different properties of the IDL shapes were shown to be unique for each source geometry and they can be used to trace back the HDR source with high accuracy. However, it is important to note that the results in this study assume the irradiation geometry is under full-scattering conditions as is the case in TG-43. In practice, this might not be always the case. For example, in applicator quality assurance, usually these applicators are taped to the film in air. In this case, the dimensions of the IDLs provided in this study cannot be used to determine the distance to the source (z). However, finding the source position (x, y) is still possible since this relies on the IDL centroids rather than their dimensions. A solution for this would be to establish a reference library for in-air geometry but this is outside the scope of this work.

In this work we assumed that the RCF can recover the IDL based on its dosimetric accuracy. The comparison between film measurements and TG-43 dosimetry was shown by different research groups: Palmer *et al* showed in two studies[21,51] the suitability of EBT3 as a dosimeter for 2D quality control of HDR brachytherapy demonstrating agreement to TG-43 calculations within 1.5%. Sellakumar *et al* also confirmed the feasibility of RCF dosimetry in characterization of the TG-43 parameters for the HDR source.[52] Sarfehnia *et al* showed agreement between RCF, ionization chamber, water calorimetry and TG-43 dose rate measurements.[38] Our group also reported agreement between RCF measurements and TG-43 calculations including a detailed uncertainty analysis.[53]

Other limitations of this work are the assumptions that the AAPM TG-43 data are applicable for SW and near the HDR source, respectively. While previous studies have shown good agreement (<1%) between in-water and in-SW dosimetry,[37,40] Ballester *et al*[54] have shown that there is an electronic disequilibrium up to 2 mm from the HDR source center (1st mm from the

6F catheter) leading to additional dose from electrons that is not considered in the AAPM TG-43 dose calculation formalism. Therefore, the use of the tracking model based on IDLs of >90% within 2 mm from the HDR source may underestimate the distance to source center and therefore should be discouraged.

The application of the 1D and 2D source tracking approaches were presented for a single dwell position in this study. For multiple dwell positions, there would be a dose contribution to every point from each dwell position. This necessitates the decomposition of each dwell position's dose profile based on the knowledge that the source dose profile can be modeled with Pearson VII fit (1D approach, See Figure 5). However, this approach (decomposition analysis) is currently under research and we intend to share results in a future work. The 2D approach is especially useful for applicator and x-ray marker coincidence QA. However, a large number of QAs is necessary to evaluate the practicality of the method and it also requires validation of the *x*-ray and film images co-registration process which is outside the scope of this work and will be submitted in the future.

To summarize the results of the source tracking model: For a filtered and normalized dose map, the source positional coordinates (x, y, z, θ_y, θ_z) correlated significantly with the following:

- Source center (x, y): with the low IDL-weighted centroid at any z, or with max-, mean-, median- of a 1 by 1 mm^2, high IDL-weighted centroid ROI at $z \geq 5$ mm.
- Distance to source (z): IDL area, perimeter.
- Source orientation (θ_y): the distance between high and low IDL-weighted centroids.
- Source orientation (θ_z): the elliptic orientation of the 60-90% IDL for a maximum z = 5 mm.
- Maximum point: high IDL-weighted centroid (any z).

6.5 Conclusion

An efficient method was introduced to accurately localize the HDR source based on a measured 2D isodose map away from the source, obtainable from RCF dosimetry. Blob analysis (area, perimeter, weighted centroids, elliptic orientation and circularity), could be used to compare the measurements of the relative isodose lines (relative to max) to a reference TG-43 library. The

effect of the digitization process was also explored. This method optimizes the accuracy of 3D source localization and the use of RCF to quantitatively determine the source position with high accuracy (±0.1 mm). Accurate source localization is essential to provide a reliable QA method for commercial and customized applicators. Additionally, the same methodology might be extended to other 2D imaging systems.

6.6 Acknowledgement

This work was supported in part by the Natural Sciences and Engineering Research Council of Canada contract no. 386009. S.A. is a Ph.D. Candidate supported by the scholarship program at King Faisal Specialist Hospital & Research Centre (KFSH & RC). S.A. acknowledges partial support by the CREATE Medical Physics Research Training Network grant of the Natural Sciences and Engineering Research Council (Grant number: 432290).

6.7 References

1. Kutcher GJ, Coia L, Gillin M, et al. Comprehensive QA for radiation oncology: Report of AAPM Radiation Therapy Committee Task Group 40. *Medical Physics*. 1994;21(4):581-618.

2. Nath R, Anderson LL, Meli JA, Olch AJ, Stitt JA, Williamson JF. Code of practice for brachytherapy physics: Report of the AAPM Radiation Therapy Committee Task Group No. 56. *Medical Physics*. 1997;24(10):1557-1598.

3. Kubo HD, Glasgow GP, Pethel TD, Thomadsen BR, Williamson JF. High dose-rate brachytherapy treatment delivery: Report of the AAPM Radiation Therapy Committee Task Group No. 59. *Medical Physics*. 1998;25(4):375-403.

4. DeWerd LA, Ibbott GS, Meigooni AS, et al. A dosimetric uncertainty analysis for photon-emitting brachytherapy sources: Report of AAPM Task Group No. 138 and GEC-ESTRO. *Medical Physics*. 2011;38(2):782-801. doi:10.1118/1.3533720

5. Nath R, Anderson LL, Luxton G, Weaver KA, Williamson JF, Meigooni AS. Dosimetry of interstitial brachytherapy sources: Recommendations of the AAPM Radiation Therapy Committee Task Group No. 43. *Medical Physics*. 1995;22(2):209-234. doi:10.1118/1.597458

6. Rivard MJ, Coursey BM, DeWerd LA, et al. Update of AAPM Task Group No. 43 Report: A revised AAPM protocol for brachytherapy dose calculations. *Medical Physics*. 2004;31(3):633-674. doi:10.1118/1.1646040

7. Taylor REP, Rogers DWO. EGSnrc Monte Carlo calculated dosimetry parameters for 192Ir and 169Yb brachytherapy sources. *Medical Physics*. 2008;35(11):4933-4944. doi:10.1118/1.2987676

8. Perez-Calatayud J, Ballester F, Das RK, et al. Dose calculation for photon-emitting brachytherapy sources with average energy higher than 50 keV: Report of the AAPM and ESTRO. *Medical Physics*. 2012;39(5):2904-2929. doi:10.1118/1.3703892

9. McLaughlin WL, Yun-Dong C, Soares CG, Miller A, Van Dyk G, Lewis DF. Sensitometry of the response of a new radiochromic film dosimeter to gamma radiation and electron beams. *Nuclear Inst and Methods in Physics Research, A*. 1991;302(1):165-176. doi:10.1016/0168-9002(91)90506-L

10. Devic S. Radiochromic film dosimetry: Past, present, and future. *Physica Medica*. 2011;27(3):122-134. doi:10.1016/j.ejmp.2010.10.001

11. Devic S, Tomic N, Lewis D. Reference radiochromic film dosimetry: Review of technical aspects. *Physica Medica*. 2016;32(4):541-556. doi:10.1016/j.ejmp.2016.02.008

12. Devic S, Tomic N, Soares CG, Podgorsak EB. Optimizing the dynamic range extension of a radiochromic film dosimetry system. *Medical Physics*. Published online 2009. doi:10.1118/1.3049597

13. Niroomand-Rad A, Blackwell CR, Coursey BM, et al. AAPM TG 55. Radiochromic film dosimetry. *Medical physics*. 1998;25:2093-2115. doi:10.1118/1.598407

14. Sutherland JGH, Rogers DWO. Monte Carlo calculated absorbed-dose energy dependence of EBT and EBT2 film. *Medical Physics*. 2010;37(3):1110-1116. doi:10.1118/1.3301574

15. Arjomandy B, Tailor R, Anand A, et al. Energy dependence and dose response of Gafchromic EBT2 film over a wide range of photon, electron, and proton beam energies. *Medical Physics*. 2010;37(5):1942-1947. doi:10.1118/1.3373523

16. Bekerat H, Devic S, Deblois F, et al. Improving the energy response of external beam therapy (EBT) GafChromic™ dosimetry films at low energies (≤100 keV). *Medical Physics*. 2014;41(2):022101. doi:10.1118/1.4860157

17. Hammer CG, Rosen BS, Fagerstrom JM, Culberson WS, DeWerd LA. Experimental investigation of GafChromic ® EBT3 intrinsic energy dependence with kilovoltage x rays, ^{137}Cs, and ^{60}Co. *Medical Physics*. 2018;45(1):448-459. doi:10.1002/mp.12682

18. Evans MDC, Devic S, Podgorsak EB. High dose-rate brachytherapy source position quality assurance using radiochromic film. *Medical Dosimetry*. 2007;32(1):13-15. doi:10.1016/j.meddos.2006.10.001

19. Asgharizadeh S, Bekerat H, Syme A, et al. Radiochromic film-based quality assurance for CT-based high-dose-rate brachytherapy. *Brachytherapy*. 2015;14(4):578-585. doi:10.1016/j.brachy.2015.02.192

20. Awunor OA, Dixon B, Walker C. Direct reconstruction and associated uncertainties of192Ir source dwell positions in ring applicators using gafchromic film in the treatment planning of HDR brachytherapy cervix patients. *Physics in Medicine and Biology*. 2013;58(10):3207-3225. doi:10.1088/0031-9155/58/10/3207

21. Palmer AL, Lee C, Ratcliffe AJ, Bradley D, Nisbet A. Design and implementation of a film dosimetry audit tool for comparison of planned and delivered dose distributions in high dose rate (HDR) brachytherapy. *Physics in Medicine and Biology*. 2013;58(19):6623-6640. doi:10.1088/0031-9155/58/19/6623

22. Palmer A, Bradley D, Nisbet A. Physics-aspects of dose accuracy in high dose rate (HDR) brachytherapy: Source dosimetry, treatment planning, equipment performance and in vivo verification techniques. *Journal of Contemporary Brachytherapy*. 2012;4(2):81-91. doi:10.5114/jcb.2012.29364

23. Jursinic PA. Quality assurance measurements for high-dose-rate brachytherapy without film. *Journal of Applied Clinical Medical Physics*. 2014;15(1):246-261. doi:10.1120/jacmp.v15i1.4586

24. Espinoza A, Petasecca M, Cutajar D, et al. Pretreatment verification of high dose rate brachytherapy plans using the 'magic phantom' system. *Biomedical Physics & Engineering Express*. 2015;1(2):025201. doi:10.1088/2057-1976/1/2/025201

25. Kertzscher G, Beddar S. Inorganic scintillation detectors for 192Ir brachytherapy. *Physics in Medicine and Biology*. 2019;64(22). doi:10.1088/1361-6560/ab421f

26. Therriault-Proulx F, Briere TM, Mourtada F, Aubin S, Beddar S, Beaulieu L. A phantom study of an in vivo dosimetry system using plastic scintillation detectors for real-time verification of 192Ir HDR brachytherapy. *Medical Physics*. 2011;38(5):2542-2551. doi:10.1118/1.3572229

27. Song H, Bowsher J, Das S, Yin FF. Tracking brachytherapy sources using emission imaging with one flat panel detector. *Medical Physics*. 2009;36(4):1109-1111. doi:10.1118/1.3081402

28. Smith RL, Haworth A, Panettieri V, Millar JL, Franich RD. A method for verification of treatment delivery in HDR prostate brachytherapy using a flat panel detector for both imaging and source tracking. *Medical Physics*. 2016;43(5):2435-2442. doi:10.1118/1.4946820

29. Okamoto H, Aikawa A, Wakita A, et al. Dose error from deviation of dwell time and source position for high dose-rate 192Ir in remote afterloading system. *Journal of Radiation Research*. 2014;55(4):780-787. doi:10.1093/jrr/rru001

30. Poulin E, Racine E, Binnekamp D, Beaulieu L. Fast, automatic, and accurate catheter reconstruction in HDR brachytherapy using an electromagnetic 3D tracking system. *Medical Physics*. 2015;42(3):1227-1232. doi:10.1118/1.4908011

31. Zhou J, Sebastian E, Mangona V, Yan D. Real-time catheter tracking for high-dose-rate prostate brachytherapy using an electromagnetic 3D-guidance device: A preliminary performance study. *Medical Physics*. 2013;40(2). doi:10.1118/1.4788641

32. Kellermeier M, Herbolzheimer J, Kreppner S, Lotter M, Strnad V, Bert C. Electromagnetic tracking (EMT) technology for improved treatment quality assurance in interstitial brachytherapy. *Journal of Applied Clinical Medical Physics*. 2017;18(1):211-222. doi:10.1002/acm2.12021

33. Wang W, Viswanathan AN, Damato AL, et al. Evaluation of an active magnetic resonance tracking system for interstitial brachytherapy. *Medical Physics*. 2015;42(12):7114-7121. doi:10.1118/1.4935535

34. Moeslund TB. BLOB Analysis. In: Moeslund TB, ed. *Introduction to Video and Image Processing: Building Real Systems and Applications*. Undergraduate Topics in Computer Science. Springer; 2012:103-115. doi:10.1007/978-1-4471-2503-7_7

35. Daskalov GM, Williamson JF, Baker R, Rogers DWO. Dosimetric Modeling of the MicroSelectron High-Dose Rate Ir-192 Source by the Multigroup Discrete Ordinates Method. *Med Phys (abstract)*. 1998;25:A119.

36. Aldelaijan S, Devic S, Papaconstadopoulos P, et al. Dose–response linearization in radiochromic film dosimetry based on multichannel normalized pixel value with an integrated spectral correction for scanner response variations. *Medical Physics*. 2019;46(11):5336-5349. doi:10.1002/mp.13818

37. Aldelaijan S, Mohammed H, Tomic N, et al. Radiochromic film dosimetry of HDR ^{192}Ir source radiation fields. *Medical Physics*. 2011;38(11). doi:10.1118/1.3651482

38. Sarfehnia A, Kawrakow I, Seuntjens J. Direct measurement of absorbed dose to water in HDR ^{192}Ir brachytherapy: Water calorimetry, ionization chamber, Gafchromic film, and TG-43. *Medical Physics*. 2010;37(4):1924-1932. doi:10.1118/1.3352685

39. Pérez-Calatayud J, Granero D, Ballester F. Phantom size in brachytherapy source dosimetric studies. *Medical Physics*. 2004;31(7):2075-2081. doi:10.1118/1.1759826

40. Schoenfeld AA, Harder D, Poppe B, Chofor N. Water equivalent phantom materials for192Ir brachytherapy. *Physics in Medicine and Biology*. 2015;60(24):9403-9420. doi:10.1088/0031-9155/60/24/9403

41. ICRU Report 89. *Prescribing, Recording, and Reporting Brachytherapy for Cancer of the Cervix:* Journal of the International Commission on Radiation Units and Measurements; 2016. 10.1093/jicru/ndw027

42. Vera Sánchez JA, Ruiz Morales C, González López A. Characterization of noise and digitizer response variability in radiochromic film dosimetry. Impact on treatment verification. *Physica Medica*. 2016;32(9):1167-1174. doi:10.1016/j.ejmp.2016.08.019

43. Gaudreault M, Reniers B, Landry G, Verhaegen F, Beaulieu L. Dose perturbation due to catheter materials in high-dose-rate interstitial 192Ir brachytherapy. *Brachytherapy*. 2014;13(6):627-631. doi:10.1016/j.brachy.2014.05.010

44. Yang L, Albregtsen F, Lønnestad T, Grøttum P. Areas and perimeters of blob-like objects: A comparison. *IAPR Workshop on Machine Vision Applications, Dec 13-15, 1994*. Published online 1994:272276.

45. Watanabe Y, Muraishi H, Takei H, et al. Automated source tracking with a pinhole imaging system during high-dose-rate brachytherapy treatment. *Physics in Medicine and Biology*. 2018;63(14). doi:10.1088/1361-6560/aacdc9

46. Smith RL, Hanlon M, Panettieri V, et al. An integrated system for clinical treatment verification of HDR prostate brachytherapy combining source tracking with pretreatment imaging. *Brachytherapy*. 2018;17(1):111-121. doi:10.1016/j.brachy.2017.08.004

47. Poder J, Cutajar D, Guatelli S, et al. HDR brachytherapy in vivo source position verification using a 2D diode array: A Monte Carlo study. *Journal of Applied Clinical Medical Physics*. 2018;19(4):163-172. doi:10.1002/acm2.12360

48. Johansen JG, Rylander S, Buus S, et al. Time-resolved in vivo dosimetry for source tracking in brachytherapy. *Brachytherapy*. 2018;17(1):122-132. doi:10.1016/j.brachy.2017.08.009

49. Alnaghy S, Loo KJ, Cutajar DL, et al. BrachyView: Multiple seed position reconstruction and comparison with CT post-implant dosimetry. *Journal of Instrumentation*. 2016;11(5). doi:10.1088/1748-0221/11/05/P05002

50. Romanyukha A, Carrara M, Mazzeo D, et al. An innovative gynecological HDR brachytherapy applicator system for treatment delivery and real-time verification. *Physica Medica*. 2019;59(December 2018):151-157. doi:10.1016/j.ejmp.2019.03.001

51. Palmer AL, Pietro PD, Alobaidli S, et al. Comparison of methods for the measurement of radiation dose distributions in high dose rate (HDR) brachytherapy: Ge-doped optical fiber, EBT3 Gafchromic film, and PRESAGE® radiochromic plastic. *Medical Physics*. 2013;40(6Part1):061707. doi:10.1118/1.4805100

52. Sellakumar P, Sathish Kumar A, Supe SS, Anand MR, Nithya K, Sajitha S. Evaluation of dosimetric functions for Ir-192 source using radiochromic film. *Nuclear Instruments and Methods in Physics Research Section B: Beam Interactions with Materials and Atoms*. 2009;267(10):1862-1866. doi:10.1016/j.nimb.2009.03.003

53. Aldelaijan S, Wadi-Ramahi S, Nobah A, Moftah B, Devic S, Jastaniyah N. Commissioning of applicator-guided stereotactic body radiation therapy boost with high-dose-rate brachytherapy for advanced cervical cancer using radiochromic film dosimetry. *Brachytherapy*. 2017;16(4):893-902. doi:10.1016/j.brachy.2017.03.009

54. Ballester F, Granero D, Pérez-Calatayud J, Melhus CS, Rivard MJ. Evaluation of high-energy brachytherapy source electronic disequilibrium and dose from emitted electrons. *Medical Physics*. 2009;36(9Part1):4250-4256. doi:10.1118/1.3194754

CHAPTER 7: Conclusion and future work

7.1 Discussion

The need for improved quality assurance in image-guided brachytherapy

Although brachytherapy (BT) has always been technically the simplest form of radiation therapy, the clinical evidence had shown it to be an effective treatment that is underutilized in favor of more complex external beam technologies aiming to create similar dose distributions. However, the incorporation of these sophisticated external beam technologies was always associated with the state-of-the-art quality assurance (QA) solutions that could also effectively alleviate contemporary work pressures. Nevertheless, as it was shown in Chapter 2, retrospective analysis of large number of patient data in the last twenty years has shown that with all technological advancements in external beam radiotherapy, it could not yet replace the physical and biological advantages of BT. Therefore, it is logical to see BT going through renaissance and more resources are still being invested to improve it. For example: the incorporation of various imaging modalities for both planning and daily treatment guidance, the invention of more accurate and precise afterloading technologies, investigation of different radiation sources and their manufacturing processes, improvement of dose calculation engines, and incorporation of fabrication technologies such as 3D printing for more patient specific treatments. On the other hand, standard BT QA procedures are still the same in general: the well-type ionization chamber for source activity measurement and qualitative assessment of source positioning with film. Although there has been development of new technologies aimed at source tracking, automatic catheter reconstruction, digital source detection devices, their incorporation in the clinic was always hindered by logistic justification and tangible improvements over standard QA tools that have always worked.

As mentioned in Chapter 2, one of the main benefits of image-guided brachytherapy (IGBT) is that it enabled direct implementation of dose escalation protocols and current ongoing clinical evidence show that this in turn is improving target local control rates. It can be argued that dose escalation should be associated with more sensitive and stringent QA procedures. However, if one constructs an approximate timeline comparing the introduction of IGBT and dose escalation (started within the decade 2000-2010), to the QA protocols that are still in use nowadays (the AAPM TG-40, TG-56, TG-59, published in 1994, 1997, 1998, respectively), it would be realized that there should be a concern about the suitability of older methods in detecting errors from today's form of BT.

Summary of the thesis outcome

The goal of this thesis was to optimize the benefits of RCF dosimetry for HDR IGBT QA requirements. Chapters 3 and 4 focused on the RCF dosimetry protocol that involved signal interpretation, film scanning and handling, dosimetric accuracy, precision and stability. Most importantly, the "fingerprint" protocol that was introduced in Chapter 4 represents the procedure that was used for reading the irradiated film pieces. This protocol was shown to improve dosimetric accuracy by accounting for the difference in scanning conditions during calibration and measurements. It was also shown to correct for response inhomogeneities in the scanning bed when using larger film sheets or pieces based only on information available in the same scanned image. Another advantage of this protocol is the linearization of film response with dose and therefore the interpretation of measured relative dose distribution would remain correct even if the dose calibration was systematically shifted. This new "fingerprint" protocol was utilized in Chapter 6 were the HDR source tracking algorithm relies on relative isodose lines. Chapter 5 focused on the film dosimetric aspects and showed how measurements can aid in the QA of BT treatment planning systems (TPS). Chapter 6 represents our view on how the RCF film dosimetry can benefit HDR IGBT QA. In that chapter all aspects that may affect QA results were taken into account such as scanning resolution, effect of noise and filtration (especially within the high dose gradient regions). It is our belief that the cost effectiveness and high resolution aspects of RCF dosimetry should make it the reliable choice for HDR IGBT QA.

Impact of the thesis work and its implementation

The main impact of this work is that it provided a framework on how to employ the advantage of RCF dosimetry while addressing its drawbacks and understand their impact on the QA results. According to the AAPM Task Group 56 report on BT code of practice, the end goals of any BT QA program are: 1) safety of the patient, the public and the institution, 2) positional accuracy, 3) temporal accuracy, and 4) dose delivery accuracy. The methods presented in this thesis technically addressed points 2-4. Chapters 3-5 focused on the dosimetry aspects and especially in Chapter 5 we showed examples of dose measurements of the HDR source with the EBT3 film model. The dosimetry is important for dose delivery accuracy assessment and its correlation with dwell times and source strength estimation. Chapter 6 focused primarily on accurate dwell position QA. Incorporation of the multidimensional source tracking algorithm into QA was shown to significantly improve the source localization accuracy. As will be shown in the next section, these techniques (dosimetry and source tracking) are intended to be used in an end-to-end quantitative IGBT QA program based on RCF dosimetry.

The methods explained in this thesis would aid the medical physicist in implementing an accurate RCF dosimetry protocol (Chapter 4) that does not take much of their time since it is based on a single scan *i.e.* no need for a pre-scan (as was shown in Chapter 3). Understanding different effects that may affect film dosimetry is important and ultimately it helps in achieving the task that the film was employed for. Combining the high resolution 2D dosimetric capability with the source tracking algorithm could be a powerful tool that can easily be implemented in the clinic since the whole process can be automated. This can help the clinic in quantifying their applicators performance and help reduce incidents related to the identification of the source distal reference position (or first dwell position) which was identified as one of the most common reported failure types by ASTRO (Thomadsen *et al*. 2014).

The utilization of RCF can also be beneficial in patient treatment delivery. In some cases of surface BT, it would be possible to use the RCF for *in-vivo* dosimetry and source tracking at the same time. An example of this is the placement of a film piece on top of the Freiburg flap taking into account the flexibility and size limits of RCF. In order to maximize the advantages of RCF, a registration method has to be developed to relate the spatial coordinate systems of the RCF, the applicator and the target area. This in turn may enable reconstruction of delivered dose

based on estimated source dwell positions and times. Additionally, RCF based QA can be advantageous for commissioning intensity modulated brachytherapy (IMBT) applicators. This is especially the case given that source positional and angular accuracies would become even more critical to ensure correct dose delivery. However, testing these aspects and the suitability of QA methods would require additional recommendations.

Another possible implementation of the RCF based QA is the dosimetry of model-based dose calculation algorithms (MBDCA). Although it was shown in Chapter 5 that the addition of bolus is advantageous in improving the agreement between measurements and TG-43 based dose calculation, it is more logical to optimize dose planning based on MDBCAs. This is because the dose to the treatment area (2-10 mm from the surface) is dominated by contributions from primary rather than scattered photons where the latter becomes more important at extended distances. This means that increasing the contribution of scatter would also increase OAR doses beyond the target. However, the use of MBDCAs would come at a cost since it can take more time to optimize/calculate dose based on the same computational hardware used for TG-43 based approach. Therefore, the need for MBDCAs should be further investigated which is in line with the recently published GEC-ESTRO / AAPM TG-253 recommendations (Fulkerson *et al*. 2020).

Implementing the methods from this thesis might not appear to be trivial since film dosimetry has always been labeled cumbersome mostly because of its non-linear dose-response, the need to scan films before and after irradiation and the need to account for different digitization issues. It is hoped that the methods introduced in this thesis (response linearization, elimination of the need for a pre-scan, "fingerprint" method) can be implemented by the medical physics community to harness the advantages of RCF dosimetry and appreciate its use in HDR IGBT QA. It is expected that the adoption of the RCF dosimetry protocol (Chapter 4) and the source tracking model (Chapter 6) could significantly improve the HDR IGBT QA using the tools available in the clinic. However, for this to happen, a user-friendly software and/or informedly-written codes should be made available for the medical physics community for testing. Such tools would be valuable to maintain safety and quality especially with the rapid technological advances in the BT field. Since RCF is a passive dosimeter (i.e. requires labor work to get the signal out of it), one can argue that in the future it can be replaced by active digital technologies in a similar fashion to radiology where films were replaced by digital radiography. However, the

convenience of cutting the film to any shape and its flexibility and robustness makes it a readily available tool that is arguably simple to position as an *in-vivo* dosimeter even in complex treatment setups. Adding the dosimetric precision, near tissue equivalence, and high spatial resolution, in our opinion, make RCF the most suited dosimeter for testing contemporary applications of HDR IGBT.

7.2 Future work

The main objective of this thesis project was to design a convenient and comprehensive set of QA tests for HDR brachytherapy based on RCF dosimetry. The hypothesis is that based on some unique irradiation patterns and advanced analysis, RCF dosimetry system will be able to reveal a set of comprehensive QA performance metrics for multiple channel HDR brachytherapy simultaneously. These performance metrics can be defined at each step of the brachytherapy process: (1) Afterloader QA: first dwell position (FDP), dwell times, dwell positions, timer linearity, source step size; (2) Source QA: source positional accuracy, source strength verification, dose rate distribution verification; (3) TPS QA: planned versus measured dose distributions of a CT-simulated QA phantom, data transfer to treatment unit; and (4) Treatment QA: pre-treatment patient specific QA, *in-vivo* passive dosimetry verification, commissioning of treatment techniques. In order to address these QA metrics, six main aims were identified for the future framework and they are summarized in Figure 7.1.

7.2.1 Film dosimetry protocol development, validation and optimization:

This aim was addressed in chapters 3 and 4 of the thesis. However, this process has to be an ongoing one in order to further improve the protocol and keep up with film/scanner manufacturing changes.

Framework for HDR brachytherapy quality assurance

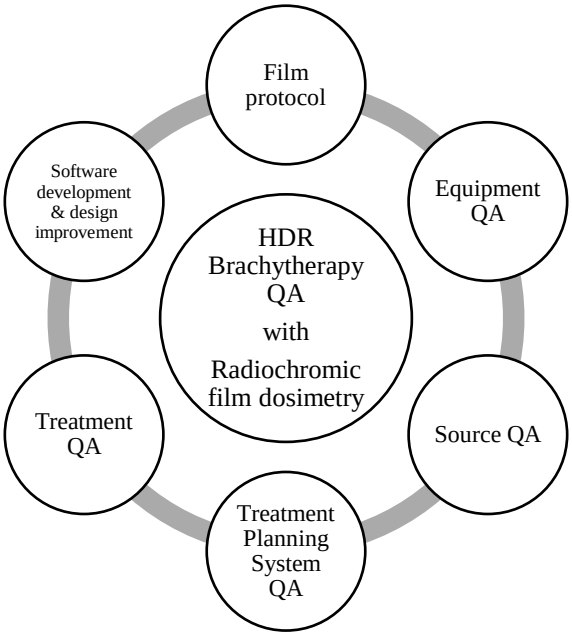

Figure 7.1: The future framework for HDR brachytherapy QA with radiochromic film dosimetry. The framework consists of six specific areas to be optimized (sub-circles). HDR: high-dose-rate, QA: quality assurance.

7.2.2 Equipment QA

This includes the QA of the afterloader unit and auxiliary components such as applicators, catheters, and simulation markers. This part was not included in the thesis because it is still under development. For the afterloader QA: a special phantom was proposed with many design features that mimic the conditions within the TPS and it also optimized practicality and dosimetric reproducibility (See Figure 7.2).

Additionally, some unique irradiation patterns and image analysis routines were designed to reveal the QA performance metrics indicated above. This was possible with the development of an algorithm that can decompose source dwell positions and dwell times for multiple channels, simultaneously (See Figure 7.3).

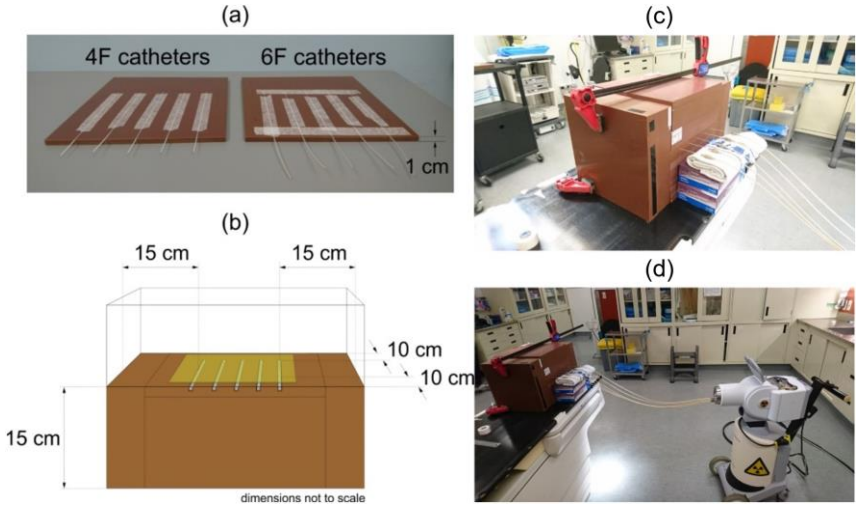

Figure 7.2: Phantom design for afterloader quality assurance made of Solid Water™ (SW): (a) choice of 4F or 6F catheters, (b) illustration of phantom design with EBT3 radiochromic film location. The dashed slab above the film is also made of SW but was made transparent for visibility. (c) Photograph of the assembled phantom. The large clamps are used to minimize the effect of air gaps. (d) Photograph of the full setup with the phantom connected to the afterloader through five transfer tubes.

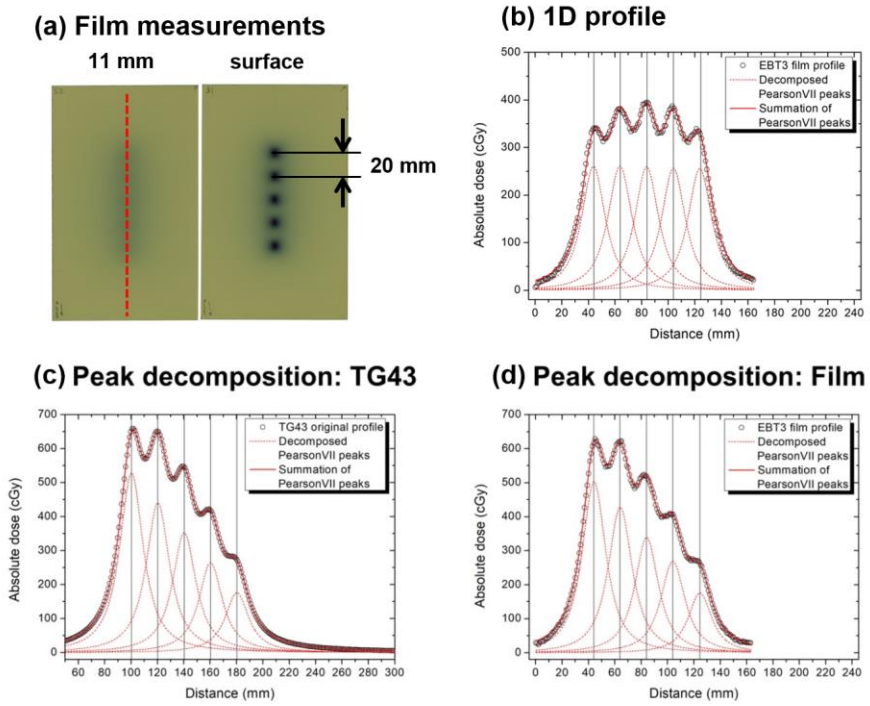

Figure 7.3: Decomposition of dose profile fit across five dwell positions using a Pearson VII model: (a) film images at 11 mm and at the surface. (b) decomposition analysis of a 1D profile across the film at 11 mm with fixed dwell times (30 sec each). (c) decomposition analysis of a 1D profile across the AAPM TG-43 protocol data at 11 mm with fixed dwell times. (d) decomposition analysis of a 1D profile across the film at 11 mm with fixed dwell times. This test can reveal dwell positions, dwell times and timer linearity.

The second part is the applicator, catheters and markers QA. Based on the source tracking algorithm introduced in Chapter 6, a QA methodology is suggested to provide a quantitative analysis of the ^{192}Ir HDR source first dwell position within the applicator structure and its coincidence with the x-ray marker. To achieve this, an image registration method between the *x*-ray and film images was developed. Figure 7.4 shows an example of the proposed method and some preliminary analysis. More than 150 applicator QAs over two years were performed and the results will be presented in a future paper.

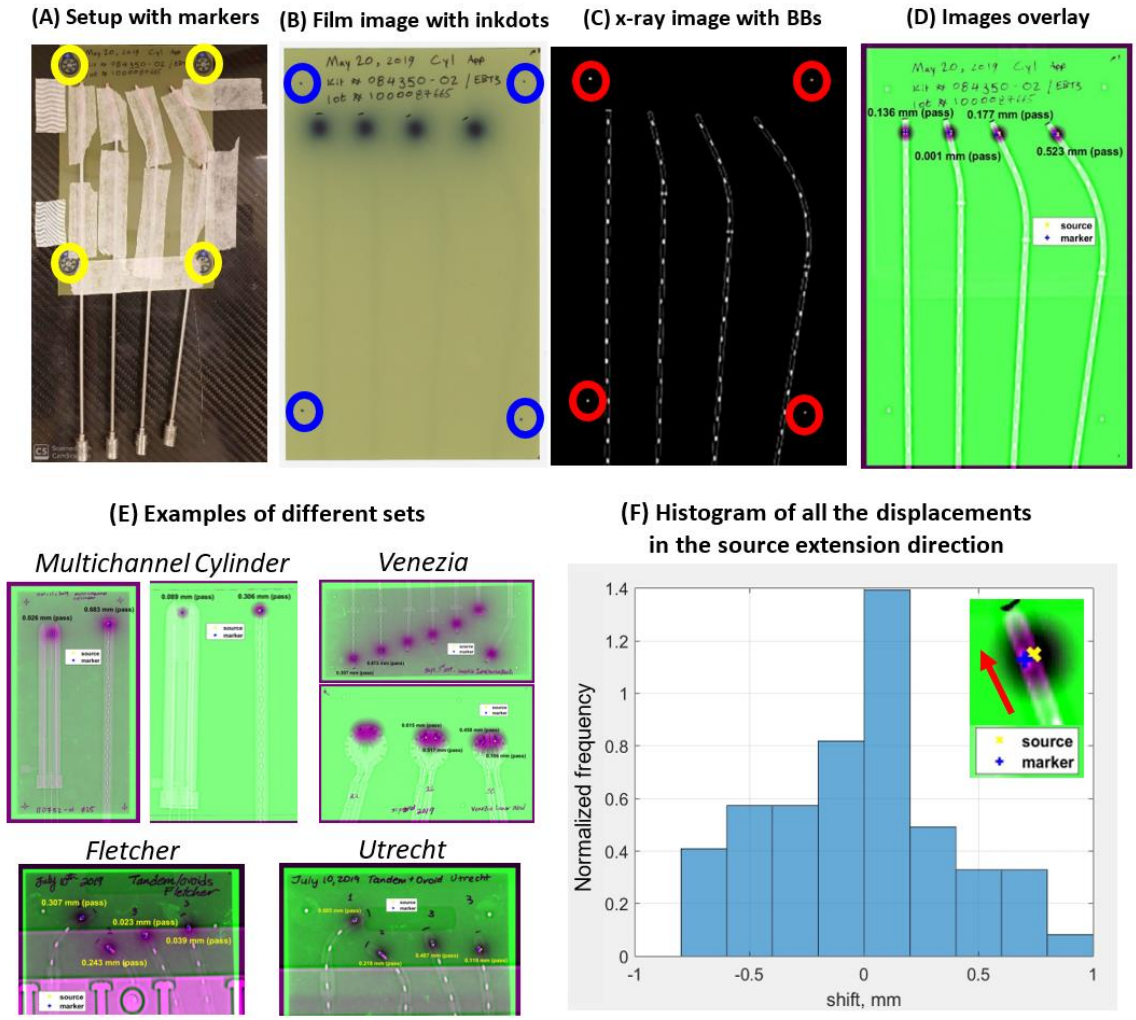

Figure 7.4: Demonstration of applicator QA with radiochromic film dosimetry and source tracking. (A) applicators attached to the film with inkdots/BBs on the corners, (B) post exposure image highlighting inkdots, (C) x-ray image highlighting registration BBs, (D) image overlay and application of source/marker auto tracking, (D) visual QA examples of different applicator sets, and (F) histogram of all displacements (total of 64 applicators, 0.10 ± 0.39 mm)

7.2.3 Source QA

This aim was addressed in Chapter 6 of the thesis. However, there are other film models that can be used for source position QA such as XRQA2, RTQA2 and EBT-XD. The localization of source position is dependent on finding the source center. This does not require a linearized response to dose and it is expected that the low IDL weighted centroid can attain this job using any of these film models but this must be verified. Chapter 6 focused mainly on the source localization problem and it would be desirable to see a comparison between dose planes registered by the film versus calculated dose planes by the AAPM TG-43 formalism.

7.2.4 Treatment planning system QA

The dosimetric performance of TG-43-based planning was partially addressed in Chapter 5. A more comprehensive TPS QA is to be designed taking into account dose calculation accuracy, digitization performance, and data transfer. This can be achieved by comparing planned versus measured dose distributions based on known metrics such as distance to agreement, dose difference and gamma analysis.

7.2.5 Treatment QA

This refers to the patient treatment verification and it consists of two steps: pre-treatment verification (published elsewhere by our group) and in-vivo dosimetry during patient treatment. The goal of the latter is to highlight the advantage of RCF 2D dosimetry in the assessment of delivered dose to the targets and organs-at-risk, and introduce adaptive planning based on the measurements (examples in Figure 7.5). These measurements will be used to quantify the need for more accurate dose calculation engines in comparison to TG-43-based planning (Figure 7.6).

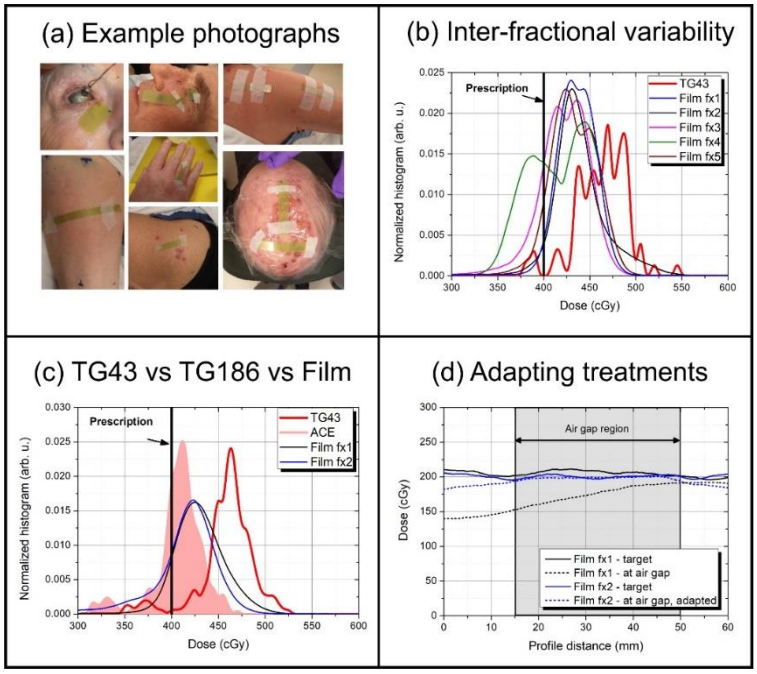

Figure 7.5: HDR surface brachytherapy *in-vivo* dosimetry with EBT3 model RCF. (a) photographs of different film pieces placed on different cases. (b) highlighting inter-fractional variability and ability to improve the applicator positioning. (c) comparison between heterogeneity-corrected dose calculation, the current standard in dose calculation and film measurements. (d) how in-vivo measurements can help in adapting radiation treatments.

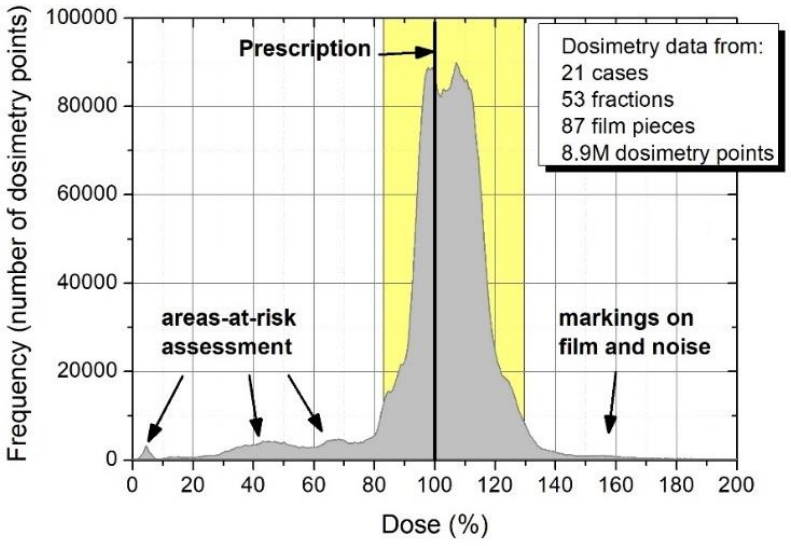

Figure 7.6: Histogram of dose measurements in the *in-vivo* study of HDR surface brachytherapy. The figure shows that a more accurate dose calculation engine might help in improving the dose delivery accuracy (*i.e.* tighten the peak and push it to the right while limiting the maximum dose to the skin).

7.2.6 Software development and design improvement

After aims 1-5 are achieved, a dynamic software package that integrates results of these aims will be developed together with a practical and optimized phantom setup. An example on the implementation of this is given in Figure 7.7 (comprehensive QA irradiation pattern) and Figure 7.8 (end-to-end QA in a single irradiation session).

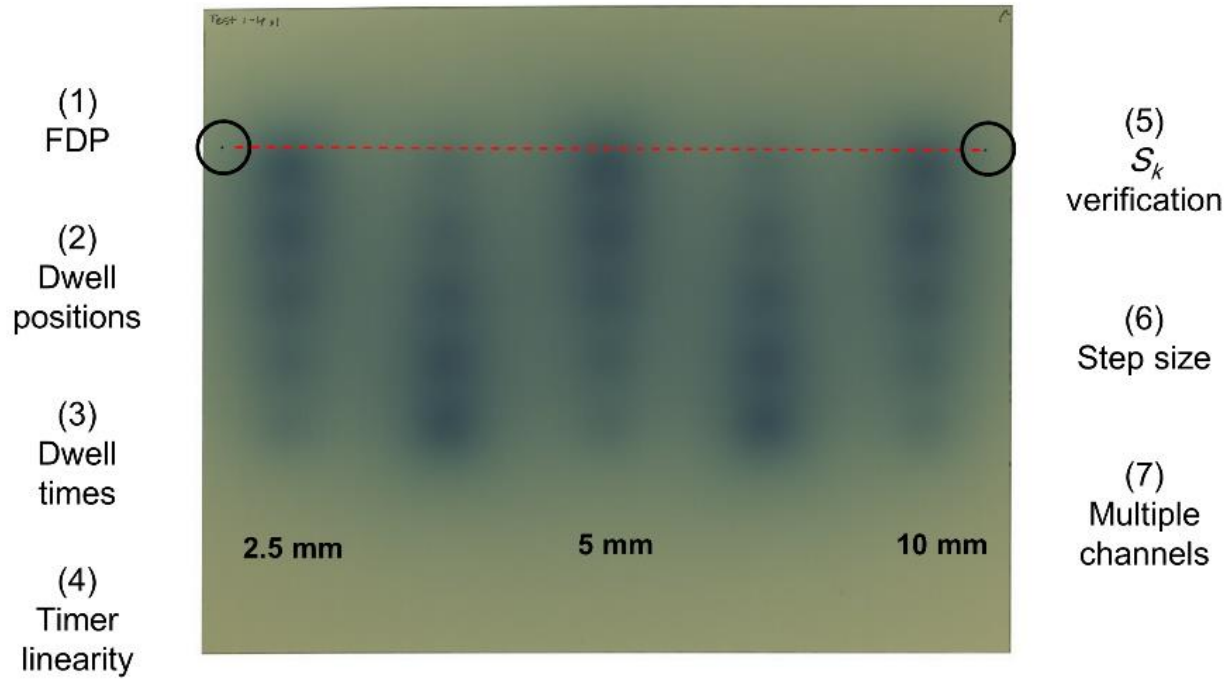

Figure 7.7: The types of tests that can be achieved with a single irradiation session in HDR brachytherapy QA: (1) First dwell position: a line connecting the physical points on the phantom that represents where the FDP should be will be compared to the measured position per catheter. (2) Dwell positions, (3) Dwell times, (4) Timer linearity (5) Source strength (S_k) verification: via source tracking and dosimetry, (6) Step size, (7) This can be done for multiple channels: five shown here.

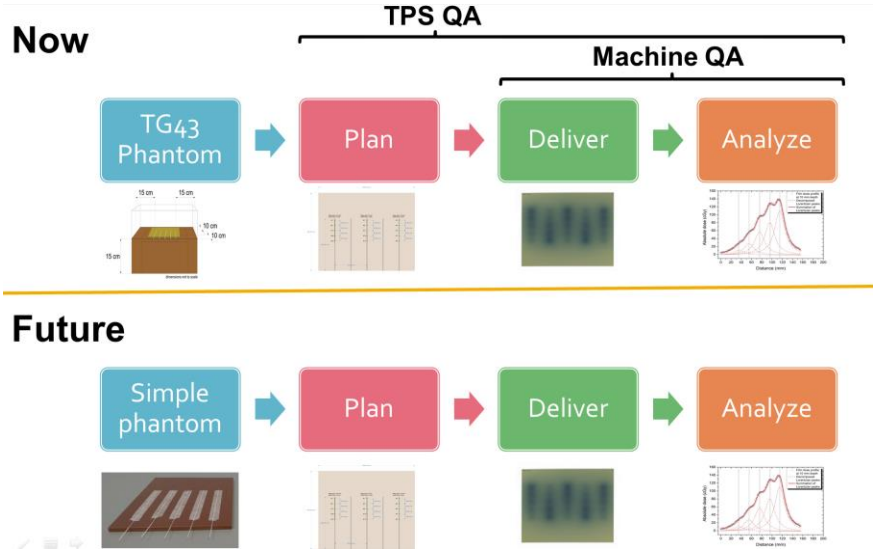

Figure 7.8: Comprehensive QA: incorporating treatment planning system quality assurance with afterloader quality assurance. This involves scanning the phantom, creating a plan and transferring it from planning unit to the treatment unit. Currently (top), a TG43 phantom is used. In the future (bottom), a simpler phantom will be created whereby dose will be calculated using a Model-Based Dose Calculation Algorithms (MBDCAs).

7.3 Conclusion

In this thesis, a QA framework was described for HDR brachytherapy using 2D RCF dosimetry. The framework is based on a film digitization protocol developed to address issues that may compromise correct representation of the expected HDR source dose distribution. Incorporation of the film dosimetric features with the proposed source tracking algorithm lead to improvements in source position QA accuracy. This allows accurate quantification of the source position with respect to the marker and catheter coordinates that can be acquired by superposition with image-guidance to allow simultaneous visualization of the source and marker within the catheter or applicator structure. These methods provided a quick and cost effective way to use tools already available in the clinic for enhanced and more reliable QA of different brachytherapy equipment. Ideas to improve the practicality and adoption of the proposed framework was also discussed and it is the belief of our group that this can only be achieved with the development of a software package that incorporates all the proposed models in dynamic routines that simplify the QA analysis and interpretation of results. These tools will allow the integration of new technologies into brachytherapy without compromising QA and patient safety.

OTHER PUBLICATIONS

In addition to the manuscripts in chapters 3-6, the following peer-reviewed articles and conference proceedings resulted in the course of fulfilling the aims of this thesis:

Journal articles

1. Moftah B, **S Aldelaijan**, M Shehadeh et al., "Calibration of MTT assay in proton beams using radiochromic films," Physica Medica (2020) in press.
2. Albert S, D Brivio, **S Aldelaijan**, E Sajo, J Hesser, P Zygmanski (2020) “Towards customizable thin-panel low-Z detector arrays: electrode design for increased spatial resolution ion chamber arrays.” *Phys Med Biol.* 65(8):08NT02.
3. Devic S, **S Aldelaijan**, H Bekerat (2019) “Impact of inertia on possible fundamental drawbacks in radiochromic film dosimetry.” *Phys Med*. 10; 66:133-134.
4. Devic S, L Liang, N Tomic, H Bekerat, M Morcos, M Popovic, P Watson, **S Aldelaijan**, J Seuntjens (2019) “Dose measurements nearby low energy electronic brachytherapy sources using radiochromic film.” *Phys Med*. 64:40-44.
5. Papaconstadopoulos P, IR Levesque, **S Aldelaijan**, K O'Grady, S Devic, J Seuntjens (2019) “Modeling the primary source intensity distribution: reconstruction and inter-comparison of six Varian TrueBeam sources.” *Phys Med Biol*. 64(13):135005.
6. Tomic N, P Papaconstadopoulos, H Bekerat, G Antunovic, **S Aldelaijan**, J Seuntjens, S Devic (2019) “Monte Carlo simulations of different CT X-ray energy spectra within CTDI phantom and the influence of its changes on radiochromic film measurements.” *Phys Med*. 62:105-110.
7. **Aldelaijan S**, N Tomic, P Papaconstadopoulos, J Schneider, J Seuntjens, S Shih, D Lewis, S Devic (2018) “Technical Note: Response time evolution of XR-QA2 GafChromic™ film models.” *Med Phys*. 45(1):488-492.

8. Tomic N, P Papaconstadopoulos, **S Aldelaijan**, J Rajala, J Seuntjens, S Devic (2018) "Image quality for radiotherapy CT simulators with different scanner bore size." *Phys Med*. 45:65-71.
9. Liang LH, N Tomic, T Vuong, **S Aldelaijan**, H Bekerat, F DeBlois, J Seuntjens, S Devic (2018) "Physics aspects of the Papillon technique-Five decades later." *Brachytherapy*. 17(1):234-243.
10. **Aldelaijan S**, S Wadi-Ramahi, A Nobah, B Moftah, S Devic, N Jastaniyah (2017) "Commissioning of applicator-guided stereotactic body radiation therapy boost with high-dose-rate brachytherapy for advanced cervical cancer using radiochromic film dosimetry." *Brachytherapy*. 16(4):893-902.

Conference abstracts (oral presentations)

1. **Aldelaijan, S**, S Devic, H Bekerat, P Papaconstadopoulos, J Schneider, J Seuntjens, R Cormack, IM Buzurovic (2020) "Implementation of a novel HDR source tracking model for source quality assurance using radiochromic film dosimetry." Joint AAPM/COMP Virtual Meeting
2. **Aldelaijan, S**, DA O'Farrell, T Harris, RA Cormack, JP Seuntjens, S Devic, PM Devlin, IM Buzurovic (2020) "In-vivo radiochromic film dosimetry indicates a need for model-based dose calculation in HDR surface brachytherapy." Joint Meeting, ABS/WCB/ESTRO, Vienna, Austria
3. **Aldelaijan, S**, P Papaconstadopoulos, H Bekerat, M Khosravi, M Bhagwat, J Seuntjens, S Devic, IM Buzurovic (2019) "Multichannel normalized pixel value as a response function for radiochromic film dosimetry enables simultaneous dose response linearization and scanner response correction." 61st AAPM Annual Meeting,
4. **Aldelaijan, S**, P Papaconstadopoulos, J Schneider, H Bekerat, J Seuntjens, I Buzurovic, S Devic (2018) "WE-AB-DBRA-2: A novel source tracking method for accurate and comprehensive HDR brachytherapy quality assurance using radiochromic film dosimetry." 60th AAPM Annual Meeting, Nashville, USA
5. **Aldelaijan, S**, P Papaconstadopoulos, J Schneider, H Bekerat, J Seuntjens, I Buzurovic, S Devic, (2018) "Abstract#278: Dosimetric impact of source position variation inside different catheter sizes in HDR brachytherapy.", ABS Annual Meeting, San Francisco, USA,

6. **Aldelaijan, S**, Wadi-Ramahi S, Nobah A, Jastaniyah N (2017) "Commissioning of applicator-guided SBRT with HDR Brachytherapy for Advanced Cervical Cancer." *Radiother Oncol* 123, S193-S194, ESTRO, Vienna, Austria

Conference abstracts (poster presentations)

1. **Aldelaijan, S**, Y Khouj, M Khosravi, T Harris, D O'Farrell, M Jacobson, J Seuntjens, S Devic, IM Buzurovic (2020) "Automatic HDR applicator and x-ray marker quality assurance using radiochromic film dosimetry." Joint AAPM/COMP Virtual Meeting
2. **Aldelaijan, S**, M Bhagwat, D O'Farrell, T Harris, M Weiler, C Guthier, R Cormack, J Seuntjens, S Devic, PM Devlin, IM Buzurovic (2019) "In-vivo dose measurements for HDR surface brachytherapy: comparing results of radiochromic film dosimetry to TG43 and advanced collapsed cone engine (ACE) dose calculations." ABS Annual Meeting, Miami, USA
3. **Aldelaijan, S**, P Papaconstadopoulos, J Schneider, H Bekerat, J Seuntjens, I Buzurovic, S Devic (2018) "Abstract#286: Decomposition of source dwell positions and dwell times: A novel method for accurate source tracking and quality assurance in HDR brachytherapy based on film dosimetry.", ABS Annual Meeting, San Francisco, USA
4. **Aldelaijan, S**, Wadi-Ramahi S, Nobah A, Moftah B, Devic S, Jastaniyah N (2017) "Commissioning of HDR Brachytherapy combined with an applicator-guided SBRT boost for advanced cervical cancer," ABS Annual Meeting, Boston, USA,
5. **Aldelaijan, S**, Bekerat H, Buzurovic I, Devlin P, DeBlois F, Seuntjens J, Collins L, Devic S (2017) "Dose accuracy of HDR Brachytherapy treatment of skin lesions using Freiburg flap applicator based on reference radiochromic film dose measurements," ABS Annual Meeting, Boston, USA,

REFERENCES

Afsharpour H, Landry G, D'Amours M, Enger S, Reniers B, Poon E, Carrier J-F, Verhaegen F and Beaulieu L 2012 ALGEBRA: ALgorithm for the heterogeneous dosimetry based on GEANT4 for BRAchytherapy *Phys. Med. Biol.* **57** 3273–3280

Aldelaijan S, Devic S, Mohammed H, Tomic N, Liang L-H, DeBlois F and Seuntjens J 2010 Evaluation of EBT-2 model GAFCHROMIC^{TM} film performance in water *Medical Physics* **37** 3687–93

Andrés C, Castillo A del, Tortosa R, Alonso D and Barquero R 2010 A comprehensive study of the Gafchromic EBT2 radiochromic film. A comparison with EBT *Medical Physics* **37** 6271–8

Arjomandy B, Tailor R, Anand A, Sahoo N, Gillin M, Prado K and Vicic M 2010 Energy dependence and dose response of Gafchromic EBT2 film over a wide range of photon, electron, and proton beam energies *Medical Physics* **37** 1942–7

Arjomandy B, Tailor R, Zhao L and Devic S 2012 EBT2 film as a depth-dose measurement tool for radiotherapy beams over a wide range of energies and modalities *Medical Physics* **39** 912–21

Aronowitz J N 2015 Afterloading: The Technique That Rescued Brachytherapy *International Journal of Radiation Oncology*Biology*Physics* **92** 479–87

Aronowitz J N 2008 The "Golden Age" of prostate brachytherapy: A cautionary tale *Brachytherapy* **7** 55–9

Aronowitz J N, Aronowitz S V and Robison R F 2007 Classics in brachytherapy: Margaret Cleaves introduces gynecologic brachytherapy *Brachytherapy* **6** 293–7

Asgharizadeh S, Bekerat H, Syme A, Aldelaijan S, DeBlois F, Vuong T, Evans M, Seuntjens J and Devic S 2015 Radiochromic film–based quality assurance for CT-based high-dose-rate brachytherapy *Brachytherapy* **14** 578–85

Avanzo M, Rink A, Dassie A, Massarut S, Roncadin M, Borsatti E and Capra E 2012 In vivo dosimetry with radiochromic films in low-voltage intraoperative radiotherapy of the breast *Medical Physics* **39** 2359–68

Awunor O A, Dixon B and Walker C 2013 Direct reconstruction and associated uncertainties of ^{192}Ir source dwell positions in ring applicators using gafchromic film in the treatment planning of HDR brachytherapy cervix patients *Physics in Medicine and Biology* **58** 3207–25

Beaulieu L, Tedgren Å C, Carrier J-F, Davis S D, Mourtada F, Rivard M J, Thomson R M, Verhaegen F, Wareing T A and Williamson J F 2012 Report of the Task Group 186 on model-based dose calculation methods in brachytherapy beyond the TG-43 formalism: Current status and recommendations for clinical implementation *Medical Physics* **39** 6208–36

Becquerel H 1896 Sur les radiations émises par phosphorescence *Comptes Rendus* **122** 501–503

Bekerat H, Devic S, Deblois F, Singh K, Sarfehnia A, Seuntjens J, Shih S, Yu X and Lewis D 2014 Improving the energy response of external beam therapy (EBT) GafChromic^{TM} dosimetry films at low energies (≤100 keV) *Medical Physics* **41** 022101

Bert C, Kellermeier M and Tanderup K 2016 Electromagnetic tracking for treatment verification in interstitial brachytherapy *Journal of Contemporary Brachytherapy* **8** 448–53

Bissonnette J-P, Balter P A, Dong L, Langen K M, Lovelock D M, Miften M, Moseley D J, Pouliot J, Sonke J-J and Yoo S 2012 Quality assurance for image-guided radiation therapy utilizing CT-based technologies: A report of the AAPM TG-179 *Medical Physics* **39** 1946–63

Bortfeld T 2006 IMRT: A review and preview *Physics in Medicine and Biology* **51** R363–R379

Butler W M, Bice W S, DeWerd L A, Hevezi J M, Huq M S, Ibbott G S, Palta J R, Rivard M J, Seuntjens J P and Thomadsen B R 2008 Third-party brachytherapy source calibrations and physicist responsibilities: Report of the AAPM Low Energy Brachytherapy Source Calibration Working Group *Medical Physics* **35** 3860–5

Butson M J, Cheung T and Yu P K N 2005 Absorption spectra variations of EBT radiochromic film from radiation exposure *Physics in Medicine and Biology* **50** N135–N140

Butson M J, Cheung T, Yu P K N and Alnawaf H 2009 Dose and absorption spectra response of EBT2 Gafchromic film to high energy x-rays *Australas. Phys. Eng. Sci. Med.* **32** 196–202

Callaghan C M, Adams Q, Flynn R T, Wu X, Xu W and Kim Y 2019 Systematic Review of Intensity-Modulated Brachytherapy (IMBT): Static and Dynamic Techniques *International Journal of Radiation Oncology*Biology*Physics* **105** 206–21

Castelnau-Marchand P, Chargari C, Haie-Meder C and Mazeron R 2016 Image-guided adaptive brachytherapy in locally advanced cervical cancer: Recent advances and perspectives *Current Opinion in Oncology* **28** 419–28

Chamberland M J P, Taylor R E P, Rogers D W O and Thomson R M 2016 egs_brachy: a versatile and fast Monte Carlo code for brachytherapy *Phys. Med. Biol.* **61** 8214–8231

Chang L, Ho S Y, Ding H J, Lee T F and Chen P Y 2014 Dependency of EBT2 film calibration curve on postirradiation time *Medical Physics* **41** 1–8

Chibani O and Ma C C-M 2014 HDRMC, an accelerated Monte Carlo dose calculator for high dose rate brachytherapy with CT-compatible applicators *Medical Physics* **41** 051712

Chibani O and Williamson J F 2005 M: A sub-minute Monte Carlo dose calculation engine for prostate implants *Medical Physics* **32** 3688–98

Chiu-Tsao S-T, Astrahan M a, Finger P T, Followill D S, Meigooni A S, Melhus C S, Mourtada F, Napolitano M E, Nath R, Rivard M J, Rogers D W O and Thomson R M 2012 TG-129 Dosimetry of (125)I and (103)Pd COMS eye plaques for intraocular tumors *Medical physics* **39** 6161–84

Cormack R A 2008 Quality Assurance Issues for Computed Tomography–, Ultrasound–, and Magnetic Resonance Imaging–Guided Brachytherapy *International Journal of Radiation Oncology*Biology*Physics* **71** S136–41

Crook J 2015 Long-term oncologic outcomes of radical prostatectomy compared with brachytherapy-based approaches for intermediate- and high-risk prostate cancer *Brachytherapy* **14** 142–7

Cunha J A M, Flynn R, Bélanger C, Callaghan C, Kim Y, Jia X, Chen Z and Beaulieu L 2020 Brachytherapy Future Directions *Seminars in Radiation Oncology* **30** 94–106

Cunha J A M, Mellis K, Sethi R, Siauw T, Sudhyadhom A, Garg A, Goldberg K, Hsu I-C and Pouliot J 2015 Evaluation of PC-ISO for customized, 3D printed, gynecologic HDR brachytherapy applicators *Journal of Applied Clinical Medical Physics* **16** 246–53

Dadkhah H, Kim Y, Wu X and Flynn R T 2015 Multihelix rotating shield brachytherapy for cervical cancer *Medical Physics* **42** 6579–88

Damato A L and Viswanathan A N 2015 Magnetic Resonance–Guided Gynecologic Brachytherapy *Magnetic Resonance Imaging Clinics of North America* **23** 633–42

D'Amico A V, Whittington R, Malkowicz S B, Schultz D, Blank K, Broderick G A, Tomaszewski J E, Renshaw A A, Kaplan I, Beard C J and Wein A 1998 Biochemical Outcome After Radical Prostatectomy, External Beam Radiation Therapy, or Interstitial Radiation Therapy for Clinically Localized Prostate Cancer **280** 6

Das R K, Patel R, Shah H, Odau H and Kuske R R 2004 3D CT–based high-dose-rate breast brachytherapy implants: treatment planning and quality assurance *International Journal of Radiation Oncology*Biology*Physics* **59** 1224–8

DeCunha J M and Enger S A 2018 A new delivery system to resolve dosimetric issues in intravascular brachytherapy *Brachytherapy* **17** 634–43

Devic S 2012 MRI simulation for radiotherapy treatment planning *Medical Physics* **39** 6701–11

Devic S 2011 Radiochromic film dosimetry: Past, present, and future *Physica Medica* **27** 122–34

Devic S, Aldelaijan S, Mohammed H, Tomic N, Liang L-H, Deblois F and Seuntjens J 2010 Absorption spectra time evolution of EBT-2 model GAFCHROMIC film *Medical Physics* **37** 2207–14

Devic S, Seuntjens J, Hegyi G, Podgorsak E B, Soares C G, Kirov A S, Ali I, Williamson J F and Elizondo A 2004 Dosimetric properties of improved GafChromic films for seven different digitizers *Medical Physics* **31** 2392–401

Devic S, Tomic N and Lewis D 2016a Reference radiochromic film dosimetry: Review of technical aspects *Physica Medica* **32** 541–56

Devic S, Tomic N and Lewis D 2016b Reference radiochromic film dosimetry: Review of technical aspects *Physica Medica* **32** 541–56

Devic S, Tomic N, Soares C G and Podgorsak E B 2009 Optimizing the dynamic range extension of a radiochromic film dosimetry system *Medical Physics* **36** 429–37

Devic S, Vuong T, Moftah B, Evans M, Podgorsak E B, Poon E and Verhaegen F 2007 Image-guided high dose rate endorectal brachytherapy *Medical Physics* **34** 4451–8

Devlin P M 2016 *Brachytherapy: applications and techniques* (Demos Medical Publishing)

DeWerd L A, Ibbott G S, Meigooni A S, Mitch M G, Rivard M J, Stump K E, Thomadsen B R and Venselaar J L M 2011 A dosimetric uncertainty analysis for photon-emitting brachytherapy sources: Report of AAPM Task Group No. 138 and GEC-ESTRO *Medical Physics* **38** 782–801

Dimopoulos J C A, Petrow P, Tanderup K, Petric P, Berger D, Kirisits C, Pedersen E M, Van Limbergen E, Haie-Meder C and Pötter R 2012 Recommendations from Gynaecological (GYN) GEC-ESTRO Working Group (IV): Basic principles and parameters for MR imaging within the frame of image based adaptive cervix cancer brachytherapy *Radiotherapy and Oncology* **103** 113–22

Enger S A, Vijande J and Rivard M J 2020 Model-Based Dose Calculation Algorithms for Brachytherapy Dosimetry *Seminars in Radiation Oncology* **30** 77–86

Espinoza A, Petasecca M, Cutajar D, Fuduli I, Howie A, Bucci J, Corde S, Jackson M, Zaider M, Lerch M L F and Rosenfeld A B 2015 Pretreatment verification of high dose rate brachytherapy plans using the ‘magic phantom’ system *Biomedical Physics & Engineering Express* **1** 025201–025201

Evans M D C, Devic S and Podgorsak E B 2007 High dose-rate brachytherapy source position quality assurance using radiochromic film *Medical Dosimetry* **32** 13–5

Famulari G, Duclos M and Enger S A 2020 A novel 169Yb-based dynamic-shield intensity modulated brachytherapy delivery system for prostate cancer *Medical Physics* **47** 859–68

Famulari G, Renaud M-A, Poole C M, Evans M D C, Seuntjens J and Enger S A 2018 RapidBrachyMCTPS: a Monte Carlo-based treatment planning system for brachytherapy applications *Phys. Med. Biol.* **63** 175007

Ford E, Conroy L, Dong L, Santos L F de L, Greener A, Kim G G-Y, Johnson J, Johnson P, Mechalakos J G, Napolitano B, Parker S, Schofield D, Smith K, Yorke E and Wells M 2020 Strategies for effective physics plan and chart review in radiation therapy: Report of AAPM Task Group 275 *Medical Physics* **47** e236–72

Fulkerson R K, Perez-Calatayud J, Ballester F, Buzurovic I, Kim Y, Niatsetski Y, Ouhib Z, Pai S, Rivard M J, Rong Y, Siebert F-A, Thomadsen B R and Weigand F 2020 Surface brachytherapy: Joint report of the AAPM and the GEC-ESTRO Task Group No. 253 *Medical Physics* **47** e951-87

Georg P, Lang S, Dimopoulos J C A, Dörr W, Sturdza A E, Berger D, Georg D, Kirisits C and Pötter R 2011 Dose–Volume Histogram Parameters and Late Side Effects in Magnetic Resonance Image–Guided Adaptive Cervical Cancer Brachytherapy *International Journal of Radiation Oncology*Biology*Physics* **79** 356–62

Gill B S, Lin J F, Krivak T C, Sukumvanich P, Laskey R A, Ross M S, Lesnock J L and Beriwal S 2014 National cancer data base analysis of radiation therapy consolidation modality for cervical cancer: The impact of new technological advancements *International Journal of Radiation Oncology Biology Physics* **90** 1083–90

Goodsitt M M, Carson P L, Witt S, Hykes D L and Kofler J M 1998 Real-time B-mode ultrasound quality control test procedures. Report of AAPM Ultrasound Task Group No. 1 *Medical Physics* **25** 1385–406

Goy B W, Burchette R, Soper M S, Chang T and Cosmatos H A 2020 Ten-Year Treatment Outcomes of Radical Prostatectomy Vs External Beam Radiation Therapy Vs Brachytherapy for 1503 Patients With Intermediate-risk Prostate Cancer *Urology* **136** 180–9

Grover S, Harkenrider M M, Cho L P, Erickson B, Small C, Small W and Viswanathan A N 2016 Image Guided Cervical Brachytherapy: 2014 Survey of the American Brachytherapy Society *International Journal of Radiation Oncology Biology Physics* **94** 598–604

Guthier C V, Devlin P M, Harris T C, O'Farrell D A, Cormack R A and Buzurovic I 2020 Development and clinical implementation of semi-automated treatment planning including 3D printable applicator holders in complex skin brachytherapy *Medical Physics* **47** 869–79

Haie-Meder C, Pötter R, Van Limbergen E, Briot E, De Brabandere M, Dimopoulos J, Dumas I, Hellebust T P, Kirisits C, Lang S, Muschitz S, Nevinson J, Nulens A, Petrow P and Wachter-Gerstner N 2005 Recommendations from Gynaecological (GYN) GEC-ESTRO Working Group (I): Concepts and terms in 3D image based 3D treatment planning in cervix cancer brachytherapy with emphasis on MRI assessment of GTV and CTV *Radiotherapy and Oncology* **74** 235–45

Hammer C G, Rosen B S, Fagerstrom J M, Culberson W S and DeWerd L A 2018 Experimental investigation of GafChromic ® EBT3 intrinsic energy dependence with kilovoltage x rays, 137 Cs, and 60 Co *Medical Physics* **45** 448–59

Han K, Marchand E-L, Croke J and Vuong T 2017 EBRT or Brachytherapy? *Emerging Technologies in Brachytherapy, Edited by William Y. Song, Kari Tanderup, Bradley R. Pieters* (CRC Press, Taylor & Francis Group) p 445

Han K, Milosevic M, Fyles A, Pintilie M and Viswanathan A N 2013 Trends in the utilization of brachytherapy in cervical cancer in the United States *International Journal of Radiation Oncology Biology Physics* **87** 111–9

Hellebust T P, Kirisits C, Berger D, Pérez-Calatayud J, De Brabandere M, De Leeuw A, Dumas I, Hudej R, Lowe G, Wills R and Tanderup K 2010 Recommendations from Gynaecological (GYN) GEC-ESTRO Working Group: Considerations and pitfalls in commissioning and applicator reconstruction in 3D image-based treatment planning of cervix cancer brachytherapy *Radiotherapy and Oncology* **96** 153–60

Horwitz E M 2012 ABS brachytherapy consensus guidelines *Brachytherapy* **11** 4–5

ICRU Report 38 1985 *Dose and Volume Specifications for Reporting Intracavitary Therapy in Gynecology* (Bethesda: International Commission on Radiation Units and Measurements)

ICRU Report 50 1993 *Prescribing , recording, and reporting photon beam therapy* (Bethesda: International Commission on Radiation Units and Measurements)

ICRU Report 58 1997 *Recommended Dose and Volume Specification for Reporting Interstitial Brachytherapy* (Bethesda: International Commission on Radiation Units and Measurements)

ICRU Report 89 2016 *Prescribing, Recording, and Reporting Brachytherapy for Cancer of the Cervix:* (Journal of the International Commission on Radiation Units and Measurements) Online: 10.1093/jicru/ndw027

Ishmael Parsai E, Ouhib Z and Orton C G 2017 In the era of IGRT and small- and focal-field external beam radiotherapy, brachytherapy is a dying modality *Medical Physics* **44** 351–4

Jursinic P A 2014 Quality assurance measurements for high-dose-rate brachytherapy without film *Journal of Applied Clinical Medical Physics* **15** 246–61

Kellermeier M, Herbolzheimer J, Kreppner S, Lotter M, Strnad V and Bert C 2017 Electromagnetic tracking (EMT) technology for improved treatment quality assurance in interstitial brachytherapy *Journal of Applied Clinical Medical Physics* **18** 211–22

Kertzscher G and Beddar S 2017 Inorganic scintillation detectors based on Eu-activated phosphors for ^{192}Ir brachytherapy *Physics in Medicine and Biology* **62** 5046–75

Kertzscher G and Beddar S 2019 Inorganic scintillation detectors for ^{192}Ir brachytherapy *Physics in Medicine and Biology* **64** 225018

Kertzscher G and Beddar S 2016 Ruby-based inorganic scintillation detectors for ^{192}Ir brachytherapy *Physics in Medicine and Biology* **61** 7744–64

Keynes G 1932 The radium treatment of carcinoma of the breast *Br J Surg* **19** 415–480

Kirisits C, Rivard M J, Baltas D, Ballester F, De Brabandere M, Van Der Laarse R, Niatsetski Y, Papagiannis P, Hellebust T P, Perez-Calatayud J, Tanderup K, Venselaar J L M and Siebert F A 2014 Review of clinical brachytherapy uncertainties: Analysis guidelines of GEC-ESTRO and the AAPM *Radiotherapy and Oncology* **110** 199–212

Klassen N V, Zwan L van der and Cygler J 1997 GafChromic MD-55: Investigated as a precision dosimeter *Medical Physics* **24** 1924–34

Kubo H D, Glasgow G P, Pethel T D, Thomadsen B R and Williamson J F 1998 High dose-rate brachytherapy treatment delivery: Report of the AAPM Radiation Therapy Committee Task Group No. 59 *Medical Physics* **25** 375–403

Kutcher G J, Coia L, Gillin M, Hanson W F, Leibel S, Morton R J, Palta J R, Purdy J A, Reinstein L E, Svensson G K, Weller M and Wingfield L 1994 Comprehensive QA for radiation oncology: Report of AAPM Radiation Therapy Committee Task Group 40 *Medical Physics* **21** 581–618

Likhacheva A O, Devlin P M, Shirvani S M, Barker C A, Beron P, Bhatnagar A, Doggett S W, Hochman L, Hsu C, Kasper M, Keisch M, Mutyala S, Prestidge B, Villalba S R, Shukla V, Sundararaman S and Kamrava M 2017 Skin surface brachytherapy: A survey of contemporary practice patterns *Brachytherapy* **16** 223–9

Lillicrap S C 2000 Physics Aspects of Quality Control in Radiotherapy (Report No. 81) *Physics in Medicine and Biology* **45** 815–815

Lindegaard J C, Madsen M L, Traberg A, Meisner B, Nielsen S K, Tanderup K, Spejlborg H, Fokdal L U and Nørrevang O 2016 Individualised 3D printed vaginal template for MRI guided brachytherapy in locally advanced cervical cancer *Radiotherapy and Oncology* **118** 173–5

MacKee G M 1921 X-rays and radium in the treatment of diseases of the skin *Publisher: Lea & Febiger*

Mahmood U, Pugh T, Frank S, Levy L, Walker G, Haque W, Koshy M, Graber W, Swanson D, Hoffman K, Kuban D and Lee A 2014 Declining use of brachytherapy for the treatment of prostate cancer *Brachytherapy* **13** 157–62

Mao X, Pineau J, Keyes R and Enger S A 2020 RapidBrachyDL: Rapid Radiation Dose Calculations in Brachytherapy via Deep Learning *International Journal of Radiation Oncology*Biology*Physics* Online: http://www.sciencedirect.com/science/article/pii/S0360301620311226

Mazeron J J, Scalliet P, Limbergen E V and Lartigau E 2003 Radiobiology of Brachytherapy and the Dose-Rate Effect *GEC-ESTRO handbook* 1–10

McLaughlin W L, Yun-Dong C, Soares C G, Miller A, Van Dyk G and Lewis D F 1991 Sensitometry of the response of a new radiochromic film dosimeter to gamma radiation and electron beams *Nuclear Inst. and Methods in Physics Research, A* **302** 165–76

Morcos M, Antaki M, Viswanathan A N and Enger S A 2020 A novel minimally invasive dynamic-shield, intensity-modulated brachytherapy system for the treatment of cervical cancer *Medical Physics* Online: https://doi.org/10.1002/mp.14459

Morcos M and Enger S A 2020 Monte Carlo dosimetry study of novel rotating MRI-compatible shielded tandems for intensity modulated cervix brachytherapy *Physica Medica: European Journal of Medical Physics* **71** 178–84

Morris W J, Tyldesley S, Rodda S, Halperin R, Pai H, McKenzie M, Duncan G, Morton G, Hamm J and Murray N 2017 Androgen Suppression Combined with Elective Nodal and Dose Escalated Radiation Therapy (the ASCENDE-RT Trial): An Analysis of Survival Endpoints for a Randomized Trial Comparing a Low-Dose-Rate Brachytherapy Boost to a Dose-Escalated External Beam Boost for High- and Intermediate-risk Prostate Cancer *International Journal of Radiation Oncology, Biology, Physics* **98** 275–85

Mutic S, Palta J R, Butker E K, Das I J, Huq M S, Loo L-N D, Salter B J, McCollough C H and Dyk J V 2003 Quality assurance for computed-tomography simulators and the computed-tomography-simulation process: Report of the AAPM Radiation Therapy Committee Task Group No. 66 *Medical Physics* **30** 2762–92

Nag S, Cardenes H, Chang S, Das I J, Erickson B, Ibbott G S, Lowenstein J, Roll J, Thomadsen B and Varia M 2004 Proposed guidelines for image-based intracavitary brachytherapy for cervical carcinoma: Report from Image-Guided Brachytherapy Working Group *International Journal of Radiation Oncology*Biology*Physics* **60** 1160–72

Nath R, Amols H, Coffey C, Duggan D, Jani S, Li Z, Schell M, Soares C, Whiting J, Cole P E, Crocker I and Schwartz R 1999 Intravascular brachytherapy physics: Report of the AAPM Radiation Therapy Committee Task Group No. 60 *Medical Physics* **26** 119–52

Nath R, Anderson L L, Luxton G, Weaver K A, Williamson J F and Meigooni A S 1995 Dosimetry of interstitial brachytherapy sources: Recommendations of the AAPM Radiation Therapy Committee Task Group No. 43 *Medical Physics* **22** 209–34

Nath R, Anderson L L, Meli J A, Olch A J, Stitt J A and Williamson J F 1997 Code of practice for brachytherapy physics: Report of the AAPM Radiation Therapy Committee Task Group No. 56 *Medical Physics* **24** 1557–98

Nath R, Bice W S, Butler W M, Chen Z, Meigooni A S, Narayana V, Rivard M J and Yu Y 2009 AAPM recommendations on dose prescription and reporting methods for permanent interstitial brachytherapy for prostate cancer: Report of Task Group 137 *Medical Physics* **36** 5310–22

Niroomand-Rad A, Blackwell C R, Coursey B M, Gall K P, Galvin J M, McLaughlin W L, Meigooni a S, Nath R, Rodgers J E and Soares C G 1998 Radiochromic film dosimetry: Recommendations of AAPM Radiation Therapy Committee Task Group 55 *Medical physics* **25** 2093–115

Okamoto H, Aikawa A, Wakita A, Yoshio K, Murakami N, Nakamura S, Hamada M, Abe Y and Itami J 2014 Dose error from deviation of dwell time and source position for high dose-rate 192Ir in remote afterloading system *Journal of Radiation Research* **55** 780–7

Palmer A, Bradley D and Nisbet A 2012 Physics-aspects of dose accuracy in high dose rate (HDR) brachytherapy: Source dosimetry, treatment planning, equipment performance and in vivo verification techniques *Journal of Contemporary Brachytherapy* **4** 81–91

Palmer A L, Bradley D A and Nisbet A 2014 Dosimetric audit in brachytherapy *British Journal of Radiology* **87** 20140105

Palmer A L, Lee C, Ratcliffe A J, Bradley D and Nisbet A 2013 Design and implementation of a film dosimetry audit tool for comparison of planned and delivered dose distributions in high dose rate (HDR) brachytherapy *Physics in Medicine and Biology* **58** 6623–40

Park S, Kang S K, Cheong K H, Hwang T, Kim H, Han T, Lee M Y, Kim K, Bae H, Su Kim H, Han Kim J, Jae Oh S and Suh J S 2012 Variations in dose distribution and optical properties of Gafchromic TM EBT2 film according to scanning mode *Medical Physics* **39** 2524–35

Perez-Calatayud J B F Das RK, Dewerd LA, Ibbott GS, Meigooni AS 2012 Dose Calculation for Photon-Emitting Brachytherapy Sources with Average Energy Higher than 50 keV: Full Report of the AAPM and ESTRO Report of the High Energy Brachytherapy Source Dosimetry (HEBD) Working Group *Med Phys* **39** 2904–29

Petereit D G, Frank S J, Viswanathan A N, Erickson B, Eifel P, Nguyen P L and Wazer D E 2015 Brachytherapy: Where Has It Gone? *JCO* **33** 980–2

Pettersen M N, Aird E and Olsen D R 2008 Quality assurance of dosimetry and the impact on sample size in randomized clinical trials *Radiotherapy and Oncology* **86** 195–9

Pfeiffer D, Sutlief S, Feng W, Pierce H M and Kofler J 2008 AAPM Task Group 128: Quality assurance tests for prostate brachytherapy ultrasound systems *Medical Physics* **35** 5471–89

Podgorsak E B 2005 *Radiation oncology physics: a handbook for teachers and students* (Vienna: International Atomic Energy Agency) Online: https://www-pub.iaea.org/mtcd/publications/pdf/pub1196_web.pdf

Pötter R, Georg P, Dimopoulos J C A, Grimm M, Berger D, Nesvacil N, Georg D, Schmid M P, Reinthaller A, Sturdza A and Kirisits C 2011 Clinical outcome of protocol based image (MRI) guided adaptive brachytherapy combined with 3D conformal radiotherapy with or without chemotherapy in patients with locally advanced cervical cancer *Radiotherapy and Oncology* **100** 116–23

Pötter R, Haie-Meder C, Van Limbergen E, Barillot I, De Brabandere M, Dimopoulos J, Dumas I, Erickson B, Lang S, Nulens A, Petrow P, Rownd J and Kirisits C 2006 Recommendations from gynaecological (GYN) GEC ESTRO working group (II): Concepts and terms in 3D image-based treatment planning in cervix cancer brachytherapy - 3D dose volume parameters and aspects of 3D image-based anatomy, radiation physics, radiobiolo *Radiotherapy and Oncology* **78** 67–77

Potters L, Cao Y, Calugaru E, Torre T, Fearn P and Wang X-H 2001 A comprehensive review of CT-based dosimetry parameters and biochemical control in patients treated with permanent prostate brachytherapy *International Journal of Radiation Oncology*Biology*Physics* **50** 605–14

Poulin E, Racine E, Binnekamp D and Beaulieu L 2015 Fast, automatic, and accurate catheter reconstruction in HDR brachytherapy using an electromagnetic 3D tracking system *Medical Physics* **42** 1227–32

Price R R, Axel L, Morgan T, Newman R, Perman W, Schneiders N, Selikson M, Wood M and Thomas S R 1990 Quality assurance methods and phantoms for magnetic resonance imaging: Report of AAPM nuclear magnetic resonance Task Group No. 1 *Medical Physics* **17** 287–95

Richley L, John A C, Coomber H and Fletcher S 2010 Evaluation and optimization of the new EBT2 radiochromic film dosimetry system for patient dose verification in radiotherapy *Phys. Med. Biol.* **55** 2601–2617

Ricotti R, Vavassori A, Bazani A, Ciardo D, Pansini F, Spoto R, Sammarco V, Cattani F, Baroni G, Orecchia R and Jereczek-Fossa B A 2016 3D-printed applicators for high dose rate brachytherapy: Dosimetric assessment at different infill percentage *Physica Medica* **32** 1698–706

Rijkmans E C, Nout R A, Rutten I H H M, Ketelaars M, Neelis K J, Laman M S, Coen V L M A, Gaarenstroom K N, Kroep J R and Creutzberg C L 2014 Improved survival of patients with cervical cancer treated with image-guided brachytherapy compared with conventional brachytherapy *Gynecologic Oncology* **135** 231–8

Rink A, Lewis D F, Varma S, Vitkin I A and Jaffray D A 2008 Temperature and hydration effects on absorbance spectra and radiation sensitivity of a radiochromic medium *Medical Physics* **35** 4545–55

Rivard M J, Coursey B M, DeWerd L A, Hanson W F, Huq M S, Ibbott G S, Mitch M G, Nath R and Williamson J F 2004 Update of AAPM Task Group No. 43 Report: A revised AAPM protocol for brachytherapy dose calculations *Medical Physics* **31** 633–74

Roozen K, Kron T, Haworth A and Franich R 2011 Evaluation of EBT radiochromic film using a multiple exposure technique *Australas Phys Eng Sci Med* **34** 281–9

Safigholi H, Han D Y, Soliman A and Song W Y 2018 Direction modulated brachytherapy (DMBT) tandem applicator for cervical cancer treatment: Choosing the optimal shielding material *Medical Physics* **45** 3524–33

Sarfehnia A, Kawrakow I and Seuntjens J 2010 Direct measurement of absorbed dose to water in HDR ^{192}Ir brachytherapy: Water calorimetry, ionization chamber, Gafchromic film, and TG-43 *Medical Physics* **37** 1924–32

Schmid M P, Fokdal L, Westerveld H, Chargari C, Rohl L, Morice P, Nesvacil N, Mazeron R, Haie-Meder C, Pötter R and Nout R A 2020 Recommendations from gynaecological (GYN) GEC-ESTRO working group – ACROP: Target concept for image guided adaptive brachytherapy in primary vaginal cancer *Radiotherapy and Oncology* **145** 36–44

Schmid M P, Nesvacil N, Pötter R, Kronreif G and Kirisits C 2016 Transrectal ultrasound for image-guided adaptive brachytherapy in cervix cancer – An alternative to MRI for target definition? *Radiotherapy and Oncology* **120** 467–72

Seneviratne D, McLaughlin C, Todor D, Kaplan B and Fields E C 2018 The CivaSheet: The new frontier of intraoperative radiation therapy or a pricier alternative to LDR brachytherapy? *Advances in Radiation Oncology* **3** 87–91

Simpson D R, Scanderbeg D J, Carmona R, McMurtrie R M, Einck J, Mell L K, McHale M T, Saenz C C, Plaxe S C, Harrison T, Mundt A J and Yashar C M 2015 Clinical Outcomes of Computed Tomography–Based Volumetric Brachytherapy Planning for Cervical Cancer *International Journal of Radiation Oncology*Biology*Physics* **93** 150–7

Smith R L, Hanlon M, Panettieri V, Millar J L, Matheson B, Haworth A and Franich R D 2018 An integrated system for clinical treatment verification of HDR prostate brachytherapy combining source tracking with pretreatment imaging *Brachytherapy* **17** 111–21

Smith R L, Haworth A, Panettieri V, Millar J L and Franich R D 2016 A method for verification of treatment delivery in HDR prostate brachytherapy using a flat panel detector for both imaging and source tracking *Medical Physics* **43** 2435–42

Song H, Bowsher J, Das S and Yin F F 2009 Tracking brachytherapy sources using emission imaging with one flat panel detector *Medical Physics* **36** 1109–11

Spratt D E, Zumsteg Z S, Ghadjar P, Kollmeier M A, Pei X, Cohen G, Polkinghorn W, Yamada Y and Zelefsky M J 2014 Comparison of high-dose (86.4 Gy) IMRT vs combined brachytherapy plus IMRT for intermediate-risk prostate cancer *BJU International* **114** 360–7

Stewart A J and Bentzen S M 2011 Radiobiological Aspects of Brachytherapy in the Era of 3-Dimensional Imaging *Gynecologic Radiation Therapy* (Berlin: Springer) p 301

Sturdza A, Pötter R, Fokdal L U, Haie-Meder C, Tan L T, Mazeron R, Petric P, Šegedin B, Jurgenliemk-Schulz I M, Nomden C, Gillham C, McArdle O, Van Limbergen E, Janssen H, Hoskin P, Lowe G, Tharavichitkul E, Villafranca E, Mahantshetty U, Georg P, Kirchheiner K, Kirisits C, Tanderup K and Lindegaard J C 2016 Image guided brachytherapy in locally advanced cervical cancer: Improved pelvic control and survival in RetroEMBRACE, a multicenter cohort study *Radiotherapy and Oncology* **120** 428–33

Sutherland J G H and Rogers D W O 2010 Monte Carlo calculated absorbed-dose energy dependence of EBT and EBT2 film *Medical Physics* **37** 1110–6

Sylvester J E, Grimm P D, Wong J, Galbreath R W, Merrick G and Blasko J C 2011 Fifteen-Year Biochemical Relapse-Free Survival, Cause-Specific Survival, and Overall Survival Following I125 Prostate Brachytherapy in Clinically Localized Prostate Cancer: Seattle Experience *International Journal of Radiation Oncology*Biology*Physics* **81** 376–81

Taggar A S, Phan T, Traptow L, Banerjee R and Doll C M 2017 Cervical cancer brachytherapy in Canada: A focus on interstitial brachytherapy utilization *Brachytherapy* **16** 161–6

Tanderup K, Beddar S, Andersen C E, Kertzscher G and Cygler J E 2013 In vivo dosimetry in brachytherapy *Medical Physics* **40** 070902

Tanderup K, Eifel P J, Yashar C M, Pötter R and Grigsby P W 2014a Curative Radiation Therapy for Locally Advanced Cervical Cancer: Brachytherapy Is NOT Optional *International Journal of Radiation Oncology*Biology*Physics* **88** 537–9

Tanderup K, Hellebust T P, Lang S, Granfeldt J, Pötter R, Lindegaard J C and Kirisits C 2008 Consequences of random and systematic reconstruction uncertainties in 3D image based brachytherapy in cervical cancer *Radiotherapy and Oncology* **89** 156–63

Tanderup K, Ménard C, Polgar C, Lindegaard J C, Kirisits C and Pötter R 2017 Advancements in brachytherapy *Advanced Drug Delivery Reviews* **109** 15–25

Tanderup K, Nielsen S K, Nyvang G-B, Pedersen E M, Røhl L, Aagaard T, Fokdal L and Lindegaard J C 2010 From point A to the sculpted pear: MR image guidance significantly improves tumour dose and sparing of organs at risk in brachytherapy of cervical cancer *Radiotherapy and Oncology* **94** 173–80

Tanderup K, Viswanathan A N, Kirisits C and Frank S J 2014b Magnetic Resonance Image Guided Brachytherapy *Seminars in Radiation Oncology* **24** 181–91

Taylor R E P, Yegin G and Rogers D W O 2007 Benchmarking BrachyDose: Voxel based EGSnrc Monte Carlo calculations of TG-43 dosimetry parameters *Medical Physics* **34** 445–57

Teoh M, Clark C H, Wood K, Whitaker S and Nisbet A 2011 Volumetric modulated arc therapy: A review of current literature and clinical use in practice *British Journal of Radiology* **84** 967–96

Therriault-Proulx F, Briere T M, Mourtada F, Aubin S, Beddar S and Beaulieu L 2011 A phantom study of an in vivo dosimetry system using plastic scintillation detectors for real-time verification of 192Ir HDR brachytherapy *Medical Physics* **38** 2542–51

Thomadsen B R, Erickson B A, Eifel P J, Hsu I-C, Patel R R, Petereit D G, Fraass B A and Rivard M J 2014 A review of safety, quality management, and practice guidelines for high-dose-rate brachytherapy: Executive summary *Practical Radiation Oncology* **4** 65–70

Viani G A, Manta G B, Stefano E J and De Fendi L I 2009 Brachytherapy for cervix cancer: Low-dose rate or high-dose rate brachytherapy - A meta-analysis of clinical trials *Journal of Experimental and Clinical Cancer Research* **28** 1–12

Vuong T, Szego P, David M, Evans M, Parent J, Mayrand S, Corns R, Burtin P, Faria S and Devic S 2005 The safety and usefulness of high-dose-rate endoluminal brachytherapy as a boost in the treatment of patients with esophageal cancer with external beam radiation with or without chemotherapy *International Journal of Radiation Oncology*Biology*Physics* **63** 758–64

Wadi-Ramahi S, Alnajjar W, Mahmood R, Jastaniyah N and Moftah B 2016 Failure modes and effects analysis in image-guided high-dose-rate brachytherapy: Quality control optimization to reduce errors in treatment volume *Brachytherapy* **15** 669–78

Wallner K, Ellis W, Russell K, Cavanagh W and Blasko J 1999 Use of TRUS to predict pubic arch interference of prostate brachytherapy *International Journal of Radiation Oncology*Biology*Physics* **43** 583–5

Wang W, Viswanathan A N, Damato A L, Chen Y, Tse Z, Pan L, Tokuda J, Seethamraju R T, Dumoulin C L, Schmidt E J and Cormack R A 2015 Evaluation of an active magnetic resonance tracking system for interstitial brachytherapy *Medical Physics* **42** 7114–21

Webster M J, Devic S, Vuong T, Han D Y, Park J C, Scanderbeg D, Lawson J, Song B, Watkins W T, Pawlicki T and Song W Y 2013 Dynamic modulated brachytherapy (DMBT) for rectal cancer *Medical Physics* **40** 011718

Williamson J F 2006 Brachytherapy technology and physics practice since 1950: A half-century of progress *Physics in Medicine and Biology* **51** R303–R325

World Health Organization 2007 *Radiotherapy Risk Profile.* (Geneva: WHO Publishing) Online: http://www.who.int/patientsafety/activities/technical/radiotherapy_risk_profile.pdf

Yu Y, Anderson L L, Li Z, Mellenberg D E, Nath R, Schell M C, Waterman F M, Wu A and Blasko J C 1999 Permanent prostate seed implant brachytherapy: Report of the American Association of Physicists in Medicine Task Group No. 64 *Medical Physics* **26** 2054–76

Zaorsky N G, Davis B J, Nguyen P L, Showalter T N, Hoskin P J, Yoshioka Y, Morton G C and Horwitz E M 2017 The evolution of brachytherapy for prostate cancer *Nat Rev Urol* **14** 415–39

Zhou J, Sebastian E, Mangona V and Yan D 2013 Real-time catheter tracking for high-dose-rate prostate brachytherapy using an electromagnetic 3D-guidance device: A preliminary performance study *Medical Physics* **40** 021716

Zhu Y, Kirov A S, Mishra V, Meigooni A S and Williamson J F 1997 Quantitative evaluation of radiochromic film response for two-dimensional dosimetry *Medical Physics* **24** 223–31